

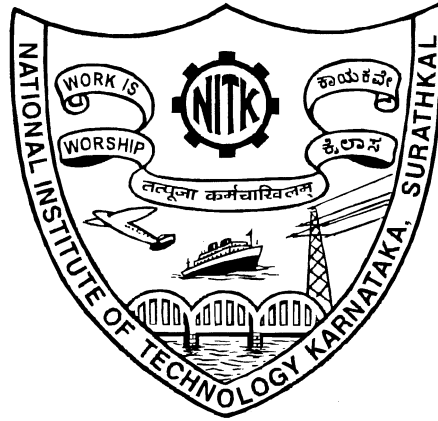
**EARLY DIAGNOSIS OF OSTEOPOROSIS
USING METACARPAL RADIOGRAMMETRY
AND TEXTURE ANALYSIS**

Thesis

Submitted in partial fulfillment of the requirements for the degree of
DOCTOR OF PHILOSOPHY

by

ANU SHAJU AREECKAL



DEPARTMENT OF ELECTRONICS AND COMMUNICATION ENGINEERING,
NATIONAL INSTITUTE OF TECHNOLOGY KARNATAKA,
SURATHKAL, MANGALORE -575025

OCTOBER, 2018

DECLARATION

I hereby *declare* that the Research Thesis entitled **EARLY DIAGNOSIS OF OSTEOPOROSIS USING METACARPAL RADIOGRAMMETRY AND TEXTURE ANALYSIS** which is being submitted to the National Institute of Technology Karnataka, Surathkal in partial fulfillment of the requirements for the award of the Degree of Doctor of Philosophy in Department of Electronics and Communication Engineering is a *bonafide report of the research work carried out by me*. The material contained in this Research Thesis has not been submitted to any University or Institution for the award of any degree.

ANU SHAJU AREECKAL, Reg.No.138044EC13F06.
Department of Electronics and Communication Engineering.

Place: NITK, Surathkal

Date:

CERTIFICATE

This is to *certify* that the Research Thesis entitled **EARLY DIAGNOSIS OF OSTEOPOROSIS USING METACARPAL RADIOGRAMMETRY AND TEXTURE ANALYSIS** submitted by **ANU SHAJU AREECKAL (Register Number: 138044EC13F06)** as the record of the research work carried out by her, is *accepted as the Research Thesis submission* in partial fulfillment of the requirements for the award of degree of Doctor of Philosophy.

Research Guide(s)

(Name and Signature with Date and Seal)

Chairman-DRPC

(Signature with Date and Seal)

ACKNOWLEDGEMENTS

First and foremost, I would like to thank God for His mercy and blessings.

I would like to extend my sincere gratitude and thanks from the bottom of my heart to my Research guide, Dr. Sumam David S., National Institute of Technology Karnataka (NITK), Surathkal, Karnataka, India. I could not thank her enough for the help, support, guidance and care extended to me throughout my PhD programme. This thesis and research work would never have been in the present form without her constant support and encouragement.

I would like to thank my additional Research Guide, Dr. Michel Kocher, Department of TIN, Haute Ecole d'Ingenierie et de Gestion du Canton de Vaud (HEIG-VD), Yverdon les-Bains, Switzerland, for his help, advice and encouragement for the research project. I would also like to thank him for the opportunity and wonderful experience I had during the research interaction at Centre of Biomedical Imaging (CIBM), University Hospital of Geneva (HUG), Geneva, Switzerland.

I would like to thank Dr. Jagannath Kamath, Department of Orthopaedics, Kasturba Medical College (KMC) Hospital, Mangalore, Manipal Academy of Higher Education (MAHE), Karnataka, India, for this research proposal, his medical guidance and help extended for the data collection and throughout the research work. I would also like to thank Dr. Nikil Jayasheelan and other doctors of the Department of Orthopaedics, KMC Hospital, Mangalore, MAHE, Karnataka, India, for their help in the data collection.

I would like to thank Tejaswini Hospital, Mangalore, Karnataka, India, for helping us with the data collection and providing us DXA scans at a discounted cost. I would like to thank District Wenlock Hospital, Mangalore, Karnataka, India, for their help.

I would like to thank Dr. Sophie Zawadynski, Department of Nuclear Medicine, HUG, Switzerland, for her medical and technical advice. I would like to thank the

Department of Radiology and Medical Informatics, HUG, Switzerland, for providing us the Swiss data from HUG for the study. I would also like to thank Dr. Francois Lazeyras, CIBM, HUG, Switzerland, for giving me an opportunity to work at CIBM.

I would like to thank and acknowledge Mathew Sam, Avinash D. Jayakumar and Gautam Sambath, B.Tech students, NITK Surathkal, India, for being a valuable part of this research project by providing their help and support for the work.

I would like to thank my Research Progress Assessment Committee (RPAC) members, Dr. Deepu Vijayaseenan and Dr. Jagannath Nayak, for their valuable advice and support during each phase of my PhD programme. I would also like to thank Dr. Muralidhar Kulkarni, Dr. M.S. Bhat, Dr. U. Sripathi Acharya and Dr. T. Laxminidhi, the Heads of the Department of Electronics and Communication Engineering (E&C), NITK, Surathkal, India, during my PhD programme for their advice and support especially regarding the data collection. I would like to thank the teaching and non-teaching faculty and students of the Department of E&C, NITK, Surathkal, India for their help.

I would like to thank Dr. Sumathi K., Department of Mathematics, Manipal Institute of Technology, MAHE, Manipal, India, for her help in the statistical analysis of the data.

I would like to thank the Reviewers of our publications whose valuable suggestions helped to improve the quality of our publications.

I would like to thank the Institutional Ethics Committee, KMC, Mangalore, MAHE, Manipal, India, for approving our study protocol.

I would like to thank and acknowledge TEQIP-II, NITK, India, for providing us the funding for data collection and for research interaction in HUG, Switzerland.

I would also like to thank the International Office, HEIG-VD, Switzerland, for giving me an opportunity for the research interaction in HUG, Switzerland.

Last but not the least, I would like to thank my friends and family, especially my mother, Mrs. Aney Shaju Areekal, and my sister, Dr. Anju Shaju Areekal, who have been the pillars of my life and whose encouragement and constant faith in me made me the individual I am today.

ABSTRACT

Osteoporosis is a disease characterized by reduction in bone mass and micro-structure, leading to increased risk of fragility fractures. The gold standard technique used for diagnosis of osteoporosis is determination of Bone Mineral Density (BMD) using Dual Energy X-ray Absorptiometry (DXA). DXA is accurate and precise, however it has a high cost of scan and low availability in developing countries. The aim of the research work is to develop a low cost prescreening tool for early diagnosis of osteoporosis using cortical radiogrammetry and trabecular texture analysis of hand and wrist radiographs.

An automatic method for segmentation of the third metacarpal bone shaft from hand and wrist radiographs is proposed using automatically detected anatomical landmarks, intensity profiles and marker-controlled watershed segmentation. From the outer and inner bone edges of the segmented third metacarpal bone shaft, cortical radiogrammetric features are extracted. The proposed method is validated on sample data of two ethnic groups: 138 Indian subjects and 65 Swiss subjects. The proposed segmentation method accurately detected the third metacarpal bone in 89% of Indian sample data and 78% of Swiss sample data. The proposed method shows better performance as compared with the state-of-the-art segmentation method, Active Appearance Model (AAM).

A segmentation approach is proposed to automatically extract the distal radius for trabecular texture analysis. The proposed method extracted the distal radius region-of-interest in 93.5% of Indian sample data and 83% of Swiss sample data. Texture analysis of the trabecular bone in distal radius is done. The extracted features are analyzed using independent sample *t*-test and Pearson correlation analysis. The cortical radiogrammetric features show high discrimination ability in the healthy and low bone mass groups of both Indian and Swiss sample data.

The cortical and texture features are divided into different feature sets. Classifiers are trained on cortical features and statistical and structural texture features for In-

dian sample data and a linear regression model is estimated. Artificial Neural Network (ANN) classifier trained using holdout validation achieves test accuracy of 90.0%. k -Nearest Neighbor (KNN) using 10-fold cross validation achieves an accuracy of 81.7%. The linear regression model developed with the cortical and texture features achieves a significant correlation of 0.671 with DXA-BMD. Classifiers are also trained separately for Indian and Swiss sample population. ANN classifiers trained with significant cortical and statistical and structural texture features show test accuracy of 92.9% with Indian data and 90.9% with Swiss data. Weighted KNN using the same feature set shows test accuracy of 96.2% using holdout validation.

A novel method to measure the cortical volume of the metacarpal bone shaft at a low cost using three dimensional reconstruction from hand X-ray images in three views (Postero-Anterior, 45° and 135° oblique views) is proposed. The Computed Tomography scan of one subject is used to create a template model, from which subject-specific models of other subjects are reconstructed. The 3D reconstruction of the bone is done iteratively by registration of projection and X-ray contours using Iterative Closest Point and Self-Organizing Map, and deformation of the template model using Laplacian surface deformation. The outer and inner bone walls of the metacarpal are modeled separately and the third metacarpal bone shaft is extracted from which cortical volume is measured. The projections of the 3D reconstructed models are compared with manually segmented X-ray images and the mean percentage error in Combined Cortical Thickness (CCT) is 11.18%.

In summary, a low cost prescreening tool for early diagnosis of osteoporosis using cortical radiogrammetry and texture analysis is proposed and validated using sample data of Indian and Swiss population. A low cost method to measure cortical volume of third metacarpal bone shaft using multi-view hand radiographs is also proposed.

This work is done in collaboration with Kasturba Medical College Hospital, Mangalore, India and University Hospital of Geneva, Switzerland.

Keywords: Osteoporosis; Metacarpal radiogrammetry; Texture analysis; Distal radius; Classification; 3D Reconstruction

TABLE OF CONTENTS

ACKNOWLEDGEMENTS	v
ABSTRACT	vii
LIST OF FIGURES	xv
LIST OF TABLES	xxi
ABBREVIATIONS	xxv
1 INTRODUCTION	1
1.1 OSTEOPOROSIS	1
1.2 NEED FOR EARLY DIAGNOSIS	2
1.3 BACKGROUND	3
1.4 MOTIVATION FOR THE RESEARCH WORK	5
1.4.1 Need for a low-cost and widely available diagnostic tool	5
1.4.2 Need for a more accurate measurement	6
1.4.3 Need for a low-cost volumetric measurement	7
1.5 OBJECTIVES OF THE THESIS	7
1.6 PROPOSED METHODOLOGY	8
1.7 MAIN CONTRIBUTIONS OF THE THESIS	9
1.8 ORGANIZATION OF THE THESIS	11
2 DIAGNOSTIC IMAGING BASED TECHNIQUES FOR ASSESSMENT OF OSTEOPOROSIS	13
2.1 INTRODUCTION	13
2.2 QUANTITATIVE IMAGING TECHNIQUES	13
2.2.1 Dual X-ray Absorptiometry (DXA)	14

2.2.2	Quantitative Computed Tomography (QCT)	17
2.2.3	High Resolution peripheral QCT (HR-pQCT)	18
2.2.4	Quantitative Ultrasound (QUS)	19
2.2.5	Magnetic Resonance Imaging (MRI)	20
2.2.6	Digital X-ray Radiogrammetry (DXR)	21
2.2.7	Radiography	22
2.3	SEGMENTATION METHODS	23
2.3.1	Threshold-based methods	23
2.3.2	Edge-based methods	25
2.3.3	Region-based methods	25
2.3.4	Deformable models	27
2.3.5	Deep neural networks	29
2.4	FEATURE EXTRACTION TECHNIQUES	29
2.4.1	Radiogrammetric measurement	30
2.4.2	Bone density measurement	31
2.4.3	Texture analysis	32
2.5	APPROACHES TO DIAGNOSTIC DECISION MAKING	40
2.5.1	Comparison with a reference value	40
2.5.2	Feature selection and supervised learning techniques	41
2.6	PREDICTION OF FRACTURE RISK	51
2.6.1	Trabecular Bone Score (TBS)	51
2.6.2	Finite Element Analysis (FEA)	51
2.6.3	Vertebral Fracture Assessment (VFA)	52
2.6.4	Fracture Risk Calculators	53
2.7	DISCUSSION	55
2.8	CONCLUSION	58
3	CORTICAL RADIOGRAMMETRY OF THIRD METACARPAL BONE	59
3.1	INTRODUCTION	59

3.1.1	Challenges in X-ray imaging	60
3.1.2	Need for automated segmentation	60
3.2	SEGMENTATION OF THIRD METACARPAL USING WATER-SHED ALGORITHM	61
3.2.1	Preprocessing	61
3.2.2	Localization of third metacarpal bone	66
3.2.3	Segmentation using watershed algorithm	68
3.3	SEGMENTATION USING AAM	72
3.3.1	Training stage	73
3.3.2	Testing stage	74
3.4	METACARPAL RADIOGRAMMETRY	74
3.5	RESULTS AND DISCUSSION	76
3.5.1	Calculation of data sample size	76
3.5.2	Dataset	77
3.5.3	Metrics for evaluation of segmentation	78
3.5.4	Segmentation results	79
3.5.5	Comparison with manual segmentation	81
3.5.6	Validation with ground truth measurements	83
3.5.7	Statistical analysis	85
3.5.8	Limitations	86
3.6	CONCLUSION	87
4	TRABECULAR TEXTURE ANALYSIS OF DISTAL RADIUS	89
4.1	INTRODUCTION	89
4.2	SEGMENTATION OF DISTAL RADIUS	90
4.3	TEXTURE ANALYSIS OF TRABECULAR BONE	92
4.4	RESULTS AND DISCUSSION	102
4.4.1	Segmentation results	102
4.4.2	Statistical analysis	103
4.5	CONCLUSION	116

5	CLASSIFICATION USING CORTICAL AND TRABECULAR BONE FEATURES	119
5.1	INTRODUCTION	119
5.2	CLASSIFICATION USING INDIAN SAMPLE DATA	120
5.2.1	Feature selection	124
5.2.2	Classifier	127
5.2.3	Regression analysis	132
5.3	CLASSIFICATION USING INDIAN AND SWISS SAMPLE DATA	133
5.3.1	Classification using statistical and structural features	134
5.3.2	Classification using LBP features	144
5.3.3	Classification using CNN features	147
5.4	DISCUSSION	150
5.5	CONCLUSION	154
6	CORTICAL VOLUMETRY USING 3D RECONSTRUCTION FROM MULTI-VIEW IMAGES	157
6.1	INTRODUCTION	157
6.2	RELATED WORK	157
6.3	THREE DIMENSIONAL RECONSTRUCTION OF THIRD METACARPAL	162
6.3.1	Creation of 3D template model	164
6.3.2	3D reconstruction by iterative deformation	164
6.3.3	Cortical volumetry	167
6.4	RESULTS AND DISCUSSION	168
6.4.1	Dataset	169
6.4.2	Validation of 3D bone reconstruction	169
6.4.3	Validation with manually segmented images	173
6.4.4	Statistical analysis	174
6.4.5	Using the new data to validate the trained classifiers	176
6.5	CONCLUSION	177

7 CONCLUSION AND FUTURE WORK	179
7.1 SUMMARY OF THE WORK	179
7.1.1 Computation time	181
7.1.2 Clinical use	182
7.1.3 Limitations	182
7.2 EXPERTS' FEEDBACK	183
7.3 FUTURE DIRECTIONS	186
 Appendix I: APPROVAL LETTERS AND DOCUMENTS USED FOR THE DATA COLLECTION	 187
 REFERENCES	 203
 LIST OF PUBLICATIONS FROM THE THESIS	 229
 CURRICULUM VITAE	 231

LIST OF FIGURES

1.1	Structure of a healthy and osteoporotic tubular bone (Rock Creek Wellness 2018)	2
1.2	Prevalence of osteoporosis in different countries in 2012 and 2022 (Insider 2013)	3
1.3	Graphical abstract of the proposed methodology	8
2.1	Pipeline of a diagnostic technique to detect osteoporosis	14
2.2	Quantitative imaging techniques used for diagnosis of osteoporosis: (a) Radiographic absorptiometry, (b) Manual radiogrammetry, (c) Photon and X-ray absorptiometry of lumbar spine, (d) DXA of proximal femur, (e) QUS of calcaneum, (f) QCT of spine and (g) DXR (Huddleston 1988; Bonnicksen 1998; Rosholm <i>et al.</i> 2001)	15
2.3	pQCT image of distal radius: (a) Scout view showing the ROI, (b) pQCT image of a premenopausal healthy woman and (c) pQCT image of a postmenopausal osteoporotic woman (Boutroy <i>et al.</i> 2005)	19
2.4	Estimation of BMD from hand radiograph using DXR (Rosholm <i>et al.</i> 2001)	22
2.5	Texture analysis of trabecular bone of (a) healthy and (b) osteoporotic bone (University of Orleans 2014)	23
2.6	An illustration of watershed segmentation using placement of markers (Fisher 2014)	27
2.7	Radiogrammetric measurement of third metacarpal bone using hand radiograph	31
2.8	Confusion Matrix	44
3.1	Flowchart of the proposed methodology	62
3.2	Denoising of hand radiographs: Denoised images (top row) and their difference images (bottom row) obtained using (a) bilateral filter, (b) NLPCA and (c) BM3D	64
3.3	Denoising of image using BM3D method: (a) and (b) Original image and denoised image (zoomed) and (c) Intensity profile of the original and denoised images along a row	64

3.4	Soft tissue subtraction: (a) Original image, (b) estimated background, (c) the corresponding intensity profiles at the carpal region of denoised image and estimated background, (d) image after soft tissue subtraction, and (e) intensity profile of the soft tissue subtracted image	65
3.5	Binary image of hand bone region: (a) Image after applying Niblack local thresholding on soft-tissue subtracted image, (b) Image after global Otsu thresholding, and (c) Intersection image of (a) and (b)	67
3.6	Detection of DRUJ: (a) and (b) Intensity profiles of radius and ulna showing two distinct peaks, (c) Detected DRUJ line	67
3.7	Hand radiograph showing the two anatomical landmarks, TDP (in blue) and DRUJ (in red) and the estimated row containing the third metacarpal centroid (in green)	68
3.8	Localization of third metacarpal bone: (a) Estimated metacarpal midregion and (b) Intensity profile of the soft tissue subtracted image along metacarpal midregion showing five prominent peaks	69
3.9	Automatic segmentation of third metacarpal bone: (a) Internal and external markers for watershed, (b) gradient image, and (c) Segmented third metacarpal bone	70
3.10	Contrast enhancement for endosteal edge segmentation: (a) Third metacarpal of original image (b) shows the estimated background and (c) shows the contrast enhanced cortical bone of third metacarpal after background subtraction	71
3.11	Segmentation of endosteal edge: (a) Internal and external markers used for watershed, (b) Gradient of the contrast enhanced image, (c) Detected endosteal edge after watershed segmentation, and (d) Extracted metacarpal shaft for radiogrammetric measurements	72
3.12	Testing the trained AAM model: (a) Initial bounding box detection, (b) Initial position of the AAM model and (c) Final segmented third metacarpal bone	75
3.13	Radiogrammetric measurement of third metacarpal bone using hand radiograph	75

3.14	Examples of the segmentation results for third metacarpal bone for two healthy images (Subjects 1 and 2) and two osteoporotic images (Subjects 3 and 4): (a) Original images with detected DRUJ line are shown in first row, (b) localization of third metacarpal in second row, (c) segmented third metacarpal bone shaft used for radiogrammetry in the last row. Radiogrammetric measurements obtained from the segmented bone shaft are as follows: Subject 1 ($CW= 10.38$ mm, $MW= 5.89$ mm, $CCT= 4.49$ mm, $CA= 57.28$ mm ²), Subject 2 ($CW= 7.61$ mm, $MW= 3.03$ mm, $CCT= 4.58$ mm, $CA= 38.26$ mm ²), Subject 3 ($CW= 9.53$ mm, $MW= 4.28$ mm, $CCT= 5.25$ mm, $CA= 56.92$ mm ²) and Subject 4 ($CW= 8.03$ mm, $MW= 3.33$ mm, $CCT= 4.71$ mm, $CA= 41.96$ mm ²)	80
3.15	Segmentation results of healthy (row 1), low bone mass (row 2) and osteoporotic subjects (row 3): (a) manual segmentation, (b) proposed segmentation method and (c) AAM segmentation. Radiogrammetric measurements of the metacarpal bone shaft for the 3 cases of the 3 images are as follows: 1(a) $CW= 7.83$ mm, $MW= 2.60$ mm, $CCT= 5.22$ mm, $CA= 42.78$ mm ² ; 1(b) $CW= 7.75$ mm, $MW= 2.45$ mm, $CCT= 5.29$ mm, $CA= 42.39$ mm ² ; 1(c) $CW= 7.34$ mm, $MW= 2.15$ mm, $CCT= 5.19$ mm, $CA= 38.65$ mm ² ; 2(a) $CW= 8.99$ mm, $MW= 5.45$ mm, $CCT= 3.55$ mm, $CA= 40.22$ mm ² ; 2(b) $CW= 9.05$ mm, $MW= 5.16$ mm, $CCT= 3.89$ mm, $CA= 43.41$ mm ² ; 2(c) $CW= 9.14$ mm, $MW= 5.02$ mm, $CCT= 4.12$ mm, $CA= 45.76$ mm ² ; 3(a) $CW= 7.32$ mm, $MW= 3.48$ mm, $CCT= 3.84$ mm, $CA= 32.58$ mm ² ; 3(b) $CW= 7.23$ mm, $MW= 3.33$ mm, $CCT= 3.90$ mm, $CA= 32.35$ mm ² ; 3(c) $CW= 7.77$ mm, $MW= 3.24$ mm, $CCT= 4.53$ mm, $CA= 39.18$ mm ²	82
3.16	Examples of poorly segmented cases: (a) Low quality image, (b) Mis-detection of DRUJ due to presence of obstacles like bangles, (c) Wrong detection of third metacarpal centroid due to mis-detection of DRUJ, (d) Wrong detection of third metacarpal bone and (e) Edge leakage of watershed lines due to a weak gradient image.	87
4.1	Extraction of distal radius ROI: (a) Detection of central axis of the radius bone after alignment, (b) shows a vertical line taken from the DRUJ row to a predetermined distance along the central axis, (c) Intensity profile along the vertical line in (b) showing the UDR as the highest peak, and (d) Segmentation of the circular ROI of distal radius	92
4.2	Illumination correction of texture image using background subtraction: (a) Raw texture image, (b) image after background subtraction, and (c) corresponding intensity profiles of the raw image and background subtracted image	94

4.3	Texture analysis using MGM: (a) morphological gradient of the texture image using square-shaped structuring element of size 7 pixels, (b) morphological gradient using disk-shaped structuring element of size 7 pixels, (c) morphological gradient using square-shaped structuring element of size 3 pixels and (d) morphological gradient using disk-shaped structuring element of size 3 pixels	99
4.4	Texture images obtained using Laws's masks: (a) $LAW S_{L5E5}$, (b) $LAW S_{L5S5}$, (c) $LAW S_{L5R5}$, (d) $LAW S_{L5W5}$, (e) $LAW S_{E5E5}$, (f) $LAW S_{E5S5}$, (g) $LAW S_{E5R5}$, (h) $LAW S_{E5W5}$, (i) $LAW S_{S5S5}$, (j) $LAW S_{S5R5}$, (k) $LAW S_{S5W5}$, (l) $LAW S_{R5R5}$, (m) $LAW S_{R5W5}$ and (n) $LAW S_{W5W5}$	100
4.5	Response of the Gabor filter of scale 4 along (a) orientation 1, (b) orientation 2, (c) orientation 3, (d) orientation 4, (e) orientation 5 and (f) orientation 6	102
4.6	Examples of the segmentation results of distal radius ROI for two healthy images (Subjects 1 and 2) and two osteoporotic images (Subjects 3 and 4): (a) the central axis and approximate centre of circular distal radius ROI in top row, and (b) the extracted circular ROI in bottom row	103
5.1	Block diagram of the proposed methodology	119
5.2	Flowchart summarizing classifiers trained with Indian sample data	121
5.3	Flowchart summarizing classifiers trained with Indian and Swiss sample data (part 1)	122
5.4	Flowchart summarizing classifiers trained with Indian and Swiss sample data (part 2)	123
5.5	Variance explained by first 10 of the 23 principal components of PCA in the feature set	128
5.6	ROC curves for the ANN classifiers trained with FS-1 (AUC=0.9459), FS-2 (AUC=0.9534) and FS-3 (AUC=0.8954)	129
5.7	ROC curves for the classifiers trained with FS-1: AUC of ANN=0.9459, AUC of LR=0.8452, AUC of SVM=0.9023 and AUC of KNN=0.9537	130
5.8	ROC curves for the classifiers trained with FS-2: AUC of ANN=0.9534, AUC of LR=0.9260, AUC of SVM=0.9023 and AUC of KNN=0.8725	131
5.9	ROC curves for the classifiers trained with FS-3: AUC of ANN=0.8954, AUC of LR=0.7726, AUC of SVM=0.6880 and AUC of KNN=0.6825	131
5.10	Feature selection using PCA on the feature set of (a) Indian sample data and (b) Swiss sample data.	140

5.11	ROC curves for the ANN classifiers trained on Indian sample data using CFS (AUC=0.9705), OFS-I (AUC=0.8825), FS-4(I) (AUC=0.9245) and FS-5(I) (AUC=0.9280)	142
5.12	ROC curves for the ANN classifiers trained on Swiss sample data using CFS (AUC=0.7824), OFS-S (AUC=0.9492), FS-4(S) (AUC=0.9583) and FS-5(S) (AUC=0.9329)	142
5.13	ROC curves for the classifiers trained with CFS: AUC of ANN=0.9705, AUC of LR=0.8012, AUC of SVM=0.8522 and AUC of KNN=0.9684	144
6.1	Flowchart of the proposed methodology for cortical volumetry	163
6.2	Multi-view radiographic images of the hand used for 3D reconstruction: (a) PA view, (b) 45 ⁰ oblique view and (c) 135 ⁰ oblique view	163
6.3	Projection contour (in blue) and X-ray contour (in red) (a) before alignment and (b) after rigid registration using ICP.	166
6.4	Projection contour (in red) and X-ray contour (in blue) (a) before non-rigid registration and (b) projection contour after registration using SOM.	167
6.5	Examples of the 3D reconstructed models of the outer and inner bones of the third metacarpal bone for a healthy subject (top row) and a subject with LBM (bottom row) : (a) Hand X-ray image in PA view, (b) hand X-ray image in oblique 45 ⁰ view, (c) hand X-ray image in oblique 135 ⁰ view, (d) reconstructed outer bone model and (e) reconstructed inner bone model of the third metacarpal bone using the proposed method. Cortical volumetric measurements of the 3D reconstructed bone shaft are as follows: Healthy subject (top row: $CV = 878.71 \text{ mm}^3$, $CV_{OV} = 0.7672$, $CV_{SA} = 0.6148 \text{ mm}$, $CV_n = 0.0330$), and subject with LBM (bottom row: $CV = 624.64 \text{ mm}^3$, $CV_{OV} = 0.8287$, $CV_{SA} = 0.5853 \text{ mm}$, $CV_n = 0.0314$).	170
6.6	Heatmap and histogram of the P2S error of the reconstructed outer bone shaft and ground truth	172
6.7	Heatmap and histogram of the P2S error of the reconstructed inner bone shaft and ground truth	172
6.8	Error distribution in CCT of projected images and X-ray images	174

LIST OF TABLES

1.1	Availability of imaging modalities used for osteoporosis in different countries (International Osteoporosis Foundation 2013; Hernlund <i>et al.</i> 2013; Johnell and Kanis 2005; Statista 2018 <i>a,b</i>)	6
2.1	Criteria for osteoporosis as defined by WHO (Kanis <i>et al.</i> 2008) . . .	15
2.2	Summary of currently available imaging-based diagnostic techniques for osteoporosis	24
2.3	Segmentation methods used in diagnostic techniques	30
2.4	Trabecular pattern indices for assessment of severity of osteoporosis	34
2.5	Choice of statistical test depending on the type of variables and number of samples	43
2.6	Trabecular bone texture characterization using radiographs	48
2.7	Fracture risk calculators	56
3.1	Clinical characteristics of the Indian and Swiss sample data	78
3.2	Comparison of success rate of metacarpal detection	81
3.3	Performance evaluation with manual segmentation	83
3.4	Statistical analysis of the evaluation metrics of the proposed and AAM segmentation methods	83
3.5	Comparison of radiogrammetric measurements with ground truth . . .	84
3.6	Significance of the cortical features in the healthy (H) and low bone mass (LBM) groups of Indian and Swiss sample data	85
3.7	Correlation of the cortical features with sBMD and T -score for Indian and Swiss sample data	86
4.1	Statistical test results of GLCM features for $d = 1, 5, 10$ and 50 pixels	96
4.2	Statistical test results of Gabor features for different scales	102
4.3	Significance test results of H and LBM groups of Indian and Swiss sample data	105

4.4	Correlation analysis of extracted features with sBMD and T -score for Indian and Swiss sample populations	112
5.1	Statistical significance results of the independent sample t -test of the significant features ($p < 0.05$) in the training set	125
5.2	Correlation of significant features of independent sample t -test ($p < 0.01$) with DXA-BMD of lumbar spine using Pearson correlation analysis	126
5.3	Correlation results of the 10 highest ranked cortical and texture features in the training set	127
5.4	Performance of the trained ANN classifiers using holdout validation	128
5.5	Performance metrics of LR, SVM and KNN classifiers using holdout validation for combined cortical and texture (GLRLM and Laws's mask) features	130
5.6	Performance metrics of 10 fold cross validation on the whole data using LR, SVM and KNN classifiers trained with cortical and texture (GLRLM and Laws's mask) features	132
5.7	Summary of the linear regression model	133
5.8	Pairwise correlation between predictors of the linear regression model	133
5.9	Significance test results of healthy (H) and low bone mass (LBM) groups of Indian and Swiss sample populations	136
5.10	Correlation analysis of extracted features with sBMD and T -score for Indian and Swiss sample populations	138
5.11	Features selected in each of the feature sets used for classification .	139
5.12	Correlation results of the 10 highest ranked cortical and texture features in the training set of Indian and Swiss sample data	139
5.13	Classification results of the trained ANN classifiers using holdout validation	141
5.14	Performance metrics of the classifiers trained with CFS features on the test data using holdout validation and 10-fold cross validation	143
5.15	Correlation analysis of LBP features with sBMD for Indian and Swiss sample populations	145
5.16	Performance metrics of the classifiers, trained with cortical and LBP feature variants, on the test data	146
5.17	Performance metrics of the classifiers using 10-fold cross validation on combined cortical and LBP feature variants	147

5.18	Performance metrics of the classifiers trained with cortical and CNN features on test data using holdout validation and 10-fold cross validation	149
5.19	Comparison of performance metrics of classifiers trained on bone radiographic texture analysis in literature	151
6.1	Clinical characteristics of the study group used for 3D reconstruction of metacarpal bone	169
6.2	Evaluation metrics of the reconstructed outer and inner bone shafts .	172
6.3	Comparison of CCT measurement of PA projections of 3D reconstructed models with those of manually segmented X-ray images . .	173
6.4	Cortical volumetric measurements extracted from the 3D reconstructed models	175
6.5	Correlation analysis of cortical volumetric measurements of the 3D reconstructed models	175
6.6	Classification results of the automatically segmented 14 images using the trained Indian classifiers	176

ABBREVIATIONS

1D	One dimensional
2D	Two dimensional
3D	Three dimensional
AAM	Active Appearance Model
Acc	Accuracy
ANN	Artificial Neural Network
ANOVA	Analysis of Variance
AP	Antero-Posterior
ASM	Active Shape Model
AUC	Area under the ROC curve
BM3D	Block Matching 3D
BMD	Bone Mineral Density
BNI	Barnett-Nordin Index
BOS	Basel Osteoporosis Study
CA	Cortical Area
CCT	Combined Cortical Thickness
CFS	Common Feature Set
CNN	Convolutional Neural Network
CT	Computed Tomography
CV	Cross-validation
CW	Cortical Width
DICOM	Digital Imaging and Communications in Medicine
DNN	Deep Neural Network
DOES	Dubbo Osteoporosis Epidemiology Study
DPA	Dual Photon Absorptiometry
DR	Distal Radius
DRUJ	Distal Radius-Ulnar Joint
DXA	Dual X-ray Absorptiometry
DXA-LS	DXA-BMD of lumbar spine
DXR	Digital X-ray Radiogrammetry
EPIDOS	Epidemiology of Osteoporosis

ESI	Exton-Smith Index
FEA	Finite Element Analysis
FD	Fractal Dimension
FN	False Negative
FORE FRC	FORE Fracture Risk Calculator
FOS	Framingham Osteoporosis Study
FP	False Positive
GLCM	Gray Level Co-occurrence Matrix
GLN	Gray Level Non-uniformity
GLRLM	Gray Level Run Length Matrix
GT	Ground Truth
H	Healthy
HGRE	High Gray level Run Emphasis
HR	High Resolution
HR-pQCT	High Resolution peripheral Quantitative Computed Tomography
ICP	Iterative Closest Point
KNN	k -Nearest Neighbour
LBM	Low Bone Mass
LBP	Local Binary Pattern
LGRE	Low Gray level Run Emphasis
LLBP	Local Line Binary Pattern
LR	Logistic Regression
LRE	Long Run Emphasis
LSD	Laplacian Surface Deformation
MCI	Metacarpal Cortical Index
MGM	Morphological Gradients Method
ML	Medio-Lateral
MRI	Magnetic Resonance Imaging
MrOS	Osteoporotic Fractures in Men
MW	Medullary Width
NLM	Non-Local Means
NLPCA	Non-Local Means with Principal Component Analysis
NORA	National Osteoporosis Risk Assessment
NPV	Negative Predictive Value
OFELY	Os des Femmes de Lyon
OFS	Optimal Feature Set
OP	Osteoporotic

OR	Odd's Ratio
OST	Osteoporosis Self-Assessment Tool
OSTA	Osteoporosis Self-Assessment Tool for Asians
P2S	Point-to-surface
PA	Postero-Anterior
PBI	Pediatric Bone Index
PCA	Principal Component Analysis
PCA_b	Percent Cortical Area of bone
PPV	Positive Predictive Value
QCT	Quantitative Computed Tomography
QUS	Quantitative Ultrasound
RF	Random Forest
RLN	Run Length Non-uniformity
RMS	Root Mean Square
ROC	Receiver Operating Characteristic
ROI	Region-of-Interest
sBMD	Standard Bone Mineral Density
SD	Standard Deviation
SEMOF	Swiss Evaluation of the Methods of Measurement of Osteoporotic Fracture Risk
SFS	Structural Fragility Score
Sn	Sensitivity
SOF	Study of Osteoporotic Fractures
SOM	Self-Organizing Map
Sp	Specificity
SPA	Single Photon Absorptiometry
SRE	Short Run Emphasis
SSM	Statistical Shape Model
SVM	Support Vector Machine
TBS	Trabecular Bone Score
TDP	Tip of Third Distal Phalanx
TN	True Negative
TP	True Positive
UDR	Ultra-Distal end of Radius bone
USD	US Dollar
VFA	Vertebral Fracture Assessment
WHO	World Health Organization

CHAPTER 1

INTRODUCTION

1.1 OSTEOPOROSIS

Osteoporosis is a bone condition characterized by decrease in bone mass and micro-structural connectivity of bone tissue, leading to increased susceptibility to fragility fractures. It is a systemic disease that affects the whole skeletal body. The main skeletal sites analyzed for detection of bone loss are hip, lumbar spine and forearm, as these sites are the most susceptible to fragility fractures.

Bone undergoes modeling and remodeling to adapt to changing biomechanical forces and to replace old bone with new one (Kini and Nandeesh 2012). Osteoporosis occurs when there is an increased imbalance in the bone formation and resorption process. Human bone has two components, namely the outer cortical or compact bone and the inner trabecular or cancellous bone. Cortical bone is dense and solid and imparts strength to the bone while taking up the stress and strain of bone. Trabecular bone has a honeycomb-like porous structure which bears the weight of the body and distributes it along all directions, making the bone light in weight. Cortical bone has an outer periosteal surface and inner endosteal surface. The region within the inner endosteal surface is occupied by trabecular bone and bone marrow. With the progression of osteoporosis, the thickness of cortical bone reduces and the trabecular bone porosity increases, as shown in Figure 1.1 (Rock Creek Wellness 2018). The trabecular bone has a higher metabolic rate than the cortical bone. Thus, changes in trabecular bone due to osteoporosis occur earlier than that of cortical bone (Adams 2009). The changes in cortical bone thickness and trabecular bone architecture can be used to identify osteoporotic subjects.

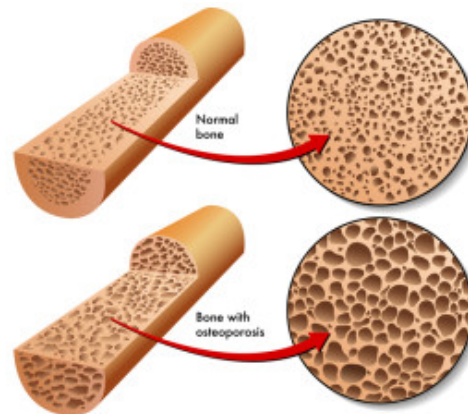


Figure 1.1: Structure of a healthy and osteoporotic tubular bone (Rock Creek Wellness 2018)

1.2 NEED FOR EARLY DIAGNOSIS

According to the World Health Organization (WHO), osteoporosis is a major global health concern, that can lead to increased morbidity, mortality and socio-economic burden. It is more prevalent among the elderly population (Nguyen *et al.* 2007). Osteoporosis-related fracture affects one in three women and one in five men over the age of 50. Osteoporosis is reported to cause more hospitalization than myocardial infarction, diabetes and breast cancer, in women above 45 years of age (International Osteoporosis Foundation 2013). Based on a statistics on the prevalence of osteoporosis in different countries, the number of people affected by osteoporosis in India in 2012 was approximately 55 million (4%) and is projected to rise to 75 million (5%) in 2022, as shown in Figure 1.2 (Insider 2013). As osteoporosis predominantly affects the elderly, with increase in aging population there will be a corresponding increase in the incidence of fragility fractures. It is projected that by 2050, there will be a 7.6-fold increase in aging population in Asia, that would result in the occurrence of more than 50% of the global fractures in Asia (International Osteoporosis Foundation 2013). Although osteoporosis has been more prevalent among the elderly, the age of onset of osteoporosis is decreasing in the recent years due to change in lifestyle and lack of nutrition and exercise. In the United States, about 40 million people in the age of 50 years and above are reported to have low bone mass and about 12 million people have osteoporosis (Myers 2013).

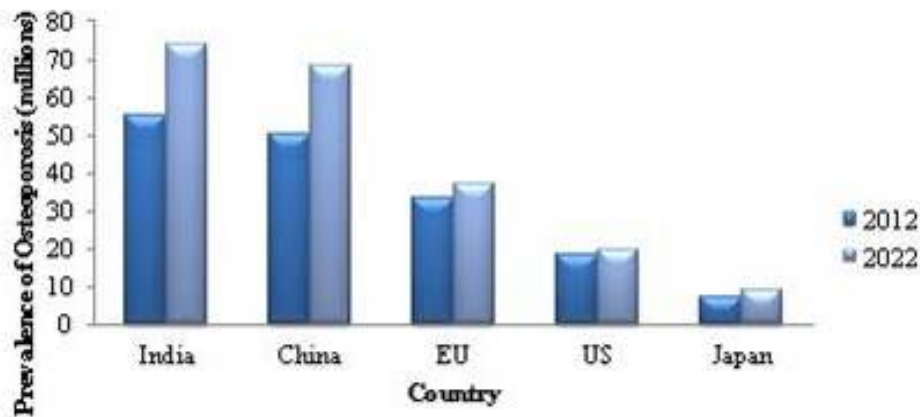


Figure 1.2: Prevalence of osteoporosis in different countries in 2012 and 2022 (Insider 2013)

Osteoporosis is a silent disease as it is painless and asymptomatic. It is often diagnosed after the occurrence of a fragility fracture. After the incidence of an osteoporotic fracture, there is an increased risk for occurrence of subsequent fractures (Center *et al.* 2007). Osteoporotic-related fracture risk is estimated to be 40% to 50% for women and 13% to 22% for men (Johnell and Kanis 2005). There is a rapid increase in prevalence of osteoporosis-related fractures in people. In comparison to the statistics in 1990, the rate of occurrence of hip fracture in women and men is expected to increase by 240% and 310% respectively, by the year 2050 (Gullberg *et al.* 1997). Fragility fractures can result in increased morbidity and mortality of the affected people. Mortality rate associated with hip fracture is about 15-20% (Melton 2000). Studies have shown that osteoporosis can be prevented and treated if it is diagnosed before the occurrence of a fracture (Harvey *et al.* 2017). This calls for a need for accurate and low cost techniques for early diagnosis of osteoporosis.

1.3 BACKGROUND

Techniques to detect osteoporosis began as early as 1930s. The earliest method used for determination of bone density was radiographic absorptiometry, in which an Aluminium wedge of different densities are placed near the region-of-interest (ROI) during X-ray image acquisition (Bonnick 1998). Step wedge phantom made of calcium hy-

droxyapatite with varied values of Bone Mineral Density (BMD) and thickness may also be used (Ligesh *et al.* 2011). Simultaneous exposure of the wedge phantom along with the ROI helps to compensate the effects of variations in acquisition settings.

Manual radiogrammetry originally proposed by Barnett and Nordin in 1960 was a technique in which radiogrammetric measurements of the bone were taken manually using rulers or vernier calipers from the radiographs, specifically the hand, femur and spine radiographs, and scores were developed to discriminate between osteoporotic and non-osteoporotic groups (Barnett and Nordin 1960).

Single Photon Absorptiometry (SPA) technique, introduced in 1963, makes use of the attenuation of photon beam by the bone to measure its density. SPA do not need a phantom for the BMD measurement. To improve the accuracy, Dual Photon Absorptiometry (DPA) was developed, which used the difference of attenuation of two photon beams for the quantification of bone density. Unlike SPA which measures BMD of peripheral skeleton only, DPA can measure BMD of peripheral skeleton, spine and proximal femur. Photon absorptiometry has the limitation of producing variations in BMD measure with decay of the radiation source, and hence is no longer used in clinical practice.

Presently, the determination of BMD using Dual Energy X-ray Absorptiometry (DXA) is considered the gold standard technique for the diagnosis of osteoporosis (Kanis *et al.* 2008). DXA is the X-ray counterpart of DPA technique. According to WHO, osteoporosis is diagnosed using T -score values, calculated as the standard deviation of the measured BMD value from the reference mean BMD. The mean BMD value of young adult Caucasian women is taken as the reference (WHO 2007). According to the T -score values, bone loss is classified as normal, osteopenic, osteoporotic and severely osteoporotic. DXA can take BMD measurement of forearm, hip, spine and even the whole body. It is accurate and highly precise and has a low radiation dose Link 2012.

Quantitative Computed Tomography (QCT) is an absorptiometric technique by which volumetric bone density measurements are obtained. A three dimensional (3D) view of bones can be constructed by capturing X-ray attenuation by tissues at different

angles. QCT can measure the trabecular bone density of the lumbar spine, hip and forearm. As QCT gives a volumetric BMD of the trabecular bone, it gives a more sensitive measurement than cortical bone measurements alone. High Resolution peripheral QCT (HR-pQCT) is an advanced QCT technique in which high resolution images of the peripheral limbs, such as radius and tibia, helps in the quantification of trabecular bone texture which can be used to diagnose osteoporosis.

Quantitative Ultrasound (QUS) is a simple low cost technique that helps to detect osteoporosis using sound waves. It measures the differential reflections and attenuation of sound waves as they traverse through the bone, and hence no radiation is involved. QUS is used to measure the bone density of mainly the calcaneal bone.

Although manual radiogrammetry is a simple low cost technique, it is highly subjective. Digital X-ray Radiogrammetry (DXR) is a computerized radiogrammetric technique used for the measurement of bone density from hand radiographs (Rosholm *et al.* 2001). DXR has a good precision and reproducibility. As it uses radiographs, it offers a low cost and convenient technique for measurement of BMD. The BMD measured by DXR shows a good correlation with BMD measured by DXA.

1.4 MOTIVATION FOR THE RESEARCH WORK

1.4.1 Need for a low-cost and widely available diagnostic tool

The existing diagnostic techniques suffer from various limitations. DXA is the most commonly used method for diagnosis of osteoporosis, but it is expensive and not widely available in developing countries. DXA is inaccessible to majority of the Indians, especially those living in the rural areas. DXA machines available per 1 million population in India is 0.26 (International Osteoporosis Foundation 2013). There are only two DXA machines available in hospitals in South Karnataka, India. Table 1.1 shows the availability of imaging modalities in different countries (International Osteoporosis Foundation 2013; Hernlund *et al.* 2013; Johnell and Kanis 2005; Statista 2018*a,b*).

Table 1.1: Availability of imaging modalities used for osteoporosis in different countries (International Osteoporosis Foundation 2013; Hernlund *et al.* 2013; Johnell and Kanis 2005; Statista 2018a,b)

Country	DXA*	CT*	MRI*
USA	35.80 (2003)	41.86 (2016)	36.72 (2016)
Japan	20.80 (2013)	107.12 (2014)	51.67 (2014)
France	29.10 (2010)	16.94 (2016)	13.54 (2016)
Germany	21.10 (2010)	35.09 (2015)	33.63 (2015)
Australia	18.00 (2013)	63.17 (2016)	14.34 (2016)

*Units are in number of devices per million population (Year)

In India, the cost of DXA scan ranges from Rs.1800 to Rs.4500, which cannot be easily afforded by most people in India, specifically the aging population (International Osteoporosis Foundation 2013). Diagnostic techniques such as QCT and Magnetic Resonance Imaging (MRI) scans cost around Rs.3000 in India. DXR, the low cost alternative to DXA, is also not widely available in India. DXR-online is a licensed version in which the cost of analysis per examination would be about Rs.2000, which makes it expensive. Lesser expensive diagnostic techniques such as QUS is limited by its low precision and reproducibility (Njeh *et al.* 2000). Hence, there is a need for developing a low cost and widely available technique for early diagnosis of osteoporosis.

1.4.2 Need for a more accurate measurement

Osteoporosis is a bone condition that affects the bone density, structure and strength. The measurement of BMD alone cannot predict the risk of fractures (McCreddie and Goldstein 2000). As early stages of osteoporosis is first reflected in the trabecular bone as compared to cortical bone, the characterization of trabecular bone is a more sensitive measure of osteoporosis than BMD (Adams 2009). Recent diagnostic techniques have explored the use of supervised machine learning using texture analysis of trabecular bones to classify people as healthy and osteoporotic. It is found that trabecular texture analysis can detect osteoporotic fractures independent of BMD. Thus, the combination of cortical measurements and texture analysis of trabecular bone would give a more accurate and sensitive measurement of the progression of osteoporosis.

1.4.3 Need for a low-cost volumetric measurement

DXA gives an areal measurement of BMD. A volumetric measurement of the bone density will increase the sensitivity and accuracy of the diagnostic technique. DXR approximates the cortical bone shaft of the metacarpal bones to a cylinder and therefore do not give a true volumetric measurement of BMD (Rosholm *et al.* 2001). Although QCT gives a true volumetric density, the initial investment and cost per examination using QCT is high. Thus, there is a need to develop a low cost method for measurement of true volumetric bone density.

1.5 OBJECTIVES OF THE THESIS

We propose to develop a low cost prescreening tool for osteoporosis using a combination of cortical radiogrammetry and trabecular texture analysis of hand and wrist radiographs. This would give an accurate and sensitive measure of bone density, structure and strength. Radiography, being a low cost and widely available imaging modality, can be used for mass-screening and timely diagnosis of osteoporosis in low economies.

The objectives of the research work are

1. To measure cortical bone density by using computerized radiogrammetry of hand radiographs.
2. To extract significant texture features from wrist radiographs, which can quantify changes in trabecular bone during progression of osteoporosis.
3. To develop a prescreening tool by combining cortical radiogrammetry and trabecular texture features and to validate its relevance for clinical practice.
4. To develop a volumetric measure of cortical bone by reconstructing a three-dimensional model from three multi-view hand radiographs.

1.6 PROPOSED METHODOLOGY

This thesis proposes a low cost prescreening diagnostic tool for the identification of people with low bone mass. The proposed prescreening tool uses a combined cortical radiogrammetric and trabecular texture analysis of hand and wrist radiographs for the characterization of bone properties in healthy and osteoporotic people. The proposed technique comprises of fully automated segmentation of the cortical and trabecular bone regions of interest and feature extraction followed by feature selection and training of classifiers, to make a diagnostic decision on the bone loss status. Figure 1.3 shows a graphical abstract of the proposed methodology. The hand and wrist radiographic images are first preprocessed to remove noise and illumination variations. The third metacarpal bone and distal radius ROI are detected and segmented automatically using intensity profiles, mathematical morphology and marker-controlled watershed segmentation. Cortical radiogrammetric measurements are taken from the third metacarpal bone and trabecular texture features are extracted from the distal radius ROI. The significant cortical and trabecular features are selected to train classifiers to classify subjects as healthy and those with low bone mass.

In this work, the third metacarpal bone and distal radius are chosen as the sites for analysis, as the third metacarpal and distal radius ROIs can be analyzed from a single hand and wrist radiograph, thus reducing the cost and radiation exposure. Third

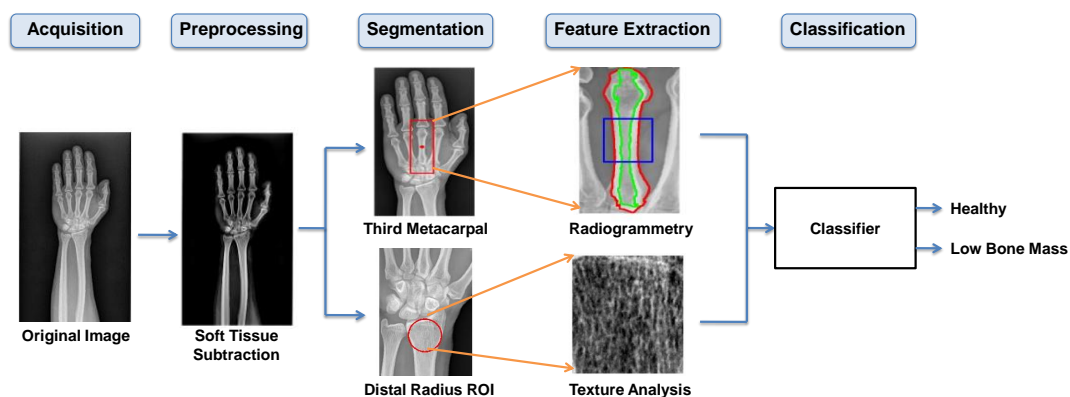


Figure 1.3: Graphical abstract of the proposed methodology

metacarpal bone is preferred over other metacarpals for radiogrammetry, as it gives a better projection profile and can be easily located in the hand radiographs, irrespective of the hand orientation. Distal radius is a better site for trabecular texture analysis than vertebra and calcaneal radiographs (Mallard *et al.* 2013).

A novel method to measure cortical volume of the third metacarpal bone shaft at a low cost is proposed using 3D reconstruction of the metacarpal bone using hand X-ray images in three views (Postero-Anterior and oblique views at 45^0 and 135^0). The Computed Tomography (CT) scan of one subject is used to create a template model, from which subject-specific models of other subjects can be reconstructed. For this, the template model is first projected onto the three planes to get projection images. The outer and inner contours of the metacarpal bone of the projection images and corresponding X-ray images are extracted and registered. The point pair correspondences in the projection contour after registration are used to deform the template model. The process of contour registration and 3D deformation is applied onto all the three views iteratively to create the subject-specific model. The cortical bone shaft is extracted from the reconstructed model and cortical volumetric measurements are determined.

This research project is an interdisciplinary work done in collaboration with the Department of Orthopaedics, Kasturba Medical College (KMC) Hospital, Mangalore, Manipal Academy of Higher Education (MAHE), Karnataka, India and in association with the Department of Radiology and Medical Informatics, University Hospital of Geneva (HUG), Switzerland and Tejaswini Hospital, Mangalore, India. The study protocol was approved by the Institutional Ethics Committee, KMC Hospital, Mangalore, MAHE, Karnataka, India.

1.7 MAIN CONTRIBUTIONS OF THE THESIS

A fully automated segmentation method to segment the third metacarpal bone shaft from hand radiographs and to measure cortical radiogrammetry is developed. The proposed method accurately detected the third metacarpal bone in 89% of Indian sample

data and 78% of Swiss sample data. Radiogrammetric measurements show mean absolute error of 0.08 mm for cortical width and 0.24 mm for medullary width. This method performs better as compared to Active Appearance Model (AAM), with mean Jaccard measure of 0.90, percent area difference of 0.03, recall of 0.96, precision of 0.94 and F1-score of 0.95. This work has resulted in the following publications:

- Anu Shaju Areeckal, Sumam David S., Michel Kocher, Nikil Jayasheelan, and Jagannath Kamath (2016), “Fully Automated Radiogrammetric Measurement of Third Metacarpal Bone from Hand Radiograph”, *11th IEEE International Conference on Signal Processing and Communication (SPCOM)*, Bangalore, India, pp.1-5, June 12-15, 2016, DOI: 10.1109/SPCOM.2016.7746608.
- Mathew Sam, Anu Shaju Areeckal, and Sumam David S. (2017), “Early Diagnosis of Osteoporosis Using Active Appearance Model and Metacarpal Radiogrammetry”, *13th IEEE International Conference on Signal Image Technology and Internet Based Systems (SITIS)*, Jaipur, India, pp.173-178, December 4-7, 2017, DOI: 10.1109/SITIS.2017.38.
- Anu Shaju Areeckal, Mathew Sam, and Sumam David S. (2018), “Computerized Radiogrammetry of Third Metacarpal Using Watershed and Active Appearance Model”, *19th IEEE International Conference on Industrial Technology (ICIT)*, Lyon, France, pp.1490-1495, February 20-22, 2018, DOI: 10.1109/ICIT.2018.8352401.

Texture features that can discriminate healthy and low bone mass subjects are determined using statistical analysis. Classifier models have been trained using combined cortical and texture features to detect people with low bone density. Artificial Neural Network (ANN) classifiers trained on Indian sample data show test accuracy of over 90% using holdout validation. Weighted k -Nearest Neighbors (KNN) shows accuracy of 81.7% using 10-fold cross-validation. A linear regression model achieves significant correlation of 0.671 with DXA-BMD of lumbar spine. ANN classifiers trained using cortical and statistical and structural texture features show test accuracy of 92.9% with Indian data and 90.9% with Swiss data. Weighted KNN shows test accuracy of 96.2% with Indian and Swiss test data. This work has resulted in the following publications:

- Anu Shaju Areeckal, Nikil Jayasheelan, Jagannath Kamath, Sophie Zawadynski, Michel Kocher, and Sumam David S. (2018), “Early Diagnosis of Osteoporosis using Radiogrammetry and Texture Analysis from Hand and Wrist Radiographs in Indian Population”, *Osteoporosis International*, Springer Nature, Vol. 29, No. 3, pp.665-673, DOI: 10.1007/s00198-017-4328-1.

- Anu Shaju Areeckal, Jagannath Kamath, Sophie Zawadynski, Michel Kocher and Sumam David S. (2018), “Combined Radiogrammetry and Texture Analysis for Early Diagnosis of Osteoporosis Using Indian and Swiss data”, *Computerized Medical Imaging and Graphics*, Elsevier, Vol. 68, No. 9, pp.25-39, DOI: 10.1016/j.compmedimag.2018.05.003.

A novel low cost technique to measure cortical bone volume of third metacarpal bone shaft by 3D reconstruction using multi-view X-ray images has been implemented. To our knowledge, this is possibly the first work on 3D reconstruction of metacarpal bone from three hand X-ray views for the measurement of cortical volume. Comparison of the combined cortical thickness (CCT) of the projected views of the reconstructed 3D metacarpal bones with CCT of manually segmented X-ray images show mean percentage error of 11.18%. This work has resulted in the following publication:

- Avinash D. Jayakar, Gautham Sambath, Anu Shaju Areeckal and Sumam David S. (2018), “Cortical Volumetry using 3D Reconstruction of Metacarpal Bone from Multiview Images”, *4th IEEE International Conference on Recent Advances in Computational Systems (RAICS)*, Thiruvananthapuram, India, pp.79-83, December 6-8, 2018, DOI: 10.1109/RAICS.2018.8635067.

This work is similar to DXR which uses computerized radiogrammetry and texture analysis of cortical bone. However, our prescreening tool is novel in the following ways:

1. Third metacarpal bone alone is used for cortical radiogrammetry.
2. Trabecular texture features of the distal radius is combined with cortical measurements for the diagnosis.
3. The prescreening tool is a low cost method that can be used for mass screening for early diagnosis of osteoporosis in low economies.

1.8 ORGANIZATION OF THE THESIS

In this thesis, we propose a prescreening tool for the early diagnosis of osteoporosis using cortical radiogrammetry of the third metacarpal bone and trabecular texture analysis of the distal radius. Chapter 2 discusses in detail the existing techniques used for the

diagnosis of osteoporosis and fracture risk prediction, their advantages and limitations. Chapter 3 details the proposed methodology for the automated segmentation of the third metacarpal bone and cortical radiogrammetry using hand radiographs. Chapter 4 explains the proposed methodology for the automatic extraction of the distal radius ROI and texture analysis of the trabecular bone. Chapter 5 explores the supervised learning techniques for detection of low bone mass using a combination of cortical radiogrammetric and trabecular texture features. Chapter 6 discusses the 3D reconstruction of the third metacarpal bone using multi-view X-ray images for the measurement of cortical bone volume at a low cost. We conclude the work in Chapter 7 by summarizing the main contributions of the thesis, discussing its limitations and future directions.

CHAPTER 2

DIAGNOSTIC IMAGING BASED TECHNIQUES FOR ASSESSMENT OF OSTEOPOROSIS

2.1 INTRODUCTION

Osteoporosis can be diagnosed by various techniques such as histological analysis, blood and urine samples, quantitative imaging techniques, etc. Histological analysis or bone biopsy helps to analyze the microscopic details of the bone structure, bone mineralization and rate of bone resorption. It has been widely used for the study of bone resorption and remodeling. However, due to its invasive nature, it is seldom used in current clinical practice for the diagnosis of osteoporosis (Marcu *et al.* 2011). Blood and urine samples can be used to determine changes in BMD and fracture risk by measuring biomarkers such as urinary hydroxyproline, C-terminal collagen telopeptide, alkaline phosphatase, osteocalcin, etc. that helps to give information on bone resorption and formation. But they suffer from biological and analytical variabilities and hence are not preferred for clinical diagnosis (Cabral *et al.* 2016; Looker *et al.* 2000). Quantitative imaging techniques are the most widely used methods for detection of osteoporosis and monitoring of therapeutic interventions. They help to acquire and view the images of bone regions while quantifying bone density and architecture. These techniques have been validated on a large number of population studies and has a high precision and reproducibility. This chapter reviews the quantitative imaging-based diagnostic tools used for the assessment of osteoporosis and fragility fracture risk.

2.2 QUANTITATIVE IMAGING TECHNIQUES

Quantitative imaging techniques are dedicated techniques developed to acquire images of the bone regions of interest and quantify the bone density and/or bone structure for

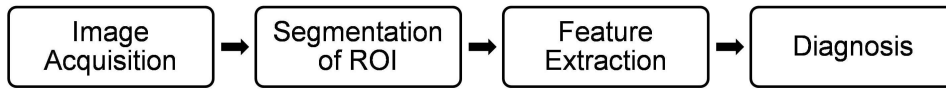


Figure 2.1: Pipeline of a diagnostic technique to detect osteoporosis

the diagnosis of osteoporosis. A general pipeline of the diagnostic imaging-based techniques used for the assessment of osteoporosis is shown in Figure 2.1. The pipeline consists of four stages, namely image acquisition, segmentation of ROI, feature extraction and diagnosis. In the first stage, quantitative imaging modalities are used to acquire the image of the bone region. In the second stage, the bone ROI is segmented for analysis. In stage 3, various features of the cortical or trabecular bone are extracted from the segmented ROI and finally in stage 4, the extracted features are used to decide the diagnosis by either comparing the features with a reference value or by using supervised machine learning techniques to classify healthy and osteoporotic people.

The most widely used clinical methods are DXA and QCT. DXA measures the areal density of the bone whereas QCT quantifies the volumetric density. Other imaging modalities that are not currently adapted to clinical practice but are extensively being investigated are HR-pQCT, QUS, MRI, DXR and radiography along with supervised learning techniques. Figure 2.2 shows some of the quantitative imaging modalities used for the diagnosis of osteoporosis.

2.2.1 Dual X-ray Absorptiometry (DXA)

According to the World Health Organization (WHO), measurement of BMD using DXA is considered as the gold standard method for the identification of osteoporosis (Kanis *et al.* 2008). DXA scans the bone region using a high energy X-ray beam (>70 keV) and a low energy X-ray beam (30-50 keV) and finds the difference in the attenuation of the X-ray beams, to produce a soft tissue subtracted image (Link 2012). DXA does an automated segmentation of the bone ROI with provision for manual refinement by qualified technicians. The ratio of bone mineral content, measured from the ROI, to the total ROI area gives the BMD of the subject, measured in g/cm^2 . This measured BMD

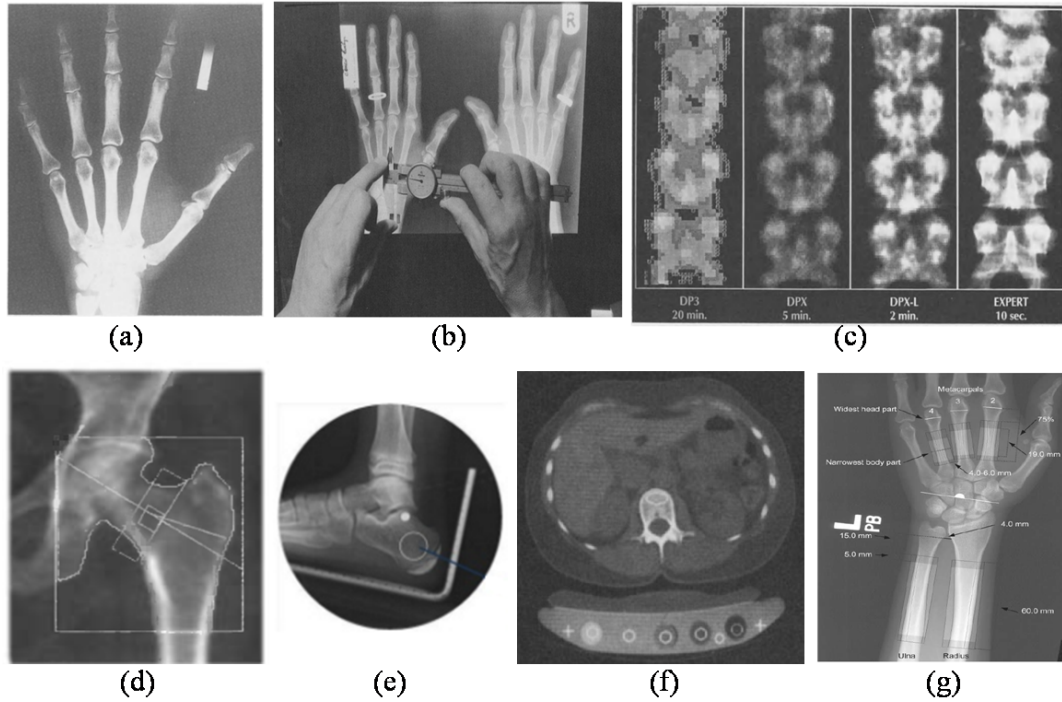


Figure 2.2: Quantitative imaging techniques used for diagnosis of osteoporosis: (a) Radiographic absorptiometry, (b) Manual radiogrammetry, (c) Photon and X-ray absorptiometry of lumbar spine, (d) DXA of proximal femur, (e) QUS of calcaneum, (f) QCT of spine and (g) DXR (Huddleston 1988; Bonnicksen 1998; Rosholm *et al.* 2001)

Table 2.1: Criteria for osteoporosis as defined by WHO (Kanis *et al.* 2008)

Diagnosis	Criteria
Normal	$T\text{-score} \geq -1$
Osteopenia	$-1 < T\text{-score} < -2.5$
Osteoporosis	$T\text{-score} \leq -2.5$
Severe osteoporosis	$T\text{-score} \leq -2.5$ and accompanied by a fragility fracture

is compared with the reference BMD value of young adult Caucasian women, in order to calculate T -scores. T -score is the standard deviation of the measured BMD from the reference BMD. Based on the values of T -scores, osteoporosis can be categorized as shown in Table 2.1 (Kanis *et al.* 2008). Z -score can be calculated for an age-matched measure of reduction in bone mass, by finding the standard deviation of the measured BMD from an age-matched and gender-matched reference BMD (International Society for Clinical Densitometry 2015). $T\text{-score} < -2.5$ or $Z\text{-score} \leq -2$ indicates the presence of osteoporosis.

DXA can measure BMD of the whole body. But the skeletal sites generally used for the measurement of BMD are the lumbar spine, hip and forearm, as these sites are more prone to fragility fracture (International Osteoporosis Foundation 2013). DXA produces different values of BMD for various skeletal sites. The lowest T -score value obtained is used for the final diagnosis. BMD measurements of the central weight-bearing bones are preferred, as they are better predictors of fracture risk.

There are mainly three companies that manufacture DXA devices worldwide, namely Hologic[®], Norland[®] and Lunar[®]. As they use different normalized population as reference, BMD measurements obtained from the three manufacturers for the same person are different. This disparity causes difficulty in comparison of BMD measurements taken with different DXA devices especially during follow-up examinations. Hence, DXA-BMD measurements from different manufacturers need to be standardized for comparison. The standardization of BMD is dependent on the skeletal site analyzed. Various studies have been carried out for the standardization of BMD of different skeletal sites (Hui *et al.* 1997; Lu *et al.* 2001). The equations used for calculation of standardized BMD at the femoral neck are

$$sBMD = 0.939 \times BMD_{Lunar} - 0.023 \quad (2.1)$$

$$sBMD = 1.087 \times BMD_{Hologic} + 0.019 \quad (2.2)$$

$$sBMD = 0.985 \times BMD_{Norland} + 0.006 \quad (2.3)$$

The equations used for calculation of standardized BMD at the lumbar spine are

$$sBMD = 0.9683 (BMD_{Lunar} - 1.100) + 1.0436 \quad (2.4)$$

$$sBMD = 1.0550 (BMD_{Hologic} - 0.972) + 1.0436 \quad (2.5)$$

$$sBMD = 0.9743 (BMD_{Norland} - 0.969) + 1.0436 \quad (2.6)$$

Although there is a need to standardize BMD values, DXA is the most widely accepted diagnostic tool for osteoporosis. DXA-BMD can explain 70% of the bone strength. DXA has a low radiation exposure (1-50 millisievert (mSv)), high precision

(with a maximum acceptable precision error of 2-2.5%) and short scanning time (Link 2012). However, the high cost of scan and low availability limits the use of DXA in low economies (International Osteoporosis Foundation 2013). DXA gives an areal BMD measurement and is not a true volumetric quantification of bone density. DXA-BMD is sensitive to variations in bone size and can overestimate BMD in people with low stature and underestimate BMD in obese people. DXA-BMD measurements can also be affected by the presence of other bone diseases such as osteoarthritis in the hip or spine, osteomalacia, etc. Moreover, measurement of BMD alone cannot completely quantify the bone strength, as osteoporosis is also affected by a degradation of bone structure.

Quantitative imaging techniques such as QCT, pQCT and MRI can give a true volumetric measurement of BMD. pQCT and MRI can further be used to quantify the changes in trabecular bone architecture. These modalities will be discussed in the following subsections.

2.2.2 Quantitative Computed Tomography (QCT)

QCT gives a volumetric measurement of BMD independent of the body size and can diagnose patients with degenerative diseases or obesity. QCT captures images at different angles around the region and measures the X-ray attenuation by the bones. The image slices can be reconstructed as a three dimensional volume. The cortical and trabecular bones can be easily separated as they have different attenuation coefficients. Use of a calibration phantom during acquisition can help to convert the attenuation of X-rays measured in Hounsfield units to BMD values measured in mg/cm^3 . The calibration phantom also helps to maintain consistent results across QCT devices. However, the T -scores calculated from the BMD measurements of QCT are lower than that of DXA and cannot be used to diagnose osteoporosis according to the WHO classification using T -scores. Computed Tomography X-ray Absorptiometry is a technique by which QCT scan of proximal femur is projected into an image and the areal absorptiometric values can be used to determine DXA-equivalent values, to which WHO classification criteria

can be applied (Brett and Brown 2015).

QCT is generally used to measure the bone density at the hip and lumbar spine. QCT gives a more sensitive measurement of BMD than DXA, due to the measurement of trabecular bone density. Volumetric BMD values obtained from QCT can help predict fracture risk. Values within the range of $110 - 80\text{mg}/\text{cm}^3$ denotes mild increase in fracture risk, a range of $80 - 50\text{mg}/\text{cm}^3$ shows moderate increase and values $< 50\text{mg}/\text{cm}^3$ indicates severe increase in fracture risk (Link 2012). However, QCT suffers from a high radiation dose (0.06-2.9 mSv) and high cost of acquisition. Image acquisition can also introduce artifacts that can reduce the measurement accuracy.

Multi-detector CT offers a higher spatial resolution than conventional QCT and gives a higher accuracy of BMD measurement (Chen *et al.* 2018). Imaging the trabecular bone architecture requires a higher spatial resolution, but at the cost of a higher radiation dose. Ultra-low-dose multi-detector CT was recently proposed to measure density and micro-structure features that can discriminate between normal and vertebral fractured subjects at a low dose (Mei *et al.* 2017).

2.2.3 High Resolution peripheral QCT (HR-pQCT)

HR-pQCT is a widely explored QCT technique that uses high resolution volumetric images of the peripheral limbs such as distal radius and tibia, for the quantification of trabecular bone structure. The bone region is semi-automatically segmented from the high resolution images using edge detection method. The bone region is denoised using Gaussian smoothing filter and thresholded to separate the cortical and trabecular bones. HR-pQCT measures bone density and architecture of the cortical and trabecular bone regions. Volumetric BMD is measured with the help of a calibration phantom. The structure and connectivity of the trabecular bone architecture is measured using morphometric features. Finite element analysis can also be performed to analyze the biomechanical properties of trabecular bone. Figure 2.3 shows the pQCT image of the trabecular bone of distal radius of normal and osteoporotic women (Boutroy *et al.* 2005).

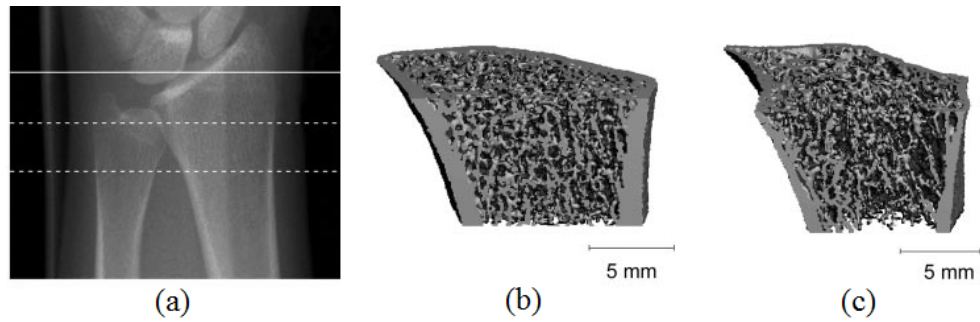


Figure 2.3: pQCT image of distal radius: (a) Scout view showing the ROI, (b) pQCT image of a premenopausal healthy woman and (c) pQCT image of a postmenopausal osteoporotic woman (Boutroy *et al.* 2005)

HR-pQCT density measurements have a high reproducibility with coefficient of variation $< 1\%$. HR-pQCT has a higher signal-to-noise ratio, resolution and lower radiation dose than multi-detector CT. pQCT features are highly correlated with micro-CT, the gold standard for quantification of bone micro-architecture, with coefficient of determination, $R^2 > 0.9$. pQCT facilitates the diagnosis of osteoporosis in morbid and fractured patients with low mobility, due to measurement at peripheral limb. pQCT can predict osteoporosis independently of DXA (Jiang *et al.* 2018; Biver *et al.* 2018; Ohlsson *et al.* 2016; de Jong *et al.* 2016). However, HR-pQCT is not yet used in clinical practice. The main limitations of HR-pQCT is that image acquisition takes a long time and motion artifacts are easily introduced. pQCT necessitates the registration of follow-up scans with high accuracy for longitudinal studies.

2.2.4 Quantitative Ultrasound (QUS)

QUS is a low cost prescreening tool used for osteoporosis. In QUS, pulsed sound waves in the frequency range of 500 kHz to 1.25 MHz are used to propagate through the bone region. Bone characteristics are measured based on attenuation and differential reflections of the propagated sound waves. The different measurements taken using QUS are Broadband Ultrasound Attenuation, Speed of Sound, QUS index, Stiffness Index, Amplitude Dependent Speed of Sound and Apparent Integrated Backscatter. These measurements help in identifying subjects with high fracture risks. According to the type of ultrasound transmission used, QUS devices may be categorized into three groups,

namely (1) trabecular sound transmission, commonly used at calcaneum bone, (2) cortical transverse transmission, used at phalanx bones, and (3) cortical axial transmission used at phalanx, radius and tibia. Of these, the calcaneal QUS devices are the most widely explored for texture analysis.

Some of the advantages of using QUS are low cost, ease of measurement due to its peripheral site, portability of equipment, etc. It does not involve any radiation exposure. QUS can help distinguish between healthy and fractured subjects (Fujiwara *et al.* 2005; Gl *et al.* 2005; Diez-Perez *et al.* 2007). However, QUS measurements taken at different skeletal sites can vary and with different manufacturers. Calcaneal QUS does not have a good correlation with DXA of spine and hip. QUS measurements can be calibrated with DXA to define diagnostic thresholds specific to the QUS device used (Hans *et al.* 2003). QUS has a low precision and sensitivity (Njeh *et al.* 2000). QUS devices have a poor reproducibility due to temperature variations and improper placement of transducers. Even though QUS is a low cost and radiation-less technique, it cannot be used as the sole diagnostic tool for osteoporosis.

2.2.5 Magnetic Resonance Imaging (MRI)

MRI is a volumetric imaging technique that involves no radiation. MRI makes use of a strong magnetic field to align the protons present in water molecules in the human body. A varying magnetic field is created by a radio frequency current from which protons absorb energy and flip their spins. When the magnetic field is removed, the protons return back to their normal spins, producing radio signals that are reconstructed into a volume data. Protons present in the cortical and trabecular bones and the surrounding soft tissues return to normal spins at different rates. MRI can thus take advantage of the water present in the porous trabecular bone. In T2 relaxometry, the difference in T2 measurements of the marrow bone interfaces and its decay characteristics are used to analyze the trabecular structure (Petrantonaki *et al.* 2005). Trabecular features such as thickness and connectivity can be measured from the trabecular bone region (Lin *et al.* 1998; Alberich-Bayarri *et al.* 2008). Although MRI shows promising results for

the identification of osteoporotic people, it is still an ongoing area of research. Disadvantages of MRI modality include motion artifacts, partial volume effects and a long acquisition time.

High resolution micro-MRI is a relatively new modality being explored for analysis of trabecular bone architecture (Wehrli 2007). HR-MRI features shows a high correlation with pQCT features. Properties of bone marrow adjoining the bone can also be quantified using Quantitative Magnetic Resonance that measures the relaxometry properties and proton Magnetic Resonance Spectroscopy that measures the adiposity of bone marrow. Bone marrow perfusion indices determined from dynamic contrast-enhanced MRI can also be used to assess the bone quality.

2.2.6 Digital X-ray Radiogrammetry (DXR)

DXR is a radiographic technique that uses computerized radiogrammetry and texture analysis to measure BMD (Rosholm *et al.* 2001). BMD is estimated from second, third and fourth metacarpal bone shafts of the hand radiograph, as shown in Figure 2.4. The metacarpal bones are automatically segmented using Active Shape Model (ASM). The radiogrammetric measure, Metacarpal Cortical Index (MCI), is combined with the texture feature, cortical porosity index, to obtain bone volume per area, which is then scaled with an empirically determined constant, c , that approximates the bone volume per area to the DXA-BMD of forearm measured using Hologic® densitometer.

$$DXR_{BMD} = c \times T \times \left(1 - \frac{T}{CW}\right) \quad (2.7)$$

where, c is a scaling constant, T is the average cortical thickness and CW is the average cortical width of the metacarpal bones.

DXR-BMD is highly correlated with DXA-BMD of the forearm, and hence DXR is a low cost alternative to DXA. However, DXR calculates the average cortical thickness assuming the bone shaft is cylindrical. But the metacarpal bone shaft is not truly cylindrical, especially towards the mid-shaft region, and hence DXR-BMD is not a true volumetric measure.



Figure 2.4: Estimation of BMD from hand radiograph using DXR (Rosholm *et al.* 2001)

DXR system is commercially available as Pronosco X-posure System™. Version-1 uses the three middle metacarpal bones, radius and ulna as the regions of interest. Version-2 uses only the three metacarpal bones to measure BMD. Sectra® OneScreen is the online version of DXR that receives the hand radiograph images and sends back the BMD results. It is available as a licensed version and the cost of analysis depends on the volume of data. Before analysis, a manual check of the quality of hand X-ray images is done by Sectra®. Hand radiographic images obtained from mammography modality is preferred as it produces high resolution images and hence gives more accurate results.

2.2.7 Radiography

Most of the quantitative imaging techniques suffer from high acquisition cost and limited availability in developing countries. Due to its low cost, ease of acquisition and wide popularity, radiography is being investigated as a potential low cost alternative for diagnosis of osteoporosis. Image processing and machine learning techniques are being investigated using radiographic images for the assessment of osteoporosis and fracture risk. The main skeletal sites used for radiographic analysis are trabecular-rich bone regions such as lumbar spine, hip, forearm, calcaneum and dental region. Figure 2.5 shows the radiographic images of the calcaneal bone texture of healthy and osteo-

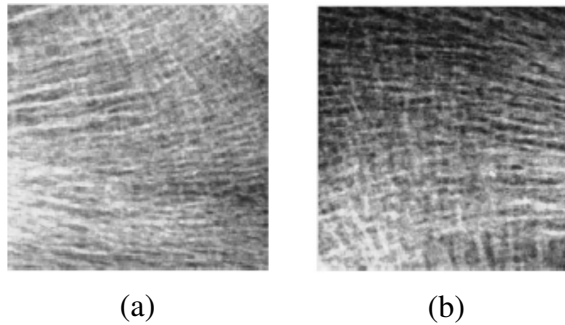


Figure 2.5: Texture analysis of trabecular bone of (a) healthy and (b) osteoporotic bone (University of Orleans 2014)

porotic people (University of Orleans 2014). Current research work focus on extraction of features from the radiographic images and supervised learning techniques for discrimination of healthy and osteoporotic subjects.

The imaging based techniques used for the diagnosis of osteoporosis that are reviewed in this section, namely DXA, QCT, pQCT, QUS, MRI, DXR and radiography, are summarized in Table 2.2.

2.3 SEGMENTATION METHODS

The previous section discussed the existing quantitative imaging techniques used for detection of osteoporosis. From the images acquired, the bone regions of interest must be segmented for further analysis. This section discusses the various semi-automated and fully automated segmentation methods used for the diagnostic techniques. The segmentation methods can be broadly categorized as threshold-based, edge-based, region-based, deformable models and deep neural networks.

2.3.1 Threshold-based methods

Thresholding is a segmentation method by which a gray level image is separated into foreground and background objects by selecting a cut-off value called threshold value. Threshold-based methods can be grouped as global thresholding and local thresholding.

Table 2.2: Summary of currently available imaging-based diagnostic techniques for osteoporosis

Diagnostic tool	ROI	Features extracted	Significance	Limitations
DXA	Lumbar spine, hip, forearm, whole body	BMD is measured as the ratio of bone mineral content and area	Gold standard, Low radiation exposure	Expensive, Not widely available in developing economies, Measures areal BMD, Does not account for details on bone structure
QCT	Lumbar spine and hip	Volumetric BMD using a calibration phantom	Provides a volumetric BMD, Sensitive due to measurements from trabecular bone	Expensive, Higher radiation dose than DXA
pQCT	Distal radius and tibia	Cortical and trabecular density and architecture	Ease of convenience due to peripheral measurement	Expensive, High radiation dose
QUS	Calcaneum, phalanx, tibia and radius	Sound attenuation and velocity	No radiation involved, Low cost, Portable device	Poor precision, sensitivity and reproducibility
MRI	Forearm, hip and spine	Histomorphometric measures	No radiation involved, Provides a volumetric measurement	Expensive
DXR	Metacarpal bones of hand	BMD is derived from radiogrammetry and cortical porosity	No subjective human error, Good correlation with DXA	Does not measure true volumetric BMD, Trabecular texture not taken into account
Radiography	Trabecular bone regions	Radiogrammetry, texture analysis	Low cost, low radiation	Areal measures, Accuracy depends on resolution and image acquisition conditions

Global thresholding uses a common threshold value to binarize the whole image into foreground and background. Otsu's method is the most commonly used global thresholding method in which an optimal threshold value is iteratively selected to maximize the inter-class variance and minimize the intra-class variance (Otsu 1975). It works best when the image to be segmented has a bimodal histogram. A drawback of global thresholding is that it is affected by uneven illumination. This can be dealt with by local thresholding methods that choose a different threshold value for different patches of the image. Niblack's method is a local thresholding method that uses a sliding rectangular window across the image to select a threshold value for each pixel by considering the mean and standard deviation of the pixels contained within the window (Wayne 1986). Threshold-based methods are usually used as a preprocessing technique and is further refined using other segmentation techniques.

2.3.2 Edge-based methods

Edge corresponds to discontinuities in gray level, texture or color. Edge-based segmentation methods help in detecting edges in the image. These methods include first derivative operators such as Roberts, Prewitt, Sobel, etc. and second derivative operators such as Laplacian of Gaussian. A drawback of edge operators is that false edges may be detected due to presence of noise or artifacts. Hence they are generally used as a preprocessing method and the results are further processed to give the final segmentation result. The detected edges can be connected by edge linking techniques to delineate the boundary of objects. Edge-based methods help to enhance the edges of objects and increase accuracy of segmented image. Edge detection algorithms have been employed for the segmentation of femur bones and lumbar vertebra for the diagnosis of osteoporosis (Santhoshini *et al.* 2013; Ghosh *et al.* 2011).

2.3.3 Region-based methods

Region-based segmentation methods exploit the similarities between pixels to identify coherent regions. Region growing is a simple region-based method where a seed point

is placed inside the object of interest and the neighboring pixels are checked for similarity with the seed points. Those pixels with a high similarity measure is included in the region and the others are regarded as background. This process is iterated till a homogeneous region is grown around the seed point to reach the object boundary. The seed point can be either defined by the user or placed automatically. Region growing methods work well for objects with nearly uniform intensities and having a high contrast with the background.

Watershed segmentation is a hybrid region growing method in which an image is considered as a topographic surface with peaks and valleys determined by the gray level intensities (Meyer 1994). Water is filled from the lowest valley points, ie. the local minima, to fill up catchment basin regions. As the water is filled, these catchment basins are prevented from leaking into each other by creating watershed lines. These watershed lines form the boundaries of the objects in the image. In watershed algorithm, the local minima of the image are labeled as markers (marker image) and the neighboring pixels are sorted in increasing order of their gray level values. If any neighbor has a lower intensity value, it indicates a local maxima and a watershed line is built. Gradient of the image to be segmented is usually used as the mask image for the watershed segmentation, as it gives a better information on the peaks or boundaries in the image. Unlike conventional region growing techniques, watershed segmentation can perform simultaneous segmentation of several regions. Raheja (2008) used watershed segmentation for segmentation of metacarpal bones in hand radiographs, which showed 75% success rate and high inter- and intra-observer agreement of 92% and 96%, respectively. A main limitation of watershed segmentation is that the resultant image may be over-segmented due to the presence of noise or a large number of local minima in the image. This can be alleviated by using marker-controlled watershed segmentation. In this method, pre-defined markers can be placed at certain regions to level-out the local minima. These markers now act as the local minima and watershed segmentation can be applied on the mask image, as shown in Figure 2.6. Marker-controlled watershed segmentation used for trabecular bone segmentation of wavelet decomposed micro-CT images showed lower segmentation error as compared to other approaches (Fourati and

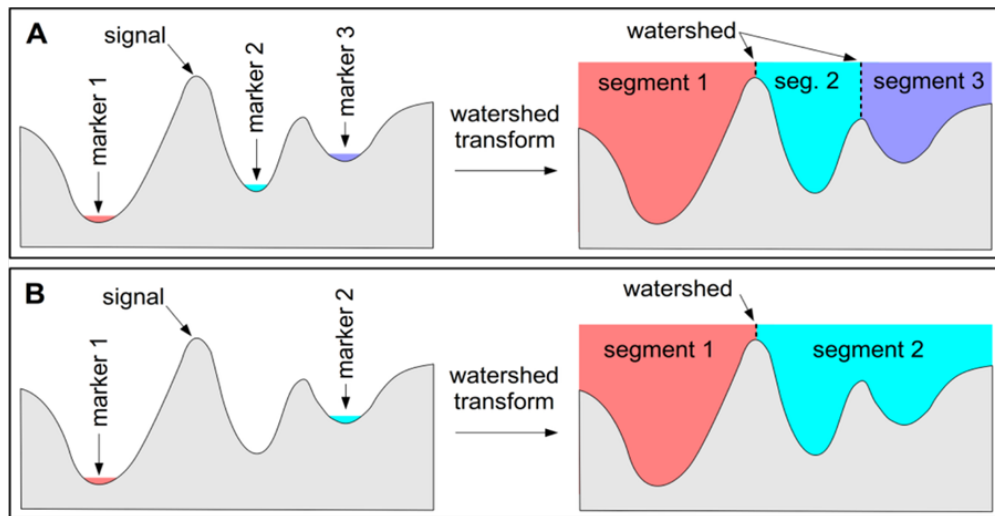


Figure 2.6: An illustration of watershed segmentation using placement of markers (Fisher 2014)

Bouhleb 2011). Another limitation of watershed segmentation is the possible edge leakage of the gradient mask image, which could be alleviated using edge-enhancement techniques such as viscous closing.

2.3.4 Deformable models

Deformable models are curves or surfaces that are able to respond to applied forces and constraints. It helps to model variabilities in shape or texture of objects belonging to a particular object class. Deformable models are robust to noise and acquisition conditions. The different deformable models used for segmentation are Active Contour Models, Active Shape Model (ASM), Active Appearance Model (AAM), etc.

Active Contour Model, also known as Snake, is a parameterized curve that moves within an image under the influence of an external energy, that guides the curve to the object boundary, and internal energy, that helps to keep the curve smooth (Kass *et al.* 1988). This method requires an initial placement of the curve and the curve is then deformed according to the energy forces. Accuracy and computation time of the segmentation method depends on the initial placement of the curve. Cortical and trabecular bones in CT images of tibia and vertebra can be automatically segmented using adaptive contour segmentation (Kovalovs and Glazs 2013). A dynamic contour model and re-

gional growth model based segmentation method was proposed by Zhang *et al.* (2017). Independent Active Contour Segmentation is a type of active contour method in which bone regions are first automatically segmented using heuristic thresholding and active contour models are then separately applied to each region (Korfiatis *et al.*). This method was proposed for trabecular bone segmentation in micro-CT images and shows lower absolute error as compared to fixed and Otsu thresholding techniques.

ASM is a deformable model in which prior shape information of the object is incorporated by learning the shape variations of the object from a set of training images (Cootes *et al.* 1995). Points along the boundary of the object in the training images are labeled manually and used to create a mean shape model of the object. All the individual shapes in the training images are assumed to be distributed in a multivariate normal distribution and the main modes of variation of the shapes are determined using Principal Component Analysis (PCA) and only the most significant modes of variation are retained. This information helps to model the shape of any given test image, irrespective of noise and background illumination. In DXR, 103 images were used to create an ASM model of the metacarpal bones and a reconstruction success of 99.5% was obtained with 5000 test images (Thodberg and Rosholm 2003). Segmentation of phalanx from hand radiographs using modified ASM models gave an average Hausdorff distance of 5.6 pixels (Dendere *et al.* 2013). Modified ASM algorithm was also used to segment distal radius in DXA images, which gave an increased segmentation accuracy of 47.4% over conventional ASM-based method (Lee *et al.* 2011).

AAM is a deformable model in which texture information is combined with shape information of the object to increase the segmentation accuracy and robustness (Cootes *et al.* 2001). AAM helps to significantly reduce the sensitivity to initial conditions. However, AAM requires a higher computation time than ASM. AAM segmentation has been shown to be promising in the segmentation of vertebra for the diagnosis of osteoporosis (Roberts *et al.* 2006).

Fischer (2009) used shape particle filter to extract metacarpal bones. It proved to be more robust than ASM and AAM. The mean landmark error obtained was 18.2 pixels. However, the precision and accuracy was poor and it took longer computation time.

2.3.5 Deep neural networks

Deep Neural Network (DNN) has become one of the most popular techniques used for segmentation and pattern recognition problems in various fields. DNN is found to surpass human accuracy in applications like object recognition. DNN is a neural network with many hidden layers of neurons in which each output neuron establishes a nonlinear function of the input neurons in the previous hidden layer and thus help to recognize complex patterns. Convolutional Neural Network (CNN) is a type of DNN in which images are fed as inputs. Complex features of the input images are extracted with the help of convolutional and pooling layers. CNN architectures have been recently used for segmentation of femur from MRI images. Hallyburton *et al.* (2017) proposed an automated segmentation method for proximal femur in MRI images by using CNN as a pixel-wise binary classifier and obtained a mean dice score of 0.702. Two CNN architectures, namely a pyramidal CNN and a u-net CNN architecture were proposed for segmentation of femur in MRI and dice score of 0.94 was obtained (Deniz *et al.* 2017). CNN has achieved a very high accuracy in many applications and are very promising. However, the main limitation of CNN is the requirement of a large set of training data to train the network.

Table 2.3 summarizes the methods used for the segmentation of bone regions in imaging based diagnostic techniques, namely watershed segmentation, active contour, ASM, AAM and CNN.

2.4 FEATURE EXTRACTION TECHNIQUES

Extraction of features that can characterize the properties of bones of normal and osteoporotic people is an important step in the diagnosis of osteoporosis. Feature extraction may be broadly categorized as radiogrammetric measurement, bone density measurement and texture analysis.

Table 2.3: Segmentation methods used in diagnostic techniques

Segmentation methods	Advantages	Disadvantages
Watershed (Meyer 1994)	Simple and easy implementation Does not require any training data	Sensitive to noise in the image Accuracy depends on the contrast of object boundary to background
Active Contour (Kass <i>et al.</i> 1988)	Placement of initial contour helps in a guided segmentation	Accuracy depends on proper placement of initial contour
ASM (Cootes <i>et al.</i> 1995)	High accuracy, precision and reliability Robust to noise and illumination conditions	Requires a large training set for high accuracy Manual annotation of training data is time consuming
AAM (Cootes <i>et al.</i> 2001)	More accurate and robust than ASM	Computationally more expensive than ASM
CNN (Deniz <i>et al.</i> 2017)	Achieves a very high accuracy	Requires a large training dataset

2.4.1 Radiogrammetric measurement

Radiogrammetry is a diagnostic technique in which physical properties of the bone are measured from radiographs. Manual radiogrammetry was the most common diagnostic technique for osteoporosis before the creation of DXA. In manual radiogrammetry, vernier calipers were used to measure the bone dimensions from radiographic films. The measurements usually taken are cortical width (CW), medullary width (MW) and length of tubular bones (L), etc. Figure 2.7 shows radiogrammetric measurements taken from the metacarpal bone of hand radiographs. Many bone indices have been derived from these radiogrammetric measurements such as Combined Cortical Thickness (CCT), Barnett-Nordin Index (BNI), Exton-Smith Index (ESI), Metacarpal Cortical Index (MCI), Pediatric Bone Index (PBI) etc. (Barnett and Nordin 1960; Thodberg *et al.* 2010).

$$CCT = T = CW - MW \quad (2.8)$$

$$BNI = \frac{T}{CW} \times 100 \quad (2.9)$$

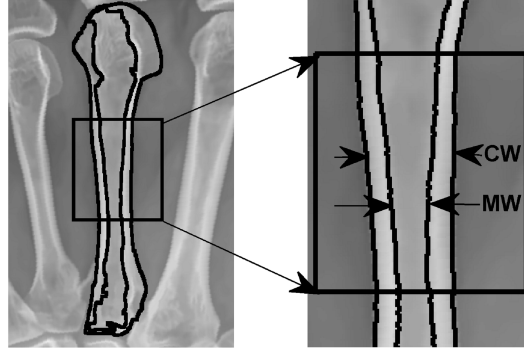


Figure 2.7: Radiogrammetric measurement of third metacarpal bone using hand radiograph

$$A = \pi \times T \times CW \left(1 - \frac{T}{CW}\right) \quad (2.10)$$

$$ESI = \frac{A}{CW \times L} \quad (2.11)$$

$$MCI = \frac{A}{CW^2} \quad (2.12)$$

$$PBI = \frac{\pi T}{CW \times L^{0.33}} \quad (2.13)$$

Manual radiogrammetry offered a simple and low cost technique for the measurement of low bone mass. However, the measurements were highly subjective. Low resolution of the radiographic films impacted the accuracy of the method. The development of computerized techniques helped to automate the radiogrammetric technique and increased the precision, accuracy and reproducibility of the method. DXR is a computerized radiogrammetric technique developed in 2001, where cortical radiogrammetric measurements of the middle three metacarpal bones are determined using automated methods. BMD measured using DXR has a good correlation with BMD measured using DXA, thus making it a potential low cost substitute for DXA.

2.4.2 Bone density measurement

The most widely accepted method for detection of osteoporosis clinically is the measurement of BMD. WHO recommends the measurement of BMD using DXA as the gold standard for the diagnosis of osteoporosis. BMD is measured by DXA as the ra-

tio of bone mineral content to the total bone area. In the case of QCT, a calibration phantom with different bone density compartments is used to convert the Hounsfield values to bone density values. QCT measures the bone density values of cortical and trabecular bone separately. DXR calculates BMD by combining cortical radiogrammetric and cortical texture features. Although measurement of BMD is the most common diagnostic feature, it can measure only the quantity of bone and not the bone structure. Hence, BMD alone is unable to accurately predict fracture risk among people (Leslie *et al.* 2015; Unnanuntana *et al.* 2010). Analysis of bone structure is thus essential to fully explain the changes in bone characteristics due to osteoporosis. As trabecular bone structure is more sensitive to progression in osteoporosis, characterization of trabecular bone architecture is an essential factor for the measurement of bone strength.

2.4.3 Texture analysis

Trabecular bone characterization using texture analysis is extensively being investigated for the study of osteoporosis. Bone strength is influenced by the shape, size, orientation and connectivity of the trabeculae. Osteoporosis results in a reduction in cortical bone thickness, a decrease in the number of trabeculae, increased inter-trabecular distance and a loss of connectivity of trabecular network. Skeletal sites rich in trabecular bone content such as distal radius, tibia, lumbar vertebra, proximal femur, calcaneum, dental images, etc. are being analyzed.

HR-pQCT and MRI can be used for the texture analysis of peripheral limb bones like distal radius and tibia. HR-pQCT, being a volumetric measurement taken from high resolution images, is highly correlated with micro-CT measurements. Features extracted using HR-pQCT and MRI images are mainly trabecular features such as thickness, number, spacing, etc.

Radiography offers a low cost modality for analysis of trabecular texture. Unlike HR-pQCT and MRI, radiograph produces a projected view of the trabecular structure. In radiographic images, the bone architecture appears as a texture constructed by the superposition of trabeculae from many planes. Radiographic texture analysis has been

done to measure roughness, orientation, granulation, periodicity, irregularity, etc. of the trabecular bone structure. Supervised learning techniques are used with texture features to classify healthy and osteoporotic subjects. However, texture analysis using radiographs is challenging because (1) the features obtained are areal measurements, (2) the trabecular texture of healthy and osteoporotic bones are visually very similar, and (3) the accuracy of measurements are affected by the resolution of the images.

Texture analysis methods used for the assessment of trabecular bone from radiographs may be broadly classified into (1) trabecular pattern indices, (2) histomorphometric analysis, (3) fractal analysis, (4) statistical analysis, (5) structural analysis and (6) transform-based analysis.

Trabecular pattern indices

Analysis of trabecular bone loss from radiographs were initially done with the help of trabecular pattern indices such as Singh Index, Saville Index and Calcaneal Index. Trabecular pattern indices are grading systems in which the difference in bone patterns visible in radiographs at different stages of osteoporosis are graded by radiologists. However, this manual assessment causes a high subjective error and are seldom used for clinical application.

Singh Index: The potential of radiographic texture analysis to discriminate between osteoporotic and non-osteoporotic groups was first demonstrated by Singh *et al.* (1970). Trabecular bone patterns visible in proximal femur radiographs is graded using Singh Index into six grades, grade 6 being normal and grade 1 being severely osteoporotic. Grade 3 or less indicates the presence of osteoporosis-related fracture. The femur radiograph to be analyzed is compared with a set of reference radiographs corresponding to the six grades and is categorized to the grade of the reference radiograph to which it matched the most. Singh Index was used as an indicator of osteoporosis and predictor of hip fracture.

Saville Index: Spinal radiographs have also been used to detect osteoporosis by grading trabecular patterns according to the appearance of patterns within the vertebra

Table 2.4: Trabecular pattern indices for assessment of severity of osteoporosis

Index	Grade	Radiographic pattern
Singh Index	6	Normal; Trabecular bone completely occupies proximal end of femur.
	5	Accentuated principal tensile and compressive trabeculae. Prominent Wards triangle.
	4	Markedly reduced principal trabeculae. But it can be traced from lateral cortex to upper part of femoral neck.
	3	Definite osteoporosis. Break in continuity of the principal tensile trabeculae opposite the greater trochanters.
	2	Only principal compressive trabeculae remain prominent
	1	Marked decrease in number of principal compressive trabeculae
Saville Index	0	Normal bone density
	1	Stenciled effect of end plates
	2	Thinner end plates and vertical striation
	3	End plates become less visible
	4	Ghost vertebra. No trabecular pattern visible. Bone density is almost that of soft tissue.
Calcaneal Index	5	Normal trabecular pattern
	4	Recession of middle region of posterior compression trabeculae
	3	Recession of the posterior tensile trabeculae
	2	Disappearance of anterior tensile trabeculae and recession of posterior tensile trabeculae
	1	Complete disappearance of posterior and anterior tensile trabeculae. Compression trabeculae reduces and becomes thinner.

(Saville 1973). Using Saville Index, the visible variations in the end plates and striations present in the vertebra are analyzed and graded into five grades, with grade 0 being healthy.

Calcaneal Index: Tensile and compression trabeculae in a healthy calcaneal bone are uniformly distributed. The anisotropic variations in calcaneal bone, caused due to faster degradation of tensile trabeculae as compared to compression trabeculae, as a result of osteoporosis can be graded using a 5-grade calcaneal index (Jhamaria *et al.* 1983). A modified 3-grade calcaneal index was later proposed by Pande *et al.* (2005). Calcaneal index has significant correlation with BMD of distal radius and hip and with QUS measurements.

The grading of trabecular pattern indices using radiographs is shown in Table 2.4.

Histomorphometric analysis

As osteoporosis progresses, the trabeculae reduces in number and breaks connectivity. This characteristic can be analyzed through connectivity analysis using histomorphometry. Histomorphometric analysis has been used to assess the risk of vertebral and hip fractures in osteoporotic people (Legrand *et al.* 2000; Blain *et al.* 2008). Histomorphometric analysis can be done using different methods such as computerized morphometry, node-strut analysis, star-volume analysis, etc. Some of the features measured using computerized morphometry are trabecular number, area, perimeter, thickness, ratio of bone volume to tissue volume, etc.

Node-strut analysis measures the trabecular profiles and the number of interconnections in a trabecular bone network obtained after a skeletonization process. Nodes refer to the junctions, struts refer to the branches and termini refers to the free ends in the trabecular skeleton. Features extracted using node-strut analysis are the number of nodes per tissue volume, ratio of node length to total skeletal length, ratio of node length to termini length, etc. Previous studies have investigated the ability of node strut analysis to quantify trabecular bone network (Schmah *et al.* 2011; Hwang *et al.* 2017; Numayama *et al.* 2002).

Star-volume analysis have been used in studies involving quantification of trabecular micro-architecture (Ikuta *et al.* 2000; Tanaka *et al.* 2001). Star-volume analysis measures the marrow star volume that estimates the mean size of the marrow space, and index of interconnectivity of the marrow cavities. Other features extracted using histomorphometric analysis include trabecular bone pattern factor, Euler number per tissue volume, etc.

Fractal analysis

Image can be regarded as a recurring pattern of self-similar sub-images with some random variations in position or orientation. Fractal analysis helps to describe the spatial pattern of textures by measuring the roughness of bone tissue based on self-similar sub-images. Fractal analysis is one of the most explored methods used for texture analysis

of trabecular bones. Fractal analysis can be done using different methods such as box counting method, directional average method, variance method, etc. (Benhamou *et al.* 2001; Jennane *et al.* 2007; Touvier *et al.* 2015).

Fractal dimension (FD), H_{mean} parameter and fractal signature are some of the features extracted using fractal analysis. To measure fractal dimension, the measured lengths and scales are plotted in a log-log graph and the slope of the best fitting line gives the fractal dimension. Irregular boundaries have higher fractal dimension. H_{mean} parameter is obtained by estimating the fractal dimension along a specific direction assuming a fractal Brownian motion model. Fractal signature quantifies the alteration in the fractal dimension and the scale at which the alteration has occurred. There is a significant difference in fractal anisotropy between healthy and osteoporotic groups (Loussot *et al.* 1996; Lemineur *et al.* 2004). A significant correlation was found between FD and BMD (Materka *et al.* 2000). Fractal signature is found to be a more sensitive method of measuring differences between osteoporotic and non-osteoporotic people as compared to FD (Harrar and Jennane 2015). Fractal analysis of X-ray images also helps to quantify changes in 3D trabecular structure (Pothuau *et al.* 2000; Jennane *et al.* 2001).

Statistical analysis

Statistical methods exploit the distribution and relationship between pixel intensities in an image. These methods help to study the connectivity of the trabecular bone. The most popular statistical methods for bone texture analysis are Gray Level Co-occurrence Matrix (GLCM), Gray Level Run Length Matrix (GLRLM), etc.

Gray Level Co-occurrence Matrix (GLCM):

GLCM is a second-order statistical method that measures the frequency of co-occurrence of a pixel pair within a fixed distance and direction (Haralick 1979). The orientations usually considered are 0° , 45° , 90° and 135° . Texture features are calculated from the resulting four matrices as well as from the summation matrix. Features that can be extracted from GLCM include energy, entropy, contrast, homogeneity, correla-

tion, etc. Texture analysis using GLCM has been used for evaluation of osteoporosis using calcaneal and dental images (Naik *et al.* 2016; Suprijanto *et al.* 2013; Pal and Anburajan 2016). GLCM features from 2D images are correlated with the 3D bone micro-architectural parameters (Shirvaikar *et al.* 2016). GLCM features of 3D pQCT volumes of distal radius are found to have discriminative ability among the healthy and osteoporotic patients (Valentinitsch *et al.* 2010).

Gray Level Run Length Matrix (GLRLM):

GLRLM is a higher order statistical method that measures the frequency of occurrence of connected pixels with the same intensity values along a particular direction (Galloway 1975). The features extracted from GLRLM are Short Run Emphasis (SRE), Long Run Emphasis (LRE), Gray Level Non-uniformity (GLN), Run Length Non-uniformity (RLN), etc. Fine textures are observed to have greater short runs with similar intensity values while coarse structures have more long runs with different intensity values. Several work have combined FD with statistical methods like GLCM and GLRLM to improve the discrimination between osteoporotic and non-osteoporotic group (Korchiyne *et al.* 2014; Lespessailles *et al.* 2008; Roberts *et al.* 2013).

Structural analysis

Structural texture methods analyze the spatial arrangements of the bone pixels in the image. They can explicitly represent the hierarchical structure of the texture. Structural methods include morphology-based methods, Laws' masks, Local Binary Pattern (LBP), etc.

Mathematical morphology:

Mathematical morphology is the process of filtering an image using non-linear operations. Geometric analysis of the objects in the image is done using structuring elements. The use of mathematical morphology for texture analysis was introduced by Werman and Peleg (1984). Each mathematical morphological operation is defined with a structuring element, whose size, shape and orientation can enhance different aspects of the image texture. The basic mathematical morphological operations, erosion and di-

lation, can be used to extract features that are invariant under linear grayscale transformations. Mathematical morphology can be used for the estimation of fractal dimension by dilating the gray level image with structuring elements of different scales. Veenland (1999) constructed Morphological Gradients Method (MGM) with different structuring elements and combined them into ratios to analyze bone texture images. MGM features performed better than fractal, Graylevel Dependence Matrix and Fourier features in distinguishing between healthy and osteoporotic subjects.

Laws' masks:

Laws' texture masks are filter masks that can assess bone texture properties from radiographic images (Laws 1980). These two-dimensional masks are created from a combination of five one-dimensional kernel vectors, namely level vector, edge vector, spot vector, ripple vector and wave vector. Level vector measures the average gray level intensity, edge vector determines the image gradient, spot and ripple vectors help to identify spot or ripple-like texture in the image and wave vector helps to measure the changes in gray level values. Texture images are filtered using these 2D masks from which features are extracted. Rachidi *et al.* (2008) used Laws' masks and statistical measures. The best discriminating ability was obtained by the combination of edge mask and average gray level mask.

Local Binary Pattern (LBP):

LBP, a combined statistical and structural method, is a promising texture analysis method. LBP encodes every pixel in the image with a binary pattern determined by thresholding the neighborhood of pixels with the corresponding centre pixel value. For bone texture analysis, either the LBP histograms of the healthy and osteoporotic groups are compared using a distance metric or statistical features are extracted from the LBP histograms to form feature vectors (Houam *et al.* 2012). One dimensional LBP applied to projections of radiographic images can better characterize bone texture as compared to 2D LBP (Houam *et al.* 2014). Three-dimensional LBP can help in describing local changes in the 3D bone structure during progression of osteoporosis (Mishra *et al.* 2011).

Transform-based analysis

Transform-based methods help to detect significant features in images that may not be visible in the spatial domain but can be captured in the transform domain. Transform-based methods include Fourier transform, Wavelet decomposition, Gabor filter, etc.

Fourier Transform:

Fourier transform provides both amplitude and phase information about an image. Applying Discrete Fourier Transform to an image represents the image as a function of sinusoidal components. Discrete Fourier Transform enhances the high frequency information in the image, but may eliminate low frequency content which may contain important information. Fourier Transform has been used for characterization of trabecular bone texture (Karunanithi *et al.* 2007). Gregory *et al.* (2004) showed that PCA and fractal parameters of the power spectral analysis of the Fourier transform could discriminate between the fractured and control groups. Chappard *et al.* (2005) and Brunet-Imbault *et al.* (2005) introduced new anisotropy indices from fast Fourier transform to measure the anisotropy of trabecular bone in calcaneal radiographs. These indices were superior in performance as compared to BMD of total femur and lumbar spine.

Wavelet Transform:

Wavelet transform is a promising transform-based method used for texture analysis. Using wavelet transform, an image can be decomposed into four sub-images by filtering it along the horizontal and vertical directions consecutively with low-pass (L) and high-pass (H) filters. The four sub-images obtained can be denoted as (1) LL that represents the original image at a lower resolution, (2) LH that enhances the vertical edges of the image, (3) HL that enhances the horizontal edges of the image and (4) HH highlights the diagonal edges of the image. The sub-images have information of a specific scale and orientation, which can be conveniently separated. Spatial information is retained within the sub-images. The sub-images may be further divided. In wavelet transform, only the LL sub-image will be further divided in the successive stages. In wavelet packet transformation, all sub-images are further divided. All sub-images have

different energies which can be extracted to obtain the feature vector. Trabecular bone characterization using wavelet transform has shown promising results in the study of osteoporosis (Houam *et al.* 2012; Yger 2014; Oulhaj *et al.* 2017a).

Gabor filter:

Gabor filter acts as a local band-pass filter with optimal joint localization properties in the spatial domain and the spatial-frequency domain. They have tunable orientation and radial frequency bandwidths and tunable centre frequency. Different sets of coefficients are obtained by filtering an image with a set of Gabor filters of different orientations and spatial frequencies. These coefficients are used to represent texture feature vector. Gabor features extracted from proximal femur radiographs correlate with the corresponding Singh index (Gaidel and Khramov 2015; Mengko and Pramudito 2002, 2004). Application of Gabor filter, wavelet transform and fractal dimension to proximal femur radiographs showed good correlation with Singh indices, with correlation values of 0.87, 0.84 and 0.79, respectively (Pramudito *et al.* 2007). Gabor features extracted from femur radiograph are also correlated with central DXA (Sapthagirivasan *et al.* 2013).

2.5 APPROACHES TO DIAGNOSTIC DECISION MAKING

The final stage of the pipeline is to make a diagnostic decision for osteoporosis based on the extracted features. The decision can be made using mainly two approaches: (1) comparison with a reference value and (2) using supervised learning techniques.

2.5.1 Comparison with a reference value

Most diagnostic tools that measure radiogrammetry and BMD make the final diagnosis by comparison of the extracted feature with a reference value. Using this approach, a reference value is determined for a measure by analyzing a large sample data of the

population. Radiogrammetric indices use the reference as the cut-off value to detect osteoporosis in subjects. Densitometric techniques use a reference BMD of a young adult population to calculate T -scores. Bone characteristics vary with gender and ethnic group and hence the reference cut-off value should be preferably determined specific to the gender and ethnicity. However, due to the lack of large population samples, WHO recommends the use of BMD of Caucasian women in the age group of 20 to 29 years as the reference for calculation of T -score for postmenopausal women and men above the age of 50 years. For pre-menopausal women and men below 50 years of age, calculation of Z -scores using an age-matched and gender-matched reference population is recommended (International Society for Clinical Densitometry 2015). Presence of osteoporosis is diagnosed if the value of T -score ≤ -2.5 or Z -score ≤ -2 .

2.5.2 Feature selection and supervised learning techniques

The second approach used for the diagnosis of osteoporosis is machine learning, in which significant features are selected and used to train classifiers to classify healthy and osteoporotic groups.

Feature selection is necessary to remove the redundant and irrelevant features, in order to improve the accuracy of classification. It also helps to reduce the complexity of the trained classifiers. There are many feature selection methods that can be used to select the best set of features for effective training of classifiers. Feature selection methods may be grouped broadly into three categories, namely filter, wrapper and embedded methods. Filter methods rank features by assigning a score to each feature. Depending on the scores, features are either selected or removed from the feature set. Examples of filter methods for feature selection are statistical tests, information gain, etc. Wrapper methods select the best feature set using a search strategy by creating different combinations of feature subsets and evaluating the performance of the model. The search strategies may be best-first search, hill climbing algorithm, forward or backward elimination, etc. Embedded methods select features that improve the accuracy of the classifier, while training. An example of embedded methods are regularization

methods such as LASSO, ridge, elastic net regression, etc.

Statistical analysis is a commonly used filter-based feature selection method for identifying texture features that characterize differences in healthy and osteoporotic bone images. The choice of statistical test used for the analysis depends on the type of variables and number of samples, as summarized in Table 2.5. Independent sample *t*-test may be used to assess whether the means of two groups are statistically significant from each other. Wilcoxon test can be used as an alternative to *t*-test to compare two matched samples in order to assess whether their population mean ranks differ. Mann Whitney test is used to test if two samples come from the same population. Kruskal Wallis test is an extension of Mean Whitney test, where it can be used to test if more than two samples come from the same population. Correlation analysis is another filter method that can be used to rank features according to their relation to the target variables. The similarity between the two groups can be tested using Pearson and Spearman correlation tests. Pearson correlation measures the linear dependence between two groups, while Spearman correlation is used to check whether the two groups are monotonically related.

Apart from feature selection methods, feature transformation using PCA can be used to reduce the feature dimension. Feature transformation method does not evaluate individual features for selection, but rather transforms the whole feature set to a low dimensional feature space, where the transformed features are combinations of original features.

Feature selection method is followed by supervised learning techniques to train classifier models. Supervised learning techniques are employed using two stages: training stage and testing stage. In training stage, training data that consists of images with prior information on the status of bone condition, is used to train classifier models. The trained classifier is then validated using unseen test data in the testing stage. Some commonly used classifiers for detection of osteoporosis are discussed below.

Artificial Neural Network (ANN) is a type of artificial intelligence that can recognize a pattern between the output classes and input features. ANN consists of an input and output layers and one or more hidden layers with hidden neurons. The weights

Table 2.5: Choice of statistical test depending on the type of variables and number of samples

Statistical test	Dependent variable	Comparison between variables				Relation between variables
		Two independent samples	Two in-paired samples	Two independent samples	More than two independent samples	
Parametric statistics	Normal data	Independent sample t -test	Paired t -test	One-way ANOVA	Repeated ANOVA	Pearson correlation
Non-parametric statistics	Ordinal data	Mann Whitney test	Wilcoxon test	Kruskal Wallis test	Friedman test	Spearman correlation

of the neurons are usually updated using a back propagation algorithm based on the input-output relation. Performance and accuracy depends on the network structure and number of inputs. ANN can efficiently handle noisy inputs. However, the training of ANN requires a large labeled training data and can be time consuming.

k -Nearest Neighbor (KNN) is a simple non-parametric supervised learning method by which a data point is classified by a majority vote of its neighbors with the object being assigned to the class most common among its k nearest neighbors. However, it is sensitive to the local structure of the data.

Logistic Regression (LR) classifier determines the relation between the independent input variables and dependent output variable by estimating the probability using a logistic function. The weights for the logistic regression classifier is adjusted over the training images. A softmax function is used to calculate the probability of belonging to an output class.

Support Vector Machine (SVM) is a non-parametric classifier that can be trained with a small dataset efficiently. SVM builds a hyper plane in a higher dimensional feature space in order to classify the two groups. Performance and accuracy depends on the hyper plane selection and kernel parameters. The determination of optimal parameters is not easy when there is a non-linearly separable data.

Random Forest (RF) classifier employs multiple decision trees from the training

		Condition		
		Condition Positive	Condition Negative	
Test Outcome	Test Outcome Positive	TP	FP	Positive Predictive Value $PPV = \frac{TP}{TP + FP}$
	Test Outcome Negative	FN	TN	Negative Predictive Value $NPV = \frac{TN}{FN + TN}$
		<i>Sensitivity</i> $= \frac{TP}{TP + FN}$	<i>Specificity</i> $= \frac{TN}{FP + TN}$	

Figure 2.8: Confusion Matrix

set and node splitting by selecting features randomly. Random forest takes a majority voting of the predicted classes of the individual classifiers for a final decision.

The classification results obtained from the classifiers may be grouped into True Positive (TP), False Positive (FP), True Negative (TN) and False Negative (FN). The presence of Low Bone Mass (LBM) in subject is taken as positive and healthy condition is taken as negative. True Positive denotes the case when LBM subject is correctly classified as LBM. False Positive is the case when a healthy subject is misclassified as LBM. True Negative is the case when healthy subject is correctly classified as healthy and False Negative denotes the LBM subject is wrongly classified as healthy. These four outcomes can be formulated into a confusion matrix as shown in Figure 2.8.

Various performance metrics such as sensitivity (Sn), specificity (Sp), precision or Positive Predictive Value (PPV), Negative Predictive Value (NPV), accuracy (Acc) and $F1$ -score may be derived from the confusion matrix as

$$Sn = \frac{TP}{TP + FN} \quad (2.14)$$

$$Sp = \frac{TN}{TN + FP} \quad (2.15)$$

$$PPV = \frac{TP}{TP + FP} \quad (2.16)$$

$$NPV = \frac{TN}{TN + FN} \quad (2.17)$$

$$Acc = \frac{TP + TN}{TP + FP + TN + FN} \quad (2.18)$$

$$F1-score = \frac{2 \times TP}{2 \times TP + FP + FN} \quad (2.19)$$

F1-score is often used when the distribution of classes are skewed, i.e. when there are more positive cases than negative cases and vice-versa.

Receiver Operating Characteristic (ROC) curve is a graphical plot between True Positive rate (sensitivity) and False Positive rate (1–specificity). Area under the curve (AUC) of the ROC measures the probability that a classifier will rank a randomly chosen positive instance higher than a randomly chosen negative one. Higher value of AUC indicates greater classification accuracy.

Odd's Ratio (OR) is another useful metric that defines the ratio of the odds of occurrence of an outcome in the presence of an exposure to the odds of occurrence of the outcome in its absence.

The following subsections discuss the previous studies on supervised learning techniques using radiographic texture analysis of trabecular bone regions.

Techniques based on Radiogrammetry:

Supervised learning techniques have been used to train classifiers with computerized radiogrammetric features for the classification of normal and osteoporotic groups. Radiographs of hand, dental and femur have been used to measure the radiogrammetric indices. Dental radiographs have been used to measure combined cortical thickness and area of trabecular bone of the mandible along with the age of subject to train classifiers and obtained a sensitivity of 92%, accuracy of 84% and Positive Predictive Value (PPV) of 85% (Kathirvelu and Anburajan 2014). Cortical width of the mandibular cortex and texture analysis using fractal dimension and GLCM obtained a better performance of sensitivity of 80%, specificity of 80% and AUC of 0.87, as compared to using radiogrammetric feature alone (Roberts *et al.* 2013).

Techniques based on Density Measurements:

As bone density does not completely describe the status of osteoporosis, several work have tried to combine bone density with texture features to increase the sensitivity of the diagnosis. Combination of BMD of lumbar spine with low H_{mean} fractal measure improved the OR of fracture from 6.1 to 9 (Benhamou *et al.* 2001). Combination of BMD of femoral neck with low H_{mean} fractal measure improved the OR of fracture from 4.78 to 14.06 (Lespessailles *et al.* 2008). Texture parameters using Fourier and fractal analysis were combined with BMD to enhance the classification performance (AUC of 0.82) as compared to BMD (AUC of 0.78) and texture features (AUC of 0.72) (Jeong *et al.* 2013). Combination of BMD with texture features, namely spinal Trabecular Bone Score (TBS) and calcaneal H parameter, helped to distinguish between subjects with and without osteoporotic fractures (Touvier *et al.* 2015). Fracture risk prediction can be enhanced by the assessment of vertebral fracture in addition to BMD (Siris *et al.* 2007).

Techniques based on Texture Analysis:

There are numerous supervised learning techniques for the classification of healthy and osteoporotic fractured groups using texture features of trabecular bone images. Histo-morphometric features combined with skeletal and fractal measures determined from distal radius radiographs attained a maximum sensitivity of 79% and specificity of 66% (Lee *et al.* 2008). Sela *et al.* (2013) used dental periapical X-ray images for extraction of trabecular texture features like porosity, number of vertices of pores and perimeter of pores, and achieved a training accuracy of 99.9% and test accuracy of 65%. Sapthagirivasan and Anburajan (2013) used hip radiographs to extract features such as trabecular area, boundedness, orientation, solidity of spur and delta, and achieved a classification accuracy of 90%, sensitivity of 90% and PPV of 89%. An interconnectivity index was developed using trabecular and node-strut features from calcaneal radiographs that achieved a classification accuracy of 94.36% (Harrar and Hamami 2013).

Supervised learning techniques using statistical methods show great results for the

classification of healthy and osteoporotic people. GLCM and GLRLM measured from calcaneal images after a variational model decomposition improved classification accuracy to 85% (Jennane *et al.* 2014). Zhou *et al.* (2016) used GLCM and GLRLM for detection of osteoporosis and obtained an accuracy of 89%. Cai *et al.* (2015) used GLCM and GLRLM features on microscopic bone tissue images and obtained a classification accuracy of 92%.

LBP is a very promising texture analysis method for the characterization of trabecular bone. Houam *et al.* (2014) applied 1D LBP on the 1D projected fields of the calcaneal X-ray images. One dimensional LBP features perform better than the classical LBP, with accuracy of 71.3% and AUC=91%.

Transform-based methods transform the images into a feature space that can help identify more discriminating features. Vokes *et al.* (2010) found that Radiographic Texture Analysis features from Fourier analysis produced a significant level of discrimination, with OR=1.5 per decrease of one standard deviation in Radiographic Texture Analysis feature. Predictive power of Fourier power spectrum-based FD in the distal radius are found to be comparable to trabecular BMD of radius (OR=1.5) but lower than that of total hip BMD (OR=2.44) (Majumdar *et al.* 2000). Yger (2014) used covariance matrix and wavelet marginals using Haar wavelets in calcaneal radiographs and obtained an accuracy of 74% for covariance matrix and 60% for wavelet marginals. El Hassani *et al.* (2012) used Dual Tree M-Band transform to achieve a high classification accuracy of 98% using calcaneal radiographs. Oulhaj *et al.* (2017b) showed that circular statistics can better characterize trabecular bone as compared to conventional statistical methods. A combination of wavelet decomposition and parametric circular models helped to improve the AUC value to as high as 96.5% for calcaneal radiographs.

The skeletal sites most investigated for radiographic texture analysis are calcaneal and dental trabecular bone regions, as these regions have a rich trabecular texture. Other skeletal regions that are potential sites for texture characterization are distal radius, lumbar vertebra and hip. Some of the classification techniques trained using calcaneal, dental and distal radius radiographs and their performance are summarized in Table 2.6.

Table 2.6: Trabecular bone texture characterization using radiographs

No.	Texture Analysis and Classification	ROI	Performance Results	Dataset	Reference
1	Dual-tree transform M-band on projected image with Renyi entropy and divergence, KNN classifier	Calcaneal	Acc of 98%	39 fractured cases and 38 controls	El Hassani <i>et al.</i> (2012)
2	Proposed an interconnectivity index, NDX, using trabecular and node-strut features, SVM classifier	Calcaneal	Acc of 94.36%	71 women with 11 healthy, 19 osteopenic, 31 OP and 10 severely OP cases	Harrar and Hamami (2013)
3	Wavelet Marginals- Haar, SVM classifier	Calcaneal	Acc of 63.8%, Sn of 62.1%, Sp of 65.5%	58 healthy and 58 OP cases	Yger (2014)
4	GLCM, GLRLM features from variational decomposition of image	Calcaneal	Acc of 85%	87 fractured cases and 87 controls	Jennane <i>et al.</i> (2014)
5	1D LBP on projected and enhanced image	Calcaneal	Acc of 71.3% and AUC of 91%	39 fractured cases and 41 controls	Houam <i>et al.</i> (2014)

No.	Texture Analysis and Classification	ROI	Performance Results	Dataset	Reference
6	Gabor filter bank, discrete wavelet frames, FD, LBP, discrete Fourier and Cosine transforms, Laws masks, edge histogram and GLCM, Bayes-Naive classifier	Calcaneal	Acc of 79.3% and AUC = 81%	58 OP cases and 58 controls	Zheng and Makrogiannis (2016)
7	Wavelet decomposition and parametric circular models	Calcaneal	AUC = 96.5%	87 fractured cases and 87 controls	Oulhaj <i>et al.</i> (2017b)
8	New anisotropic Discrete Dual Tree Wavelet Transform, SVM classifier	Calcaneal	Sn=90%, Sp=93%, Acc = 91%	87 fractured cases and 87 controls	Oulhaj <i>et al.</i> (2017a)
9	First and second order statistical features trained on SVM, KNN, Naive Bayes, ANN classifiers	Calcaneal	For SVM: Sn=100%, Sp=95.74%, Acc = 97.87%	87 fractured cases and 87 controls	Singh <i>et al.</i> (2017)
10	1D projection modeled as fractional Brownian motion, SVM classifier	Calcaneal	Acc of 94.5%, Sn of 96.9%, Sp of 97.6%	-	Tafraouti <i>et al.</i> (2017)
11	Fractional Brownian model and Rao geodesic distance, KNN classifier	Calcaneal	Acc of 96.6%, Sn of 97.8%, Sp of 95.4%	348 healthy and 348 OP cases	El Hassouni <i>et al.</i> (2017)
12	Oriental fractal analysis	Calcaneal	Acc of 71.8%, Sn of 72%, Sp of 71%	87 healthy and 87 OP cases	Harrar <i>et al.</i> (2018)

No.	Texture Analysis and Classification	ROI	Performance Results	Dataset	Reference
13	Mandibular cortical width, FD, GLCM with RF classifier	Dental	AUC=0.872, Sn=Sp=80%	663 women with 140 OP cases and 523 controls	Roberts <i>et al.</i> (2013)
14	CCT, mandibular trabecular area, age	Dental	Acc = 84%, Sn = 92%, PPV = 85%, AUC=0.89	36 OP cases and 28 controls	Kathirvelu and Anburajan (2014)
15	Proposed Mandibular Cortical degree, Support Vector Regression	Dental	AUC = 0.88	12 OP cases, 18 osteopenic and 69 controls	Muramatsu <i>et al.</i> (2016)
16	Fractal, radiogrammetric and histomorphometric analysis of mandibular bone, Genetic Swarm Fuzzy classifier	Dental	Sn=99.1%, Sp=98.4%, Acc = 98.9% using hip BMD	141 women with 20 OP and 121 controls as per hip BMD	Kavitha <i>et al.</i> (2016)
17	Histogram of Gradients features, SVM classifier	Dental	Acc = 72.5%	19 OP cases and 21 controls	Bo <i>et al.</i> (2017)
18	Fourier power spectrum-based fractal analysis	DR	OR=1.5 comparable to trabecular BMD	30 OP cases and 27 controls	Majumdar <i>et al.</i> (2000)
19	Fractal, histomorphometric and skeletal measures, SVM classifier	DR	Max Sn = 79% and Sp = 66%	47 OP cases and 47 controls	Lee <i>et al.</i> (2008)

2.6 PREDICTION OF FRACTURE RISK

Apart from diagnosis of osteoporosis, prediction of fracture risk is emerging as an important area of research. However, there are just a few fracture risk assessment tools being currently used in clinical practice. Some of these fracture prediction tools are discussed in the following subsections.

2.6.1 Trabecular Bone Score (TBS)

TBS is a measure of bone texture analyzed from DXA images of the lumbar spine (Pothuaud *et al.* 2008). TBS is used to predict the risk of fracture by quantifying local variations in gray level of the DXA image. Mean value of individual assessments of the lumbar vertebrae is estimated. Variogram, which is the mean variation between two pixel intensity values with a separation vector, is computed. TBS is determined from the slope at the origin of log-log plot of the variogram. A higher value of TBS indicates a well-connected bone architecture. A value of $TBS > 1.35$ denotes a healthy bone and $TBS < 1.20$ indicates a weak bone with degraded micro-structure. TBS values in the range of 1.20 to 1.35 implies partial degradation of bone quality. TBS can be measured from the software, TBS iNsight™. TBS correlates well with micro-CT features and with the mechanical behavior of vertebra in ex-vivo studies (Silva and Leslie 2017). TBS can be used in the prediction of osteoporotic fractures in men above the age of 50 years and postmenopausal women (Ripamonti *et al.* 2018). TBS can identify people with osteoporosis and fracture risk independent of DXA-BMD, due to the assessment of early changes in the trabecular bone structure. TBS along with DXA-BMD and fracture risk score, FRAX, can be used to adjust FRAX fracture risk in aged people (International Society for Clinical Densitometry 2015).

2.6.2 Finite Element Analysis (FEA)

FEA is a computerized technique for analysis of structural behavior in bone due to applied stress. FEA measures the bone's ability to resist bending, torsion and compres-

sion (Burr 2016). The bone structure is divided into a number of finite elements whose geometry is defined by its nodes. These elements are assigned properties of the underlying bone tissues. A virtual load is applied to the elements and stress and strain inside the structure and its deformation are determined. This helps to analyze the impact of a fall on the bone structure, as the occurrence of a fragility fracture is highly dependent on density, thickness and strength of the bone. Several work are being investigated on FEA of DXA and CT images for fracture risk assessment (Razmkhah and Ghasemnejad 2016; Naylor *et al.* 2013; Reddy *et al.* 2016; Lahari *et al.* 2011). Finite element models are better predictors of vertebral body compressive strength than bone density measured from QCT (Crawford *et al.* 2003). FEA of HR-pQCT images of radius and tibia can detect osteoporosis-related fractures independent of DXA in postmenopausal women (Liu *et al.* 2012). Three dimensional finite element models have been generated from 2D radiographs as a cost-effective technique for the estimation of patient-specific failure loads (Thevenot *et al.* 2014). FEA can be used with texture analysis methods like histomorphometry for the measurement of bone strength (Xu *et al.* 2016).

2.6.3 Vertebral Fracture Assessment (VFA)

VFA is a fracture assessment tool that analyzes DXA images of the whole spine and identifies prevalent vertebral fractures. The presence of a fracture indicates a high risk for another osteoporosis-related fracture at spine, hip or wrist. VFA is recommended for men above the age of 80 years and women above the age of 70 years with a T -score < -1 , previous history of vertebral fracture after the age of 45 years, height loss of more than 4 cm and/or undergoing glucocorticoid therapy for at least three months (International Society for Clinical Densitometry 2015). The significance of VFA measurement is the identification of vertebral fractures in patients who are asymptomatic and have no back pain. About 40% of the patients detected with vertebral fracture have DXA T -score > -2.5 (International Society for Clinical Densitometry 2012). Hence VFA is a better predictor of fragility fractures than DXA-BMD.

2.6.4 Fracture Risk Calculators

Clinical factors are important determinants for the incidence of osteoporotic fractures. Inclusion of clinical risk factors along with BMD measurement can greatly improve the prognosis of future fracture risk (Unnanuntana *et al.* 2010; Kanis 2002). Some of the major clinical risk factors are gender, age, body weight, exercise, nutrition, consumption of alcohol, tobacco, drugs, history of parental or personal osteoporosis-related fractures, etc. These clinical factors have been used for the development of fracture risk calculators that can predict the risk of future fractures. Some of the fracture risk calculators are FRAX[®], FORE fracture risk calculator, QFracture[®], Garvan, FRACTURE Index, Structural fragility score, Osteoporosis self-assessment tool, etc.

FRAX[®]

FRAX[®] is a fracture risk calculator that uses DXA-BMD and clinical factors to predict a 10-year fracture risk score (University of Sheffield 2008). FRAX[®] was developed from nine population-based cohorts and is available for various population groups belonging to different ethnicity. FRAX[®] can calculate fracture risks in people above the age of 40 years. FRAX[®] has been incorporated into DXA so that fracture risk scores are displayed along with DXA-BMD results. If DXA-BMD is unknown, FRAX[®] uses body mass index of the subject to calculate the fracture risk score. However, FRAX[®] measured using body mass index may not be very accurate as there is no information on bone mass. FRAX[®] gives two scores, namely hip fracture risk score and major osteoporotic fracture risk score which includes hip, spine, forearm or humerus. Although FRAX[®] has been recommended by WHO for clinical use, FRAX[®] may underestimate the risk of fracture for patients who have had a recent fracture (Roux *et al.* 2014). Compared to other fracture risk assessment tools, FRAX[®] shows a low positive predictive value and high negative predictive value (Dagan *et al.* 2017). Moreover, it does not include fall risk, vertebral fracture and other known risk factors and depends on adequacy of epidemiological information.

FORE Fracture Risk Calculator (FORE FRC™)

FORE FRC™ is a fracture risk calculator predicts fracture risk into three classes: low, medium and high fracture risk groups. FORE FRC™ model also uses clinical parameters and BMD to predict fracture risk. FORE FRC™ yields higher fracture rates in women with shorter life expectancy (FORE 2012).

QFracture®

QFracture® risk calculator is developed from the sample population of United Kingdom (ClinRisk 2016). QFracture® predicts the fracture risk from clinical parameters and detailed medical history of a person (Hippisley-Cox and Coupland 2012). QFracture® is observed to be a better fracture risk predictor of the hip than FRAX® (Dagan *et al.* 2017).

Garvan

Garvan calculator is a simple online calculator, developed from the sample population of Australia. Garvan fracture risk calculator considers very few risk factors for prediction of fracture risk in people (Garvan 2008).

FRACTURE Index

FRACTURE Index is a fracture risk model, developed from the Study of Osteoporotic Fractures and validated on the Epidemiology of Osteoporosis study (Black *et al.* 2001). FRACTURE Index can be used for men and women of all age groups. FRACTURE Index predicts a five-year risk of occurrence of hip, vertebral and non-vertebral fracture by using clinical risk factors such as age, weight, maternal history of fracture, smoking habit, use of arms to stand up from a sitting position, and BMD *T*-score (Medscape 2001).

Structural Fragility Score (SFS)

A recently introduced fracture risk predictor, SFS, was developed using a cohort of 589 postmenopausal women aged 42 to 94 years in France. SFS combines age, cortical porosity and trabecular density measured by HR-pQCT at the distal radius. It was found that a threshold of 22 can predict imminent and overall fracture independently of the femoral neck T -score of <2.5 and FRAX[®] $>20\%$.

Osteoporosis Self-Assessment Tool for Asians (OSTA) index

OSTA index is a simple and free risk assessment tool based on age and bodyweight, developed for postmenopausal Asian women (Koh *et al.* 2001). Osteoporosis Self-Assessment Tool (OST) is a similar prescreening calculator developed for men and women of Caucasian ethnicity. For women, OST score ≤ -4 indicates high risk group, index ≥ 1 indicates low risk group and index between 0 and -3 refers to an intermediate risk group (Medscape 2002; Geusens *et al.* 2002). For men, OST score ≤ -2 indicates high risk group, index ≥ 4 indicates low risk group and index between -1 and 3 refers to an intermediate risk group (Adler *et al.* 2003). It is recommended to screen men with OST score < 4 and women with OST score < 1 .

Table 2.7 summarizes some of the freely available online fracture risk calculators that can be used for the prediction of fragility fracture risk.

2.7 DISCUSSION

As discussed in Section 2.2, the gold standard technique used for the detection of osteoporosis is DXA. However, its greatest limitations are the high cost and low availability in developing countries. The use of other diagnostic techniques such as QCT, DXR and MRI are also limited by the high cost of scans in low economies. Hence, there is a need for a cost-effective alternative for diagnosis of osteoporosis which would be more accessible and affordable to the people living in a developing country like India.

Table 2.7: Fracture risk calculators

Risk model	Inclusion criteria	Clinical risk factors	Outcome	Weblink
FRAX [®]	Men and women aged 40-90 years	Age, gender, ethnicity, weight, height, history of previous fracture, parental history of fractured hip, smoking and drinking habits, use of glucocorticoids, presence of rheumatoid arthritis or secondary osteoporosis.	10 year probability of a hip fracture and a major osteoporotic fracture, with or without BMD measurement	(University of Sheffield 2008)
FORE FRC [™]	Postmenopausal women and men aged above 45 years	Age, gender, ethnicity, weight, height, history of previous fracture, parental history of fractured hip, smoking and drinking habits, use of glucocorticoids, presence of rheumatoid arthritis or secondary osteoporosis.	10 year probability of a hip fracture and a major osteoporotic fracture, with BMD measurement	(FORE 2012)
QFracture [®]	Men and women aged 30-99 years	Age, gender, ethnicity, weight, height, history of previous fracture, parental history of fractured hip, smoking and drinking habits, use of glucocorticoids, antidepressants, steroids or estrogen, presence of rheumatoid arthritis, secondary osteoporosis, diabetes, dementia, cancer, asthma, stroke, chronic liver or kidney disease, Parkinsons disease, epilepsy, malabsorption and endocrine problems.	1 to 10 year probability of a hip fracture and a major osteoporotic fracture without BMD measurement	(ClinRisk 2016)
Garvan	Men and women aged 50-96 years	Age, gender, weight, history of previous fracture.	5 and 10 year probability of a hip fracture and a major osteoporotic fracture, with or without BMD measurement	(Garvan 2008)

Moreover, DXA gives an areal measurement of BMD, which can overestimate or underestimate bone density in people with low stature or obesity, respectively. DXA do not take into account the structure of the bone, and hence cannot fully characterize the changes in bone due to osteoporosis. Presence of previous fractures and compression fractures may make it difficult to diagnose osteoporosis using BMD alone (Jeong *et al.* 2013). Studies have shown that texture analysis of trabecular bone can discriminate fractured and non-fractured groups in cases where BMD values overlap. Hence, inclusion of the trabecular bone features would give a more sensitive measurement for the detection of osteoporosis and fracture risk prediction. QCT, HR-pQCT and MRI give true volumetric measure of the bone density and architecture, but they are quite expensive. QCT and HR-pQCT acquisition also cause a high radiation exposure.

A cost-effective solution to this would be the use of X-ray imaging for a combined diagnostic approach through cortical radiogrammetric and trabecular texture analysis, thus accounting for both reduction in bone mass and structure. For a low-cost volumetric measurement, determination of the cortical bone volume using 3D reconstruction of the bone from biplanar X-ray images is a promising approach. This low-cost diagnostic tool for osteoporosis can give a volumetric measurement of bone density at a low radiation exposure using a widely available imaging modality like X-ray, in order to benefit the elderly population in low economies.

The NHANES-III database containing BMD measurements of Caucasian women is recommended by WHO to be used as the reference to calculate T -scores for men and women belonging to all ethnic groups, in case of a lack of normalized database for the population (Kanis *et al.* 2008). However, the physical characteristics of the bone varies with gender and ethnicity. The African ethnic group has a higher mean reference BMD value and Asian race have a lower mean reference BMD value than their counterparts in American and European population. Thus, measurement of DXA-BMD using Caucasian women as the reference standard may overestimate or underestimate the T -scores for population groups belonging to other ethnic groups. Hence, there is a need to build a database for each population group using a large normalized population sample data.

There are several multi-centre cohort databases being studied, some of which are the Study of Osteoporotic Fractures (SOF) (The Study of Osteoporotic Fractures (SOF) 1986), Framingham Osteoporosis Study (FOS) (Hannan *et al.* 1992), Dubbo Osteoporosis Epidemiology Study (DOES) (Chang *et al.* 2004), Epidemiology of Osteoporosis (EPIDOS) (Schott *et al.* 2005; Garnero *et al.* 1996), National Osteoporosis Risk Assessment (NORA) (Siris *et al.* 2002), Os des Femmes de Lyon (OFELY) (Albrand *et al.* 2003; Sornay-Rendu *et al.* 2005), Swiss Evaluation of the Methods of Measurement of Osteoporotic Fracture Risk (SEMOF) (Krieg *et al.* 2006; Popp *et al.* 2016), Osteoporotic Fractures in Men (MrOS) (Orwoll *et al.* 2005; Cawthon *et al.* 2016; Bauer *et al.* 2007), Basel Osteoporosis Study (BOS) (Hollaender *et al.* 2009), etc. Although image-based databases with follow-up studies have been built for the study of osteoporosis and related fractures, they are not publicly available and hence limits the research in this field.

2.8 CONCLUSION

In this chapter, the current diagnostic imaging-based techniques for detection of osteoporosis and assessment of fracture risk have been discussed. DXA is the gold standard for detection of osteoporosis, but is not extensively used in low economies due to the high cost of scans and low availability. DXA do not give a true measurement of BMD and a very accurate prediction of fracture risk. The structural deterioration of the trabecular bone is also not taken into account for DXA analysis. Radiographic analysis is a potential alternative to DXA. Supervised learning techniques using a combined cortical radiogrammetry and trabecular texture analysis of radiographic images is a promising low-cost solution for assessment of osteoporosis and fracture risk.

CHAPTER 3

CORTICAL RADIOGRAMMETRY OF THIRD METACARPAL BONE

3.1 INTRODUCTION

Osteoporosis is a systemic disease in which bone loss affects all sites of the skeleton. The analysis of any skeletal site can reflect the overall bone loss status of the human body. This work uses hand and wrist radiographs for the analysis of bone loss due to the convenience of image acquisition of the peripheral limb for people suffering from morbidity, spinal deformity and fractures.

Metacarpal radiogrammetry is a well-established technique for the detection of bone loss in people (Barnett and Nordin 1960). The development of computerized techniques has helped to automate metacarpal radiogrammetry and is used as a low cost technique for the diagnosis of osteoporosis (Adami *et al.* 1996; Rosholm *et al.* 2001; Raheja 2008). DXR measures BMD by analyzing the metacarpal bones of hand X-ray images. DXR-BMD is observed to have a good correlation with DXA-BMD of the forearm, hip and spine (Rosholm *et al.* 2001). Hence, metacarpal radiogrammetry from hand radiographs can help to measure the bone loss due to osteoporosis. Radiogrammetric measures of the second, third and fourth metacarpal bones are well correlated with each other, and thus cortical radiogrammetry of a single metacarpal bone is sufficient. In this work, the third metacarpal bone is used as it gives a better projection profile in the radiographic image as compared to the second and fourth metacarpal bones.

This chapter discusses the proposed automated segmentation and radiogrammetric analysis of the third metacarpal bone from hand and wrist radiographs.

3.1.1 Challenges in X-ray imaging

A hand radiograph is obtained by projecting X-ray beam from an X-ray source onto the hand. The amount of X-ray absorbed by hand bone depends on its density and composition. The attenuated X-rays are captured by a detector that produces a superimposed 2D image of the hand. As bone is denser than the surrounding soft tissue, it produces a higher intensity on the radiograph. X-ray images pose various challenges for segmentation and accurate geometric measurements. The challenges of hand X-ray imaging are given below.

Blurring: Blurring of the radiographic image may be caused either due to patient motion or finite size of the X-ray source. X-ray focal spot is not an ideal point source. It behaves as a collection of many point sources, each forming its own image of the bones. Hence the bone edges may not be formed at the same point and appears blurred. Blurring increases with size of the focal spot and varies with the imaging system used.

Magnification due to X-ray source to detector distance: Hand X-ray images are magnified while X-ray is projected from the source to the detector. The amount of magnification increases as distance between the X-ray source to the hand decreases. Magnification affects the apparent dimension of the hand and decreases the accuracy of cortical measurements.

Contrast variation due to X-ray exposure conditions: Hand X-ray images may be overexposed or underexposed depending on the image acquisition conditions. Contrast of X-ray images depend on the radiation dose used, distance of the hand from X-ray source and thickness of the hand. A higher peak kilovoltage (kVp) at the X-ray source produces a stronger penetrating beam, which gives a good contrast for thick objects and a poor contrast for thin objects.

3.1.2 Need for automated segmentation

Manual segmentation is considered the most accurate segmentation, but it is highly subjective and time consuming. Manual segmentation may show high intra-observer and

inter-observer variabilities. Automated segmentation methods help to mitigate the problem of high subjective error and time consumption. Automation improves the precision and reliability of the measurements. Therefore, there is a need to develop automated segmentation methods for the segmentation of bone regions in diagnostic tools.

3.2 SEGMENTATION OF THIRD METACARPAL USING WATERSHED ALGORITHM

The proposed segmentation approach comprises of mainly four stages, namely (1) pre-processing of hand X-ray image to remove noise and soft tissue regions, (2) automatic detection of anatomical landmarks and localization of third metacarpal bone, (3) segmentation of outer and inner edges of the third metacarpal bone using marker-controlled watershed algorithm and (4) radiogrammetric analysis of the third metacarpal bone shaft. A flowchart of the proposed segmentation approach is shown in Figure 3.1.

3.2.1 Preprocessing

Preprocessing of X-ray images is necessary to increase the accuracy of segmentation and radiogrammetric analysis. The preprocessing techniques used in this work to overcome the challenges posed by X-ray images are discussed below.

Magnification and blurring effects

Magnification correction can be done if the distance between X-ray source and detector is known. It can also be overcome by placing a calibration device of known size along with hand during image acquisition. Since actual size of the device is known, dimension of image pixel can be determined as

$$\text{Pixel dimension} = \frac{\text{Actual dimension (cm)}}{\text{Measured dimension (cm)}} \quad (3.1)$$

In case of images in Digital Imaging and Communications in Medicine (DICOM) format, the pixel dimension can be obtained directly from the header file of the DICOM image.

Blurring of the bone edges of hand X-ray images can be reduced by edge enhancement techniques. In this work, the hand bone edges are enhanced by the use of mathematical morphological operations, which will be discussed in Section 3.2.3.

Denoising

Patch-based denoising methods, that depend on the self-similarity of image pixels, can help to preserve the edges while smoothing the noise in hand X-ray images. Some common patch-based methods are bilateral filters, Non-Local Means (NLM), Block Matching 3D (BM3D) etc. While Gaussian filter does a weighted averaging of pixels in which the weights depend on the spatial position of the neighborhood pixels with respect to the center pixel, a bilateral filter (also called Yaroslavsky filter) does a

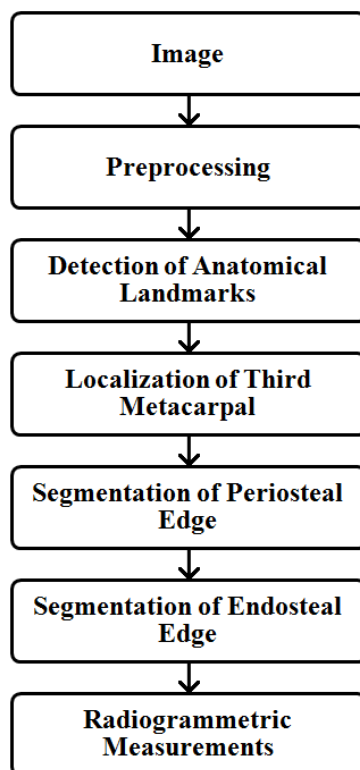


Figure 3.1: Flowchart of the proposed methodology

data-dependent weighted average of pixels, where the weights depend on both the spatial and intensity proximity of the neighborhood pixels (Tomasi and Manduchi 1998). Higher the similarity between pixels, higher the weights of the bilateral filter. This helps to prevent blurring at the object edges in the image. NLM does a data-dependent weighted average of patches with weights depending on spatial proximity and similarity in patches (Buades *et al.* 2005). In NLM filter, pixel intensity is the weighted average of all pixels in the image whose Gaussian neighborhood is similar to the neighborhood of the pixel. NLPCA denoising method implements NLM along with PCA for removing redundancy in the similar patches and thus helps in a faster implementation of the algorithm. BM3D algorithm is based on non-local image modeling and frequency domain filtering (Dabov *et al.* 2007). Instead of a weighted averaging in spatial domain, similar patches are transformed to wavelet domain where hard thresholding and Wiener filtering is done to remove noise while preserving the edges. In this algorithm, image is first divided into a number of 2D fragments, from which similar fragments are grouped together to form 3D stack. A collaborative filtering is then performed to achieve sparsity. The filtered fragments are returned back to their original positions to reconstruct the denoised image.

Figure 3.2 shows the comparison of different denoising methods. Difference image of the original and denoised images are displayed for a qualitative analysis of the amount of noise removed. As seen in Figure 3.2, bilateral filter removes noise in the darker regions quite well, but not in the brighter regions. NLPCA and BM3D methods removes noise in all areas quite well, while preserving the edges. As compared to the other denoising techniques, BM3D algorithm shows the best performance (lowest mean square error) for the removal of Poisson and Gaussian noise from images. Hence, BM3D algorithm is used in this work for the removal of noise from hand and wrist radiographs. Figure 3.3 shows the original image and denoised image filtered using BM3D method and their intensity profiles along a row. BM3D method smooths homogeneous regions while preserving the bone edges.

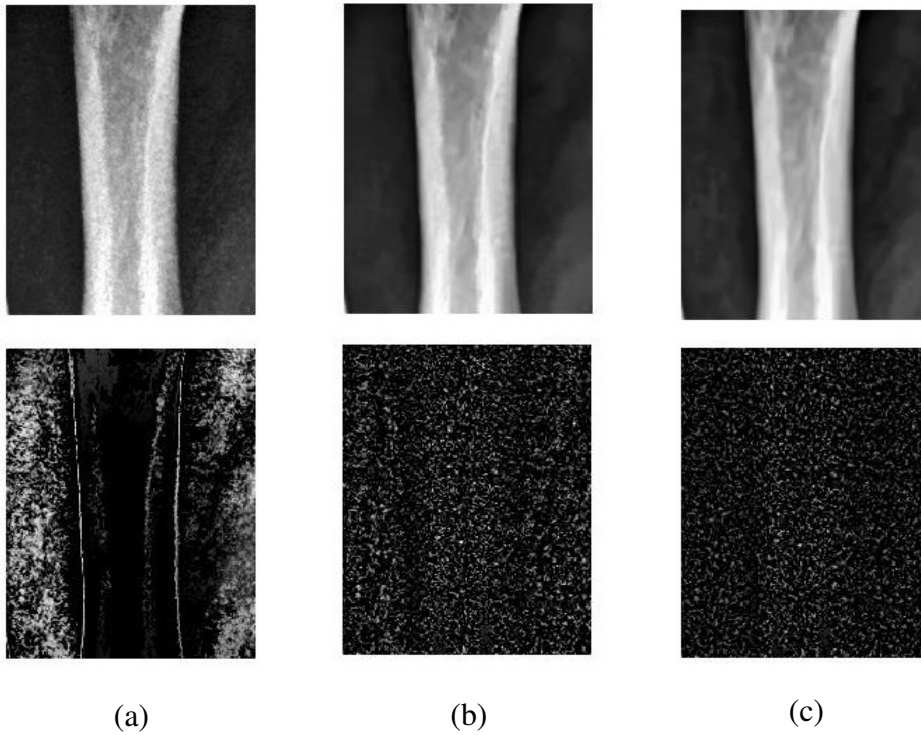


Figure 3.2: Denoising of hand radiographs: Denoised images (top row) and their difference images (bottom row) obtained using (a) bilateral filter, (b) NLPCA and (c) BM3D

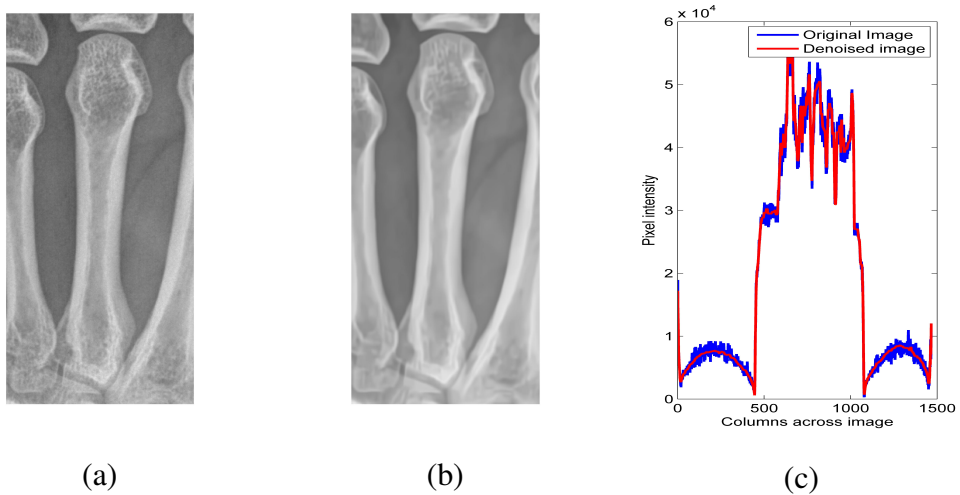


Figure 3.3: Denoising of image using BM3D method: (a) and (b) Original image and denoised image (zoomed) and (c) Intensity profile of the original and denoised images along a row

Illumination correction

Non-uniform illumination of background during image acquisition causes difficulty in producing a good binary and gradient image for segmentation. Illumination variation

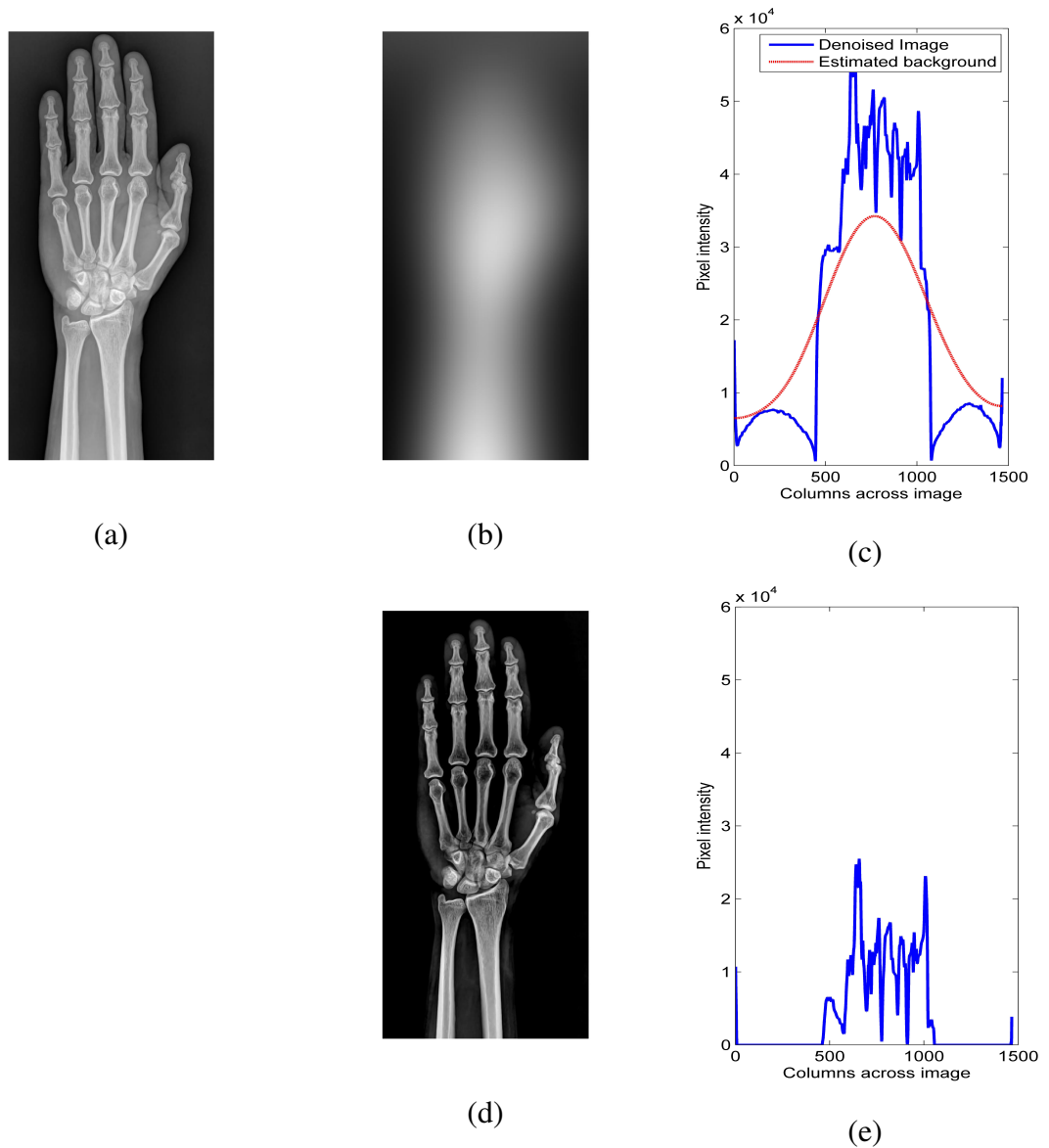


Figure 3.4: Soft tissue subtraction: (a) Original image, (b) estimated background, (c) the corresponding intensity profiles at the carpal region of denoised image and estimated background, (d) image after soft tissue subtraction, and (e) intensity profile of the soft tissue subtracted image

can be compensated by using background subtraction methods. Gaussian filtering is a commonly used method for background subtraction. A Gaussian filter with standard deviation of 200 pixels is used to form an estimate of the background and soft tissue, as shown in Figure 3.4(b). The estimated background is then subtracted from the original image to obtain a skeletal image of the hand bones, as shown in Figure 3.4(d).

3.2.2 Localization of third metacarpal bone

The next stage after preprocessing is to automatically locate the third metacarpal bone with the help of two automatically detected anatomical landmarks and to estimate the centroid of the third metacarpal bone in order to use it as a marker for the watershed segmentation.

Detection of anatomical landmarks

Anatomical landmarks are essential for proper localization of the third metacarpal bone and estimation of its centroid. The proposed automatic detection of anatomical landmarks require the detection of bounding box of the hand region in the X-ray image. The hand region is extracted by finding the binary image of the background subtracted image and extracting the largest connected component. The binary image is found by using global and local thresholding methods. Otsu's method is a global thresholding method in which a threshold is chosen such that interclass variance between two classes is the maximum (Otsu 1975). In Niblack's local thresholding method, thresholds are computed over local regions according to the local mean and standard deviation in the image window (Wayne 1986). Niblack's method is done using windows of size 400 pixels. Niblack's local thresholding results in noisy white patches in the background. Otsu's thresholding can fuse closely spaced bones in the binary image. Hence, the intersection of the resultant images of the Otsu's and Niblack's methods is taken and morphologically closed with a disk structuring element of size 20 pixels, to obtain a good binary image of hand bone region, as shown in Figure 3.5. The largest connected object of the binary image is extracted and its bounding box is determined.

Two anatomical landmarks are used for the localization of third metacarpal bone, namely (1) the tip of third distal phalanx (TDP), and (2) the Distal Radius-Ulnar Joint (DRUJ). TDP is the topmost end of the third distal phalanx and lies at the upper boundary of the bounding box of the hand. Hence, the row containing TDP is located as the top border of the hand bounding box. DRUJ is located by determining the row at which the binary regions representing the radius and ulna converge. This is done by

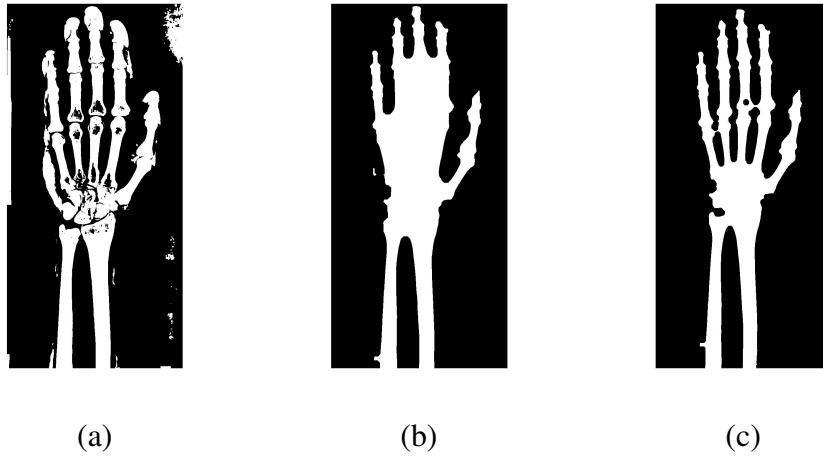


Figure 3.5: Binary image of hand bone region: (a) Image after applying Niblack local thresholding on soft-tissue subtracted image, (b) Image after global Otsu thresholding, and (c) Intersection image of (a) and (b)

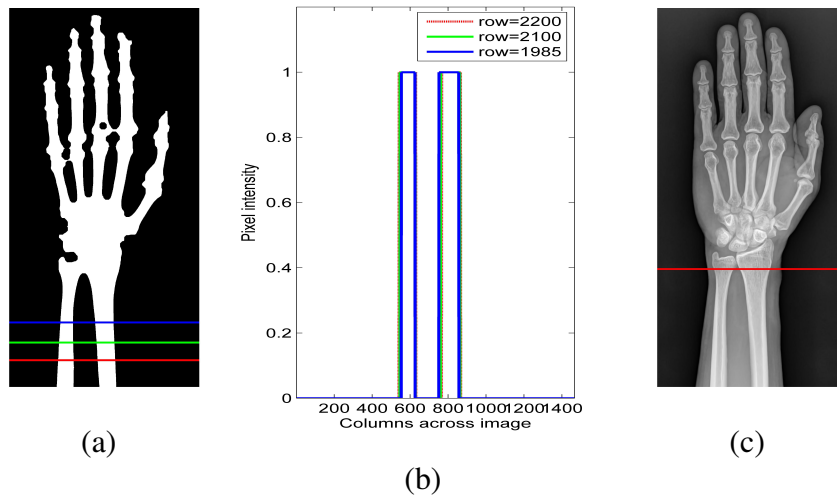


Figure 3.6: Detection of DRUJ: (a) and (b) Intensity profiles of radius and ulna showing two distinct peaks, (c) Detected DRUJ line

observing the intensity row profiles at specific intervals, starting from the lower border of the binary image. The search region for the detection of DRUJ is considered between 225 mm and 170 mm below the top border of the hand bounding box. Intensity profiles along image rows at intervals of 5 pixels within this region is observed. The rows below DRUJ will have two distinct peaks, as shown in Figure 3.6, while the row containing DRUJ converges to a single peak in the intensity profile of the binary image.



Figure 3.7: Hand radiograph showing the two anatomical landmarks, TDP (in blue) and DRUJ (in red) and the estimated row containing the third metacarpal centroid (in green)

Estimation of third metacarpal centroid

The centroid of the third metacarpal bone is empirically determined to lie at the row corresponding to the mean distance of 125 mm below TDP and 70 mm above DRUJ, as

$$MC3_{centroid}(x) = \frac{(TDP + 125) + (DRUJ - 70)}{2} \quad (3.2)$$

Figure 3.7 shows the detected anatomical landmarks, TDP and DRUJ, and the estimated row containing the centroid of the third metacarpal bone. The row corresponding to the mean distance passes through the metacarpal mid-region, whose intensity row profile shows peaks along the metacarpal bones, as shown in Figure 3.8. The intensity profile obtained is filtered using a zero-phase digital filter to obtain the most prominent peaks. The five most prominent peaks corresponding to the five metacarpal bones are detected. The third peak gives the location of the centroid of the third metacarpal bone. This centroid will be used for the placement of markers for the watershed segmentation.

3.2.3 Segmentation using watershed algorithm

The proposed segmentation approach uses mathematical morphology and watershed method for the delineation of periosteal (outer) and endosteal (inner) edges of the third metacarpal bone. Watershed segmentation is a region-growing technique that begins

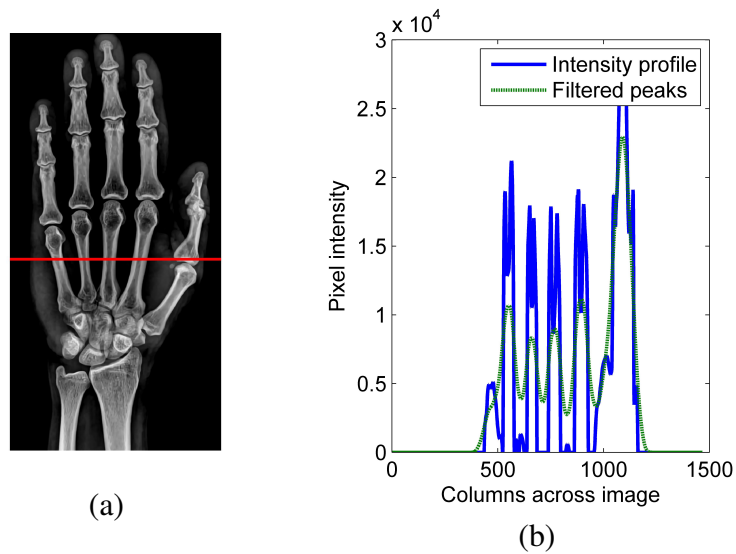


Figure 3.8: Localization of third metacarpal bone: (a) Estimated metacarpal midregion and (b) Intensity profile of the soft tissue subtracted image along metacarpal midregion showing five prominent peaks

at the local minima of the image and creates watershed lines at the object boundaries (Meyer 1994). Watershed method is sensitive to noise in images and may lead to over-segmentation. Placing markers at the desired edges helps to level out the noise. Marker-controlled watershed segmentation treats the markers as the local minima from which water is flooded till watershed lines are constructed. The hand X-ray images are first vertically aligned and then markers are placed with respect to the estimated centroid of the third metacarpal bone in order to guide the watershed segmentation. The accuracy of the watershed segmentation depends on the strength of the edges in the gradient image used for the watershed.

Vertical alignment of metacarpal bone

The hand and wrist radiograph is vertically aligned with respect to the third metacarpal bone to improve the accuracy of the segmentation. The orientation of the third metacarpal bone is determined from its central axis, which is determined by interpolating the third most prominent peaks of intensity profiles 5 mm above and 5 mm below the third metacarpal centroid. The vertically aligned hand X-ray image will be used for the watershed segmentation and radiogrammetric measurements.

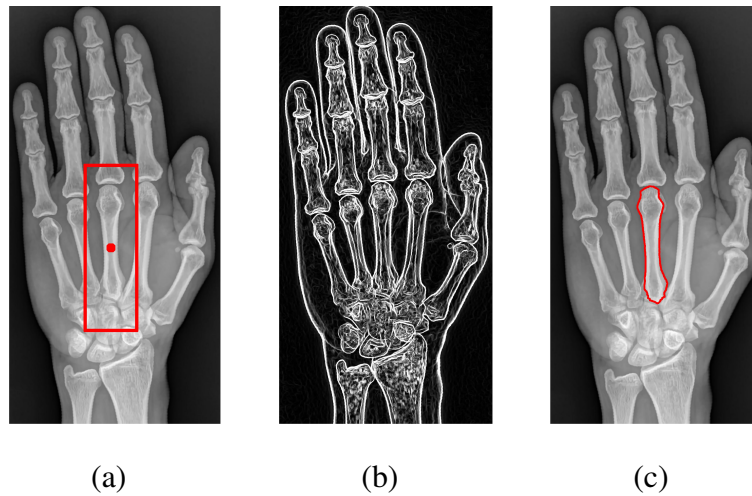


Figure 3.9: Automatic segmentation of third metacarpal bone: (a) Internal and external markers for watershed, (b) gradient image, and (c) Segmented third metacarpal bone

Segmentation of periosteal edge

The third metacarpal bone is segmented using watershed method guided by external and internal markers. The internal marker is a dilated centroid of the third metacarpal bone, obtained by employing a morphological dilation of the centroid with a circular structuring element of size 2 mm. A rectangular box with borders 45 mm above and below the centroid and 14 mm on either sides of the centroid is used as the external marker. These markers are placed on the mask image for segmentation of the outer bone. The mask image used is the morphological Beucher gradient image of the hand, obtained by subtracting the eroded image from the dilated image with a disk shaped structuring element of radius 1 pixel (Beucher 1990). As the watershed lines tend to leak at the bone edge discontinuities, viscous closing of the morphological gradient image is applied to get a strong gradient image of the hand bones. Marker-controlled watershed segmentation is applied on the gradient mask image to form watershed lines along the periosteal edge, thus segmenting the third metacarpal bone, as shown in Figure 3.9.

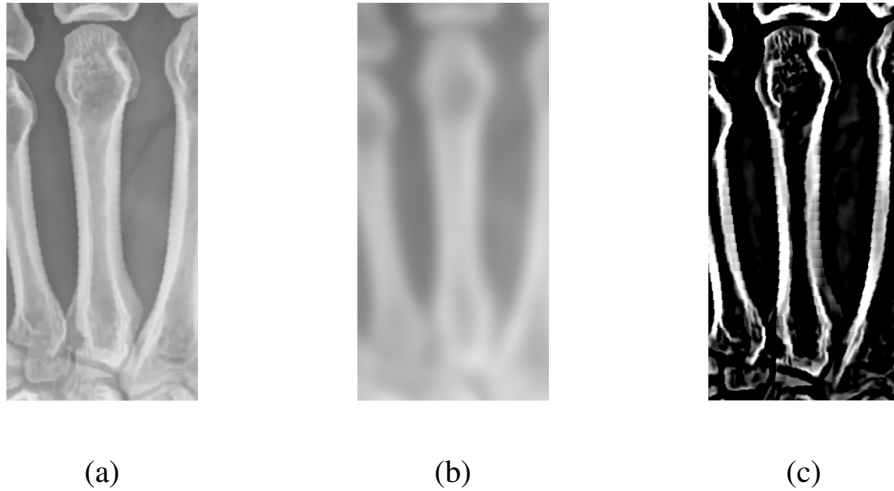


Figure 3.10: Contrast enhancement for endosteal edge segmentation: (a) Third metacarpal of original image (b) shows the estimated background and (c) shows the contrast enhanced cortical bone of third metacarpal after background subtraction

Segmentation of endosteal edge

Metacarpal radiogrammetry requires delineation of the periosteal and endosteal edges for extracting the cortical bone measurements. Radiogrammetric measurements are taken along the tubular shaft of the third metacarpal bone. The third metacarpal bone shaft ROI is automatically extracted by discarding 35% of the metacarpal length from the upper and lower ends of the segmented third metacarpal bone.

The endosteal edge of the third metacarpal bone is then segmented using watershed with the help of the previously segmented periosteal edge as the external marker and the medial line of the bone shaft ROI as the internal marker. The mask image used for the watershed is obtained by a further contrast enhancement using a Gaussian filter of standard deviation 10 pixels, as shown in Figure 3.10. Figure 3.11 shows the delineation of the endosteal edge of the third metacarpal bone using marker-controlled watershed segmentation. The inner and outer edge delineations along the third metacarpal bone shaft is used for metacarpal radiogrammetry.

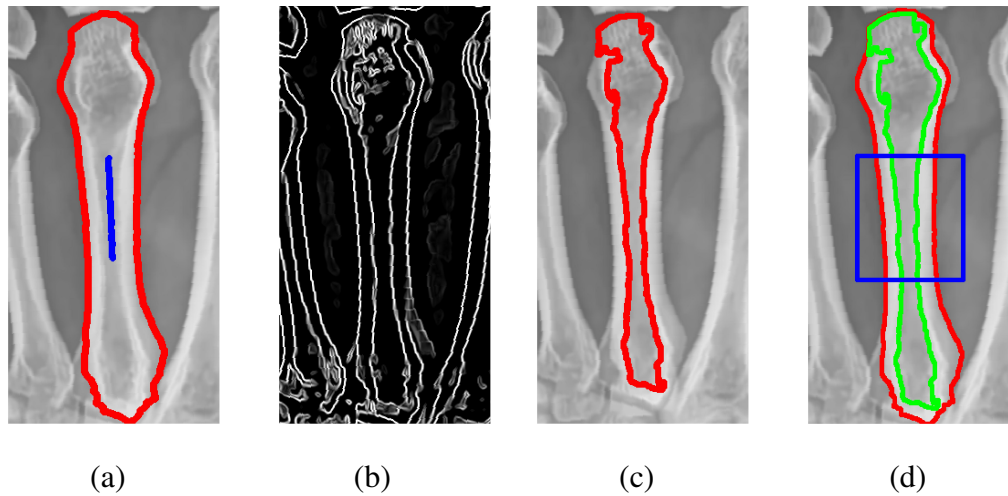


Figure 3.11: Segmentation of endosteal edge: (a) Internal and external markers used for watershed, (b) Gradient of the contrast enhanced image, (c) Detected endosteal edge after watershed segmentation, and (d) Extracted metacarpal shaft for radiogrammetric measurements

3.3 SEGMENTATION USING AAM

The performance of the proposed segmentation approach is compared with AAM method which has been widely used for segmentation of medical images. This section discusses in brief about AAM segmentation and its implementation for the automatic segmentation of third metacarpal bone in hand radiographs.

AAM is a deformable model that uses prior shape and texture information for segmentation of objects (Cootes *et al.* 2001). Given a set of training images with manually annotated landmark points along the object boundary, AAM creates a statistical shape and appearance models of the object. Landmarks represent correspondences at the object edges, T-junctions, etc. The more the landmark points used for annotation, the better the shape information captured. The shapes in the training images are first rigidly aligned with respect to their centre of gravity and the mean shape model of the object is determined. Each of the individual shapes is then aligned to the mean shape model using Generalized Procrustes Analysis. In order to model the variations in the aligned shapes, PCA is done. PCA helps to reduce the dimensionality of the shape space. The principal components that capture the major variations in the aligned shapes of the training set are used to describe the modes of shape variations of the object. Thus

each individual shape can be defined as the mean shape model varied along one or more of the modes of shape variation.

Along with the model points, the local region at each landmark point is also modeled. This helps to search around the landmark points to find the best match during optimization. However, the local region models are independent of each other. In order to create a more accurate model that makes use of the whole image information, the appearance of the object is also modeled. Once the mean shape model is constructed, the images of the individual objects are warped onto the mean shape to create a mean appearance model. PCA is again applied to capture the variations in the appearance of the individual images in the training set. Thus the modeled variations in the shape and appearance of the object helps to segment objects in images by finding the best match. The accuracy of the AAM segmentation method depends on the number and variations in the images present in the training set.

Segmentation using AAM comprises of two stages: training and testing. In the training stage, the objects of interest are manually segmented on a set of training images. Landmark points are marked along the edges of the object. Using these landmark points and the global texture information, AAM forms a mean shape and appearance model by a rigid registration of the individual shapes using translation, scaling and rotation. PCA is then used to describe the shape and appearance variations of the individual objects from the mean model. The principal components represent the different modes of shape and appearance. The mean model and the variations of the individual objects are stored. For a new unseen image, AAM finds the best match of the model to the object in the image.

3.3.1 Training stage

Metacarpal bones of the hand are quite similar in shape and appearance and lie close to each other. This poses a challenge to AAM to accurately detect and segment the third metacarpal bone. Accuracy of detection of third metacarpal bone can be increased by employing a vertical alignment of the hand prior to segmentation. The orientation of

the hand is determined by binarizing the centre region of the hand image by adaptive thresholding and estimating the orientation using image moments. Using this orientation information, the hand image is vertically aligned.

AAM of the third metacarpal is built from a set of manually annotated training images. A template of 46 landmark points is used for the manual annotation of the periosteal and endosteal edges of the third metacarpal bone. The annotated training images are cropped to the bounding box of the landmark points with 20% padding around the boundary. The cropped images are rescaled if the image diagonal has more than 400 pixels. This is done to ensure that the training samples are not too small in size. The bounding box of the training images are then trained. Holistic AAM segmentation approach with Fast Dense Scale Invariant Feature Transform features is used to generate the AAM model of the third metacarpal bone. The individual shape and appearance variations are described by 20 shape and 150 appearance components.

3.3.2 Testing stage

The performance of the AAM segmentation can be tested by fitting the trained AAM model onto unseen test images. Test image is initially vertically aligned and the bounding box of the third metacarpal bone is detected. The AAM model is then fitted onto the third metacarpal by iteratively moving the landmark point location and using Lucas Kanade optimization. Figure 3.12 shows the detection of the bounding box, initial placement of the mean model on the third metacarpal bone and the final fitted model. The final landmark points are interpolated to obtain a connected boundary along the third metacarpal bone edges, from which radiogrammetric measurements are taken.

3.4 METACARPAL RADIOGRAMMETRY

Metacarpal radiogrammetry is measured from the tubular shaft of the third metacarpal bone. The metacarpal bone shaft is automatically segmented by removing 35% of the metacarpal length from the upper and lower ends that represent the head and base re-

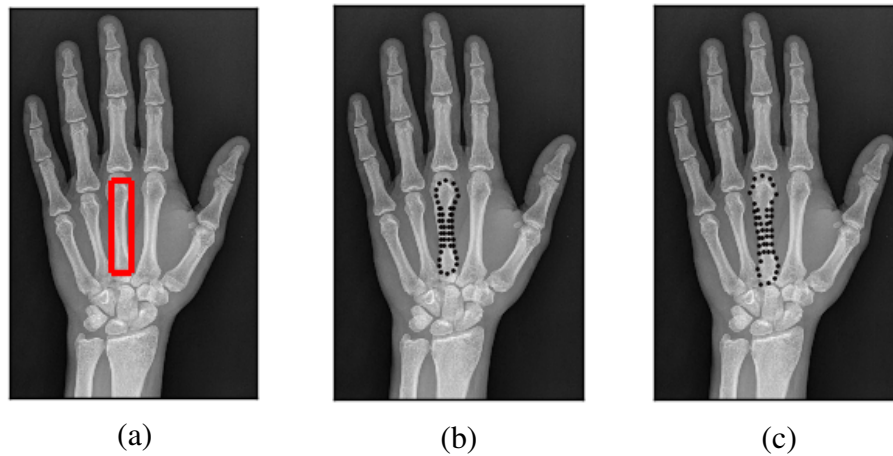


Figure 3.12: Testing the trained AAM model: (a) Initial bounding box detection, (b) Initial position of the AAM model and (c) Final segmented third metacarpal bone

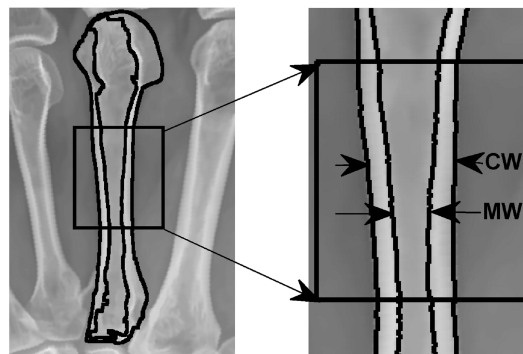


Figure 3.13: Radiogrammetric measurement of third metacarpal bone using hand radiograph

gions of the metacarpal bone. The radiogrammetric measurements determined from the metacarpal bone shaft are cortical width (CW), medullary width (MW) and length of the bone. CW is the diameter of the outer bone shaft and is measured by averaging the total number of pixels in the segmented bone shaft ROI over 100 measurement rows. MW is the diameter of the inner bone delineated by the endosteal edge. MW is measured by averaging the total number of pixels in the segmented inner bone shaft region over 100 measurement rows. The measurements obtained in pixels is converted to mm units using the pixel dimension information from DICOM header file of the images. Figure 3.13 shows the radiogrammetric measurements taken from the automatically segmented third metacarpal bone shaft.

Radiogrammetric bone indices calculated from the CW and MW measurements of the metacarpal bone shaft are CCT , Cortical Area (CA), Percent Cortical Area of bone (PCA_b) and BNI as

$$CCT = CW - MW \quad (3.3)$$

$$CA = \frac{\pi}{4} \times (CW^2 - MW^2) \quad (3.4)$$

$$PCA_b = \frac{CW^2 - MW^2}{CW^2} \times 100 \quad (3.5)$$

$$BNI = \frac{CCT}{CW} \times 100 \quad (3.6)$$

3.5 RESULTS AND DISCUSSION

This section discusses about the dataset used in this thesis and the evaluation of the proposed segmentation method using manually segmented images and ground truth images. Statistical analysis of the radiogrammetric features measured are also done using independent sample t-test and Pearson correlation test.

3.5.1 Calculation of data sample size

Assuming a confidence level of 95% and power of 80%, the minimum sample size required for the study can be calculated (Varkevisser *et al.* 2003; Geddam 2009) for both healthy and low bone mass groups as

$$n = \frac{(U + V)^2 \times (s_1^2 + s_2^2)}{(m_1 - m_2)^2} \quad (3.7)$$

$$n = \frac{(0.84 + 1.96)^2 \times (0.15^2 + 0.15^2)}{(0.07)^2} = 72 \quad (3.8)$$

where, U is the Z value corresponding to the power level and is 0.84 for power of 80%. V is the Z value corresponding to the confidence level and is 1.96 for confidence level of 95%. The standard deviation of BMD in both groups, s_1 and s_2 , is 0.15 g/cm^2 and the expected differences in mean of the two groups, $(m_1 - m_2)$, is 0.07 g/cm^2 (Geddam

2009). Thus, the total required sample size is at least 72 for healthy and low bone mass groups each.

3.5.2 Dataset

In this thesis, sample data from Indian and Swiss sample population are used. The Indian sample data comprises of 138 volunteers from Tejaswini Hospital and District Wenlock Hospital in Karnataka, India. Postero-Anterior (PA) view hand and wrist radiographs of the subjects were taken using 400mA Allengers[®] HF Advantage (deviation index in the range -2.25 to 3.6) and Digital Radiography Agfa[®] DX-D 300 (X-ray tube voltage=52 kV, X-ray tube current=160 mA, exposure time=32 ms, varying source-to-object distance of 990 to 1370 mm and deviation index in the range -8.1 to -1.8). The radiographic images were obtained in 16-bit DICOM format with image dimensions ranging from 1813×998 to 3052×3052. DXA-BMD of lumbar spine (DXA-LS) of the same subjects were also taken using GE Lunar[®] densitometer. The *T*-score values obtained from DXA-LS will be used to categorize the subjects as healthy or having low bone mass, in order to validate our results. The DXA-BMD values are also used for statistical analysis in order to determine the significant feature sets. Men and women above 30 years of age were included in the study. Subjects undergoing glucocorticoid treatment in the last three months and pregnant women were excluded from the study. Informed consent was obtained from the volunteers. The study protocol was approved by the Institutional Ethics Committee, Kasturba Medical College, Mangalore, Manipal University, Karnataka, India.

Swiss sample data includes hand and wrist radiographs and DXA-BMD of lumbar spine of 65 subjects from the University Hospital of Geneva (HUG), Switzerland. Thirty hand and wrist X-ray images of patients were acquired using Computed Radiography Siemens[®] Fluorospot Compact (X-ray tube voltage=43.8 kV, X-ray tube current from 299 to 329 mA, exposure time from 8 to 11 ms, source to detector distance of 1195 to 1839 mm and relative X-ray exposure of 205 to 1005). Twenty four hand and wrist X-ray images were acquired with Philips[®] Medical Systems DigitalDiagnost (X-

Table 3.1: Clinical characteristics of the Indian and Swiss sample data

Clinical characteristics	Indian sample data (138 subjects)		Swiss sample data (65 subjects)	
	H (67 subjects) ($\mu \pm \sigma$)	LBM (71 subjects) ($\mu \pm \sigma$)	H (24 subjects) ($\mu \pm \sigma$)	LBM (41 subjects) ($\mu \pm \sigma$)
<i>Age (years)</i>	45.6 \pm 10.6	52.7 \pm 10.6	70.38 \pm 10.11	69.81 \pm 8.14
<i>Height (cm)</i>	161.25 \pm 8.62	157.41 \pm 6.02	161.96 \pm 11.48	158.32 \pm 10.32
<i>Weight (kg)</i>	66.84 \pm 9.58	58.61 \pm 9.21	75.58 \pm 15.31	67.32 \pm 19.95
<i>T-score</i>	0.07 \pm 1.03	-2.55 \pm 1.05	0.59 \pm 2.79	-1.96 \pm 0.71

H- Healthy, LBM- Low Bone Mass

ray tube voltage=52 kV, exposure time from 5 to 10 ms, source to detector distance from 1008 to 1200 mm and relative X-ray exposure of 240 to 722). The remaining images were acquired using Computed Radiography Agfa[®] ADC_51xx and DX Agfa[®] DXD30_Wireless with X-ray tube voltage=55 kV, X-ray tube current=160 mA and exposure time=16 ms). The images were obtained in 16-bit DICOM format with image dimensions ranging from 1479 \times 994 to 2370 \times 3000. DXA scans of lumbar spine were taken using either Hologic[®] Horizon A or Hologic[®] Discovery A.

The subjects in the sample data are categorized into two groups based on the T -score values. Subjects with T -score ≥ -1 belong to healthy (H) group and subjects with T -score < -1 belong to low bone mass (LBM) group. Indian sample data includes 67 healthy subjects (32 men and 35 women) and 71 low bone mass subjects (26 men and 45 women). Swiss sample data consists of 24 healthy subjects (8 men and 16 women) and 41 low bone mass subjects (7 men and 34 women). The clinical characteristics of the Indian and Swiss sample data are given in Table 3.1.

3.5.3 Metrics for evaluation of segmentation

The evaluation metrics used for the quantitative assessment of the proposed method and AAM segmentation are Jaccard measure, percent area difference, recall, precision and F1-score. These metrics are used to compare the automatically segmented results with the manually segmented ground truth (GT) images. Jaccard measure helps to measure the overlap between the automatically segmented region ($Area_{auto}$) and the GT region ($Area_{man}$). Percent area difference measures the difference in area of the automated

and manual segmentation methods, normalized by the total area of the GT region.

$$Jaccard\ measure = \frac{|Area_{auto} \cap Area_{man}|}{|Area_{auto} \cup Area_{man}|} \quad (3.9)$$

$$Percent\ area\ difference = \frac{|Area_{auto} - Area_{man}|}{Area_{man}} \quad (3.10)$$

Confusion matrix can be used to compare the pixel-wise segmentation results with the GT region. Bone pixel contained in the cortical bone shaft is taken as positive and those pixels that do not belong to the cortical bone shaft are considered negative. The cortical bone pixels and the background pixels that are correctly segmented are taken as TP and TN, respectively. When a cortical bone pixel is misclassified as background, it is a FN case and the vice-versa is a FP case. The metrics that can be calculated from confusion matrix to evaluate the segmentation results are recall, precision and F1-score. Recall is the ratio of true positive pixels to the actual number of cortical bone pixels. Precision is the ratio of true positive pixels to all the pixels segmented as cortical bone pixels. F1-score is the harmonic mean of recall and precision. The metrics can be calculated using the equations given below.

$$Recall = \frac{TP}{TP + FN} \quad (3.11)$$

$$Precision = \frac{TP}{TP + FP} \quad (3.12)$$

$$F1\text{-score} = 2 \times \frac{Recall \times Precision}{Recall + Precision} \quad (3.13)$$

3.5.4 Segmentation results

The proposed segmentation method is implemented using Matlab[®] R2016b and SDC toolbox for Matlab[®] (Dougherty *et al.* 2003). AAM segmentation of third metacarpal bone is implemented using Menpo[®] (Alabort-i Medina *et al.* 2014).

An Indian sample data of 138 hand and wrist radiographic images and a Swiss sample data of 65 images are used to validate the performance of the proposed segmenta-

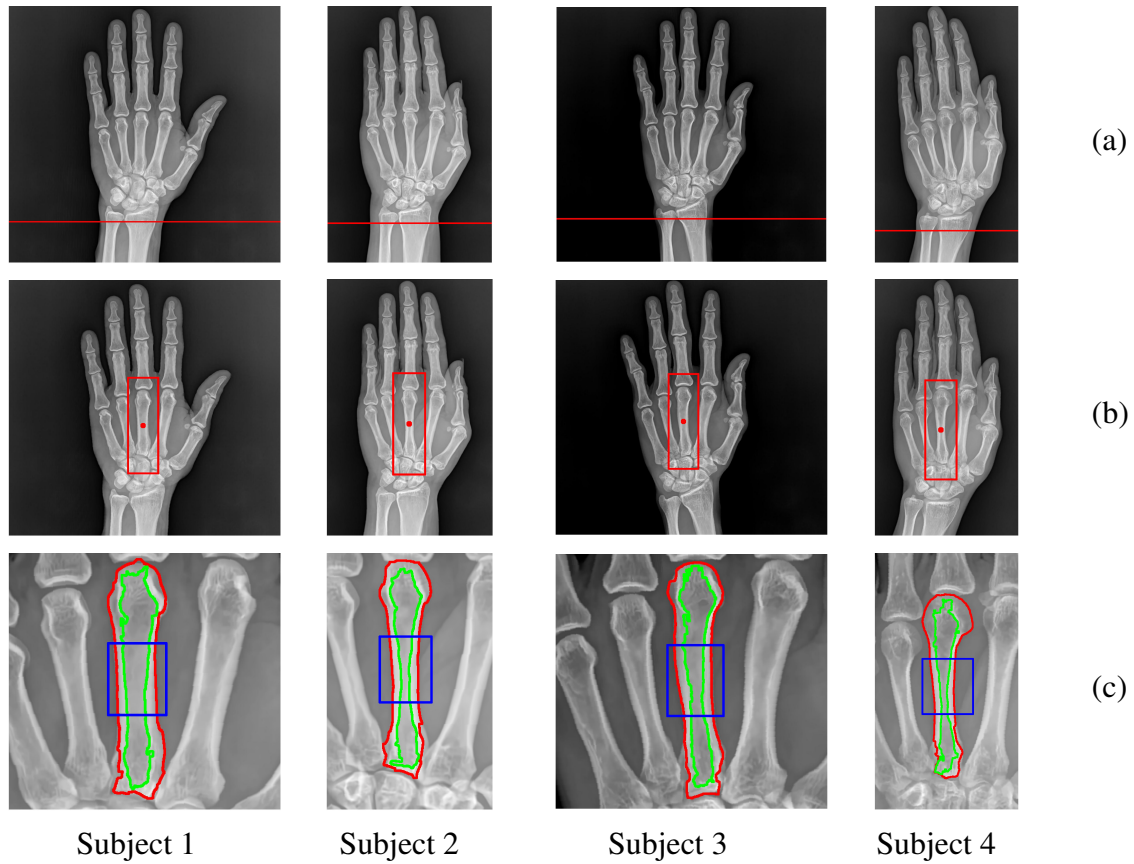


Figure 3.14: Examples of the segmentation results for third metacarpal bone for two healthy images (Subjects 1 and 2) and two osteoporotic images (Subjects 3 and 4): (a) Original images with detected DRUJ line are shown in first row, (b) localization of third metacarpal in second row, (c) segmented third metacarpal bone shaft used for radiogrammetry in the last row. Radiogrammetric measurements obtained from the segmented bone shaft are as follows: Subject 1 ($CW= 10.38$ mm, $MW= 5.89$ mm, $CCT= 4.49$ mm, $CA= 57.28$ mm²), Subject 2 ($CW= 7.61$ mm, $MW= 3.03$ mm, $CCT= 4.58$ mm, $CA= 38.26$ mm²), Subject 3 ($CW= 9.53$ mm, $MW= 4.28$ mm, $CCT= 5.25$ mm, $CA= 56.92$ mm²) and Subject 4 ($CW= 8.03$ mm, $MW= 3.33$ mm, $CCT= 4.71$ mm, $CA= 41.96$ mm²)

tion approach. Figure 3.14 shows the segmentation results of the third metacarpal bone shaft using the proposed method for two healthy and two osteoporotic subjects. Figure 3.14(a) shows the automatically detected DRUJ line, (b) shows the detected centroid of the third metacarpal bone and (c) shows the final segmented periosteal and endosteal edges along with the extracted bone shaft used for radiogrammetric measurements.

The proposed method shows a success rate of 89% in detecting and segmenting the third metacarpal bone shaft in the Indian sample data and 78% in the Swiss sample

Table 3.2: Comparison of success rate of metacarpal detection

Segmentation Method	Success rate (%)	Test images	Reference
Snake	73.9	59	Luis-Garcia <i>et al.</i> (2003)
ASM	99.5	5000	Thodberg and Rosholm (2003)
Watershed	75	357	Raheja (2008)
AAM	81	138	(Indian sample data)
Proposed work	89	138	(Indian sample data)
	78	65	(Swiss sample data)

data. For AAM segmentation, 39 training images are used to build the AAM of the third metacarpal bone. A success rate of 81% is obtained with AAM segmentation on the Indian sample data. Table 3.2 shows a comparison of the success rate in automatic detection of the metacarpal bone using the proposed method and other segmentation methods in literature.

3.5.5 Comparison with manual segmentation

A manual segmentation of the third metacarpal bone shaft in five hand X-ray images are used as ground truth images to evaluate the performance of the proposed segmentation method and AAM method. Figure 3.15 shows the segmentation results of the manual segmentation, the proposed segmentation method and AAM method.

The segmentation results are quantitatively assessed using the evaluation metrics discussed in Section 3.5.3. The evaluation results of the proposed segmentation and AAM segmentation methods are given in Table 3.3. A Jaccard measure of 0.90 and percent area difference of 0.03 is obtained using the proposed method, while Jaccard measure of 0.82 and percent area difference of 0.11 is obtained using AAM method. The proposed method shows mean recall of 0.96, precision of 0.94 and F1-score of 0.95, whereas AAM segmentation shows mean recall of 0.95, precision of 0.86 and F1-score of 0.90. The proposed method obtains better performance values for all the evaluation metrics as compared to the AAM method.

The statistical significance of the evaluation metrics of our proposed segmentation

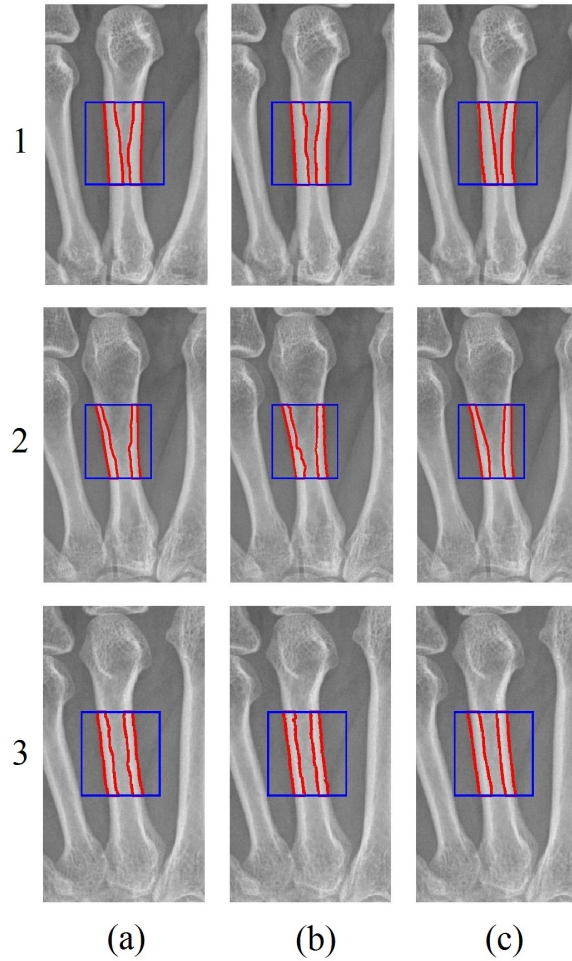


Figure 3.15: Segmentation results of healthy (row 1), low bone mass (row 2) and osteoporotic subjects (row 3): (a) manual segmentation, (b) proposed segmentation method and (c) AAM segmentation. Radiogrammetric measurements of the metacarpal bone shaft for the 3 cases of the 3 images are as follows: 1(a) $CW=7.83$ mm, $MW=2.60$ mm, $CCT=5.22$ mm, $CA=42.78$ mm²; 1(b) $CW=7.75$ mm, $MW=2.45$ mm, $CCT=5.29$ mm, $CA=42.39$ mm²; 1(c) $CW=7.34$ mm, $MW=2.15$ mm, $CCT=5.19$ mm, $CA=38.65$ mm²; 2(a) $CW=8.99$ mm, $MW=5.45$ mm, $CCT=3.55$ mm, $CA=40.22$ mm²; 2(b) $CW=9.05$ mm, $MW=5.16$ mm, $CCT=3.89$ mm, $CA=43.41$ mm²; 2(c) $CW=9.14$ mm, $MW=5.02$ mm, $CCT=4.12$ mm, $CA=45.76$ mm²; 3(a) $CW=7.32$ mm, $MW=3.48$ mm, $CCT=3.84$ mm, $CA=32.58$ mm²; 3(b) $CW=7.23$ mm, $MW=3.33$ mm, $CCT=3.90$ mm, $CA=32.35$ mm²; 3(c) $CW=7.77$ mm, $MW=3.24$ mm, $CCT=4.53$ mm, $CA=39.18$ mm².

method and AAM method is analyzed using non-parametric Mann-Whitney U test, as shown in Table 3.4. Jaccard measure, precision and F1-score shows significant difference between the proposed and AAM methods.

Table 3.3: Performance evaluation with manual segmentation

Images	Jaccard Measure		Percent Area Difference		Recall		Precision		F1-score	
	Proposed	AAM	Proposed	AAM	Proposed	AAM	Proposed	AAM	Proposed	AAM
1	0.91	0.84	0.01	0.01	0.96	0.91	0.95	0.91	0.95	0.91
2	0.94	0.82	0.02	0.03	0.96	0.92	0.98	0.89	0.97	0.90
3	0.88	0.84	0.10	0.16	0.99	0.99	0.90	0.85	0.94	0.91
4	0.87	0.76	0.03	0.15	0.94	0.93	0.92	0.81	0.93	0.86
5	0.90	0.83	0.01	0.18	0.95	0.99	0.94	0.84	0.95	0.91
Mean	0.90	0.82	0.03	0.11	0.96	0.95	0.94	0.86	0.95	0.90
SD	0.03	0.03	0.04	0.08	0.02	0.04	0.03	0.04	0.02	0.02

SD- Standard deviation

Table 3.4: Statistical analysis of the evaluation metrics of the proposed and AAM segmentation methods

Evaluation metrics	Significance value
Jaccard measure	0.0079 [†]
Percent Area Difference	0.1746
Recall	0.4921
Precision	0.0159*
F1-score	0.0079 [†]

*p<0.05, † p<0.01

3.5.6 Validation with ground truth measurements

Ground truth measurements of the cortical and medullary widths of six healthy and eight LBM images were obtained from experts. The images used for creating the ground truth were randomly selected. The radiogrammetric measurements obtained using the proposed automated radiogrammetry and AAM method are compared with the ground truth measurements, as given in Table 3.5. Our proposed automatic radiogrammetry achieves lower mean absolute error for the cortical width measurement. This is because of enhanced contrast of the outer bone edge resulting from background subtraction and viscous closing of the morphological gradient. The mean absolute error for the medullary width using proposed method and AAM are comparable. Using the proposed method, a mean absolute error of 0.04 mm (0.51%) and 0.12 mm (1.54%) are obtained for *CW* measurements of the healthy and low bone mass groups, respectively. *MW* measurements of the healthy and low bone mass groups shows a mean absolute error of 0.22 mm (5.81%) and 0.26 mm (7.86%), respectively. AAM segmentation achieves mean absolute error of 0.43 mm (4.78%) for *CW* and 0.12 mm (3.66%) for *MW* in

Table 3.5: Comparison of radiogrammetric measurements with ground truth

Images	Ground truth		Proposed method				AAM segmentation				
	Actual CW (mm)	Actual MW (mm)	Measured CW (mm)	Absolute error (mm)	Measured MW (mm)	Absolute error (mm)	Measured CW (mm)	Absolute error (mm)	Measured MW (mm)	Absolute error (mm)	
Healthy	1	8.75	4.19	8.72	0.03	3.54	0.65	8.33	0.42	4.18	0.01
	2	9.14	4.42	9.04	0.10	4.17	0.25	8.69	0.45	4.58	0.16
	3	10.45	5.85	10.43	0.02	5.84	0.01	9.74	0.71	5.68	0.17
	4	8.89	3.98	8.90	0.01	3.75	0.23	8.56	0.33	3.92	0.06
	5	7.55	2.62	7.51	0.04	2.57	0.05	7.10	0.45	2.79	0.17
	6	7.72	2.22	7.78	0.06	2.09	0.13	7.53	0.19	2.38	0.16
	Mean	8.75	3.88	8.73	0.04	3.66	0.22	8.33	0.43	3.92	0.12
SD	1.06	1.31	1.04	0.03	1.32	0.23	0.93	0.17	1.20	0.07	
Low bone mass	7	6.61	2.89	6.39	0.22	2.36	0.53	6.86	0.25	3.14	0.25
	8	10.27	4.92	9.96	0.31	4.45	0.47	8.94	1.33	4.97	0.05
	9	7.94	2.63	7.98	0.04	2.73	0.10	8.00	0.06	3.09	0.46
	10	7.89	3.18	7.92	0.03	3.27	0.09	7.97	0.08	4.21	1.03
	11	8.48	4.20	8.34	0.14	4.14	0.06	7.99	0.49	4.68	0.48
	12	8.44	2.92	8.40	0.04	3.06	0.14	8.16	0.28	2.96	0.04
	13	6.73	3.17	6.53	0.20	2.50	0.67	7.34	0.61	3.51	0.34
14	8.48	4.88	8.48	0.00	4.93	0.05	8.82	0.34	5.16	0.28	
Mean	8.11	3.59	8.00	0.12	3.43	0.26	8.01	0.43	3.97	0.37	
SD	1.15	0.93	1.14	0.11	0.96	0.25	0.69	0.41	0.90	0.31	

SD- Standard deviation

the healthy group, and mean absolute error of 0.43 mm (5.08%) for *CW* and 0.37 mm (11.10%) for *MW* in the low bone mass group.

The correlation of *CW* and *MW* measurements of the proposed and AAM methods with the ground truth measurements of the 14 images are analyzed using Pearson correlation test. The *CW* measurement of the proposed method shows a higher correlation of $r = 0.99$, as compared to that of AAM with $r = 0.93$. For *MW* measurement, both the proposed and AAM methods show a similar correlation value of $r = 0.96$.

Combined cortical thickness (*CCT*) of the third metacarpal bone shaft is obtained by taking the difference of *CW* and *MW*. *CCT* measured using the proposed method show a mean absolute error of 0.2 mm (4.26%) and 0.17 mm (4.18%) in the healthy and low bone mass groups, respectively. AAM method show a mean absolute error of 0.47 mm (9.68%) and 0.54 mm (11.40%) for the measurement of *CCT* in the healthy and low bone mass groups, respectively. In comparison to AAM, the proposed method shows lower error percentage for the measurement of *CCT* in both H and LBM groups.

Table 3.6: Significance of the cortical features in the healthy (H) and low bone mass (LBM) groups of Indian and Swiss sample data

Features extracted	Indian-H ($\mu \pm \sigma$)	Indian-LBM ($\mu \pm \sigma$)	p-value	Swiss-H ($\mu \pm \sigma$)	Swiss-LBM ($\mu \pm \sigma$)	p-value
<i>CCT</i> (mm)	4.48 \pm 0.58	3.90 \pm 0.55	8.9E-08 [§]	4.36 \pm 0.64	3.75 \pm 0.66	5.8E-05 [§]
<i>CA</i> (mm ²)	43.13 \pm 7.28	36.54 \pm 6.82	9.1E-07 [§]	41.73 \pm 7.97	36.92 \pm 8.34	0.0095 [†]
<i>PCA_b</i> (%)	78.12 \pm 7.21	74.06 \pm 7.14	0.0022 [†]	77.21 \pm 7.78	70.58 \pm 7.25	0.0002 [‡]
<i>BNI</i>	53.88 \pm 7.86	49.55 \pm 6.99	0.0016 [†]	52.94 \pm 8.12	46.15 \pm 6.57	8.8E-05 [§]

*p<0.05, † p<0.01, ‡ p<0.001, § p<0.0001

3.5.7 Statistical analysis

Statistical analysis can be used to assess the significance of the cortical radiogrammetric measurements taken from the third metacarpal bone shaft. For the statistical analysis, the whole sample data of the Indian sample population ($n = 134$) and Swiss sample population ($n = 65$) are considered. The hand X-ray images that are poorly segmented by the proposed automated segmentation method, are semi-automatically segmented by manually selecting the third metacarpal centroid. The radiogrammetric measurements of the automatically segmented and semi-automatically segmented images are combined for the statistical analysis. Four images out of the total 138 images of the Indian sample data could not be segmented semi-automatically and hence excluded from the statistical analysis.

Independent sample t -test is used to test the ability of the cortical features to discriminate between healthy subjects and those with low bone mass, in the Indian and Swiss sample data. Table 3.6 shows the significance results of the independent sample t -test for the cortical features in the Indian and Swiss sample population. All the cortical features, namely *CCT*, *CA*, *PCA_b* and *BNI*, achieve high significance ($p < 0.01$) in differentiating healthy and LBM groups in both Indian and Swiss sample population.

The cortical radiogrammetric indices are tested for correlation with DXA-BMD of the lumbar spine using Pearson correlation. As the BMD values for the Indian and Swiss subjects were obtained using different DXA densitometers, namely GE Lunar densitometer (BMD_{Lunar}) and Hologic densitometer ($BMD_{Hologic}$), the BMD values need to be standardized for comparison. The standardization of BMD is dependent on

Table 3.7: Correlation of the cortical features with sBMD and T -score for Indian and Swiss sample data

Features extracted	Indian sample population		Swiss sample population	
	sBMD	T -score	sBMD	T -score
CCT	0.5133 [§]	0.4806 [§]	0.4773 [§]	0.3974 [‡]
CA	0.4527 [§]	0.4035 [§]	0.4207 [§]	0.3198 [†]
PCA_b	0.3569 [§]	0.3524 [§]	0.3489 [†]	0.3106 [†]
BNI	0.3595 [§]	0.3560 [§]	0.3625 [‡]	0.3300 [†]

* $p < 0.05$, † $p < 0.01$, ‡ $p < 0.001$, § $p < 0.0001$

the skeletal site analyzed (Lu *et al.* 2001). The BMD analyzed at the lumbar spine is standardized using the equations given below (Hui *et al.* 1997).

$$sBMD = 0.9683 (BMD_{Lunar} - 1.100) + 1.0436 \quad (3.14)$$

$$sBMD = 1.0550 (BMD_{Hologic} - 0.972) + 1.0436 \quad (3.15)$$

Correlation of the cortical features with sBMD and T -score is assessed using Pearson correlation test for Indian and Swiss sample data, as given in Table 3.7. All the cortical radiogrammetric features show highly significant correlation with $p < 0.01$. The best correlated cortical feature is CCT for both the Indian and Swiss sample population.

3.5.8 Limitations

Although the proposed segmentation method shows promising results, it is dependent on intensity variations in the X-ray images. The proposed method may fail for underexposed and overexposed images. The proposed method failed to detect the third metacarpal bone shaft in some cases due to close proximity of the second and fourth metacarpal bones, low contrast images, improper binarization of hand bone region resulting in mis-detection of DRUJ, and edge leakage of watershed segmentation due to a weak gradient image. Some examples of poorly segmented images are shown in Figure 3.16.

Background subtraction using Gaussian filter with a large size may remove fine

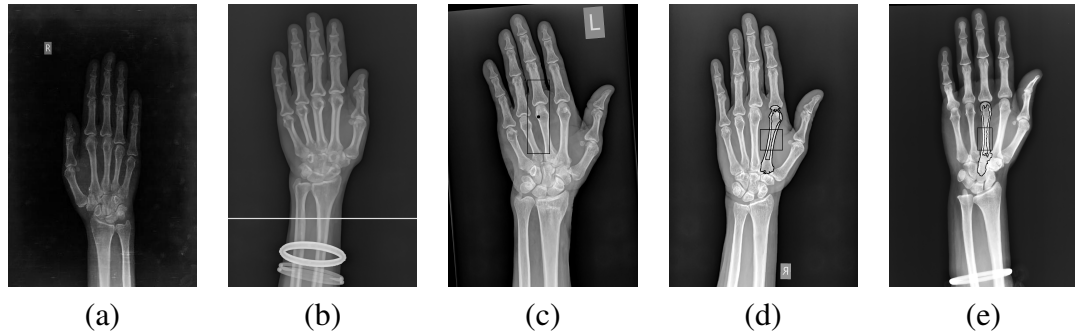


Figure 3.16: Examples of poorly segmented cases: (a) Low quality image, (b) Mis-detection of DRUJ due to presence of obstacles like bangles, (c) Wrong detection of third metacarpal centroid due to mis-detection of DRUJ, (d) Wrong detection of third metacarpal bone and (e) Edge leakage of watershed lines due to a weak gradient image.

edge details in the image. A good alternative to this could be illumination correction using white top hat transform, in which the difference between the image and its morphological opening is taken to extract the bone regions. The accuracy of the proposed segmentation method could be further improved by making it robust to illumination and exposure conditions. Although AAM is robust to intensity variations, the accuracy depends greatly on the images used in the training set. A large training data with manually annotated images will increase the accuracy but it is time consuming.

3.6 CONCLUSION

A segmentation approach for automatic segmentation and radiogrammetry of third metacarpal bone from hand and wrist radiographs has been proposed. The proposed method uses anatomical landmarks and marker-controlled watershed segmentation for automatic detection and delineation of the metacarpal bone edges. Soft tissue subtraction and mathematical morphological operations ensured enhanced contrast of the bone edges. The proposed segmentation method was compared with AAM segmentation and achieved better performance metrics when validated with manual segmentation and ground truth measurements. The extracted cortical radiogrammetric features showed high discrimination ability in the healthy and low bone mass groups of both Indian and Swiss sample data. The cortical features are also significantly correlated with DXA-

BMD of the lumbar spine. The proposed method is thus promising as a fully automated technique for radiogrammetry of the third metacarpal bone using hand and wrist radiographs.

CHAPTER 4

TRABECULAR TEXTURE ANALYSIS OF DISTAL RADIUS

4.1 INTRODUCTION

Cortical radiogrammetry, although a low cost and efficient technique for measurement of bone mass, does not completely characterize the changes in bone properties due to osteoporosis. Osteoporosis is defined by the loss in bone quantity as well as degradation of the bone structure. The initial stages of osteoporosis is reflected in the trabecular bone structure much earlier than the cortical bone (Adams 2009). Thus trabecular bone characterization would be a sensitive measurement of the progression of osteoporosis. The combination of cortical radiogrammetry and texture analysis of trabecular bone can help to develop a more efficient tool for detection of osteoporosis.

Calcaneal bone is the most explored skeletal site for the trabecular texture analysis using radiographs. As calcaneal bone is a weight-bearing bone, it shows different patterns of distribution of the tensile and compression trabeculae at different stages of osteoporosis progression. The calcaneal index grading has been developed based on the visual analysis of this pattern in radiographs by experts. Such a pattern of tensile and compression trabeculae is not present in distal radius. However, a study comparing vertebral, distal radius and calcaneal radiographic texture analysis suggest that distal radius is a better site for trabecular texture analysis (Mallard *et al.* 2013). The incidence of fracture at the distal radius is observed to increase after menopause as compared to other fragility fractures (Wigderowitz *et al.* 2000). Distal radius can be used as a potential surrogate site for assessment of vertebral fractures (Gomberg *et al.* 2003). Trabecular texture analysis of the distal radius has also been widely investigated using 3D imaging modalities. pQCT is being used for measurement of distal radius and tibia.

The trabecular volumetric BMD and stiffness of distal radius by HR-pQCT are found to be comparable to BMD measurements of lumbar spine using DXA and QCT (Liu *et al.* 2010). pQCT measures are associated with vertebral fractures and deformities, even though distal tibia shows stronger association than distal radius (Rajapakse *et al.* 2014). A study on MRI of distal radius and calcaneum shows that structure measures of the distal radius are better correlated with QCT of lumbar spine than measures of calcaneal bone and hence distal radius is better suited for prediction of spinal fractures (Link *et al.* 2002). Hence in this thesis, we choose distal radius as the skeletal site for trabecular texture analysis. Radiographic analysis of the distal radius is easier due to the relatively lesser amount of soft tissue surrounding the distal radius as compared to other skeletal sites such as vertebra and femur. Moreover, the use of a single hand and wrist radiograph for the whole diagnostic technique helps to reduce the cost of acquisition and radiation exposure in patients.

This chapter proposes an automated method for segmentation of the distal radius ROI and explores the different texture analysis methods that can be used for the characterization of trabecular bone in the distal radius. Features that can effectively capture the changes in bone texture in the healthy and LBM groups are identified using statistical analysis.

4.2 SEGMENTATION OF DISTAL RADIUS

The distal region of the radius bone is segmented for the texture analysis of trabecular bone. The ROI used for texture analysis is a square region obtained from the largest circle that fits the distal radius. This square ROI is rich in trabecular texture that are distinctly visible in hand and wrist radiographs.

Segmentation of the distal radius is challenging due to its close proximity with the ulna and carpal bones. In the proposed method, segmentation of the distal radius ROI is done with the help of previously detected anatomical landmark, DRUJ. The automatic detection of anatomical landmarks is discussed in Section 3.2.2. Additionally, a land-

mark that identifies the ultra-distal end of the radius bone (UDR) is also detected. Using these two landmarks, the largest circle that can be inscribed in the ultra-distal end of the radius bone is determined, from which the square ROI is extracted for texture analysis.

The trabeculae fibres visible in the texture region run approximately parallel to the central axis of the radius bone. Hence the initial vertical alignment of the radius bone is essential to ensure proper texture analysis. The orientation of the radius bone is determined by finding the central axis of the radius bone in a manner similar to finding the central axis of the third metacarpal bone, as discussed in Section 3.2.3. The intensity profiles of rows at specific intervals below the DRUJ row is determined from the binary image and the peak corresponding to the radius bone gives the location of the central axis at that row. The peaks thus obtained are linearly interpolated to give the central axis of the radius bone. The hand and wrist radiograph is then vertically aligned with respect to the radius bone.

The center of the circular distal radius ROI is approximately estimated by finding the point of intersection of the central axis of the vertically aligned radius bone and a horizontal line placed 3 mm below DRUJ, as shown in Figure 4.1(a). The intensity profile along this horizontal line in the binary image shows two peaks corresponding to the radius and ulna. The wider peak in the profile gives the width of the distal radius, which is considered as the approximate diameter of the circular ROI. The approximate center and radius of the circular ROI thus obtained is further refined to ensure that the ROI lies at the most distal region of the radius bone. This is done with the help of a second landmark, UDR, that identifies the ultra-distal end of the radius bone. UDR is located by finding the intensity profile along the central axis of the distal radius, starting from the estimated approximate center to a distance of 20 mm above, as shown in Figure 4.1(b). Since the distal radius has a marked contrast at its ultra-distal boundary, UDR is determined as the most prominent peak in the vertical intensity profile, as shown in Figure 4.1(c). By finding the distance of the approximate center from UDR, the center of the circular ROI is re-adjusted to fit the distal end of the radius bone. Figure 4.1(d) shows the circular ROI segmented from the distal radius. The largest square region that can be fitted in the distal radius circular ROI is extracted for the texture analysis of

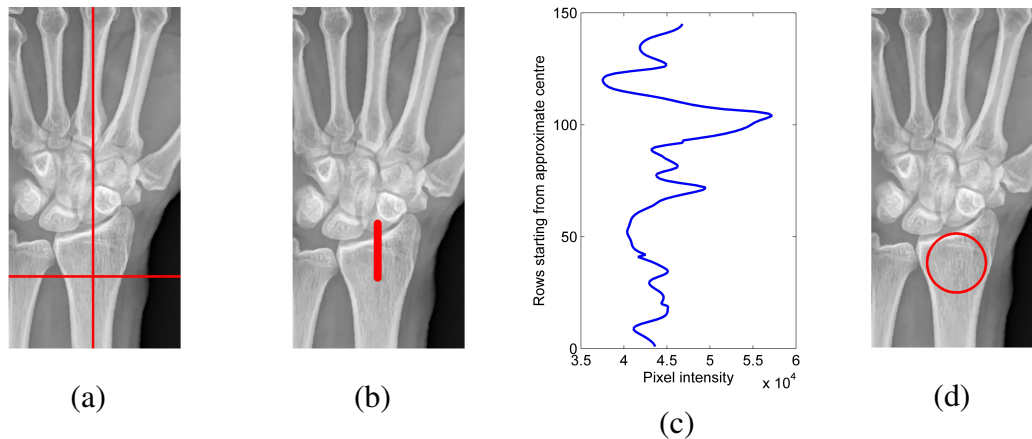


Figure 4.1: Extraction of distal radius ROI: (a) Detection of central axis of the radius bone after alignment, (b) shows a vertical line taken from the DRUJ row to a predetermined distance along the central axis, (c) Intensity profile along the vertical line in (b) showing the UDR as the highest peak, and (d) Segmentation of the circular ROI of distal radius

trabecular bone. Extracting the largest fitting circular ROI at the distal radius of images would help in yielding a standardized region for texture analysis, in terms of physical dimensions for varying hand sizes and varying image sizes.

We choose the centre of the distal radius ROI at 3 mm below DRUJ because this region is more prone to fracture and has been analyzed in previous studies (Lee *et al.* 2008; Wigderowitz *et al.* 2000; Gomberg *et al.* 2003; Mallard *et al.* 2013). The ROI used in pQCT for trabecular texture analysis also intersects with the ROI chosen in this work.

4.3 TEXTURE ANALYSIS OF TRABECULAR BONE

This section discusses the various texture features used in this work for the assessment of trabecular bone of the distal radius. The texture features extracted are first order and higher order statistical features, structural features and transform-based features, as discussed in the sections below.

Histogram features

The first order statistical features, also called histogram features, measure the properties of the probability distribution of image pixel intensities. It is a measure of the global image characteristics. As the raw texture images of the healthy and osteoporotic subjects are visually similar to the naked eye, their histograms also do not show distinct characteristics. However, the histograms of preprocessed texture images after background subtraction show distinct properties for the healthy and osteoporotic groups. Hence, preprocessing of the images is necessary in order to characterize the trabecular bone texture more distinctly. The contrast of the extracted distal radius ROI is enhanced by linearly mapping the image pixels to the full dynamic range. The image is then resized to 170×170 pixels using bicubic interpolation, to make the features extracted independent of the image size. The effects of non-uniform illumination is removed by background subtraction, employed using a Gaussian filter with standard deviation of 50 pixels. This filter size is empirically found to show better features than other filter sizes. Figure 4.2 illustrates the illumination correction of a raw texture image using background estimation and subtraction.

The features extracted from the histogram of preprocessed images are variance, skewness and kurtosis, denoted as $Hist_{var}$, $Hist_{skew}$ and $Hist_{kurt}$. Variance denotes the average of squared difference between the histogram values and the mean. Skewness measures the asymmetry of the histogram. Skewness is negative for a histogram with more pixels of lower intensities. Kurtosis is a measure of the peakedness of the histogram. The more peaked the histogram, the more positive is the kurtosis value. The first order features are calculated using the equations given below.

$$Variance, var = \sum_i \left(\frac{X_i - \bar{X}}{n} \right)^2 \quad (4.1)$$

$$Skewness, skew = \frac{\sum_i \left(\frac{X_i - \bar{X}}{\sigma} \right)^3}{n} \quad (4.2)$$

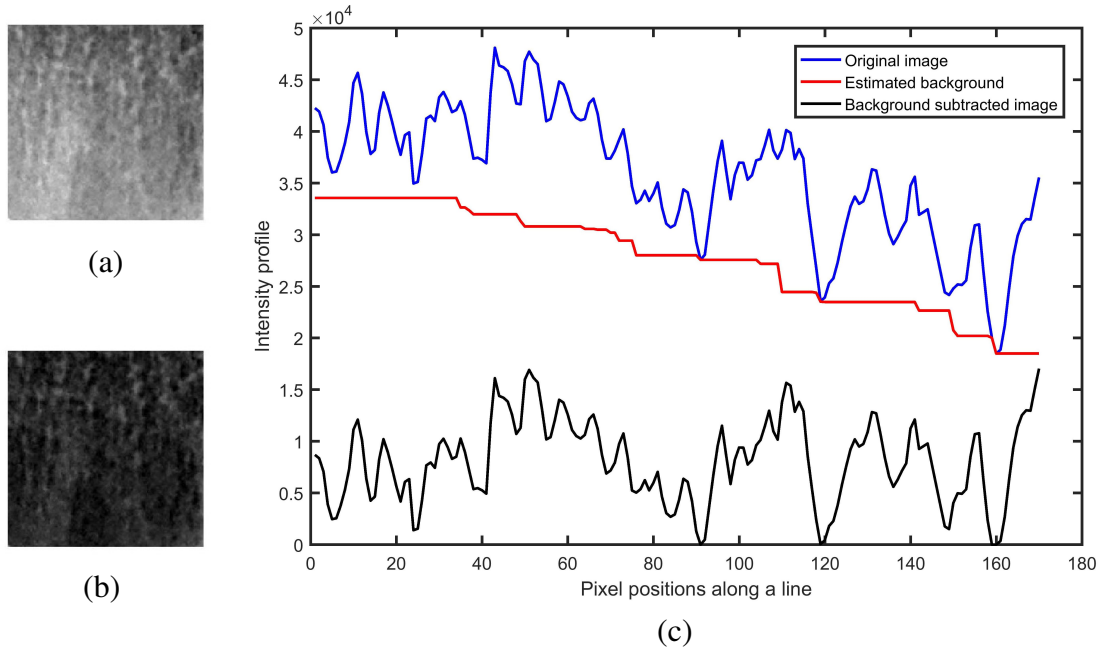


Figure 4.2: Illumination correction of texture image using background subtraction: (a) Raw texture image, (b) image after background subtraction, and (c) corresponding intensity profiles of the raw image and background subtracted image

$$Kurtosis, kurt = \frac{\sum_i \left(\frac{X_i - \bar{X}}{\sigma} \right)^4}{n} - 3 \quad (4.3)$$

where, X_i is the data point, \bar{X} is the mean and n is the number of data points.

Gray Level Co-occurrence Matrix (GLCM)

A drawback of the histogram features is that they do not assess the relative position of the image pixels. GLCM (Haralick 1979) are second order statistical features that help to capture the spatial relation of image pixels. The images are resized to 170×170 and the background of the raw image is subtracted using a Gaussian filter of standard deviation 50 pixels. The images are re-quantized to 256 gray level intensities for a higher contrast in order to ensure better capture of image pixel pair information. GLCM matrices are determined at a distance of d pixels along four directions, 0° , 45° , 90° and 135° to the horizontal. Features extracted from GLCM matrices are energy (en), homogeneity (hom), contrast ($cont$), correlation ($corr$) and entropy (ent). Energy is the

sum of square of the image pixel intensities. Homogeneity measures the similarity of the spatially close image intensities. Contrast measures the difference in intensity of a pixel and its neighbors. Correlation is a measure of how well-correlated a pixel is to its neighbor pixels. Entropy captures the amount of useful information in an image. These five features are extracted from all four GLCM matrices and thus a total of 20 GLCM features are extracted.

If i and j are the image row and column and $p(i, j)$ is the matrix element at row i and column j , the features are calculated using the following equations.

$$\text{Energy, } en = \sum_{i,j} p(i, j)^2 \quad (4.4)$$

$$\text{Homogeneity, } hom = \sum_{i,j} \frac{p(i, j)}{1 + |i - j|} \quad (4.5)$$

$$\text{Contrast, } cont = \sum_{i,j} |i - j|^2 p(i, j) \quad (4.6)$$

$$\text{Correlation, } corr = \sum_{i,j} \frac{(i - \mu_i)(j - \mu_j)p(i, j)}{\sigma_i \sigma_j} \quad (4.7)$$

$$\text{Entropy, } ent = \sum_n k(n) \times \log_2 k(n) \quad (4.8)$$

where $p(i, j)$ is the matrix element value along i^{th} row and j^{th} column, μ_i , σ_i , μ_j and σ_j are the mean and standard deviation along i^{th} row and j^{th} column respectively. k denotes the total number of counts in bin n of the image histogram.

GLCM features are extracted for distances $d = 1, 5, 10$ and 50 pixels. Table 4.1 shows the significance of the GLCM features using independent sample t-test. GLCM features with distance $d = 10$ pixels give more significant features, as compared to $d = 1, 5$ and 50 pixels, and hence $d = 10$ pixels is used.

Table 4.1: Statistical test results of GLCM features for $d = 1, 5, 10$ and 50 pixels

Sl. no.	GLCM features	$d = 1$	$d = 5$	$d = 10$	$d = 50$
1	$GLCM_{0_{cont}}$	0.5568	0.0615	0.0005 [‡]	0.0001 [‡]
2	$GLCM_{0_{corr}}$	0.0062 [†]	0.9126	0.0150*	0.0020 [†]
3	$GLCM_{0_{hom}}$	0.8369	0.0133*	9E-05 [§]	0.0002 [‡]
4	$GLCM_{0_{en}}$	0.0296*	0.0005 [‡]	0.0003 [‡]	0.0004 [‡]
5	$GLCM_{0_{ent}}$	0.1401	0.0012 [†]	0.0008 [‡]	0.0007 [‡]
6	$GLCM_{45_{cont}}$	0.7918	0.0181*	0.0003 [‡]	0.0022 [†]
7	$GLCM_{45_{corr}}$	0.0094 [†]	0.9646	0.0485*	0.4354
8	$GLCM_{45_{hom}}$	0.7125	0.0053 [†]	0.0001 [‡]	0.0005 [‡]
9	$GLCM_{45_{en}}$	0.0187*	0.0004 [‡]	0.0003 [‡]	0.0003 [‡]
10	$GLCM_{45_{ent}}$	0.0730	0.0009 [‡]	0.0006 [‡]	0.0003 [‡]
11	$GLCM_{90_{cont}}$	0.6088	0.1273	0.0215*	0.0189*
12	$GLCM_{90_{corr}}$	0.0266*	0.1927	0.4541	0.0173*
13	$GLCM_{90_{hom}}$	0.9748	0.0972	0.0096 [†]	0.0013 [†]
14	$GLCM_{90_{en}}$	0.0374*	0.0019 [†]	0.0007 [‡]	0.0005 [‡]
15	$GLCM_{90_{ent}}$	0.2007	0.0053 [†]	0.0019 [†]	0.0008 [‡]
16	$GLCM_{135_{cont}}$	0.7407	0.0104*	0.0001 [‡]	0.0022 [†]
17	$GLCM_{135_{corr}}$	0.0114*	0.5602	0.0127*	0.7369
18	$GLCM_{135_{hom}}$	0.6118	0.0031 [†]	5E-05 [§]	0.0002 [‡]
19	$GLCM_{135_{en}}$	0.0187*	0.0003 [‡]	0.0002 [‡]	0.0002 [‡]
20	$GLCM_{135_{ent}}$	0.0801	0.0009 [‡]	0.0005 [‡]	0.0004 [‡]

* $p < 0.05$, † $p < 0.01$, ‡ $p < 0.001$, § $p < 0.0001$

Gray Level Run Length Matrix (GLRLM)

GLRLM (Galloway 1975) is a higher order statistical method that measures the connectivity of similar gray level pixels along a specific direction. Fine textures have more short runs with similar gray level intensities while coarse textures have more long runs with different intensities. The raw images are preprocessed by resizing to 150×150 and a background subtraction using Gaussian filter of standard deviation of 20 pixels. As all the pixel intensities in 16 bits is not useful to calculate GLRLM, the texture image is re-quantized to 256 gray level intensities. GLRLM is calculated along four directions, namely 0° , 45° , 90° and 135° to the horizontal. The features extracted from GLRLM are Short Run Emphasis (SRE), Long Run Emphasis (LRE), Gray Level Non-uniformity (GLN), Run Length Non-uniformity (RLN), Low Gray level Run Emphasis (LGRE) and High Gray level Run Emphasis (HGRE). SRE is a measure of the distribution of short runs in the image and LRE is a measure of the occurrence of long runs. The non-uniformity of the gray level values and run lengths in the image are measured by GLN and RLN, respectively. LGRE and HGRE measure the differences in gray level

distributions in texture images having the same values for SRE and LRE. These six features are extracted from the four GLRLM matrices to obtain a total of 24 features using GLRLM.

Let $p(i, j)$ be the number of runs with pixels of intensity values i and run length j , N_g be the number of gray levels and N_r be the run length.

$$SRE = \frac{1}{n_r} \sum_{i=1}^{N_g} \sum_{j=1}^{N_r} \frac{p(i, j)}{j^2} \quad (4.9)$$

$$LRE = \frac{1}{n_r} \sum_{i=1}^{N_g} \sum_{j=1}^{N_r} p(i, j) \times j^2 \quad (4.10)$$

$$GLN = \frac{1}{n_r} \sum_{i=1}^{N_g} \left[\sum_{j=1}^{N_r} p(i, j) \right]^2 \quad (4.11)$$

$$RLN = \frac{1}{n_r} \sum_{j=1}^{N_r} \left[\sum_{i=1}^{N_g} p(i, j) \right]^2 \quad (4.12)$$

$$LGRE = \frac{1}{n_r} \sum_{i=1}^{N_g} \sum_{j=1}^{N_r} \frac{p(i, j)}{i^2} \quad (4.13)$$

$$HGRE = \frac{1}{n_r} \sum_{i=1}^{N_g} \sum_{j=1}^{N_r} p(i, j) \times i^2 \quad (4.14)$$

where,

$$n_r = \sum_{i=1}^{N_g} \sum_{j=1}^{N_r} p(i, j) \quad (4.15)$$

Morphological gradients method (MGM)

MGM (Veenland 1999) is a texture method developed for texture analysis of trabecular bone in the assessment of osteoporosis. The raw images are resized to 170×170 and the contrast is enhanced using a background subtraction using 50 pixels. In this method, pixel intensities of morphological gradient images, constructed using different structuring elements, are summed up and various features such as GR_i , $GSS_{i,j}$ and $GSR_{i,j}$ are

extracted using the equations below.

$$g = (f \oplus b) - (f \ominus b) \quad (4.16)$$

$$GR_i = \frac{\sum \sum gs_{i,i}(x, y) - \sum \sum gc_i(x, y)}{\sum \sum gs_{i,i}(x, y) + \sum \sum gc_i(x, y)} \quad (4.17)$$

$$GSS_{i,j} = \frac{\sum \sum gs_{i,i}(x, y) - \sum \sum gs_{j,j}(x, y)}{\sum \sum gs_{i,i}(x, y) + \sum \sum gs_{j,j}(x, y)} \quad (4.18)$$

$$GSR_{i,j} = \frac{\sum \sum gc_i(x, y) - \sum \sum gc_j(x, y)}{\sum \sum gc_i(x, y) + \sum \sum gc_j(x, y)} \quad (4.19)$$

where $gs_{i,j}$ denotes Beucher gradient image obtained using a rectangular structuring element of size $i \times j$, and gc_i is the Beucher gradient image obtained using a disk structuring element of radius i .

GR_i measures the roundness of the edges, while $GSS_{i,j}$ and $GSR_{i,j}$ assess the size of the edges in the image. In this work, we choose the same size of structuring elements as used in the original work by Veenland (1999). GR_i is determined for $i = 5$ and 7. The features $GSS_{i,j}$ and $GSR_{i,j}$ are calculated for $i = 7, 9, 11$ and $j = 3, 5, 7$. Eight features are extracted using MGM, namely GR_5 , GR_7 , $GSS_{7,3}$, $GSS_{9,5}$, $GSS_{11,7}$, $GSR_{7,3}$, $GSR_{9,5}$ and $GSR_{11,7}$.

Figure 4.3 shows the morphological gradient of the texture image using square and disk-shaped structuring elements of size 7 and 3 pixels each. As an example, GR_7 is calculated from the morphological gradients formed from square and disk-shaped structuring elements of size 7 pixels (Figure 4.3(a) and (b)). $GSS_{7,3}$ is calculated from morphological gradient of the image using square-shaped structuring elements of size 7 and 3 pixels (Figure 4.3(a) and (c)). $GSR_{7,3}$ is obtained from morphological gradient using disk-shaped structuring elements of size 7 and 3 pixels (Figure 4.3(b) and (d)).

Laws's masks

Laws' texture masks (Laws 1980) use five 1D kernel vectors of 5 pixels length, namely level vector ($L5$), edge vector ($E5$), spot vector ($S5$), ripple vector ($R5$) and wave vector

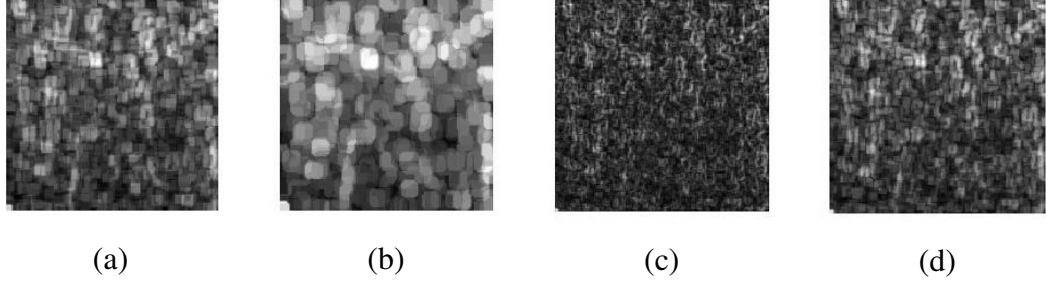


Figure 4.3: Texture analysis using MGM: (a) morphological gradient of the texture image using square-shaped structuring element of size 7 pixels, (b) morphological gradient using disk-shaped structuring element of size 7 pixels, (c) morphological gradient using square-shaped structuring element of size 3 pixels and (d) morphological gradient using disk-shaped structuring element of size 3 pixels

($W5$), to characterize the texture images.

$$\begin{aligned}
 L5 &= [1 \ 4 \ 6 \ 4 \ 1] \\
 E5 &= [-1 \ -2 \ 0 \ 2 \ 1] \\
 S5 &= [-1 \ 0 \ 2 \ 0 \ -1] \\
 R5 &= [1 \ -4 \ 6 \ -4 \ 1] \\
 W5 &= [-1 \ 2 \ 0 \ -2 \ -1]
 \end{aligned}$$

These 1D masks are convolved to create 25 filter masks of size 5×5 , such as $L5L5$, $L5E5$, $L5S5$, etc. The raw images are first resized to 150×150 and contrast enhanced using Gaussian filter of standard deviation of 20 pixels, and then filtered using these 25 filter masks. The filtered images obtained using symmetric Laws masks such as $L5E5$ and $E5L5$, are fused together as they capture similar information. The filtered image obtained from $L5L5$ is discarded as it produces just the average of the texture image. Thus, 14 texture images are generated using Laws' masks, namely $LAW S_{L5E5}$, $LAW S_{L5S5}$, $LAW S_{L5R5}$, $LAW S_{L5W5}$, $LAW S_{E5E5}$, $LAW S_{E5S5}$, $LAW S_{E5R5}$, $LAW S_{E5W5}$, $LAW S_{S5S5}$, $LAW S_{S5R5}$, $LAW S_{S5W5}$, $LAW S_{R5R5}$, $LAW S_{R5W5}$ and $LAW S_{W5W5}$, as shown in Figure 4.4. Energy, contrast, correlation and homogeneity of these texture images are extracted, resulting in 56 features.

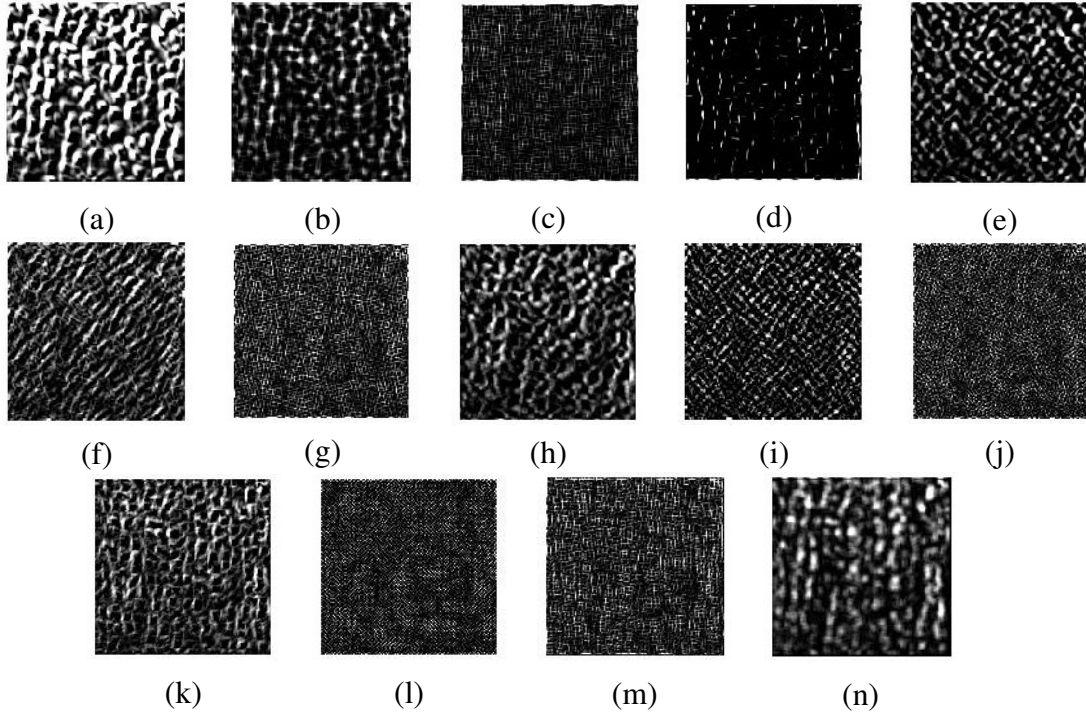


Figure 4.4: Texture images obtained using Laws's masks: (a) $LAW S_{L5E5}$, (b) $LAW S_{L5S5}$, (c) $LAW S_{L5R5}$, (d) $LAW S_{L5W5}$, (e) $LAW S_{E5E5}$, (f) $LAW S_{E5S5}$, (g) $LAW S_{E5R5}$, (h) $LAW S_{E5W5}$, (i) $LAW S_{S5S5}$, (j) $LAW S_{S5R5}$, (k) $LAW S_{S5W5}$, (l) $LAW S_{R5R5}$, (m) $LAW S_{R5W5}$ and (n) $LAW S_{W5W5}$

Local Binary Pattern (LBP)

In this work, all pixels in the raw texture image are encoded using rotation-invariant LBP method and a LBP histogram is constructed. First order features such as mean, variance, skew, kurtosis and energy, are extracted from the LBP histograms. These features are denoted as LBP_{mean} , LBP_{var} , LBP_{skew} , LBP_{kurt} and LBP_{en} .

Many improved variants of the LBP method has been proposed for texture analysis. One such variant is the Local Line Binary Pattern (LLBP) (Petpon and Srisuk 2009). LLBP has been developed for segmentation and recognition of objects in medical images. LLBP is a 1D feature extractor that considers a linear neighborhood for the binary encoding of center pixels. The encoding can be done in horizontal and vertical directions, and hence oriental information is captured by LLBP. LLBP is a promising technique for trabecular bone characterization as trabecular tissue in the distal radius

region appears as approximately vertical linear structures. In this work, LLBP features are extracted with a line of length 17 pixels as the neighborhood (Rosdi *et al.* 2011). The features extracted using LLBP are mean, variance, skew, kurtosis, energy and entropy of LLBP ($LLBP_{mean}$, $LLBP_{var}$, $LLBP_{skew}$, $LLBP_{kurt}$, $LLBP_{en}$ and $LLBP_{ent}$), horizontal LLBP ($LLBP_{Hor_{mean}}$, $LLBP_{Hor_{var}}$, $LLBP_{Hor_{skew}}$, $LLBP_{Hor_{kurt}}$, $LLBP_{Hor_{en}}$ and $LLBP_{Hor_{ent}}$) and vertical LLBP ($LLBP_{Vert_{mean}}$, $LLBP_{Vert_{var}}$, $LLBP_{Vert_{skew}}$, $LLBP_{Vert_{kurt}}$, $LLBP_{Vert_{en}}$ and $LLBP_{Vert_{ent}}$).

Gabor features

Gabor filters (Kuse *et al.* 2011) comprises of two components: (a) Radial component, which controls the frequency band that the filter responds to, and (b) Angular component, which controls the orientation that the filter responds to. Gabor filter have tunable orientation and centre frequency. For each scale and orientation, the radial and angular components are multiplied together to construct the filter. By convolving the Fourier transform of input image with a set of log-Gabor filters of different orientations and spatial frequencies, different sets of transformed images are obtained. The mean amplitude of the Gabor filter responses are extracted as features.

The images are preprocessed by resizing to 170×170 and correcting the uneven illumination using Gaussian filter of standard deviation of 50 pixels. Gabor filters of scales of 1 to 5 are used with 6 different orientations. The significance of the mean amplitude of the Gabor filter responses using independent sample t-test are shown in Table 4.2. Gabor filter of scale 4 give more significant features, as compared to other scales.

Figure 4.5 shows the images filtered by log-Gabor filter of scale 4 along 6 orientations. $Gabor_{4,1}$, $Gabor_{4,2}$, $Gabor_{4,3}$, $Gabor_{4,4}$, $Gabor_{4,5}$ and $Gabor_{4,6}$ denotes the mean amplitude of the response of Gabor filter of scale 4 and orientations 1, 2, 3, 4, 5 and 6, respectively.

Table 4.2: Statistical test results of Gabor features for different scales

Orientation	<i>Scale</i> = 1	<i>Scale</i> = 2	<i>Scale</i> = 3	<i>Scale</i> = 4	<i>Scale</i> = 5
1	0.4500	0.6990	2.7E-04 [‡]	3.3E-08 [§]	2.7E-04 [‡]
2	0.7970	0.4236	4.6E-04 [‡]	6.7E-07 [§]	0.0010 [†]
3	0.9914	0.1721	0.0014 [†]	1.3E-05 [§]	0.0075 [†]
4	0.9323	0.1483	0.0032 [†]	0.0028 [†]	0.2237
5	0.9510	0.2319	0.0025 [†]	3.7E-05 [§]	0.0145*
6	0.6768	0.5543	0.0015 [†]	2.2E-07 [§]	1.7E-04 [‡]

*p<0.05, † p<0.01, ‡ p<0.001, § p<0.0001

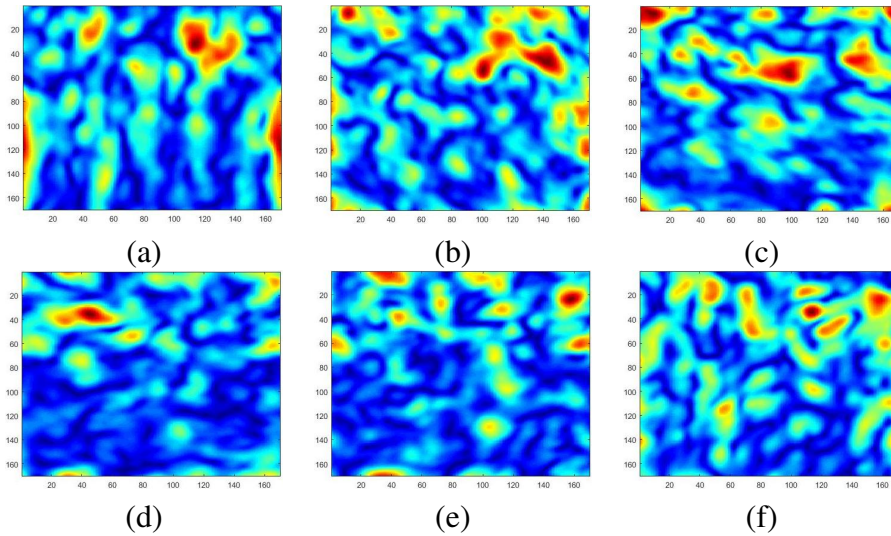


Figure 4.5: Response of the Gabor filter of scale 4 along (a) orientation 1, (b) orientation 2, (c) orientation 3, (d) orientation 4, (e) orientation 5 and (f) orientation 6

4.4 RESULTS AND DISCUSSION

In this section, we discuss the results of the proposed segmentation approach to automatically extract the distal radius ROI, and the results of the statistical tests used to quantitatively assess the ability of the extracted features to distinguish between the healthy and low bone mass groups.

4.4.1 Segmentation results

The proposed automated method for locating and extracting the distal radius is validated on hand and wrist radiographs from Indian and Swiss sample data. The success rate for accurate detection of distal radius ROI is 93.5% in Indian sample data and 83% in Swiss

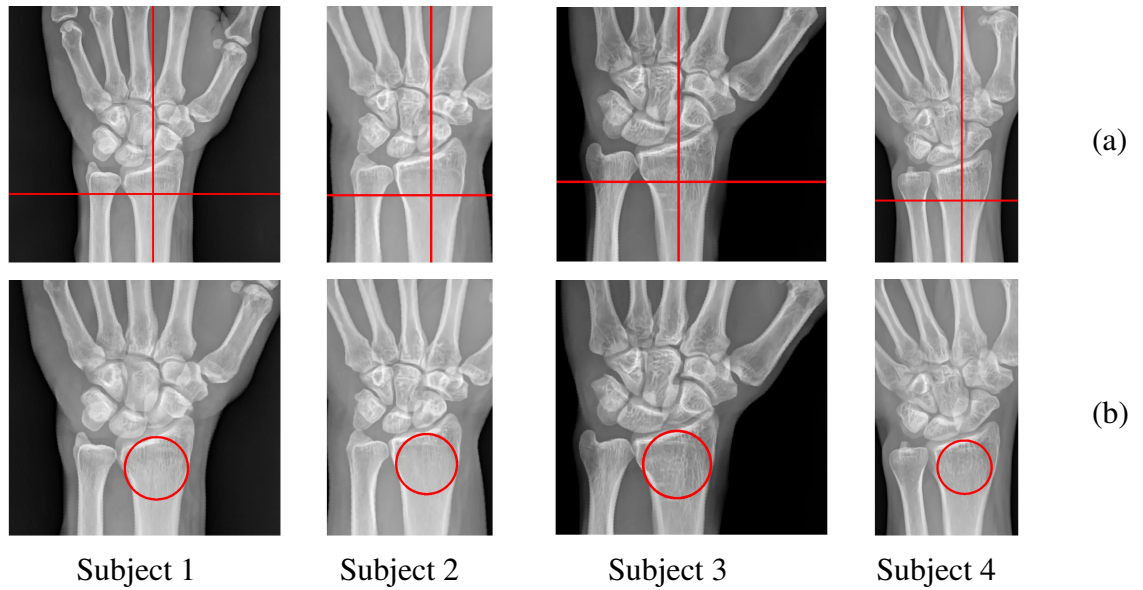


Figure 4.6: Examples of the segmentation results of distal radius ROI for two healthy images (Subjects 1 and 2) and two osteoporotic images (Subjects 3 and 4): (a) the central axis and approximate centre of circular distal radius ROI in top row, and (b) the extracted circular ROI in bottom row

sample data. Figure 4.6 shows the segmentation results of the distal radius ROI using the proposed method for two healthy and two osteoporotic subjects.

The proposed segmentation approach failed to detect the ROI in some cases due to mis-detection of DRUJ and improper vertical alignment of the radius bone. This happens in images with obstacles like bangles or where the length of the radial bone in the radiographic image is less, thus not being able to find the central axis of the radial bone for its vertical alignment. This can be alleviated by ensuring careful positioning of the hand and proper image acquisition.

4.4.2 Statistical analysis

Statistical analysis is done to test the feasibility of the extracted texture features for the assessment of osteoporosis. Independent sample t -test is used to find the ability of features to discriminate between the healthy and LBM groups. The statistical tests are performed on the Indian and Swiss sample data separately. The automatically segmented trabecular bone ROI are used for the analysis. The distal radius of the remain-

ing poorly segmented images were semi-automatically segmented and included for the statistical analysis. Table 4.3 shows the mean and standard deviation of the extracted texture features in the healthy (H) and low bone mass (LBM) groups and the results of the independent sample t -test. The statistical significance is set at $p < 0.05$.

In the Indian sample data, histogram features extracted from the texture images show statistical significance of $p < 0.01$. All GLCM features except $GLCM_{90_{corr}}$ are significant. The most significant features with $p < 0.0001$ are $GLCM_{0_{hom}}$ and $GLCM_{135_{hom}}$. Out of the 24 GLRLM features extracted, 19 features are significant. The most significant features with $p < 0.0001$ are $GLRLM_{0_{SRE}}$, $GLRLM_{0_{RLN}}$, $GLRLM_{0_{LGRE}}$, $GLRLM_{45_{SRE}}$, $GLRLM_{45_{RLN}}$, $GLRLM_{45_{LGRE}}$, $GLRLM_{90_{LGRE}}$, $GLRLM_{135_{SRE}}$, $GLRLM_{135_{RLN}}$ and $GLRLM_{135_{LGRE}}$. All the MGM features are significant with $p < 0.001$. Twenty nine of the 56 Laws's mask features extracted are significant. The most significant Laws's feature is $LAW S_{L5S5_{hom}}$. Of the 23 LBP features and its variants, 19 features are significant. The most significant LBP features are $LLBP_{var}$, $LLBP_{kurt}$, $LLBP_{en}$, $LLBP_{ent}$, $LLBP_{Hor_{mean}}$, $LLBP_{Hor_{skew}}$, $LLBP_{Hor_{en}}$ and $LLBP_{Hor_{ent}}$ with $p < 0.0001$. All Gabor features are significant with $p < 0.0001$ except $Gabor_{4,4}$, which is significant with $p < 0.01$. In the Swiss sample data, none of the features are significant except $GLCM_{135_{corr}}$, having a significance of $p < 0.05$. This may be due to the very few samples present in the healthy group of the Swiss sample data.

Correlation of the extracted texture features with sBMD and T -score is assessed using Pearson correlation test. Table 4.4 shows the correlation values and the corresponding significance of the texture features with sBMD and T -score for Indian and Swiss sample population, respectively.

In the Indian sample data, the histogram features are significantly correlated with sBMD and T -score. All GLCM features extracted along the horizontal direction is significantly correlated with sBMD and T -score. The GLCM features along the diagonals are significantly correlated except $GLCM_{45_{corr}}$. The GLCM features along the vertical direction has low correlation with sBMD and T -score. Among the GLRLM features, LRE is not significantly correlated with sBMD. The most significantly correlated

Table 4.3: Significance test results of H and LBM groups of Indian and Swiss sample data

Texture feature	Sl. no.	Features extracted	Indian-H ($\mu \pm \sigma$)	Indian-LBM ($\mu \pm \sigma$)	p-value	Swiss-H ($\mu \pm \sigma$)	Swiss-LBM ($\mu \pm \sigma$)	p-value
Histogram	1	$Hist_{var}$	1199.99 ± 278.35	1347.83 ± 275.56	0.0024 [†]	1532.07 ± 229.00	1547.32 ± 294.52	0.8282
	2	$Hist_{skew}$	0.68 ± 0.40	0.51 ± 0.24	0.0040 [†]	0.39 ± 0.23	0.35 ± 0.14	0.4023
	3	$Hist_{kurt}$	1.34 ± 1.66	0.63 ± 0.85	0.0021 [†]	0.17 ± 0.52	0.08 ± 0.44	0.4729
GLCM	1	$GLCM_{0_{cont}}$	1755.29 ± 574.32	2083.50 ± 481.00	0.0005 [‡]	2418.38 ± 494.06	2540.03 ± 576.14	0.3907
	2	$GLCM_{0_{corr}}$	0.26 ± 0.13	0.21 ± 0.09	0.0150*	0.20 ± 0.09	0.17 ± 0.07	0.0682
	3	$GLCM_{0_{hom}}$	0.08 ± 0.01	0.07 ± 0.01	9E-05 [§]	0.07 ± 0.01	0.07 ± 0.01	0.3409
	4	$GLCM_{0_{en}}$	0.00 ± 0.00	0.00 ± 0.00	0.0003 [‡]	0.00 ± 0.00	0.00 ± 0.00	0.4553
	5	$GLCM_{0_{ent}}$	0.83 ± 0.07	0.87 ± 0.06	0.0008 [‡]	0.90 ± 0.04	0.90 ± 0.05	0.9306
	6	$GLCM_{45_{cont}}$	1907.44 ± 575.29	2245.97 ± 485.56	0.0003 [‡]	2575.98 ± 512.64	2691.81 ± 596.87	0.4301
	7	$GLCM_{45_{corr}}$	0.16 ± 0.10	0.13 ± 0.08	0.0485*	0.13 ± 0.08	0.10 ± 0.07	0.1342
	8	$GLCM_{45_{hom}}$	0.08 ± 0.01	0.07 ± 0.01	0.0001 [‡]	0.07 ± 0.01	0.06 ± 0.01	0.3435
	9	$GLCM_{45_{en}}$	0.00 ± 0.00	0.00 ± 0.00	0.0003 [‡]	0.00 ± 0.00	0.00 ± 0.00	0.4580
	10	$GLCM_{45_{ent}}$	0.82 ± 0.08	0.86 ± 0.06	0.0006 [‡]	0.89 ± 0.04	0.89 ± 0.05	0.8623
	11	$GLCM_{90_{cont}}$	1477.94 ± 434.90	1638.11 ± 359.54	0.0215*	1989.00 ± 426.33	2121.12 ± 508.88	0.2887
	12	$GLCM_{90_{corr}}$	0.35 ± 0.09	0.36 ± 0.09	0.4541	0.33 ± 0.09	0.30 ± 0.08	0.1641
	13	$GLCM_{90_{hom}}$	0.08 ± 0.01	0.08 ± 0.01	0.0096 [†]	0.07 ± 0.01	0.07 ± 0.01	0.2479
	14	$GLCM_{90_{en}}$	0.00 ± 0.00	0.00 ± 0.00	0.0007 [‡]	0.00 ± 0.00	0.00 ± 0.00	0.3891
	15	$GLCM_{90_{ent}}$	0.82 ± 0.08	0.85 ± 0.06	0.0020 [†]	0.88 ± 0.04	0.89 ± 0.05	0.7732
	16	$GLCM_{135_{cont}}$	1873.60 ± 554.86	2230.58 ± 485.15	0.0001 [‡]	2543.92 ± 482.11	2683.09 ± 580.15	0.3255

Texture feature	Sl. no.	Features extracted	Indian-H ($\mu \pm \sigma$)	Indian-LBM ($\mu \pm \sigma$)	p-value	Swiss-H ($\mu \pm \sigma$)	Swiss-LBM ($\mu \pm \sigma$)	p-value
	17	$GLCM_{135_{corr}}$	0.17 ± 0.10	0.13 ± 0.08	0.0127*	0.14 ± 0.07	0.10 ± 0.06	0.0196*
	18	$GLCM_{135_{hom}}$	0.08 ± 0.01	0.07 ± 0.01	5.8E-05 [§]	0.07 ± 0.01	0.06 ± 0.01	0.2221
	19	$GLCM_{135_{en}}$	0.00 ± 0.00	0.00 ± 0.00	0.0002 [‡]	0.00 ± 0.00	0.00 ± 0.00	0.4323
	20	$GLCM_{135_{ent}}$	0.82 ± 0.08	0.86 ± 0.06	0.0005 [‡]	0.89 ± 0.04	0.89 ± 0.05	0.8423
GLRLM	1	$GLRLM_{0_{SRE}}$	0.22 ± 0.01	0.21 ± 0.01	1.8E-06 [§]	0.23 ± 0.02	0.23 ± 0.02	0.9902
	2	$GLRLM_{0_{LRE}}$	3533.94 ± 1042.14	3868.73 ± 1095.50	0.0853	4236.28 ± 823.23	4349.81 ± 1007.53	0.6726
	3	$GLRLM_{0_{GLN}}$	4971.78 ± 106.39	5025.87 ± 115.48	0.0080 [†]	4831.70 ± 208.66	4755.69 ± 183.70	0.1649
	4	$GLRLM_{0_{RLN}}$	386.39 ± 50.54	344.75 ± 46.22	5.2E-06 [§]	413.13 ± 96.52	408.14 ± 98.89	0.8572
	5	$GLRLM_{0_{LGRE}}$	0.84 ± 0.01	0.85 ± 0.01	6.7E-06 [§]	0.83 ± 0.01	0.83 ± 0.01	0.5652
	6	$GLRLM_{0_{HGRE}}$	5.27 ± 0.62	5.53 ± 0.53	0.0147*	5.05 ± 0.86	5.37 ± 1.12	0.2851
	7	$GLRLM_{45_{SRE}}$	0.25 ± 0.01	0.24 ± 0.02	5.3E-06 [§]	0.25 ± 0.03	0.26 ± 0.02	0.5562
	8	$GLRLM_{45_{LRE}}$	3425.97 ± 1008.43	3743.68 ± 1059.99	0.0914	4122.64 ± 818.25	4207.59 ± 968.31	0.7442
	9	$GLRLM_{45_{GLN}}$	5096.91 ± 116.37	5137.63 ± 107.89	0.0463*	4985.15 ± 244.96	4921.17 ± 251.83	0.3656
	10	$GLRLM_{45_{RLN}}$	480.64 ± 51.38	437.88 ± 54.54	1.8E-05 [§]	499.43 ± 112.34	509.14 ± 111.29	0.7583
	11	$GLRLM_{45_{LGRE}}$	0.84 ± 0.01	0.84 ± 0.01	1.6E-05 [§]	0.84 ± 0.01	0.83 ± 0.01	0.2974
	12	$GLRLM_{45_{HGRE}}$	4.29 ± 0.41	4.46 ± 0.36	0.0153*	4.51 ± 0.74	4.63 ± 0.87	0.6128
	13	$GLRLM_{90_{SRE}}$	0.18 ± 0.01	0.17 ± 0.01	0.0023 [†]	0.19 ± 0.03	0.18 ± 0.03	0.8589
	14	$GLRLM_{90_{LRE}}$	3738.53 ± 1101.35	4066.64 ± 1151.82	0.1093	4504.03 ± 885.44	4617.63 ± 1082.68	0.6940
	15	$GLRLM_{90_{GLN}}$	5099.92 ± 106.55	5163.36 ± 116.34	0.0021 [†]	4914.89 ± 183.71	4867.83 ± 150.34	0.3057
	16	$GLRLM_{90_{RLN}}$	245.83 ± 36.83	227.33 ± 37.11	0.0064 [†]	262.74 ± 76.25	255.91 ± 71.53	0.7410

Texture feature	Sl. no.	Features extracted	Indian-H ($\mu \pm \sigma$)	Indian-LBM ($\mu \pm \sigma$)	p-value	Swiss-H ($\mu \pm \sigma$)	Swiss-LBM ($\mu \pm \sigma$)	p-value
	17	$GLRLM_{90_{LGRE}}$	0.87 ± 0.01	0.88 ± 0.01	$9.8E-05^{\S}$	0.87 ± 0.01	0.87 ± 0.01	0.8790
	18	$GLRLM_{90_{HGRE}}$	8.89 ± 1.05	9.33 ± 1.03	0.0220*	9.22 ± 2.33	9.63 ± 2.41	0.5373
	19	$GLRLM_{135_{SRE}}$	0.25 ± 0.01	0.24 ± 0.02	$2.0E-06^{\S}$	0.26 ± 0.02	0.26 ± 0.02	0.9249
	20	$GLRLM_{135_{LRE}}$	3404.31 ± 1003.76	3730.80 ± 1061.48	0.0825	4081.79 ± 787.00	4194.72 ± 974.94	0.6631
	21	$GLRLM_{135_{GLN}}$	5119.94 ± 121.19	5139.98 ± 104.62	0.3275	4995.71 ± 227.02	4918.09 ± 252.95	0.2640
	22	$GLRLM_{135_{RLN}}$	501.78 ± 64.66	448.93 ± 56.70	$4.1E-06^{\S}$	531.18 ± 115.10	522.20 ± 120.50	0.7888
	23	$GLRLM_{135_{LGRE}}$	0.84 ± 0.01	0.84 ± 0.01	$6.8E-05^{\S}$	0.83 ± 0.01	0.83 ± 0.01	0.4547
	24	$GLRLM_{135_{HGRE}}$	4.16 ± 0.42	4.38 ± 0.33	0.0033^{\ddagger}	4.31 ± 0.73	4.56 ± 0.96	0.3164
MGM	1	GR_5	26.64 ± 2.47	28.58 ± 2.30	$6.5E-06^{\S}$	23.65 ± 3.02	23.25 ± 3.40	0.6406
	2	GR_7	23.67 ± 2.60	25.29 ± 2.25	0.0002^{\ddagger}	21.47 ± 3.00	20.77 ± 3.05	0.3711
	3	$GSS_{7,3}$	183.23 ± 13.23	193.77 ± 12.95	$7.6E-06^{\S}$	164.56 ± 18.23	162.49 ± 20.87	0.6882
	4	$GSS_{9,5}$	106.13 ± 9.49	112.54 ± 8.85	$8.8E-05^{\S}$	96.38 ± 11.45	93.83 ± 12.86	0.4266
	5	$GSS_{11,7}$	72.01 ± 7.79	76.33 ± 6.61	$7.1E-04^{\ddagger}$	65.98 ± 8.51	63.40 ± 9.19	0.2667
	6	$GSR_{7,3}$	204.80 ± 13.75	216.29 ± 13.55	$3.1E-06^{\S}$	183.21 ± 19.91	181.38 ± 23.01	0.7453
	7	$GSR_{9,5}$	114.61 ± 9.51	121.80 ± 9.26	$1.9E-05^{\S}$	103.31 ± 11.99	101.18 ± 13.82	0.5329
	8	$GSR_{11,7}$	77.91 ± 7.66	82.78 ± 6.96	0.0002^{\ddagger}	71.01 ± 8.70	68.67 ± 9.79	0.3364
Laws mask	1	$LAWS_{L5E5_{cont}}$	1906.99 ± 33.97	1893.99 ± 38.10	0.0484*	1881.96 ± 53.38	1892.44 ± 40.52	0.4120
	2	$LAWS_{L5E5_{corr}}$	-0.00 ± 0.02	0.00 ± 0.02	0.0725	0.01 ± 0.03	0.00 ± 0.02	0.4200
	3	$LAWS_{L5E5_{nom}}$	0.07 ± 0.00	0.07 ± 0.00	0.3960	0.07 ± 0.00	0.07 ± 0.00	0.6664
	4	$LAWS_{L5E5_{en}}$	0.00 ± 0.00	0.00 ± 0.00	0.8422	0.00 ± 0.00	0.00 ± 0.00	0.7648

Texture feature	Sl. no.	Features extracted	Indian-H ($\mu \pm \sigma$)	Indian-LBM ($\mu \pm \sigma$)	p-value	Swiss-H ($\mu \pm \sigma$)	Swiss-LBM ($\mu \pm \sigma$)	p-value
	5	$LAW S_{L5S5_{cont}}$	1947.77 ± 41.54	1924.27 ± 43.84	0.0028^\dagger	1927.03 ± 72.30	1934.02 ± 45.48	0.6567
	6	$LAW S_{L5S5_{corr}}$	0.00 ± 0.02	0.01 ± 0.02	0.0148*	0.01 ± 0.03	0.01 ± 0.02	0.7237
	7	$LAW S_{L5S5_{hom}}$	0.07 ± 0.00	0.07 ± 0.00	$8.9E-04^\S$	0.07 ± 0.00	0.07 ± 0.00	0.5292
	8	$LAW S_{L5S5_{en}}$	0.00 ± 0.00	0.00 ± 0.00	0.2756	0.00 ± 0.00	0.00 ± 0.00	0.8479
	9	$LAW S_{L5R5_{cont}}$	1963.11 ± 45.54	1950.83 ± 44.83	0.1344	1920.95 ± 75.93	1923.11 ± 52.68	0.9005
	10	$LAW S_{L5R5_{corr}}$	0.00 ± 0.02	0.01 ± 0.02	0.0047^\dagger	0.02 ± 0.03	0.01 ± 0.02	0.3710
	11	$LAW S_{L5R5_{hom}}$	0.07 ± 0.00	0.07 ± 0.00	0.0457*	0.07 ± 0.00	0.07 ± 0.00	0.9183
	12	$LAW S_{L5R5_{en}}$	0.00 ± 0.00	0.00 ± 0.00	0.0143*	0.00 ± 0.00	0.00 ± 0.00	0.8107
	13	$LAW S_{L5W5_{cont}}$	2118.11 ± 141.22	2050.12 ± 142.49	0.0090^\dagger	2083.11 ± 137.68	2077.91 ± 133.03	0.8911
	14	$LAW S_{L5W5_{corr}}$	0.00 ± 0.05	0.04 ± 0.06	0.0013^\dagger	0.02 ± 0.06	0.03 ± 0.05	0.8593
	15	$LAW S_{L5W5_{hom}}$	0.07 ± 0.01	0.07 ± 0.01	0.2578	0.07 ± 0.00	0.07 ± 0.00	0.5380
	16	$LAW S_{L5W5_{en}}$	0.00 ± 0.00	0.00 ± 0.00	0.8320	0.00 ± 0.00	0.00 ± 0.00	0.7102
	17	$LAW S_{E5E5_{cont}}$	1883.32 ± 70.31	1846.07 ± 72.56	0.0046^\dagger	1851.64 ± 87.35	1843.21 ± 87.92	0.7337
	18	$LAW S_{E5E5_{corr}}$	0.01 ± 0.03	0.02 ± 0.03	0.0601	0.02 ± 0.06	0.02 ± 0.04	0.8693
	19	$LAW S_{E5E5_{hom}}$	0.07 ± 0.00	0.07 ± 0.00	0.0484*	0.07 ± 0.00	0.07 ± 0.00	0.7007
	20	$LAW S_{E5E5_{en}}$	0.00 ± 0.00	0.00 ± 0.00	0.3764	0.00 ± 0.00	0.00 ± 0.00	0.8080
	21	$LAW S_{E5S5_{cont}}$	1920.52 ± 63.68	1877.67 ± 70.31	$5.8E-04^\ddagger$	1884.30 ± 92.27	1875.40 ± 85.99	0.7207
	22	$LAW S_{E5S5_{corr}}$	0.01 ± 0.03	0.02 ± 0.03	0.0042^\dagger	0.02 ± 0.05	0.02 ± 0.04	0.7794
	23	$LAW S_{E5S5_{hom}}$	0.07 ± 0.00	0.07 ± 0.00	0.0714	0.07 ± 0.00	0.07 ± 0.00	0.9383
	24	$LAW S_{E5S5_{en}}$	0.00 ± 0.00	0.00 ± 0.00	0.4648	0.00 ± 0.00	0.00 ± 0.00	0.3777
	25	$LAW S_{E5R5_{cont}}$	2012.52 ± 64.66	1980.49 ± 59.07	0.0048^\dagger	1960.33 ± 105.09	1950.58 ± 79.30	0.6966

Texture feature	Sl. no.	Features extracted	Indian-H ($\mu \pm \sigma$)	Indian-LBM ($\mu \pm \sigma$)	p-value	Swiss-H ($\mu \pm \sigma$)	Swiss-LBM ($\mu \pm \sigma$)	p-value
	26	$LAW S_{E5R5_{corr}}$	-0.00 ± 0.03	0.01 ± 0.03	$4.2E-04^{\ddagger}$	0.02 ± 0.05	0.02 ± 0.03	0.8473
	27	$LAW S_{E5R5_{hom}}$	0.07 ± 0.00	0.07 ± 0.00	0.0379*	0.07 ± 0.00	0.07 ± 0.00	0.4464
	28	$LAW S_{E5R5_{en}}$	0.00 ± 0.00	0.00 ± 0.00	0.0912	0.00 ± 0.00	0.00 ± 0.00	0.7794
	29	$LAW S_{E5W5_{cont}}$	1902.45 ± 84.26	1861.42 ± 71.60	0.0042^{\dagger}	1882.49 ± 89.14	1857.88 ± 79.76	0.2956
	30	$LAW S_{E5W5_{corr}}$	0.01 ± 0.03	0.02 ± 0.03	0.0647	0.01 ± 0.05	0.02 ± 0.04	0.4659
	31	$LAW S_{E5W5_{hom}}$	0.07 ± 0.00	0.07 ± 0.00	0.8343	0.07 ± 0.00	0.07 ± 0.00	0.4963
	32	$LAW S_{E5W5_{en}}$	0.00 ± 0.00	0.00 ± 0.00	0.5714	0.00 ± 0.00	0.00 ± 0.00	0.4990
	33	$LAW S_{S5S5_{cont}}$	1961.03 ± 65.96	1914.17 ± 78.02	$4.8E-04^{\ddagger}$	1917.74 ± 92.79	1907.72 ± 84.31	0.6841
	34	$LAW S_{S5S5_{corr}}$	0.00 ± 0.03	0.02 ± 0.03	0.0010^{\dagger}	0.01 ± 0.05	0.02 ± 0.04	0.7328
	35	$LAW S_{S5S5_{hom}}$	0.07 ± 0.00	0.07 ± 0.00	0.0111*	0.07 ± 0.00	0.07 ± 0.00	0.4311
	36	$LAW S_{S5S5_{en}}$	0.00 ± 0.00	0.00 ± 0.00	0.6658	0.00 ± 0.00	0.00 ± 0.00	0.5173
	37	$LAW S_{S5R5_{cont}}$	2029.76 ± 61.72	1996.53 ± 64.75	0.0043^{\dagger}	1978.58 ± 100.18	1973.27 ± 82.18	0.8316
	38	$LAW S_{S5R5_{corr}}$	-0.01 ± 0.02	0.01 ± 0.03	$2.4E-04^{\ddagger}$	0.02 ± 0.05	0.02 ± 0.03	0.7681
	39	$LAW S_{S5R5_{hom}}$	0.07 ± 0.00	0.07 ± 0.00	0.1022	0.07 ± 0.00	0.07 ± 0.00	0.8244
	40	$LAW S_{S5R5_{en}}$	0.00 ± 0.00	0.00 ± 0.00	0.4847	0.00 ± 0.00	0.00 ± 0.00	0.7221
	41	$LAW S_{S5W5_{cont}}$	1861.29 ± 70.92	1811.56 ± 66.37	0.0001^{\ddagger}	1840.24 ± 90.69	1823.19 ± 80.37	0.4725
	42	$LAW S_{S5W5_{corr}}$	0.01 ± 0.03	0.03 ± 0.03	0.0010^{\dagger}	0.02 ± 0.05	0.02 ± 0.04	0.7499
	43	$LAW S_{S5W5_{hom}}$	0.07 ± 0.00	0.07 ± 0.00	0.0089^{\dagger}	0.07 ± 0.00	0.07 ± 0.00	0.9880
	44	$LAW S_{S5W5_{en}}$	0.00 ± 0.00	0.00 ± 0.00	0.2339	0.00 ± 0.00	0.00 ± 0.00	0.2422
	45	$LAW S_{R5R5_{cont}}$	1978.83 ± 68.95	1969.32 ± 67.98	0.4428	1974.87 ± 115.41	1963.17 ± 88.09	0.6722
	46	$LAW S_{R5R5_{corr}}$	-0.01 ± 0.03	0.00 ± 0.03	0.0924	0.02 ± 0.04	0.01 ± 0.04	0.2934

Texture feature	Sl. no.	Features extracted	Indian-H ($\mu \pm \sigma$)	Indian-LBM ($\mu \pm \sigma$)	p-value	Swiss-H ($\mu \pm \sigma$)	Swiss-LBM ($\mu \pm \sigma$)	p-value
	47	$LAW S_{R5R5_{hom}}$	0.07 ± 0.00	0.07 ± 0.00	0.5958	0.07 ± 0.00	0.07 ± 0.00	0.4549
	48	$LAW S_{R5R5_{en}}$	0.00 ± 0.00	0.00 ± 0.00	0.9734	0.00 ± 0.00	0.00 ± 0.00	0.6485
	49	$LAW S_{R5W5_{cont}}$	1958.68 ± 63.34	1931.20 ± 65.46	0.0197*	1924.41 ± 102.90	1915.37 ± 74.17	0.7051
	50	$LAW S_{R5W5_{corr}}$	0.00 ± 0.03	0.02 ± 0.03	0.0018 [†]	0.02 ± 0.05	0.01 ± 0.03	0.7791
	51	$LAW S_{R5W5_{hom}}$	0.07 ± 0.00	0.07 ± 0.00	0.1584	0.07 ± 0.00	0.07 ± 0.00	0.5585
	52	$LAW S_{R5W5_{en}}$	0.00 ± 0.00	0.00 ± 0.00	0.9373	0.00 ± 0.00	0.00 ± 0.00	0.7994
	53	$LAW S_{W5W5_{cont}}$	1876.44 ± 107.66	1825.94 ± 100.78	0.0082 [†]	1836.59 ± 96.01	1812.06 ± 72.76	0.2865
	54	$LAW S_{W5W5_{corr}}$	0.02 ± 0.04	0.03 ± 0.05	0.1873	0.01 ± 0.05	0.02 ± 0.03	0.4664
	55	$LAW S_{W5W5_{hom}}$	0.07 ± 0.00	0.07 ± 0.00	0.0066 [†]	0.07 ± 0.00	0.07 ± 0.00	0.6826
	56	$LAW S_{W5W5_{en}}$	0.00 ± 0.00	0.00 ± 0.00	0.4576	0.00 ± 0.00	0.00 ± 0.00	0.6924
LBP	1	LBP_{mean}	1.76 ± 0.13	1.71 ± 0.13	0.0433*	1.81 ± 0.12	1.80 ± 0.12	0.8976
	2	LBP_{var}	2.06 ± 0.47	1.90 ± 0.48	0.0536	2.22 ± 0.44	2.20 ± 0.46	0.8684
	3	LBP_{skew}	2.94 ± 0.30	3.07 ± 0.32	0.0161*	2.84 ± 0.30	2.85 ± 0.31	0.8558
	4	LBP_{kurt}	12.80 ± 2.42	13.98 ± 2.67	0.0094 [†]	11.92 ± 2.33	12.07 ± 2.46	0.8179
	5	LBP_{en}	0.45 ± 0.03	0.46 ± 0.03	0.0164*	0.43 ± 0.03	0.43 ± 0.03	0.9017
	6	$LLBP_{mean}$	4.66 ± 0.01	4.66 ± 0.01	0.0018 [†]	4.68 ± 0.02	4.69 ± 0.02	0.1101
	7	$LLBP_{var}$	4.70 ± 0.12	4.57 ± 0.14	1.9E-07 [§]	4.73 ± 0.13	4.70 ± 0.13	0.3400
	8	$LLBP_{skew}$	-0.16 ± 0.02	-0.16 ± 0.02	0.1451	-0.16 ± 0.02	-0.17 ± 0.02	0.1732
	9	$LLBP_{kurt}$	1.96 ± 0.03	1.99 ± 0.04	5.6E-08 [§]	1.95 ± 0.04	1.96 ± 0.04	0.3399
	10	$LLBP_{en}$	0.13 ± 0.00	0.13 ± 0.00	9.4E-08 [§]	0.13 ± 0.00	0.13 ± 0.00	0.3093

Texture feature	Sl. no.	Features extracted	Indian-H ($\mu \pm \sigma$)	Indian-LBM ($\mu \pm \sigma$)	p-value	Swiss-H ($\mu \pm \sigma$)	Swiss-LBM ($\mu \pm \sigma$)	p-value
	11	$LLBP_{ent}$	2.06 ± 0.01	2.05 ± 0.01	$1.2E-07^{\S}$	2.06 ± 0.00	2.06 ± 0.01	0.3509
	12	$LLBP_{Hor_{mean}}$	4.80 ± 0.03	4.83 ± 0.03	$1.1E-08^{\S}$	4.83 ± 0.02	4.83 ± 0.04	0.8236
	13	$LLBP_{Hor_{var}}$	7.05 ± 0.19	7.01 ± 0.20	0.2536	6.78 ± 0.28	6.85 ± 0.21	0.2424
	14	$LLBP_{Hor_{skew}}$	-0.31 ± 0.03	-0.33 ± 0.03	$1.3E-07^{\S}$	-0.33 ± 0.03	-0.32 ± 0.03	0.6869
	15	$LLBP_{Hor_{kurt}}$	1.57 ± 0.04	1.59 ± 0.04	0.0155*	1.63 ± 0.05	1.62 ± 0.04	0.1790
	16	$LLBP_{Hor_{en}}$	0.18 ± 0.01	0.18 ± 0.01	$2.1E-05^{\S}$	0.17 ± 0.01	0.17 ± 0.01	0.5421
	17	$LLBP_{Hor_{ent}}$	1.88 ± 0.03	1.85 ± 0.03	$2.2E-05^{\S}$	1.91 ± 0.04	1.90 ± 0.04	0.5224
	18	$LLBP_{Vert_{mean}}$	4.88 ± 0.03	4.90 ± 0.03	$9.9E-04^{\ddagger}$	4.91 ± 0.04	4.92 ± 0.04	0.4176
	19	$LLBP_{Vert_{var}}$	6.48 ± 0.14	6.44 ± 0.16	0.1077	6.51 ± 0.18	6.46 ± 0.16	0.3284
	20	$LLBP_{Vert_{skew}}$	-0.40 ± 0.04	-0.42 ± 0.04	0.0010^{\dagger}	-0.40 ± 0.04	-0.41 ± 0.04	0.4574
	21	$LLBP_{Vert_{kurt}}$	1.71 ± 0.04	1.74 ± 0.05	0.0034^{\dagger}	1.72 ± 0.04	1.73 ± 0.05	0.2714
	22	$LLBP_{Vert_{en}}$	0.18 ± 0.01	0.19 ± 0.01	0.0040^{\dagger}	0.17 ± 0.01	0.18 ± 0.01	0.8570
	23	$LLBP_{Vert_{ent}}$	1.86 ± 0.04	1.85 ± 0.03	0.0069^{\dagger}	1.88 ± 0.04	1.88 ± 0.04	0.9329
Gabor	1	$Gabor_{4,1}$	1276.76 ± 251.19	1562.86 ± 308.80	$3.3E-08^{\S}$	1416.96 ± 321.63	1396.07 ± 339.78	0.8081
	2	$Gabor_{4,2}$	1006.17 ± 171.95	1179.45 ± 209.68	$6.7E-07^{\S}$	1084.41 ± 276.34	1068.12 ± 260.03	0.8126
	3	$Gabor_{4,3}$	851.70 ± 139.28	969.08 ± 159.32	$1.3E-05^{\S}$	899.57 ± 187.73	830.90 ± 181.48	0.2037
	4	$Gabor_{4,4}$	923.44 ± 197.07	1030.41 ± 208.83	0.0028^{\dagger}	929.40 ± 182.22	886.09 ± 186.58	0.3659
	5	$Gabor_{4,5}$	813.16 ± 148.50	929.29 ± 165.48	$3.7E-05^{\S}$	840.53 ± 135.07	830.24 ± 160.67	0.7928
	6	$Gabor_{4,6}$	985.62 ± 202.95	1194.06 ± 236.66	$2.2E-07^{\S}$	1098.97 ± 244.94	1052.80 ± 238.86	0.4590

*p<0.05, † p<0.01, ‡ p<0.001, § p<0.0001

GLRLM features are $GLRLM_{0_{SRE}}$, $GLRLM_{0_{RLN}}$, $GLRLM_{45_{SRE}}$, $GLRLM_{45_{RLN}}$, $GLRLM_{45_{LGRE}}$, $GLRLM_{90_{LGRE}}$, $GLRLM_{135_{SRE}}$ and $GLRLM_{135_{RLN}}$. All MGM features are significantly correlated with sBMD and T -score with $p < 0.0001$. Out of the 56 extracted Laws's features, 31 features are significantly correlated to both sBMD and T -score. The most significantly correlated Laws's texture feature is $LAW S_{S5S5_{cont}}$ with $p < 0.0001$. All LBP features except $LLBP_{Hor_{var}}$ are significantly correlated with sBMD. LLBP features are more significantly correlated with sBMD than the conventional LBP features. Considering the directional analysis of LLBP, LLBP features extracted along the horizontal direction shows higher correlation to sBMD as compared to the vertical direction. All Gabor features except $Gabor_{4,4}$ are significantly correlated with sBMD and T -score, with $Gabor_{4,1}$, $Gabor_{4,2}$ and $Gabor_{4,6}$ showing the highest correlations. In the Swiss sample data, only the LLBP features are significantly correlated with sBMD and T -score, with the most correlated feature being $LLBP_{Vert_{kurt}}$ with $r = -0.3239$. The correlation values of the extracted features with DXA-BMD of lumbar spine is less due to the different sites of measurement of the X-ray and DXA. Although the correlation values are less, the correlation is significant with $p < 0.05$.

Table 4.4: Correlation analysis of extracted features with sBMD and T -score for Indian and Swiss sample populations

Texture feature	Sl. no.	Features extracted	Indian sample population		Swiss sample population	
			sBMD	T -score	sBMD	T -score
Histogram	1	$Hist_{var}$	-0.2072*	-0.2158*	-0.0876	-0.1218
	2	$Hist_{skew}$	0.2098*	0.2226 [†]	0.1331	0.1081
	3	$Hist_{kurt}$	0.2270 [†]	0.2363 [†]	0.0977	0.0816
GLCM	1	$GLCM_{0_{cont}}$	-0.2565 [†]	-0.2626 [†]	-0.1021	-0.1187
	2	$GLCM_{0_{corr}}$	0.2047*	0.2055*	0.0729	0.0586
	3	$GLCM_{0_{hom}}$	0.2658 [†]	0.2763 [†]	0.0865	0.0987
	4	$GLCM_{0_{en}}$	0.2577 [†]	0.2686 [†]	0.0947	0.1157
	5	$GLCM_{0_{ent}}$	-0.2193*	-0.2286 [†]	-0.0476	-0.0746
	6	$GLCM_{45_{cont}}$	-0.2506 [†]	-0.2564 [†]	-0.1040	-0.1230
	7	$GLCM_{45_{corr}}$	0.1241	0.1244	0.0352	0.0287
	8	$GLCM_{45_{hom}}$	0.2639 [†]	0.2737 [†]	0.0941	0.1119
	9	$GLCM_{45_{en}}$	0.2604 [†]	0.2714 [†]	0.0927	0.1150

Texture feature	Sl. no.	Features extracted	Indian sample population		Swiss sample population	
			sBMD	T-score	sBMD	T-score
	10	$GLCM_{45_{ent}}$	-0.2306 [†]	-0.2401 [†]	-0.0563	-0.0837
	11	$GLCM_{90_{cont}}$	-0.1336	-0.1463	-0.0551	-0.0817
	12	$GLCM_{90_{corr}}$	-0.1153	-0.1042	-0.0425	-0.0347
	13	$GLCM_{90_{hom}}$	0.1407	0.1555	0.0365	0.0547
	14	$GLCM_{90_{en}}$	0.2358 [†]	0.2489 [†]	0.0832	0.1054
	15	$GLCM_{90_{ent}}$	-0.2022*	-0.2132*	-0.0430	-0.0721
	16	$GLCM_{135_{cont}}$	-0.2828 [‡]	-0.2881 [‡]	-0.0945	-0.1191
	17	$GLCM_{135_{corr}}$	0.1920*	0.1909*	0.0036	0.0122
	18	$GLCM_{135_{hom}}$	0.2868 [‡]	0.2953 [‡]	0.0795	0.1012
	19	$GLCM_{135_{en}}$	0.2664 [†]	0.2775 [†]	0.0998	0.1217
	20	$GLCM_{135_{ent}}$	-0.2350 [†]	-0.2442 [†]	-0.0617	-0.0892
GLRLM	1	$GLRLM_{0_{SRE}}$	0.4180 [§]	0.4005 [§]	0.1614	0.1475
	2	$GLRLM_{0_{LRE}}$	-0.1238	-0.1145	-0.1531	-0.1270
	3	$GLRLM_{0_{GLN}}$	-0.1860*	-0.1847*	0.0720	0.0936
	4	$GLRLM_{0_{RLN}}$	0.3958 [§]	0.3773 [§]	0.1435	0.1332
	5	$GLRLM_{0_{LGRE}}$	-0.3378 [‡]	-0.3242 [‡]	-0.0946	-0.0702
	6	$GLRLM_{0_{HGRE}}$	-0.1639	-0.1488	-0.1318	-0.1391
	7	$GLRLM_{45_{SRE}}$	0.4340 [§]	0.4187 [§]	0.0806	0.0758
	8	$GLRLM_{45_{LRE}}$	-0.1233	-0.1141	-0.1386	-0.1143
	9	$GLRLM_{45_{GLN}}$	-0.1769	-0.1802*	0.0711	0.0950
	10	$GLRLM_{45_{RLN}}$	0.4096 [§]	0.3932 [§]	0.0672	0.0660
	11	$GLRLM_{45_{LGRE}}$	-0.4129 [§]	-0.4038 [§]	0.0809	0.1063
	12	$GLRLM_{45_{HGRE}}$	-0.2874 [†]	-0.2750 [†]	-0.0470	-0.0653
	13	$GLRLM_{90_{SRE}}$	0.3140 [‡]	0.3118 [‡]	0.2246	0.2260
	14	$GLRLM_{90_{LRE}}$	-0.1150	-0.1068	-0.1580	-0.1343
	15	$GLRLM_{90_{GLN}}$	-0.2669 [†]	-0.2600 [†]	0.0586	0.0685
	16	$GLRLM_{90_{RLN}}$	0.2735 [†]	0.2705 [†]	0.2126	0.2138
	17	$GLRLM_{90_{LGRE}}$	-0.3723 [§]	-0.3652 [§]	-0.1823	-0.1933
	18	$GLRLM_{90_{HGRE}}$	-0.2618 [†]	-0.2587 [†]	-0.2169	-0.2345
	19	$GLRLM_{135_{SRE}}$	0.4054 [§]	0.3921 [§]	0.2228	0.2107
	20	$GLRLM_{135_{LRE}}$	-0.1241	-0.1151	-0.1612	-0.1356
	21	$GLRLM_{135_{GLN}}$	-0.0835	-0.0877	0.1115	0.1317
	22	$GLRLM_{135_{RLN}}$	0.3886 [§]	0.3746 [§]	0.2083	0.1999
	23	$GLRLM_{135_{LGRE}}$	-0.3254 [‡]	-0.3190 [‡]	-0.0604	-0.0275

Texture feature	Sl. no.	Features extracted	Indian sample population		Swiss sample population	
			sBMD	<i>T</i> -score	sBMD	<i>T</i> -score
	24	$GLRLM_{135_{HG\text{RE}}}$	-0.2468 [†]	-0.2360 [†]	-0.1659	-0.1732
MGM	1	GR_5	-0.4609 [§]	-0.4354 [§]	-0.0249	-0.0240
	2	GR_7	-0.3996 [§]	-0.3750 [§]	0.0184	0.0243
	3	$GSS_{7,3}$	-0.4476 [§]	-0.4221 [§]	-0.0341	-0.0347
	4	$GSS_{9,5}$	-0.4087 [§]	-0.3844 [§]	-0.0007	0.0069
	5	$GSS_{11,7}$	-0.3736 [§]	-0.3526 [§]	0.0166	0.0302
	6	$GSR_{7,3}$	-0.4586 [§]	-0.4322 [§]	-0.0420	-0.0446
	7	$GSR_{9,5}$	-0.4348 [§]	-0.4100 [§]	-0.0165	-0.0113
	8	$GSR_{11,7}$	-0.3975 [§]	-0.3745 [§]	0.0094	0.0201
Laws mask	1	$LAW S_{L5E5_{cont}}$	0.0789	0.0765	-0.0772	-0.0873
	2	$LAW S_{L5E5_{corr}}$	-0.0624	-0.0615	0.1048	0.1277
	3	$LAW S_{L5E5_{hom}}$	0.0420	-0.0368	0.0040	0.0192
	4	$LAW S_{L5E5_{en}}$	-0.0119	-0.0171	0.1296	0.1072
	5	$LAW S_{L5S5_{cont}}$	0.2170*	0.2023*	0.0997	0.0873
	6	$LAW S_{L5S5_{corr}}$	-0.1883*	-0.1776*	-0.0382	-0.0186
	7	$LAW S_{L5S5_{hom}}$	-0.2054*	-0.2015*	0.0273	0.0298
	8	$LAW S_{L5S5_{en}}$	-0.1224	-0.1217	-0.0489	-0.0688
	9	$LAW S_{L5R5_{cont}}$	0.1289	0.1177	0.0047	-0.0007
	10	$LAW S_{L5R5_{corr}}$	-0.2711 [†]	-0.2618 [†]	0.0369	0.0557
	11	$LAW S_{L5R5_{hom}}$	-0.1848*	-0.1824*	-0.0643	-0.0560
	12	$LAW S_{L5R5_{en}}$	-0.2554 [†]	-0.2516 [†]	-0.0880	-0.0988
	13	$LAW S_{L5W5_{cont}}$	0.1868*	0.1875*	0.2268	0.2112
	14	$LAW S_{L5W5_{corr}}$	-0.2595 [†]	-0.2583 [†]	-0.1565	-0.1379
	15	$LAW S_{L5W5_{hom}}$	-0.1158	-0.1153	-0.1060	-0.0921
	16	$LAW S_{L5W5_{en}}$	-0.0841	-0.0938	0.1105	0.1126
	17	$LAW S_{E5E5_{cont}}$	0.2688 [†]	0.2585 [†]	0.0046	-0.0059
	18	$LAW S_{E5E5_{corr}}$	-0.1958*	-0.1945*	-0.0550	-0.0400
	19	$LAW S_{E5E5_{hom}}$	-0.1789*	-0.1855*	0.0253	0.0374
	20	$LAW S_{E5E5_{en}}$	0.0040	-0.0058	-0.0778	-0.0759
	21	$LAW S_{E5S5_{cont}}$	0.3393 [‡]	0.3313 [‡]	0.0492	0.0323
	22	$LAW S_{E5S5_{corr}}$	-0.2929 [†]	-0.2916 [†]	-0.0888	-0.0684
	23	$LAW S_{E5S5_{hom}}$	-0.2040*	-0.2012*	-0.0236	0.0043
	24	$LAW S_{E5S5_{en}}$	0.0378	0.0270	0.0579	0.0468
	25	$LAW S_{E5R5_{cont}}$	0.2509 [†]	0.2491 [†]	0.0418	0.0306

Texture feature	Sl. no.	Features extracted	Indian sample population		Swiss sample population	
			sBMD	<i>T</i> -score	sBMD	<i>T</i> -score
	26	$LAW S_{E5R5_{corr}}$	-0.3318 [‡]	-0.3364 [‡]	-0.0831	-0.0590
	27	$LAW S_{E5R5_{hom}}$	-0.1994*	-0.1953*	-0.0829	-0.0676
	28	$LAW S_{E5R5_{en}}$	-0.2215*	-0.2272*	-0.1334	-0.1366
	29	$LAW S_{E5W5_{cont}}$	0.2343 [†]	0.2195*	0.1520	0.1430
	30	$LAW S_{E5W5_{corr}}$	-0.1565	-0.1514	-0.1263	-0.1112
	31	$LAW S_{E5W5_{hom}}$	-0.0430	-0.0333	0.0075	0.0460
	32	$LAW S_{E5W5_{en}}$	0.0614	0.0558	0.1406	0.1192
	33	$LAW S_{S5S5_{cont}}$	0.3570 [§]	0.3522 [§]	0.0553	0.0375
	34	$LAW S_{S5S5_{corr}}$	-0.3358 [‡]	-0.3364 [‡]	-0.0807	-0.0598
	35	$LAW S_{S5S5_{hom}}$	-0.2819 [†]	-0.2833	-0.0436	-0.0358
	36	$LAW S_{S5S5_{en}}$	-0.0201	-0.0240	-0.2395	-0.2577
	37	$LAW S_{S5R5_{cont}}$	0.2696 [†]	0.2699 [†]	0.0681	0.0531
	38	$LAW S_{S5R5_{corr}}$	-0.3488 [‡]	-0.3570 [‡]	-0.1196	-0.0900
	39	$LAW S_{S5R5_{hom}}$	-0.1891*	-0.1929*	-0.0409	-0.0340
	40	$LAW S_{S5R5_{en}}$	-0.1218	-0.1228	-0.2065	-0.2118
	41	$LAW S_{S5W5_{cont}}$	0.3066 [‡]	0.2906 [†]	0.0900	0.0818
	42	$LAW S_{S5W5_{corr}}$	-0.2647 [†]	-0.2558 [†]	-0.0773	-0.0643
	43	$LAW S_{S5W5_{hom}}$	-0.2434 [†]	-0.2319 [†]	-0.0835	-0.0610
	44	$LAW S_{S5W5_{en}}$	0.1188	0.1109	0.1094	0.1039
	45	$LAW S_{R5R5_{cont}}$	0.0958	0.0954	-0.0307	-0.0328
	46	$LAW S_{R5R5_{corr}}$	-0.2112*	-0.2161*	-0.0048	0.0287
	47	$LAW S_{R5R5_{hom}}$	-0.1347	-0.1366	-0.0276	-0.0345
	48	$LAW S_{R5R5_{en}}$	-0.0914	-0.0813	-0.2738	-0.2672
	49	$LAW S_{R5W5_{cont}}$	0.1890*	0.1828*	0.0386	0.0336
	50	$LAW S_{R5W5_{corr}}$	-0.2848 [†]	-0.2836 [†]	-0.0698	-0.0477
	51	$LAW S_{R5W5_{hom}}$	-0.1789*	-0.1761	-0.0895	-0.0721
	52	$LAW S_{R5W5_{en}}$	-0.0467	-0.0501	-0.1963	-0.1895
	53	$LAW S_{W5W5_{cont}}$	0.1555	0.1381	0.2071	0.2064
	54	$LAW S_{W5W5_{corr}}$	-0.0600	-0.0505	-0.1430	-0.1414
	55	$LAW S_{W5W5_{hom}}$	-0.2050*	-0.1950*	-0.0767	-0.0555
	56	$LAW S_{W5W5_{en}}$	-0.0067	-0.0072	-0.0306	-0.0537
LBP	1	LBP_{mean}	0.2294 [†]	0.2009*	0.1491	0.1308
	2	LBP_{var}	0.2248 [†]	0.1960*	0.1494	0.1324
	3	LBP_{skew}	-0.2533 [†]	-0.2218*	-0.1650	-0.1444

Texture feature	Sl. no.	Features extracted	Indian sample population		Swiss sample population	
			sBMD	T-score	sBMD	T-score
	4	$LLBP_{kurt}$	-0.2660†	-0.2325†	-0.1727	-0.1524
	5	$LLBP_{en}$	-0.2500†	-0.2201*	-0.1582	-0.1373
	6	$LLBP_{mean}$	-0.2769†	-0.2579†	-0.2406	-0.2476
	7	$LLBP_{var}$	0.4510§	0.4434§	0.2957*	0.2983*
	8	$LLBP_{skew}$	0.1750*	0.1592	0.2383	0.2593*
	9	$LLBP_{kurt}$	-0.4800§	-0.4667§	-0.2596*	-0.2652*
	10	$LLBP_{en}$	-0.4773§	-0.4577§	-0.2576*	-0.2713*
	11	$LLBP_{ent}$	0.4801§	0.4597§	0.2472	0.2587*
	12	$LLBP_{Hor_{mean}}$	-0.4943§	-0.4743§	-0.0352	0.0020
	13	$LLBP_{Hor_{var}}$	0.0552	0.0623	-0.1577	-0.1931
	14	$LLBP_{Hor_{skew}}$	0.4666§	0.4475§	0.0036	-0.0376
	15	$LLBP_{Hor_{kurt}}$	-0.1841*	-0.1818*	0.1417	0.1924
	16	$LLBP_{Hor_{en}}$	-0.4311§	-0.4047§	-0.1353	-0.1393
	17	$LLBP_{Hor_{ent}}$	0.4293§	0.4025§	0.1372	0.1418
	18	$LLBP_{Vert_{mean}}$	-0.3528§	-0.3380§	-0.2395	-0.2559*
	19	$LLBP_{Vert_{var}}$	0.1799*	0.1907*	0.2587*	0.2779*
	20	$LLBP_{Vert_{skew}}$	0.3629§	0.3516§	0.2514*	0.2711*
	21	$LLBP_{Vert_{kurt}}$	-0.3274‡	-0.3254‡	-0.3239†	-0.3430†
	22	$LLBP_{Vert_{en}}$	-0.3163‡	-0.2978‡	-0.1118	-0.1268
	23	$LLBP_{Vert_{ent}}$	0.2949‡	0.2757†	0.0952	0.1081
Gabor	1	$Gabor_{4,1}$	-0.4469§	-0.4430§	-0.0500	-0.0549
	2	$Gabor_{4,2}$	-0.4048§	-0.4018§	-0.0748	-0.0753
	3	$Gabor_{4,3}$	-0.2738†	-0.2758†	0.0821	0.0671
	4	$Gabor_{4,4}$	-0.1523	-0.1457	0.0538	0.0196
	5	$Gabor_{4,5}$	-0.3256‡	-0.3175‡	0.0471	0.0138
	6	$Gabor_{4,6}$	-0.4269§	-0.4259§	0.0701	0.0575

*p<0.05, † p<0.01, ‡ p<0.001, § p<0.0001

4.5 CONCLUSION

In this chapter, the texture analysis of trabecular bone of distal radius using hand and wrist radiographs was discussed. An automated segmentation approach to locate and

segment the distal radius ROI was proposed. The proposed method was able to accurately extract the distal radius ROI in 93.5% cases of Indian sample data and 83% cases in Swiss sample data. Texture analysis methods such as first order histogram features, GLCM, GLRLM, MGM, Laws's masks, LBP and its variants, and Gabor filter, were used to extract texture features from the distal radius ROI. The ability of these texture features to distinctly characterize trabecular bone in healthy and low bone mass subjects were analyzed using statistical tests. In the Indian sample population, majority of the extracted texture features are significant with *t*-test and well-correlated with DXA-BMD of lumbar spine using Pearson correlation. The Swiss sample data did not show significant statistical results for the extracted texture features. This could be due to less number of samples in the healthy group. As discussed in Section 2.7, the bone characteristics of people varies with ethnicity. Hence, we can expect differences in the bone texture features of the sample data from the Indian and Swiss population. The trabecular bone texture features can thus be efficiently used to train classifier models to develop the proposed prescreening tool.

CHAPTER 5

CLASSIFICATION USING CORTICAL AND TRABECULAR BONE FEATURES

5.1 INTRODUCTION

Recent research on diagnosis of osteoporosis has emphasized the need for low cost diagnostic techniques in order to facilitate timely and affordable screening of the low income population. In this thesis, we develop a prescreening tool to detect subjects with low bone mass using radiographic image of the hand and wrist. The cortical radiogrammetric features measured in Chapter 3 and the trabecular texture features extracted in Chapter 4 are combined together to train different classifiers and their performance is evaluated. Figure 5.1 shows the block diagram of the proposed methodology. The combination of cortical and trabecular bone features is investigated for an improved diagnosis of osteoporosis.

The extracted features are used to train four types of classifiers, namely ANN, LR, SVM and KNN classifiers, in order to classify the data as healthy (H) or low bone mass (LBM). ANN classifier is a multi-layered network having an input layer, one or more hidden layers and an output layer. The extracted features are fed as input to the ANN

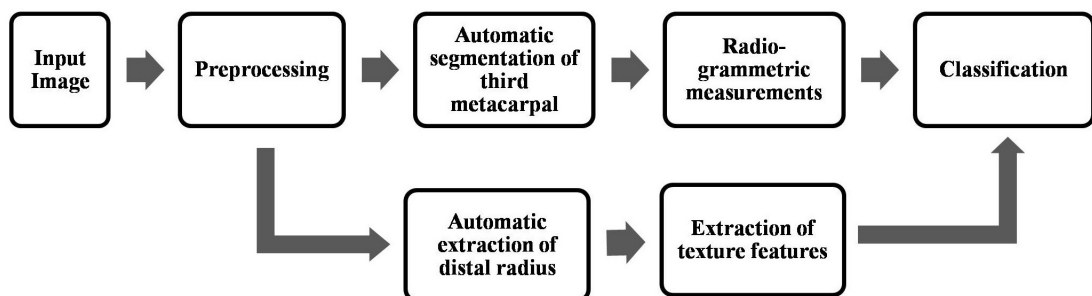


Figure 5.1: Block diagram of the proposed methodology

and the output nodes classify the samples to H and LBM classes. In this work, ANN is trained using scaled conjugate gradient method. The performance of the training and back propagation is evaluated using mean squared error. Logistic regression classifier determines the relation between the input and output variables by estimating the probability using logistic function. SVM builds a hyper plane in a higher dimensional feature space in order to classify the H and LBM groups. SVM with a Gaussian kernel of scale 3.5 is used. Gaussian kernel gives a more complex boundary than a hyperplane and helps in better classification of data samples that are not linearly separable. KNN classifies samples by a majority vote of its neighbors with the sample being assigned to the class most common among its k nearest neighbors. Weighted KNN with 10 nearest neighbors, a Euclidean distance metric and a squared inverse distance weight is used. While ANN shows a good accuracy with a large training dataset, the LR, SVM and KNN classifiers can be efficiently trained with lesser data samples.

In this work, data from Indian sample population (sample size of 138) and Swiss sample population (sample size of 65) are used. We first investigate the significant features of the Indian sample data and develop classifier models for the Indian population, as shown in Figure 5.2 and discussed in Section 5.2. We then select the significant features common to both Indian and Swiss sample data and train individual and combined classifiers for both the population, as shown in Figure 5.3 and Figure 5.4, and discussed in Section 5.3. The performance of the trained classifiers are evaluated using performance metrics.

5.2 CLASSIFICATION USING INDIAN SAMPLE DATA

The Indian sample data consists of 138 images of the hand and wrist radiographs. The proposed segmentation approach is applied on the Indian dataset. The automatic extraction of the third metacarpal bone shaft failed for 11% of the cases and of the distal radius ROI failed for 6.5% of the cases. The poorly segmented images are removed and

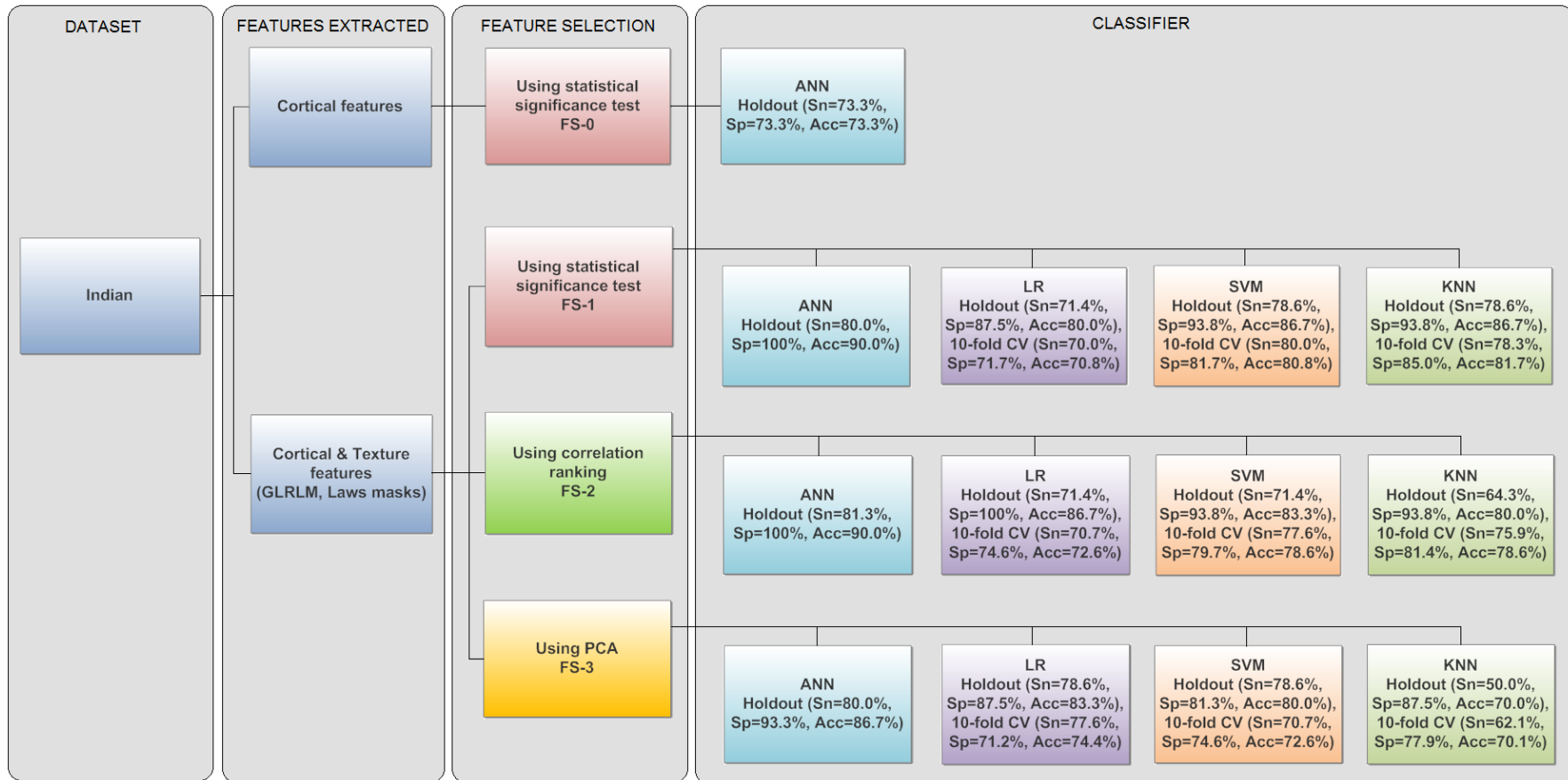


Figure 5.2: Flowchart summarizing classifiers trained with Indian sample data

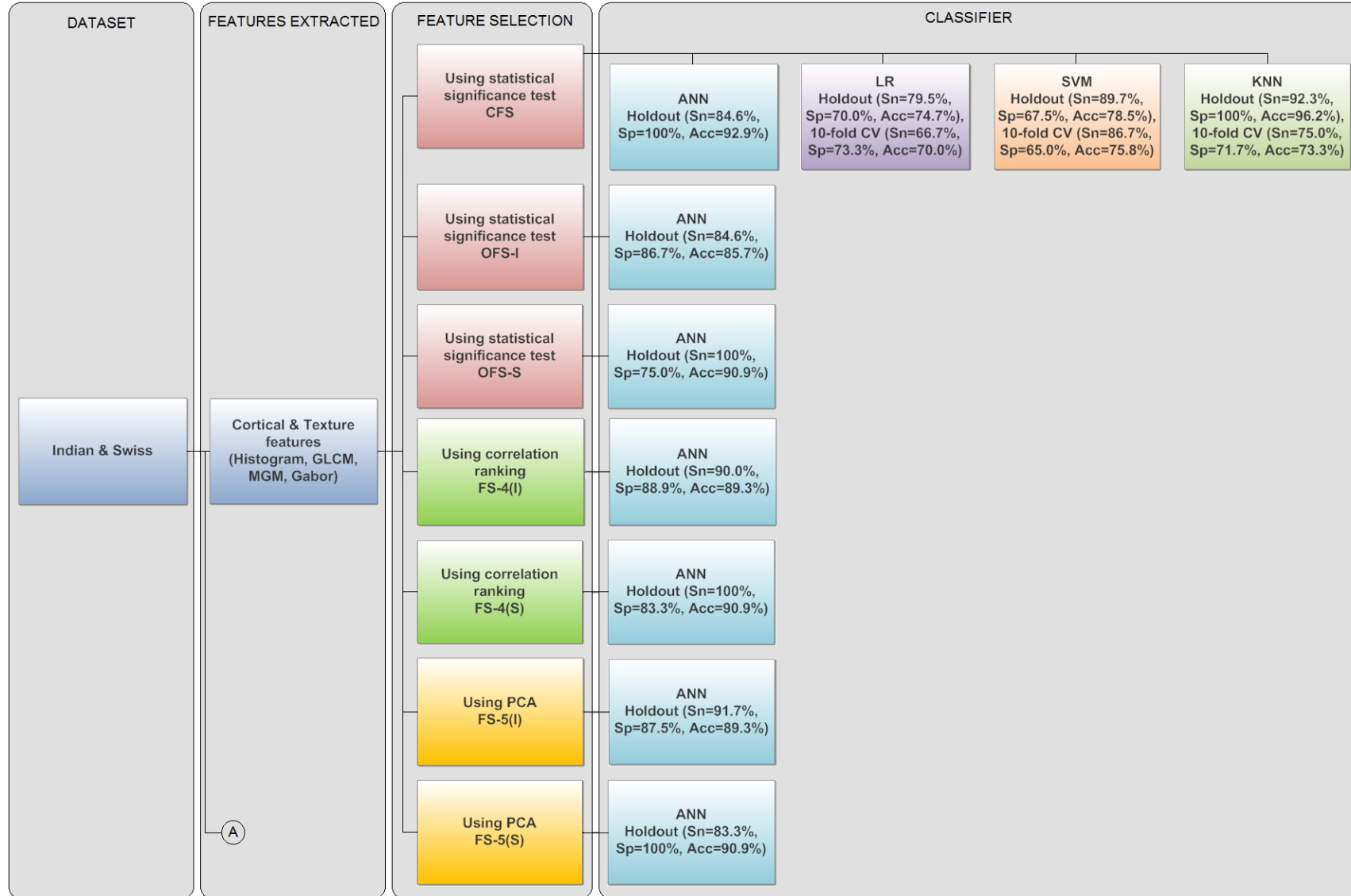


Figure 5.3: Flowchart summarizing classifiers trained with Indian and Swiss sample data (part 1)

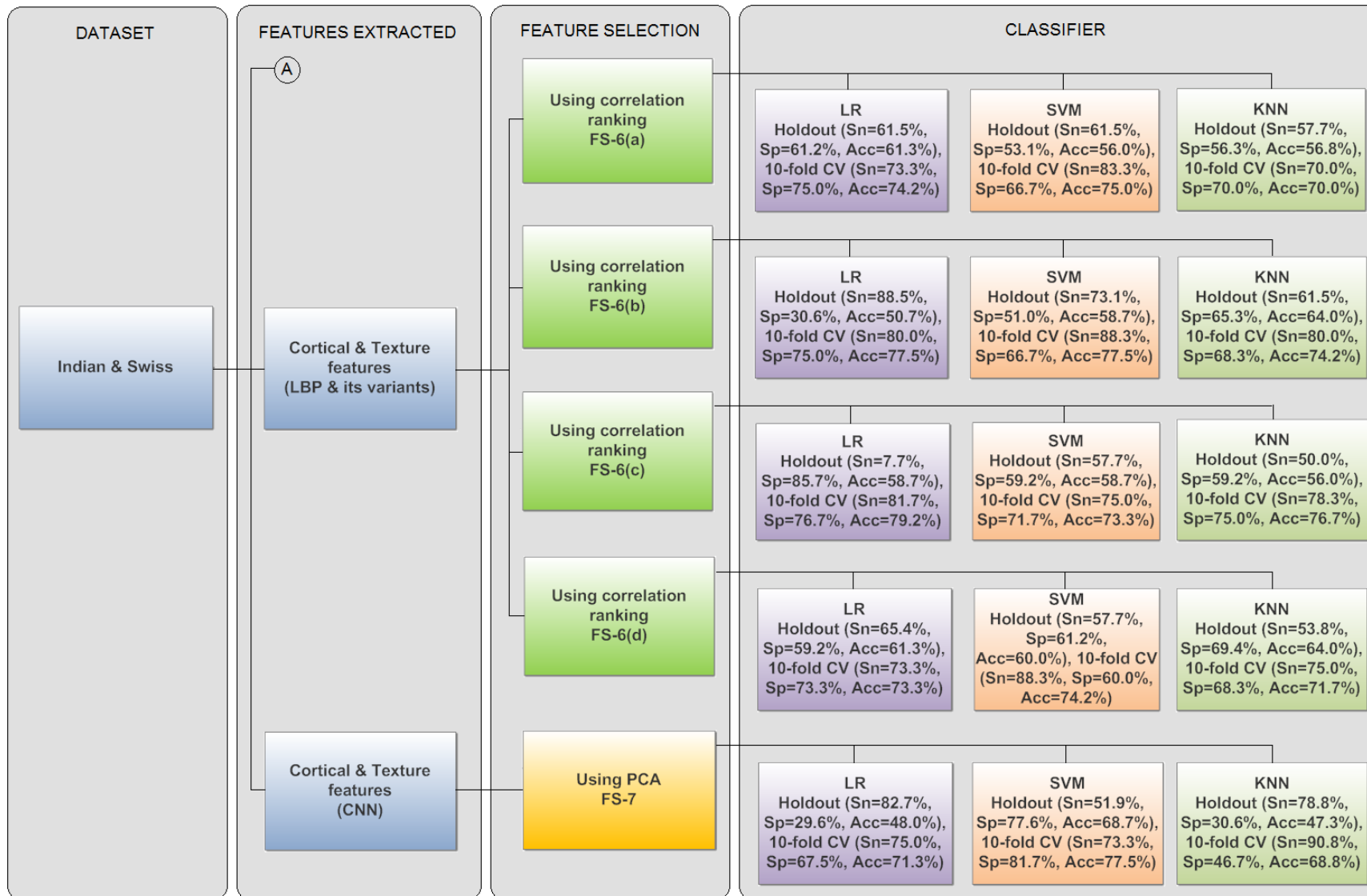


Figure 5.4: Flowchart summarizing classifiers trained with Indian and Swiss sample data (part 2)

the remaining 117 cases is taken as the study group for feature extraction and classification. Among the 117 images, 57 belonged to healthy (H) group and 60 belonged to LBM group. This study group is divided into a training and validation set of 87 images (42 H and 45 LBM) and test set of 30 images (15 H and 15 LBM). The features of the training set is used for feature selection and training of classifiers. The test set is used for evaluating the performance of the trained classifiers.

5.2.1 Feature selection

Using statistical significance test:

In this section, cortical features (3 features) obtained using cortical radiogrammetry and texture features (80 features) obtained using GLRLM and Laws' masks are used. The significant features are selected for training the classifiers. Feature selection is necessary to remove insignificant features and to reduce the dimensionality of the feature set. Statistical analysis is used as the feature selection method. The input features used for training classifiers are selected based on the results of the independent sample *t*-test on the training data. The study group with 117 images is divided into a training set of 73 images, validation set of 14 images and unseen test set of 30 images. The results of the *t*-test on the cortical and texture features of the training set are listed in Table 5.1. Only those features with statistical significance of $p < 0.05$ are included in the table. All the cortical features are significant with $p < 0.05$ and 3 cortical features are significant with $p < 0.01$. *CCT* shows the highest significance with $p < 0.0001$. Among the 80 trabecular features, 38 trabecular features are significant with $p < 0.05$ and 12 trabecular features are significant with $p < 0.01$.

Pearson correlation is used to test the correlation of the significant cortical and trabecular features, that are highly significant with *t*-test ($p < 0.01$), with DXA-BMD of the lumbar spine (DXA-LS). Fifteen cortical and trabecular features are highly significant with *t*-test ($p < 0.01$). Table 5.2 shows the results of the Pearson correlation analysis of the 15 highly significant features with DXA-LS tested on the whole study group. All the 15 highly significant features of *t*-test are also significantly correlated with DXA-LS

Table 5.1: Statistical significance results of the independent sample t -test of the significant features ($p < 0.05$) in the training set

Sl. no.	Significant Features	Healthy group ($\mu \pm \sigma$)	LBM group ($\mu \pm \sigma$)	Significance ($p - value$)
1	$CCT(mm)$	4.5 \pm 0.6	3.8 \pm 0.5	2.6744e-06 [§]
2	$CA(mm^2)$	42.9 \pm 7.0	35.8 \pm 6.5	0.0001 [‡]
3	BNI	54.5 \pm 8.1	48.9 \pm 6.8	0.0046 [†]
4	$GLRLM_{0_{SRE}}$	0.22 \pm 0.01	0.21 \pm 0.02	0.0013 [†]
5	$GLRLM_{0_{GLN}}$	4964.50 \pm 97.97	5.03 \pm 108.29	0.0042 [†]
6	$GLRLM_{0_{RLN}}$	379.78 \pm 51.36	347.46 \pm 49.56	0.0038 [†]
7	$GLRLM_{0_{LGRE}}$	0.84 \pm 0.01	0.85 \pm 0.01	0.0001 [†]
8	$GLRLM_{45_{SRE}}$	0.25 \pm 0.01	0.24 \pm 0.02	0.0059 [†]
9	$GLRLM_{45_{GLN}}$	5087.00 \pm 106.48	5136.40 \pm 98.85	0.0285
10	$GLRLM_{45_{RLN}}$	473.41 \pm 49.74	445.63 \pm 56.31	0.0175
11	$GLRLM_{45_{LGRE}}$	0.84 \pm 0.01	0.84 \pm 0.01	0.0011 [†]
12	$GLRLM_{90_{GLN}}$	5098.50 \pm 101.47	5156.60 \pm 109.51	0.0126
13	$GLRLM_{90_{LGRE}}$	0.87 \pm 0.01	0.88 \pm 0.01	0.0145
14	$GLRLM_{135_{SRE}}$	0.25 \pm 0.02	0.24 \pm 0.02	0.0008 [‡]
15	$GLRLM_{135_{RLN}}$	496.11 \pm 66.56	452.38 \pm 60.29	0.0019 [†]
16	$GLRLM_{135_{LGRE}}$	0.84 \pm 0.00	0.84 \pm 0.01	0.0004 [‡]
17	$LAWS_{L5E5_{cont}}$	1906.10 \pm 34.10	1893.00 \pm 35.80	0.0360
18	$LAWS_{L5E5_{corr}}$	-0.00 \pm 0.02	0.00 \pm 0.02	0.0350
19	$LAWS_{L5S5_{cont}}$	1949.80 \pm 41.50	1923.90 \pm 44.10	0.0026 [†]
20	$LAWS_{L5S5_{corr}}$	0.00 \pm 0.02	0.01 \pm 0.02	0.0083 [†]
21	$LAWS_{L5S5_{hom}}$	0.07 \pm 0.00	0.07 \pm 0.00	0.0012 [†]
22	$LAWS_{L5R5_{corr}}$	0.00 \pm 0.02	0.02 \pm 0.02	0.0410
23	$LAWS_{L5W5_{cont}}$	2128.00 \pm 135.40	2057.80 \pm 145.80	0.0373
24	$LAWS_{L5W5_{corr}}$	0.00 \pm 0.05	0.04 \pm 0.06	0.0067 [†]
25	$LAWS_{E5E5_{cont}}$	1887.10 \pm 69.80	1845.40 \pm 70.10	0.0072 [†]
26	$LAWS_{E5E5_{corr}}$	0.01 \pm 0.03	0.03 \pm 0.03	0.0424
27	$LAWS_{E5S5_{cont}}$	1923.90 \pm 63.00	1879.30 \pm 70.10	0.0029 [†]
28	$LAWS_{E5S5_{corr}}$	0.01 \pm 0.03	0.02 \pm 0.03	0.0079 [†]
29	$LAWS_{E5R5_{corr}}$	-0.00 \pm 0.03	0.01 \pm 0.03	0.0259
30	$LAWS_{E5W5_{cont}}$	1907.30 \pm 82.90	1859.30 \pm 67.70	0.0055 [†]
31	$LAWS_{E5W5_{corr}}$	0.01 \pm 0.03	0.02 \pm 0.03	0.0351
32	$LAWS_{S5S5_{cont}}$	1964.00 \pm 65.60	1916.80 \pm 78.10	0.0032 [†]
33	$LAWS_{S5S5_{corr}}$	0.00 \pm 0.03	0.02 \pm 0.03	0.0036 [†]
34	$LAWS_{S5S5_{hom}}$	0.07 \pm 0.00	0.07 \pm 0.00	0.0199
35	$LAWS_{S5R5_{corr}}$	-0.01 \pm 0.03	0.01 \pm 0.03	0.0147
36	$LAWS_{S5W5_{cont}}$	1865.10 \pm 69.60	1812.30 \pm 66.40	0.0005 [‡]
37	$LAWS_{S5W5_{corr}}$	0.01 \pm 0.03	0.03 \pm 0.03	0.0006 [‡]
38	$LAWS_{S5W5_{hom}}$	0.07 \pm 0.00	0.07 \pm 0.00	0.0096 [†]
39	$LAWS_{R5W5_{corr}}$	0.00 \pm 0.03	0.02 \pm 0.03	0.0276
40	$LAWS_{W5W5_{cont}}$	1878.90 \pm 109.70	1818.60 \pm 80.00	0.0055 [†]
41	$LAWS_{W5W5_{hom}}$	0.07 \pm 0.00	0.07 \pm 0.00	0.0301

† $p < 0.01$, ‡ $p < 0.001$, § $p < 0.0001$

$GLRLM_{x_y}$ = 'y' feature of GLRLM measured along 'x' direction to the horizontal

$LAWS_{u_v}$ = 'v' feature measured from Laws' texture image 'u'

Table 5.2: Correlation of significant features of independent sample t -test ($p < 0.01$) with DXA-BMD of lumbar spine using Pearson correlation analysis

Sl. no.	Significant Features ($p < 0.01$)	Correlation (r)	Significance ($p - value$)
1	<i>CCT</i>	0.5632	3.8314E-11 [§]
2	<i>CA</i>	0.4839	3.2371E-08 [§]
3	<i>BNI</i>	0.4002	7.8116E-06 [§]
4	<i>GLRLM</i> _{0SRE}	0.3928	1.1840E-05 [§]
5	<i>GLRLM</i> _{0RLN}	0.3716	3.7151E-05 [§]
6	<i>GLRLM</i> _{0LGRE}	-0.3273	0.0003 [‡]
7	<i>GLRLM</i> _{45SRE}	0.4070	5.2590E-06 [§]
8	<i>GLRLM</i> _{45LGRE}	-0.4005	7.6494E-06 [§]
9	<i>GLRLM</i> _{135SRE}	0.3823	2.1009E-05 [§]
10	<i>GLRLM</i> _{135RLN}	0.3657	5.0337E-05 [§]
11	<i>GLRLM</i> _{135LGRE}	-0.3078	0.0007 [‡]
12	<i>LAWSE</i> _{5S5cont}	0.3368	0.0002 [‡]
13	<i>LAWSE</i> _{5S5corr}	-0.3013	0.0009 [‡]
14	<i>LAWSS</i> _{5S5cont}	0.3561	8.1551E-05 [§]
15	<i>LAWSS</i> _{5S5corr}	-0.3413	0.0001 [‡]

† $p < 0.01$, ‡ $p < 0.001$, § $p < 0.0001$

with $p < 0.001$. Cortical radiogrammetric features are more correlated with DXA-LS as compared to trabecular texture features. *CCT* is the most significantly correlated feature with correlation coefficient of $r = 0.5632$ and $p < 0.0001$.

Among the significant 15 features, two features namely, contrast and correlation features of the Laws' texture image *LAWSS*_{5S5} are discarded as they are highly correlated with contrast and correlation of Laws' texture image *LAWSE*_{5S5}. The remaining 13 features, namely *CCT*, *CA*, *BNI*, *GLRLM*_{0SRE}, *GLRLM*_{0RLN}, *GLRLM*_{0LGRE}, *GLRLM*_{45SRE}, *GLRLM*_{45LGRE}, *GLRLM*_{135SRE}, *GLRLM*_{135RLN}, *GLRLM*_{135LGRE}, *LAWSE*_{5S5cont} and *LAWSE*_{5S5corr}, are used as the input feature vector, denoted as FS-1, for training the classifiers.

Using correlation ranking:

In this method, the extracted cortical and texture features of the training set are ranked based on their correlation with DXA-BMD of lumbar spine using Pearson correlation test. Pearson correlation of the extracted features with DXA-BMD gives correlation values that range between +1 and -1. Positive correlation values indicate that the respective features are positively correlated with DXA-BMD and negative corre-

Table 5.3: Correlation results of the 10 highest ranked cortical and texture features in the training set

Sl. no.	Features (FS-2)	Correlation (r)	Significance ($p - value$)
1	<i>CCT</i>	0.4634	3.30E-06 [§]
2	<i>CA</i>	0.4610	3.76E-06 [§]
3	<i>LAWS_{S5W5_{hom}}</i>	-0.3914	0.0001 [‡]
4	<i>LAWS_{S5S5_{hom}}</i>	-0.3809	0.0002 [‡]
5	<i>GLRLM_{0_{LGRE}}</i>	-0.3718	0.0003 [‡]
6	<i>LAWS_{L5S5_{hom}}</i>	-0.3608	0.0004 [‡]
7	<i>GLRLM_{135_{SRE}}</i>	0.3573	0.0005 [‡]
8	<i>GLRLM_{135_{LGRE}}</i>	-0.3522	0.0006 [‡]
9	<i>LAWS_{S5W5_{corr}}</i>	-0.3498	0.0006 [‡]
10	<i>GLRLM_{45_{LGRE}}</i>	-0.3426	0.0008 [‡]

† $p < 0.01$, ‡ $p < 0.001$, § $p < 0.0001$

lation values indicate that the features are negatively correlated with DXA-BMD. The highest ranked 10 features are selected as the second feature set to train the classifiers, and is denoted as FS-2. Among the 83 features extracted using cortical radiogrammetry, GLRLM and Laws' masks, the highest ranked 10 features are shown in Table 5.3.

Using PCA:

Eighty three features are extracted using cortical radiogrammetry (*CCT*, *CA*, *BNI*), GLRLM and Laws's masks. The dimensionality of the feature space is reduced by using PCA. PCA helps to capture the variations in the feature space with minimal number of principal components. Feature selection is done by selecting the principal components that captures 95% variance in the feature space of the training set. The 23 principal components thus obtained are selected as the third feature set, denoted as FS-3. Figure 5.5 shows the variance in the feature space explained by the first 10 principal components.

5.2.2 Classifier

Firstly, ANN is used for the classification. For feature set FS-1, ANN classifier is constructed as a three layer network having one input layer with 13 nodes, one hidden layer with 8 nodes and an output layer with 2 nodes. The number of hidden nodes is chosen by trial and error such that the classification accuracy obtained is maximized.

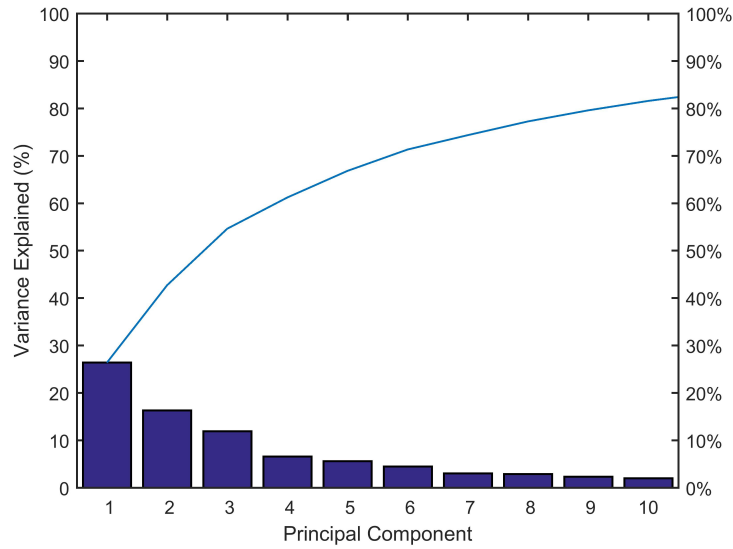


Figure 5.5: Variance explained by first 10 of the 23 principal components of PCA in the feature set

Table 5.4: Performance of the trained ANN classifiers using holdout validation

Features	Feature set	Partition	TP	FP	TN	FN	Sn	Sp	PPV	NPV	Acc	F1-score
Cortical	FS-0	Training	34	8	37	8	80.9	82.2	80.9	82.2	81.6	80.9
		Testing	11	4	11	4	73.3	73.3	73.3	73.3	73.3	73.3
		Overall	45	12	48	12	78.9	80.0	78.9	80.0	79.5	78.9
Cortical and trabecular	FS-1	Training	40	3	42	2	95.2	93.3	93.0	95.5	94.3	94.1
		Test	12	0	15	3	80.0	100	100	83.3	90.0	88.9
		Overall	52	3	57	5	91.2	95.0	94.5	91.9	93.2	92.9
Cortical and trabecular	FS-2	Training	34	9	36	8	80.9	80.0	79.1	81.8	80.5	80.0
		Test	13	0	14	3	81.3	100	100	82.4	90.0	89.7
		Overall	47	9	50	11	81.0	84.7	83.9	81.9	82.9	82.5
Cortical and trabecular	FS-3	Training	40	5	39	3	93.0	88.6	88.9	92.9	90.8	90.9
		Test	12	1	14	3	80.0	93.3	92.3	82.4	86.7	85.7
		Overall	52	6	53	6	89.7	89.8	89.7	89.8	89.7	89.7

The input to the ANN classifier is the feature set FS-1 of the training set. The training set is normalized before classification. The output nodes correspond to H and LBM classes. Table 5.4 shows the performance metrics of the trained classifier, namely sensitivity (Sn), specificity (Sp), Positive Predictive Value (PPV), Negative Predictive Value (NPV), Accuracy (Acc) and F1-score. The trained ANN classifier shows a training accuracy of 94.3% and test accuracy of 90.0%. The sensitivity and specificity measures of the test data are 80.0% and 100% respectively.

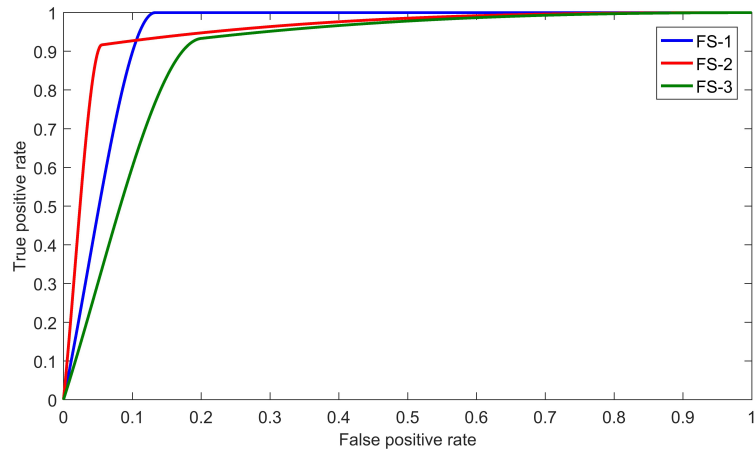


Figure 5.6: ROC curves for the ANN classifiers trained with FS-1 (AUC=0.9459), FS-2 (AUC=0.9534) and FS-3 (AUC=0.8954)

For FS-2 and FS-3, ANN classifiers are constructed with 8 hidden nodes and 10 hidden nodes, respectively. The accuracy of the train data and test data using FS-2 shows 80.5% and 90.0%. ANN classifier trained on FS-3 shows training accuracy of 90.8% and test accuracy of 86.7%. Thus, the features selected using *t*-test analysis (FS-1) shows the best performance over feature selection using correlation ranking (FS-2) and PCA (FS-3). ROC curves for the ANN classifiers trained with feature sets FS-1, FS-2 and FS-3 are shown in Figure 5.6. AUC of the ANN classification on test data using the feature sets FS-1, FS-2 and FS-3 are 0.9459, 0.9534 and 0.8954, respectively.

In order to show the significance of the inclusion of trabecular features with cortical features to improve the classification accuracy, an ANN classifier is trained using just the three cortical features only, denoted as FS-0. This ANN classifier is designed with 3 input nodes, 3 hidden nodes and 2 output nodes. The trained ANN classifier using the cortical features achieves a training and validation accuracy of 81.6% and test accuracy of 73.3%. The sensitivity and specificity of the test data are both 73.3%. Thus, as shown in Table 5.4, the combination of cortical and trabecular features helps to improve the performance of the classifier.

Other simple classifiers such as LR, SVM and KNN classifiers are also trained and tested on the Indian sample population. SVM with a Gaussian kernel of scale 3.5 is used. Weighted KNN with 10 nearest neighbors, a Euclidean distance metric and a

Table 5.5: Performance metrics of LR, SVM and KNN classifiers using holdout validation for combined cortical and texture (GLRLM and Laws’s mask) features

Feature set	Classifier	TP	FP	TN	FN	Sn	Sp	PPV	NPV	Acc	F1-score
FS-1	LR	10	2	14	4	71.4	87.5	83.3	77.8	80.0	76.9
	SVM	11	1	15	3	78.6	93.8	91.7	83.3	86.7	84.6
	KNN	11	1	15	3	78.6	93.8	91.7	83.3	86.7	84.6
FS-2	LR	10	0	16	4	71.4	100	100	80.0	86.7	83.3
	SVM	10	1	15	4	71.4	93.8	90.9	78.9	83.3	80.0
	KNN	9	1	15	5	64.3	93.8	90.0	75.0	80.0	75.0
FS-3	LR	11	2	14	3	78.6	87.5	84.6	82.4	83.3	81.5
	SVM	11	3	13	3	78.6	81.3	78.6	81.3	80.0	78.6
	KNN	7	2	14	7	50.0	87.5	77.8	66.7	70.0	60.9

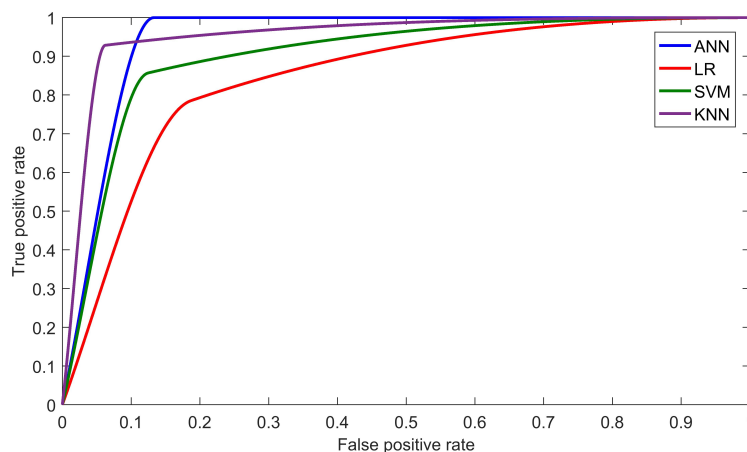


Figure 5.7: ROC curves for the classifiers trained with FS-1: AUC of ANN=0.9459, AUC of LR=0.8452, AUC of SVM=0.9023 and AUC of KNN=0.9537

squared inverse distance weight is used. Table 5.5 shows the performance of the classifiers using holdout validation. The best test results are obtained with SVM and KNN classifiers trained on feature set obtained using t -test, FS-1, with accuracy of 86.7%, sensitivity of 78.6% and specificity of 93.8%. The best test results of classifiers trained on FS-2 is LR with accuracy of 86.7% and those trained on FS-3 is LR with 83.3%. For all the feature sets, ANN classifiers show the best performance on test data using holdout validation. ROC curves of the ANN, LR, SVM and KNN classifiers trained with the feature sets, FS-1, FS-2 and FS-3, are shown in Figures 5.7,5.8 and 5.9.

Due to limited samples in the dataset, performance of LR, SVM and KNN classifiers trained using a 10-fold cross validation are analyzed. In k -fold cross validation, the

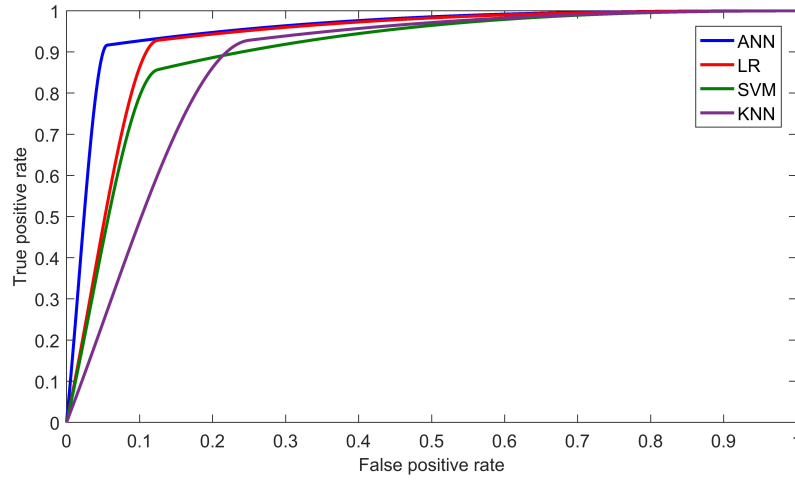


Figure 5.8: ROC curves for the classifiers trained with FS-2: AUC of ANN=0.9534, AUC of LR=0.9260, AUC of SVM=0.9023 and AUC of KNN=0.8725

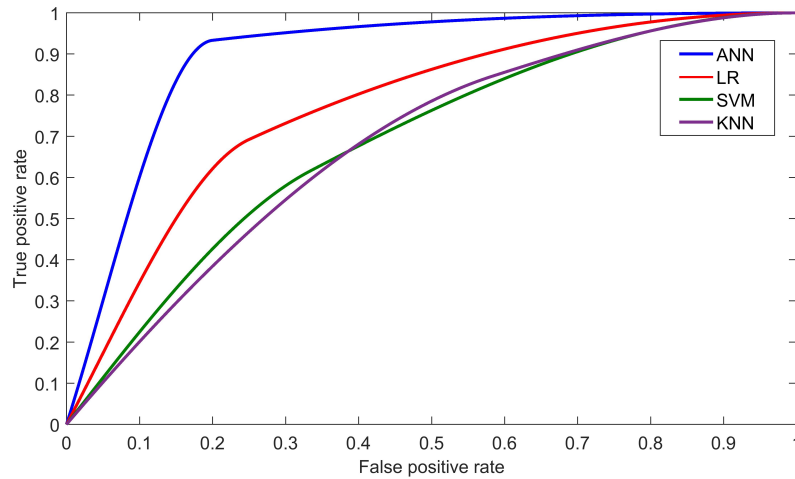


Figure 5.9: ROC curves for the classifiers trained with FS-3: AUC of ANN=0.8954, AUC of LR=0.7726, AUC of SVM=0.6880 and AUC of KNN=0.6825

total images are divided into k distinct sets of equal number of images and k iterations of training and validation is performed. For each iteration, $k - 1$ image sets are used for training the classifier and the remaining 1 image set is used as the test data to evaluate the trained classifier. This is repeated for k iterations with each image set being used as the test data at least once. The evaluation metrics of each of the test data over the k iterations are averaged to obtain the cross-validation metrics. Table 5.6 shows the results of the 10-fold cross validation using the feature sets FS-1, FS-2 and FS-3. Weighted KNN trained on FS-1 shows the best cross-validation accuracy of 81.7%. Ten-fold cross

Table 5.6: Performance metrics of 10 fold cross validation on the whole data using LR, SVM and KNN classifiers trained with cortical and texture (GLRLM and Laws's mask) features

Feature set	Classifier	TP	FP	TN	FN	Sn	Sp	PPV	NPV	Acc	F1-score
FS-1	LR	42	17	43	18	70.0	71.7	71.2	70.5	70.8	70.6
	SVM	48	11	49	12	80.0	81.7	81.4	80.3	80.8	80.7
	KNN	47	9	51	13	78.3	85.0	83.9	79.7	81.7	81.0
FS-2	LR	41	15	44	17	70.7	74.6	73.2	72.1	72.6	71.9
	SVM	45	12	47	13	77.6	79.7	78.9	78.3	78.6	78.3
	KNN	44	11	48	14	75.9	81.4	80.0	77.4	78.6	77.9
FS-3	LR	45	17	42	13	77.6	71.2	72.6	76.4	74.4	75.0
	SVM	41	15	44	17	70.7	74.6	73.2	72.1	72.6	71.9
	KNN	36	13	46	22	62.1	77.9	73.5	67.6	70.1	67.3

validation using LR and SVM achieves accuracy of 70.8% and 80.8%, respectively. Classifiers trained on FS-2 and FS-3 achieves a maximum cross validation accuracy of 78.6% and 74.4%, respectively.

5.2.3 Regression analysis

A backward linear regression analysis is done to combine the significant cortical and trabecular features of the feature set FS-1. The correlation of the linear combination of the features with DXA-LS is studied. The regression equation is

$$BMD = -0.017 + 0.007CA + 0.009BNI + 0.001GLRLM_{135_{RLN}} - 1.091LAWS_{E5S5_{corr}} \quad (5.1)$$

Table 5.7 shows the predictor variables of the linear regression model and the significance and collinearity statistics. The problem of multicollinearity is alleviated, as observed in the Variance Inflation Factor (VIF) values of all the predictor variables. The pairwise correlation analysis, given in Table 5.8, shows low correlation between the predictor variables of the linear regression model.

The regression model shows a highly significant correlation of $r = 0.671$ ($p < 0.001$) with DXA-LS using Pearson correlation analysis. This is higher than the correlation of DXR-BMD with DXA-LS, which is reported to be $r = 0.62$ (Rosholm *et al.* 2001). Thus

the multivariate analysis using backward linear regression shows that the combination of cortical and trabecular features helps to improve the diagnosis of osteoporosis.

5.3 CLASSIFICATION USING INDIAN AND SWISS SAMPLE DATA

In the previous section, we discussed the training of classifiers using the Indian dataset using independent sample t -test, correlation analysis and PCA. In this section, the features significant to both Indian and Swiss dataset are investigated and classifiers are trained for the detection of low bone mass across the two different sample population.

The proposed segmentation approach detects the third metacarpal bone shaft in 89.9% images of Indian dataset and 78% images of Swiss dataset and automatically segments the distal radius ROI in 93.5% and 83% images of Indian and Swiss dataset, respectively. The ROIs from the poorly segmented images is semi-automatically segmented by manual selection of the third metacarpal centroid and DRUJ line, followed by automatic segmentation of third metacarpal bone shaft and/or distal radius ROI. This is

Table 5.7: Summary of the linear regression model

Model	Coefficients	p-value	95% confidence interval		Collinearity statistics	
			Lower bound	Upper bound	Tolerance	VIF
(Constant)	-0.017	0.902	-0.291	0.257		
CA	0.007	0.001 [†]	0.003	0.011	0.739	1.353
BNI	0.009	0.000 [‡]	0.005	0.012	0.914	1.094
$GLRLM_{135_{RLN}}$	0.001	0.002 [†]	0.000	0.001	0.744	1.344
$LAWSE_{5S5_{corr}}$	-1.091	0.011 [*]	-1.931	-0.252	0.960	1.042

* $p < 0.05$, [†] $p < 0.01$, [‡] $p < 0.001$

Table 5.8: Pairwise correlation between predictors of the linear regression model

Parameters	CA	BNI	$GLRLM_{135_{RLN}}$	$LAWSE_{5S5_{corr}}$
CA	1.000			
BNI	0.192 [*]	1.000		
$GLRLM_{135_{RLN}}$	0.451 [‡]	-0.100	1.000	
$LAWSE_{5S5_{corr}}$	-0.130	-0.069	-0.177 [*]	1.000

* $p < 0.05$, [†] $p < 0.01$, [‡] $p < 0.001$

done so as to include the whole dataset for the classification. Four images of the Indian dataset fails with semi-automated segmentation and are discarded from further analysis. Hence, the study group considered in this section includes 134 images of Indian dataset and 65 images of Swiss dataset.

The ability of cortical radiogrammetric features of third metacarpal with statistical, structural and transform-based texture features of trabecular bone, in detecting subjects with low bone mass in both Indian and Swiss sample population is studied. Three different groups of texture features are investigated. The first group of texture features comprises of histogram features, GLCM and MGM features extracted from the background subtracted images of the distal radius ROI. The second group of features are LBP features and its variants extracted directly from the raw texture images. The third group of features are CNN features extracted from the raw images using transfer learning. The extracted features are selected using different feature selection methods. Classifiers are trained with selected feature sets of the three groups of cortical and texture features and their performances are compared.

5.3.1 Classification using statistical and structural features

Here, we discuss about classifiers trained using the first group of texture features, namely histogram features, GLCM, MGM and Gabor features along with cortical features of the Indian and Swiss sample data. We also investigate the importance of considering the ethnic group when using texture features for classification. Bone characteristics largely depend on the ethnic group they belong to. Asian ethnic group have a less dense bone to their age counterparts in the Western countries and are affected by bone loss at an earlier age. Hence, the texture features of the bone varies with ethnic groups and is best analyzed within a regional population. We show this by comparing the performance of classifiers trained from texture features of two different ethnic groups, the Indian and Swiss population. The bone features extracted from both the sample population are analyzed for statistical significance and correlation with DXA-LS. Classifiers with the same architecture are trained using the common significant features from both

the sample population and compared to classifiers trained from an optimal set of features within a particular sample population.

Feature selection

Using statistical significance test:

The cortical radiogrammetric features and texture features such as histogram features, GLCM, MGM and Gabor features extracted from the background subtracted images are analyzed using statistical test. The ability of the extracted features to discriminate between healthy and osteoporotic groups is analyzed using independent sample *t*-test. The statistical tests are tested on the Indian and Swiss sample data separately. The *t*-test was done on both the population, after removing data with T -score < -4 and T -score > 2 in order to remove outliers. Since the Swiss dataset contains very few samples in the healthy group, 20 images from the Indian healthy sample data is included in the Swiss sample data for training. Table 5.9 shows the *t*-test results with significance values for all features extracted from the Indian and Swiss sample population, respectively. Out of the total 41 features extracted, 40 features are statistically significant ($p < 0.05$) for the Indian sample data. In case of Swiss sample data, 36 features are statistically significant with $p < 0.05$.

Table 5.10 shows the correlation values of the extracted features with sBMD and T -score for the Indian and Swiss sample population, respectively. For the Indian sample data, 36 features are significantly correlated with sBMD and T -score. All the cortical features show a very good correlation with $p < 0.0001$. Texture features derived from MGM also shows a very high correlation with $p < 0.001$. Thirty six features are significantly correlated with sBMD and T -score for Swiss sample data. The highest correlated feature with sBMD and T -score is *CCT* for both ethnic groups.

Feature selection is done using the results of *t*-test. Two sets of features are selected, common feature set (CFS) and optimal feature sets of the Indian and Swiss sample data (OFS-I and OFS-S). In CFS, the features common to significant features of Indian data ($p < 0.01$) and significant features of Swiss data ($p < 0.01$) are selected. In OFS-I, the

Table 5.9: Significance test results of healthy (H) and low bone mass (LBM) groups of Indian and Swiss sample populations

Sl. no.	Features extracted	Indian-H ($\mu \pm \sigma$)	Indian-LBM ($\mu \pm \sigma$)	p-value	Swiss-H ($\mu \pm \sigma$)	Swiss-LBM ($\mu \pm \sigma$)	p-value
1	<i>CCT</i> (mm)	4.48 \pm 0.58	3.90 \pm 0.55	8.9E-08 [§]	4.36 \pm 0.64	3.75 \pm 0.66	5.8E-05 [§]
2	<i>CA</i> (mm ²)	43.13 \pm 7.28	36.54 \pm 6.82	9.1E-07 [§]	41.73 \pm 7.97	36.92 \pm 8.34	0.0095 [†]
3	<i>PCA</i> (%)	78.12 \pm 7.21	74.06 \pm 7.14	0.0022 [†]	77.21 \pm 7.78	70.58 \pm 7.25	0.0002 [‡]
4	<i>BNI</i>	53.88 \pm 7.86	49.55 \pm 6.99	0.0016 [†]	52.94 \pm 8.12	46.15 \pm 6.57	8.8E-05 [§]
5	<i>Hist_{var}</i>	1198.73 \pm 269.27	1337.80 \pm 257.95	0.0041 [†]	1368.90 \pm 297.46	1529.85 \pm 275.90	0.0136 [*]
6	<i>Hist_{skew}</i>	0.67 \pm 0.38	0.50 \pm 0.23	0.0033 [†]	0.53 \pm 0.30	0.35 \pm 0.15	0.0009 [‡]
7	<i>Hist_{kurt}</i>	1.29 \pm 1.51	0.60 \pm 0.72	0.0015 [†]	0.67 \pm 0.94	0.09 \pm 0.44	0.0007 [‡]
8	<i>GLCM_{0cont}</i>	1751.99 \pm 560.16	2066.26 \pm 441.28	0.0007 [‡]	2057.61 \pm 640.16	2518.25 \pm 566.13	0.0009 [‡]
9	<i>GLCM_{0corr}</i>	0.26 \pm 0.13	0.21 \pm 0.09	0.0231 [*]	0.25 \pm 0.12	0.17 \pm 0.07	0.0004 [‡]
10	<i>GLCM_{0hom}</i>	0.08 \pm 0.01	0.07 \pm 0.01	0.0002 [‡]	0.07 \pm 0.01	0.07 \pm 0.01	0.0004 [‡]
11	<i>GLCM_{0en}</i>	0.00 \pm 0.00	0.00 \pm 0.00	0.0003 [‡]	0.00 \pm 0.00	0.00 \pm 0.00	0.0014 [†]
12	<i>GLCM_{0ent}</i>	0.83 \pm 0.07	0.87 \pm 0.05	0.0008 [‡]	0.86 \pm 0.06	0.90 \pm 0.05	0.0102 [*]
13	<i>GLCM_{45cont}</i>	1908.57 \pm 561.49	2238.35 \pm 456.93	0.0005 [‡]	2235.06 \pm 647.09	2671.11 \pm 589.37	0.0022 [†]
14	<i>GLCM_{45corr}</i>	0.16 \pm 0.10	0.12 \pm 0.08	0.0484 [*]	0.15 \pm 0.10	0.10 \pm 0.07	0.0120 [†]
15	<i>GLCM_{45hom}</i>	0.08 \pm 0.01	0.07 \pm 0.01	0.0002 [‡]	0.07 \pm 0.01	0.06 \pm 0.01	0.0007 [‡]
16	<i>GLCM_{45en}</i>	0.00 \pm 0.00	0.00 \pm 0.00	0.0003 [‡]	0.00 \pm 0.00	0.00 \pm 0.00	0.0015 [†]
17	<i>GLCM_{45ent}</i>	0.82 \pm 0.07	0.86 \pm 0.05	0.0007 [‡]	0.85 \pm 0.06	0.89 \pm 0.05	0.0085 [†]
18	<i>GLCM_{90cont}</i>	1475.59 \pm 424.57	1648.32 \pm 347.83	0.0151 [*]	1713.17 \pm 492.76	2114.97 \pm 513.82	0.0006 [‡]
19	<i>GLCM_{90corr}</i>	0.35 \pm 0.09	0.36 \pm 0.08	0.7942	0.35 \pm 0.09	0.29 \pm 0.08	0.0084 [†]
20	<i>GLCM_{90hom}</i>	0.09 \pm 0.01	0.08 \pm 0.01	0.0069 [†]	0.08 \pm 0.01	0.07 \pm 0.01	0.0003 [‡]

Sl. no.	Features extracted	Indian-H ($\mu \pm \sigma$)	Indian-LBM ($\mu \pm \sigma$)	p-value	Swiss-H ($\mu \pm \sigma$)	Swiss-LBM ($\mu \pm \sigma$)	p-value
21	$GLCM_{90_{en}}$	0.00 ± 0.00	0.00 ± 0.00	0.0007 [‡]	0.00 ± 0.00	0.00 ± 0.00	0.0010 [†]
22	$GLCM_{90_{ent}}$	0.82 ± 0.07	0.85 ± 0.05	0.0019 [†]	0.85 ± 0.07	0.89 ± 0.05	0.0057 [†]
23	$GLCM_{135_{cont}}$	1873.11 ± 545.16	2218.92 ± 453.76	0.0002 [‡]	2172.25 ± 624.56	2658.90 ± 566.21	0.0004 [‡]
24	$GLCM_{135_{corr}}$	0.17 ± 0.10	0.13 ± 0.08	0.0133 [*]	0.17 ± 0.09	0.09 ± 0.06	9.3E-05 [§]
25	$GLCM_{135_{hom}}$	0.08 ± 0.01	0.07 ± 0.01	9.6E-05 [§]	0.07 ± 0.01	0.06 ± 0.01	6.8E-05 [§]
26	$GLCM_{135_{en}}$	0.00 ± 0.00	0.00 ± 0.00	0.0003 [‡]	0.00 ± 0.00	0.00 ± 0.00	0.0011 [†]
27	$GLCM_{135_{ent}}$	0.82 ± 0.07	0.86 ± 0.05	0.0006 [‡]	0.85 ± 0.06	0.89 ± 0.05	0.0066 [†]
28	$Gabor_{4,1}$	1283.09 ± 252.51	1536.03 ± 276.88	5.4E-07 [§]	1349.12 ± 309.95	1383.40 ± 334.15	0.6335
29	$Gabor_{4,2}$	1010.27 ± 171.46	1163.42 ± 182.75	4.7E-06 [§]	1057.13 ± 247.13	1059.43 ± 257.23	0.9674
30	$Gabor_{4,3}$	856.30 ± 139.87	972.13 ± 159.19	3.6E-05 [§]	902.68 ± 171.00	837.09 ± 183.42	0.0999
31	$Gabor_{4,4}$	927.60 ± 198.86	1037.47 ± 215.11	0.0039 [†]	971.87 ± 200.23	882.75 ± 187.71	0.0421 [*]
32	$Gabor_{4,5}$	813.00 ± 150.19	919.33 ± 158.48	0.0002 [‡]	842.09 ± 141.25	826.43 ± 160.83	0.6426
33	$Gabor_{4,6}$	986.18 ± 205.11	1172.47 ± 211.43	2.3E-06 [§]	1044.98 ± 242.12	1045.12 ± 236.72	0.9980
34	GR_5	26.73 ± 2.50	28.40 ± 2.23	0.0001 [‡]	25.27 ± 3.18	23.18 ± 3.41	0.0056 [†]
35	GR_7	23.72 ± 2.66	25.13 ± 2.11	0.0016 [†]	22.69 ± 2.84	20.71 ± 3.07	0.0034 [†]
36	$GSS_{7,3}$	183.55 ± 13.32	192.75 ± 12.26	0.0001 [‡]	174.45 ± 18.72	161.95 ± 20.84	0.0057 [†]
37	$GSS_{9,5}$	106.32 ± 9.66	111.86 ± 8.15	0.0008 [‡]	101.65 ± 11.03	93.52 ± 12.86	0.0031 [†]
38	$GSS_{11,7}$	72.21 ± 7.93	75.81 ± 6.09	0.0056 [†]	69.29 ± 7.97	63.19 ± 9.21	0.0020 [†]
39	$GSR_{7,3}$	205.13 ± 13.73	215.24 ± 12.99	5.3E-05 [§]	194.54 ± 20.92	180.78 ± 22.98	0.0061 [†]
40	$GSR_{9,5}$	114.83 ± 9.66	121.06 ± 8.62	0.0002 [‡]	109.39 ± 11.92	100.84 ± 13.81	0.0038 [†]
41	$GSR_{11,7}$	78.09 ± 7.80	82.26 ± 6.43	0.0016 [†]	74.81 ± 8.30	68.44 ± 9.81	0.0023 [†]

*p<0.05, † p<0.01, ‡ p<0.001, § p<0.0001

Table 5.10: Correlation analysis of extracted features with sBMD and T -score for Indian and Swiss sample populations

Sl. no.	Features extracted	Indian sample population		Swiss sample population	
		sBMD	T -score	sBMD	T -score
1	<i>CCT</i>	0.5133 [§]	0.4806 [§]	0.4773 [§]	0.3974 [‡]
2	<i>CA</i>	0.4527 [§]	0.4035 [§]	0.4207 [§]	0.3198 [†]
3	<i>PCA</i>	0.3569 [§]	0.3524 [§]	0.3489 [†]	0.3106 [†]
4	<i>BNI</i>	0.3595 [§]	0.3560 [§]	0.3625 [‡]	0.3300 [†]
5	<i>Hist_{var}</i>	-0.2072 [*]	-0.2158 [*]	-0.3572 [†]	-0.3760 [‡]
6	<i>Hist_{skew}</i>	0.2098 [*]	0.2226 [†]	0.5178 [§]	0.4630 [§]
7	<i>Hist_{kurt}</i>	0.2270 [†]	0.2363 [†]	0.4923 [§]	0.4429 [§]
8	<i>GLCM_{0_{cont}}</i>	-0.2565 [†]	-0.2626 [†]	-0.4658 [§]	-0.4585 [§]
9	<i>GLCM_{0_{corr}}</i>	0.2047 [*]	0.2055 [*]	0.4767 [§]	0.4378 [§]
10	<i>GLCM_{0_{hom}}</i>	0.2658 [†]	0.2763 [†]	0.4901 [§]	0.4764 [§]
11	<i>GLCM_{0_{en}}</i>	0.2577 [†]	0.2686 [†]	0.4534 [§]	0.4458 [§]
12	<i>GLCM_{0_{ent}}</i>	-0.2193 [*]	-0.2286 [†]	-0.3867 [‡]	-0.3911 [‡]
13	<i>GLCM_{45_{cont}}</i>	-0.2506 [†]	-0.2564 [†]	-0.4324 [§]	-0.4302 [§]
14	<i>GLCM_{45_{corr}}</i>	0.1241	0.1244	0.3109 [†]	0.2938 [†]
15	<i>GLCM_{45_{hom}}</i>	0.2639 [†]	0.2737 [†]	0.4637 [§]	0.4564 [§]
16	<i>GLCM_{45_{en}}</i>	0.2604 [†]	0.2714 [†]	0.4506 [§]	0.4445 [§]
17	<i>GLCM_{45_{ent}}</i>	-0.2306 [†]	-0.2401 [†]	-0.3954 [‡]	-0.3995 [‡]
18	<i>GLCM_{90_{cont}}</i>	-0.1336	-0.1463	-0.4577 [§]	-0.4732 [§]
19	<i>GLCM_{90_{corr}}</i>	-0.1153	-0.1042	0.2999 [†]	0.3149 [†]
20	<i>GLCM_{90_{hom}}</i>	0.1407	0.1555	0.4647 [§]	0.4631 [§]
21	<i>GLCM_{90_{en}}</i>	0.2358 [†]	0.2489 [†]	0.4625 [§]	0.4576 [§]
22	<i>GLCM_{90_{ent}}</i>	-0.2022 [*]	-0.2132 [*]	-0.4111 [‡]	-0.4190 [§]
23	<i>GLCM_{135_{cont}}</i>	-0.2828 [‡]	-0.2881 [‡]	-0.4742 [§]	-0.4780 [§]
24	<i>GLCM_{135_{corr}}</i>	0.1920 [*]	0.1909 [*]	0.4396 [§]	0.4381 [§]
25	<i>GLCM_{135_{hom}}</i>	0.2868 [‡]	0.2953 [‡]	0.5142 [§]	0.5100 [§]
26	<i>GLCM_{135_{en}}</i>	0.2664 [†]	0.2775 [†]	0.4635 [§]	0.4566 [§]
27	<i>GLCM_{135_{ent}}</i>	-0.2350 [†]	-0.2442 [†]	-0.4060 [‡]	-0.4101 [‡]
28	<i>Gabor_{4,1}</i>	-0.4469 [§]	-0.4430 [§]	-0.1285	-0.1192
29	<i>Gabor_{4,2}</i>	-0.4048 [§]	-0.4018 [§]	-0.0526	-0.0378
30	<i>Gabor_{4,3}</i>	-0.2738 [†]	-0.2758 [†]	0.1883	0.1614
31	<i>Gabor_{4,4}</i>	-0.1523	-0.1457	0.2887 [†]	0.2263 [*]
32	<i>Gabor_{4,5}</i>	-0.3256 [‡]	-0.3175 [‡]	0.0687	0.0221
33	<i>Gabor_{4,6}</i>	-0.4269 [§]	-0.4259 [§]	-0.0504	-0.0543
34	<i>GR₅</i>	-0.4609 [§]	-0.4354 [§]	0.3201 [†]	0.3193 [†]
35	<i>GR₇</i>	-0.3996 [§]	-0.3750 [§]	0.3494 [†]	0.3579 [†]
36	<i>GSS_{7,3}</i>	-0.4476 [§]	-0.4221 [§]	0.3256 [†]	0.3223 [†]
37	<i>GSS_{9,5}</i>	-0.4087 [§]	-0.3844 [§]	0.3515 [†]	0.3613 [‡]
38	<i>GSS_{11,7}</i>	-0.3736 [§]	-0.3526 [§]	0.3578 [†]	0.3764 [‡]
39	<i>GSR_{7,3}</i>	-0.4586 [§]	-0.4322 [§]	0.3187 [†]	0.3122 [†]
40	<i>GSR_{9,5}</i>	-0.4348 [§]	-0.4100 [§]	0.3422 [†]	0.3478 [†]
41	<i>GSR_{11,7}</i>	-0.3975 [§]	-0.3745 [§]	0.3559 [†]	0.3701 [‡]

*p<0.05, †p<0.01, ‡p<0.001, §p<0.0001

most significant features of Indian data alone (p<0.001) are selected. Similarly, in OFS-S, the most significant features of Swiss data (p<0.001) are selected. The features selected for feature sets, CFS, OFS-I and OFS-S, are shown in Table 5.11.

Table 5.11: Features selected in each of the feature sets used for classification

Feature set	Features
CFS ($n = 28$)	$CCT, CA, PCA, BNI, Hist_{skew}, Hist_{kurt}, GLCM_{0_{cont}}, GLCM_{0_{hom}}, GLCM_{0_{en}}, GLCM_{45_{cont}}, GLCM_{45_{hom}}, GLCM_{45_{en}}, GLCM_{45_{ent}}, GLCM_{90_{hom}}, GLCM_{90_{en}}, GLCM_{90_{ent}}, GLCM_{135_{cont}}, GLCM_{135_{hom}}, GLCM_{135_{en}}, GLCM_{135_{ent}}, GR_5, GR_7, GSS_{7,3}, GSS_{9,5}, GSS_{11,7}, GSR_{7,3}, GSR_{9,5}, GSR_{11,7}$
OFS-I ($n = 14$)	$CCT, CA, PCA, BNI, GLCM_{0_{hom}}, GLCM_{45_{hom}}, GLCM_{135_{hom}}, Gabor_{4,1}, Gabor_{4,2}, Gabor_{4,3}, Gabor_{4,6}, GR_5, GSS_{7,3}, GSR_{7,3}$
OFS-S ($n = 14$)	$CCT, PCA, BNI, Hist_{skew}, Hist_{kurt}, GLCM_{0_{cont}}, GLCM_{0_{corr}}, GLCM_{0_{hom}}, GLCM_{45_{hom}}, GLCM_{90_{cont}}, GLCM_{90_{hom}}, GLCM_{135_{cont}}, GLCM_{135_{corr}}, GLCM_{135_{hom}}$

Table 5.12: Correlation results of the 10 highest ranked cortical and texture features in the training set of Indian and Swiss sample data

Sl. no.	Indian sample data (FS-4(I))		Swiss sample data (FS-4(S))	
	Features	Correlation	Features	Correlation
1	CCT	0.5883 [§]	$Hist_{skew}$	0.5177 [§]
2	CA	0.5344 [§]	$GLCM_{135_{hom}}$	0.5137 [§]
3	$GSR_{7,3}$	-0.4037 [§]	$Hist_{kurt}$	0.4920 [§]
4	$GSS_{7,3}$	-0.3894 [§]	$GLCM_{0_{hom}}$	0.4902 [§]
5	GR_5	-0.3867 [§]	CCT	0.4775 [§]
6	$GSR_{9,5}$	-0.3783 [§]	$GLCM_{0_{corr}}$	0.4762 [§]
7	BNI	0.3765 [§]	$GLCM_{135_{cont}}$	-0.4744 [§]
8	PCA_b	0.3709 [§]	$GLCM_{0_{cont}}$	-0.4660 [§]
9	$GSS_{9,5}$	-0.3548 [‡]	$GLCM_{90_{hom}}$	0.4650 [§]
10	$Gabor_{4,1}$	-0.3448 [‡]	$GLCM_{45_{hom}}$	0.4640 [§]

† $p < 0.01$, ‡ $p < 0.001$, § $p < 0.0001$

Using correlation ranking:

Feature ranking using Pearson correlation analysis is done to determine the most significantly correlated cortical and texture features of the Indian and Swiss sample population. The 10 highest ranked features of the Indian training data are selected as feature set FS-4(I) and the 10 highest ranked features of the Swiss training data are selected as feature set FS-4(S). Table 5.12 shows the correlation results of the 10 highest ranked features in the Indian and Swiss sample data.

Using PCA:

PCA analysis is carried out on the extracted features for dimensionality reduction. The principal components that capture 95% variance in the extracted features of the

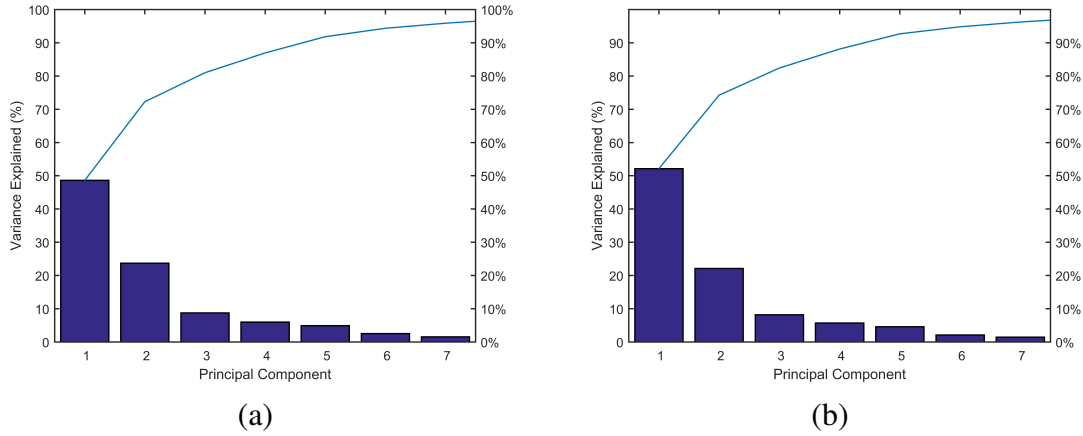


Figure 5.10: Feature selection using PCA on the feature set of (a) Indian sample data and (b) Swiss sample data.

Indian and Swiss sample data are selected as feature sets FS-5(I) and FS-5(S), respectively. Figure 5.10 shows the variance explained by each principal components. The first 6 features explain 95% variance in the feature set of Indian and Swiss sample data.

Classifier

Each of the feature sets selected using *t*-test, namely CFS, OFS-I and OFS-S, are used to train ANN classifiers. Two ANN classifiers are trained with Indian sample data using CFS and OFS-I, and another two ANN classifiers are trained with Swiss sample data using CFS and OFS-S. ANN classifiers with CFS are modeled with 20 nodes in 1 hidden layer and classifiers with OFS-I and OFS-S are modeled with 8 nodes in 1 hidden layer. Feature sets selected using ranking by correlation values, namely FS-4(I) and FS-4(S), are used to train ANN classifiers designed with 1 hidden layer having 8 nodes. Feature sets selected using PCA, namely FS-5(I) and FS-5(S), are used to train ANN classifiers with 3 hidden nodes. The total data is partitioned into training, validation and test images. Classifiers trained on the features of Indian sample population uses training data and test data from the Indian sample data only. For classifiers trained for Swiss population, due to limited data samples in the Swiss data, 20 images of the Indian healthy sample data are included in the training set of the ANN classifiers. The features are normalized prior to training the classifiers. The trained classifiers are then tested on

Table 5.13: Classification results of the trained ANN classifiers using holdout validation

Data	Feature set	Partition set	TP	FP	TN	FN	Sn	Sp	PPV	NPV	Acc	F1-score
Indian	CFS	Training	49	6	46	5	90.7	88.5	89.1	90.2	89.6	89.9
		Test	11	0	15	2	84.6	100.0	100.0	88.2	92.9	91.7
		Overall	60	6	61	7	89.6	91.0	90.9	89.7	90.3	90.2
Indian	OFS-I	Training	49	4	49	4	92.5	92.5	92.5	92.5	92.5	92.5
		Test	11	2	13	2	84.6	86.7	84.6	86.6	85.7	84.6
		Overall	60	6	62	6	90.9	91.2	90.9	91.2	91.0	90.9
Indian	FS-4(I)	Training	46	14	36	10	82.1	72.0	76.7	78.3	77.4	79.3
		Test	9	2	16	1	90.0	88.9	81.8	94.1	89.3	85.7
		Overall	55	16	52	11	83.3	76.5	77.5	82.5	79.9	80.3
Indian	FS-5(I)	Training	42	13	39	12	77.8	75.0	76.4	76.5	76.4	77.1
		Test	11	2	14	1	91.7	87.5	84.6	93.3	89.3	88.0
		Overall	53	15	53	13	80.3	77.9	77.9	80.3	79.1	79.1
Swiss	CFS	Training	33	6	32	2	94.3	84.2	84.6	94.1	89.0	89.2
		Test	3	1	7	0	100.0	87.5	75.0	100.0	90.9	85.7
		Overall	36	7	39	2	94.7	84.8	83.7	95.1	89.3	88.9
Swiss	OFS-S	Training	31	4	38	0	100.0	90.5	88.6	100.0	94.5	93.9
		Test	7	1	3	0	100.0	75.0	87.5	100.0	90.9	93.3
		Overall	38	5	41	0	100.0	89.1	88.4	100.0	94.0	93.8
Swiss	FS-4(S)	Training	29	9	26	10	74.4	74.3	76.3	72.2	74.3	75.3
		Test	5	1	5	0	100.0	83.3	83.3	100.0	90.9	90.9
		Overall	34	10	31	10	77.3	75.6	77.3	75.6	76.5	77.3
Swiss	FS-5(S)	Training	25	7	29	13	65.8	80.6	78.1	69.0	72.9	71.4
		Test	5	0	5	1	83.3	100.0	100.0	83.3	90.9	90.9
		Overall	30	7	34	14	68.2	82.9	81.1	70.8	75.3	74.1

test set containing Swiss data only.

The trained ANN classifiers are evaluated using confusion matrices. Table 5.13 shows the classification results of the classifiers trained with the Indian and Swiss population separately with the different feature sets. Among the ANN classifiers trained using Indian sample data, OFS-I shows the best performance with training accuracy of 92.5% and test accuracy of 85.7%. CFS shows a training accuracy of 89.6% and test accuracy of 92.9%. Among the ANN classifiers trained using Swiss sample data, OFS-S shows the best performance with training accuracy of 94.5% and test accuracy of 90.9%, while CFS shows training accuracy of 89.0% and test accuracy of 90.9%. Classifiers trained with feature sets selected using correlation ranking and PCA, namely FS-4 and FS-5, shows lesser overall accuracy than CFS and OFS for both Indian and Swiss sample data.

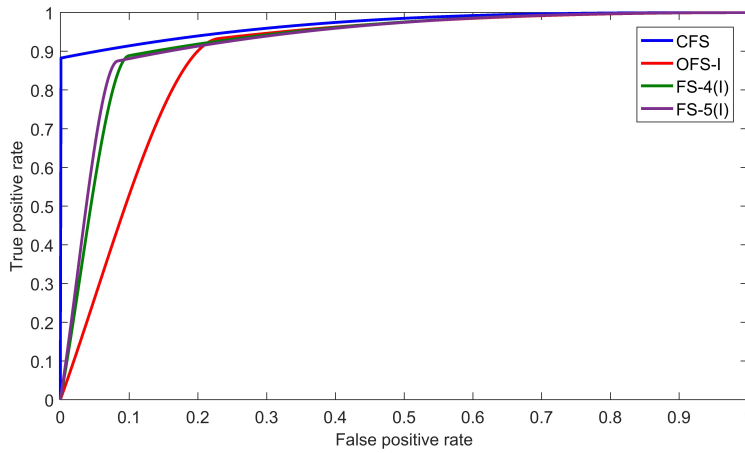


Figure 5.11: ROC curves for the ANN classifiers trained on Indian sample data using CFS (AUC=0.9705), OFS-I (AUC=0.8825), FS-4(I) (AUC=0.9245) and FS-5(I) (AUC=0.9280)

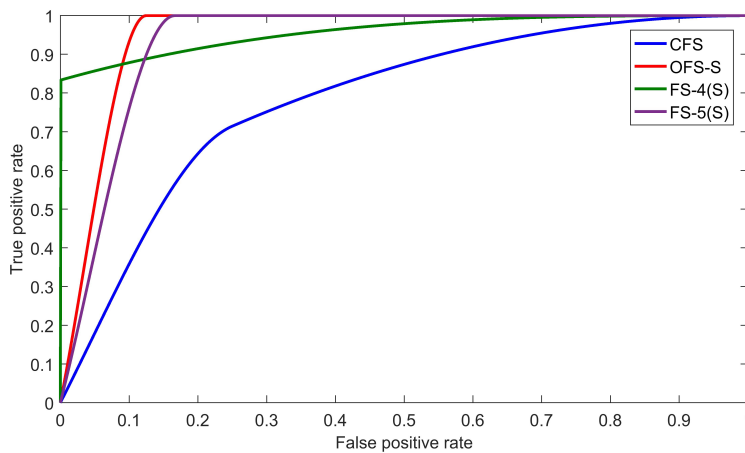


Figure 5.12: ROC curves for the ANN classifiers trained on Swiss sample data using CFS (AUC=0.7824), OFS-S (AUC=0.9492), FS-4(S) (AUC=0.9583) and FS-5(S) (AUC=0.9329)

ROC curves for the ANN classifiers trained on Indian sample data using feature sets CFS, OFS-I, FS-4(I) and FS-5(I) are shown in Figure 5.11. Figure 5.12 shows the ROC curves for the ANN classifiers trained on Swiss sample data using feature sets CFS, OFS-S, FS-4(S) and FS-5(S).

As shown in Table 5.13, ANN classifier trained with OFS-I on Indian sample population shows an overall accuracy of 91.0%, while that trained with CFS shows an overall accuracy of 90.3%. Similarly, classifier trained with OFS-S on Swiss sample population

Table 5.14: Performance metrics of the classifiers trained with CFS features on the test data using holdout validation and 10-fold cross validation

Validation	Classifier	TP	FP	TN	FN	Sn	Sp	PPV	NPV	Acc	F1-score
Test data	LR	31	12	28	8	79.5	70.0	72.1	77.8	74.7	75.6
	SVM	35	13	27	4	89.7	67.5	72.9	87.1	78.5	80.5
	KNN	36	0	40	3	92.3	100	100	93.0	96.2	96.0
10-fold cross validation	LR	40	16	44	20	66.7	73.3	71.4	68.8	70.0	68.9
	SVM	52	21	39	8	86.7	65.0	71.2	82.9	75.8	78.2
	KNN	45	17	43	15	75.0	71.7	72.6	74.1	73.3	73.8

shows an overall accuracy of 94.0%, while that trained with CFS shows an overall accuracy of 89.3%. Thus, classifiers that are trained with the optimal sets of features show better performance as compared to the classifiers trained with common features. This shows that taking into account the differences in bone characteristics in different ethnic groups for feature extraction and classification helps to build more accurate diagnostic tools.

However, training separate classifiers for different sample population is practically tedious. It would be more convenient if common classifiers could be trained for detecting low bone mass in different population samples. Therefore, we further explore the use of the common feature set, CFS, in training other classifiers such as LR, SVM and KNN. These classifiers are trained on a training set of Indian sample data and tested using test data comprising Indian and Swiss sample data. The training set of the classifiers comprises of 120 images of the Indian sample data (60 H and 60 LBM) and the test data comprises of 14 test images of the Indian sample data and all images of the Swiss sample data. The performance of the trained classifiers for Indian and Swiss test data using holdout validation are given in Table 5.14. Weighted KNN shows the best test accuracy of 96.2%, while logistic regression classifier gives test accuracy of 74.7% and SVM gives test accuracy of 78.5%. A 10-fold cross validation is also done on the training set to show the efficiency of the classifiers trained using a limited dataset, as shown in Table 5.14. SVM achieves the best cross-validation accuracy of 75.8% while logistic regression classifier shows cross-validation accuracy of 70.0% and weighted KNN shows cross-validation accuracy of 73.3%.

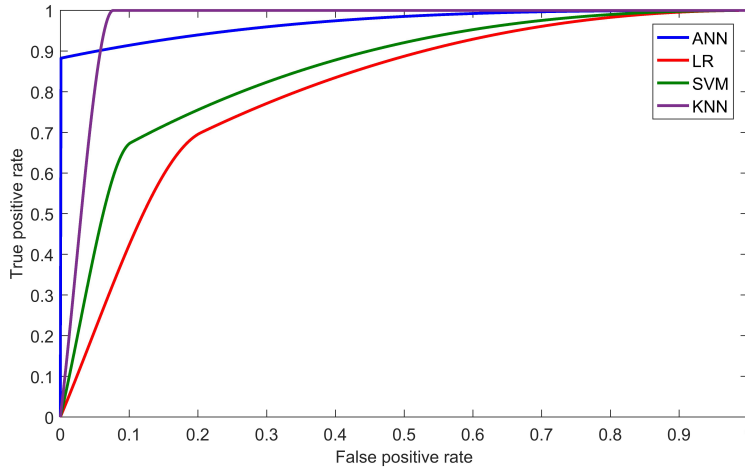


Figure 5.13: ROC curves for the classifiers trained with CFS: AUC of ANN=0.9705, AUC of LR=0.8012, AUC of SVM=0.8522 and AUC of KNN=0.9684

ROC curves for the ANN, LR, SVM and KNN classifiers trained with CFS feature set using holdout validation is shown in Figure 5.13. The best performance is shown by ANN and KNN classifiers with AUC=0.9705 and AUC=0.9684, respectively.

5.3.2 Classification using LBP features

Next, we discuss about classifiers trained using the second group of texture features, namely LBP, LLBP, horizontal LLBP and vertical LLBP. LBP features used are rotation-invariant features with a neighborhood of 8 pixels. LLBP features are extracted with a line of length 17 pixels as the neighborhood. The LBP features and its variants are extracted from the raw texture images of the distal radius ROI. The features extracted from the histograms of LBP and its variants are mean, variance, skew, kurtosis, energy and entropy. Feature sets are selected using correlation analysis and used for training classifiers.

Feature selection

The extracted LBP and LLBP features are tested for correlation with sBMD of Indian and Swiss sample data, as shown in Table 5.15. The features that are the most significantly correlated are selected as the features used for classification. The sig-

Table 5.15: Correlation analysis of LBP features with sBMD for Indian and Swiss sample populations

LBP methods	Features	Indian sample population	Swiss sample population
LBP	LBP_{mean}	0.2231*	0.3285*
	LBP_{var}	0.2182*	0.3305*
	LBP_{skew}	-0.2487†	-0.3348*
	LBP_{kurt}	-0.2625†	-0.3248*
	LBP_{en}	-0.2449†	-0.3073
LLBP	$LLBP_{mean}$	-0.2777†	-0.3581*
	$LLBP_{var}$	0.4805§	0.2169
	$LLBP_{skew}$	0.1659	0.3639*
	$LLBP_{kurt}$	-0.5052§	-0.2720
	$LLBP_{en}$	-0.4918§	-0.3159*
Horizontal LLBP	$LLBP_{ent}$	0.4948§	0.3257*
	$LLBP_{Hor_{mean}}$	-0.5273§	-0.3544*
	$LLBP_{Hor_{var}}$	0.0739	-0.2018
	$LLBP_{Hor_{skew}}$	0.5012§	0.3189*
	$LLBP_{Hor_{kurt}}$	-0.2096*	0.0810
Vertical LLBP	$LLBP_{Hor_{en}}$	-0.4433§	-0.3376*
	$LLBP_{Hor_{ent}}$	0.4401§	0.3449*
	$LLBP_{Vert_{mean}}$	-0.3568§	-0.3770*
	$LLBP_{Vert_{var}}$	0.1972*	0.0110
	$LLBP_{Vert_{skew}}$	0.3682§	0.3588*
	$LLBP_{Vert_{kurt}}$	-0.3434§	-0.2684
	$LLBP_{Vert_{en}}$	-0.3143‡	-0.2886
	$LLBP_{Vert_{ent}}$	0.2901‡	0.2808

*p<0.05, † p<0.01, ‡ p<0.001, § p<0.0001

nificantly correlated features with sBMD of Indian and Swiss sample data are LBP (LBP_{mean} , LBP_{var} , LBP_{skew} , LBP_{kurt}), LLBP ($LLBP_{mean}$, $LLBP_{en}$, $LLBP_{ent}$), horizontal LLBP ($LLBP_{Hor_{mean}}$, $LLBP_{Hor_{skew}}$, $LLBP_{Hor_{en}}$, $LLBP_{Hor_{ent}}$) and vertical LLBP ($LLBP_{Vert_{mean}}$, $LLBP_{Vert_{skew}}$). The significant cortical radiogrammetric features (CCT , CA , PCA_b , BNI) are combined with the significant texture features of LBP, LLBP, horizontal LLBP and vertical LLBP to get feature sets FS-6(a), FS-6(b), FS-6(c) and FS-6(d), respectively. These feature sets are used for training LR, SVM and KNN classifiers.

Classifier

LR, SVM and KNN classifiers are trained using the selected feature sets FS-6(a), FS-6(b), FS-6(c) and FS-6(d) on the training set. Classifiers trained using the selected feature sets are tested on the Indian and Swiss test data and the achieved performance

Table 5.16: Performance metrics of the classifiers, trained with cortical and LBP feature variants, on the test data

Feature set	Classifier	TP	FP	TN	FN	Sn	Sp	PPV	NPV	Acc	F1-score
FS-6(a)	LR	16	19	30	10	61.5	61.2	45.7	75.0	61.3	52.5
	SVM	16	23	26	10	61.5	53.1	41.0	72.2	56.0	49.2
	KNN	15	21	27	11	57.7	56.3	41.7	71.1	56.8	48.4
FS-6(b)	LR	23	34	15	3	88.5	30.6	40.4	83.3	50.7	55.4
	SVM	19	24	25	7	73.1	51.0	44.2	78.1	58.7	55.1
	KNN	16	17	32	10	61.5	65.3	48.5	76.2	64.0	54.2
FS-6(c)	LR	2	7	42	24	7.7	85.7	22.2	63.6	58.7	11.4
	SVM	15	20	29	11	57.7	59.2	42.9	72.5	58.7	49.2
	KNN	13	20	29	13	50.0	59.2	39.4	69.0	56.0	44.1
FS-6(d)	LR	17	20	29	9	65.4	59.2	45.9	76.3	61.3	53.9
	SVM	15	19	30	11	57.7	61.2	44.1	73.2	60.0	50.0
	KNN	14	15	34	12	53.8	69.4	48.3	73.9	64.0	50.9

is shown in Table 5.16. The best test accuracy of 64.0% (Sn=61.5% and Sp=65.3%) is obtained by weighted KNN classifier trained with LLBP feature set, FS-6(b). It is observed that a better performance is achieved with LLBP and its variants (FS-6(b), FS-6(c) and FS-6(d)) as compared to conventional LBP (FS-6(a)). Thus linear feature descriptors like LLBP help to better characterize the trabecular bone in osteoporosis.

ROC curves for all the classifiers trained using feature sets FS-6(a), FS-6(b), FS-6(c) and FS-6(d) are analyzed. AUC values obtained were low, ranging from 0.4670 to 0.6342.

Classifiers are also trained using 10-fold cross validation with the selected feature sets FS-6(a), FS-6(b), FS-6(c) and FS-6(d). The performance of the classifiers using 10-fold cross validation are shown in Table 5.17. The best performance is achieved with SVM classifiers trained using FS-6(a), FS-6(b) and FS-6(d) features, with cross-validation accuracy of 75.0%, 77.5% and 74.2%, respectively. For horizontal LLBP features, FS-6(c), LR classifier shows better cross validation results with an accuracy of 79.2%.

A comparison of the test accuracy of the classifiers trained using statistical and structural features, and LBP features show that the classifiers trained with combined cortical, histogram, GLCM and MGM features show the best test accuracy for Indian

Table 5.17: Performance metrics of the classifiers using 10-fold cross validation on combined cortical and LBP feature variants

Feature set	Classifier	TP	FP	TN	FN	Sn	Sp	PPV	NPV	Acc	F1-score
FS-6(a)	LR	44	15	45	16	73.3	75.0	74.6	73.8	74.2	73.9
	SVM	50	20	40	10	83.3	66.7	71.4	80.0	75.0	76.9
	KNN	42	18	42	18	70.0	70.0	70.0	70.0	70.0	70.0
FS-6(b)	LR	48	15	45	12	80.0	75.0	76.2	78.9	77.5	78.1
	SVM	53	20	40	7	88.3	66.7	72.6	85.1	77.5	79.7
	KNN	48	19	41	12	80.0	68.3	71.6	77.4	74.2	75.6
FS-6(c)	LR	49	14	46	11	81.7	76.7	77.8	80.7	79.2	79.7
	SVM	45	17	43	15	75.0	71.7	72.6	74.1	73.3	73.8
	KNN	47	15	45	13	78.3	75.0	75.8	77.6	76.7	77.1
FS-6(d)	LR	44	16	44	16	73.3	73.3	73.3	73.3	73.3	73.3
	SVM	53	24	36	7	88.3	60.0	68.8	83.7	74.2	77.4
	KNN	45	19	41	15	75.0	68.3	70.3	73.2	71.7	72.6

and Swiss test data, while the cortical features combined with horizontal LLBP shows the best cross-validation accuracy.

5.3.3 Classification using CNN features

We have discussed so far on texture analysis methods that extract statistical and structural details of the trabecular texture image. In the recent years, pattern recognition using deep learning has shown a vast improvement over traditional methods. Deep learning using CNN helps to capture complex features from texture images. Texture analysis and classification using CNN requires a very large dataset, which is generally not available for medical data. In such scenario where data availability is limited, deep learning can be done with the help of techniques such as data augmentation, transfer learning, etc. Data augmentation comprises of creation of new training data from the existing data using transformations such as reflection, scaling, translation, rotation, etc. The augmented data can then used to train CNN. In application where data augmentation is difficult or if the augmented dataset is not large enough for training CNN, transfer learning using existing deep architectures pretrained with a very large dataset can be used. Transfer learning can be done by either fine tuning a pretrained CNN using the augmented training data or by using CNN as a fixed feature extractor.

In this thesis, we explore CNN feature extraction by transfer learning using a pre-trained CNN architecture, AlexNet (Krizhevsky *et al.* 2012). AlexNet is a pretrained CNN that is trained with more than a million images to classify 1000 image categories. AlexNet consists of five convolutional layers and three fully connected layers. Each convolutional layer performs a convolution and maxpooling. AlexNet captures high-level texture features in images with each higher convolutional layer. CNN features are extracted from the last fully connected layer of AlexNet, after removal of the final classification layer, and used to train other classifiers such as LR, SVM and KNN.

Feature selection

The raw texture images are resized to $227 \times 227 \times 3$, in order to train the images using AlexNet. The grayscale texture image is replicated to all the 3 channels. The images are then augmented using reflection. Augmentation using translation, scaling and rotation of the texture images are not considered as it may affect the appearance of texture in original trabecular texture images. For instance, the distal radius ROI is extracted from the largest fitting circle at the distal end of the vertically aligned radius bone. Scaling of these images affects the size of trabeculae in the region. Translation and rotation affects the spatial and oriental distribution of the trabecular network. The augmented data is fed as input to AlexNet, and CNN features are extracted. This is implemented in Matlab[®] R2017b.

The feature dimension of the CNN features extracted using AlexNet is 4096. The cortical features (*CCT*, *CA*, *PCA_b*, *BNI*) are combined with CNN features that results in a feature dimension of 4100. In order to reduce the high dimensional feature space of the combined cortical and CNN features, feature transformation using PCA is done. The principal components that capture 90% variance in the combined cortical and CNN features are selected and used to train classifiers.

Table 5.18: Performance metrics of the classifiers trained with cortical and CNN features on test data using holdout validation and 10-fold cross validation

Validation	Classifier	TP	FP	TN	FN	Sn	Sp	PPV	NPV	Acc	F1-score
Test data	LR	43	69	29	9	82.7	29.6	38.4	76.3	48.0	52.4
	SVM	27	22	76	25	51.9	77.6	55.1	75.2	68.7	53.5
	KNN	41	68	30	11	78.8	30.6	37.6	73.2	47.3	50.9
10-fold cross validation	LR	90	39	81	30	75.0	67.5	69.8	72.9	71.3	72.3
	SVM	88	22	98	32	73.3	81.7	80.0	75.4	77.5	76.5
	KNN	109	64	56	11	90.8	46.7	63.0	83.6	68.8	74.4

Classifier

The features extracted are used to train LR, SVM and KNN classifiers. CNN features are extracted from 60 images belonging to H group and 60 images belonging to LBM group of Indian sample data. The training set, after data augmentation by reflection, consists of 240 images. PCA captures 90% variance in the combined cortical and CNN features of the training data using 106 principal components, which are selected as feature set FS-7. Classifiers are trained with FS-7 on the training set and tested on 150 test images, comprising of 24 unseen augmented test images of Indian sample data and 126 augmented test images of Swiss sample data. Performance of the classifiers on the test data are shown in Table 5.18. Performance of classifiers trained with FS-7 using 10-fold cross validation on the training data are also shown.

As observed in Table 5.18, SVM gives the best performance with test accuracy of 68.7% using holdout validation and 10-fold cross validation accuracy of 77.5%. The 10-fold cross validation of LR and KNN shows accuracy of 71.3% and 68.8%, respectively.

There is no reported work on deep learning on trabecular texture of distal radius. Texture analysis of calcaneal radiographic images have been explored using deep features. Pretrained CNN architectures such as VGG-M, VGG-F and VGG-S, were used to extract CNN features from 116 calcaneal images (Paul *et al.* 2017). Features were selected using relief-f and symmetric uncertainty feature ranking and trained using different classifiers. The best 10-fold cross validation accuracy of 79.3% was obtained with random forest classifier trained using features extracted from VGG-M. However, the test accuracy obtained with 58 blind images was only 44.8%. Nasser *et al.* (2017)

used stacked sparse autoencoder to extract deep features from 32×32 image patches of 87 calcaneal radiographs. An accuracy of 95.5% was obtained by training a linear SVM classifier using 10-fold cross validation. Hence, transfer learning using deep features is promising for trabecular texture analysis of radiographs. However, CNN did not show good results in this work due to the lack of sufficient data. The use of a larger dataset was limited by availability of funding resources.

5.4 DISCUSSION

As discussed in Chapter 2, related work on radiographic texture analysis of trabecular bone using distal radius is limited. Therefore, previous work on diagnosis of osteoporosis using texture analysis of calcaneal radiographs are used for comparison with the results obtained in this work. Table 5.19 shows the cross validation results of classifiers trained on calcaneal radiographic texture features and our proposed classifiers trained on combined cortical and trabecular features of hand and wrist radiographs. Most of the previous work on texture analysis of radiographs use manual segmentation of ROI by experts using anatomical landmarks.

Cortical features combined with GLRLM and Laws's mask texture features, selected using statistical t -test, achieve the best cross validation accuracy of 81.7% using weighted KNN classifier. CFS feature set comprising of cortical features, histogram features, GLCM and MGM texture features shows 10-fold cross validation accuracy of 75.8% with SVM classifier. Combination of cortical features with LLBP, horizontal LLBP and vertical LLBP gives 10-fold cross validation accuracy of 77.5%, 79.2% and 74.2%, respectively. From Table 5.19, it is observed that our proposed classifiers perform better than related work on distal radius radiographs and work on calcaneal radiographs using fractal analysis, statistical and structural features (Lee *et al.* 2008; Yger 2014; Houam *et al.* 2014; Zheng and Makrogiannis 2016; Harrar *et al.* 2018). However, it does not perform as good as the classifiers reported in recent work that uses wavelet transform, fractional Brownian motion, etc. (Tafraouti *et al.* 2017; El Hassouni *et al.* 2017; Singh *et al.* 2017; Oulhaj *et al.* 2017*a,b*). The texture analysis methods

Table 5.19: Comparison of performance metrics of classifiers trained on bone radiographic texture analysis in literature

Sl no.	Texture features	ROI (Segmentation)	Dataset	Classifier	Sn	Sp	PPV	NPV	Acc	F1-score	Reference
1	Wavelet Haar	Marginals-	Calcaneal (Manual)	SVM	62.1	65.5	64.3	63.3	63.8	63.2	Yger (2014)
2	1D LBP		Calcaneal (Manual)	KNN	-	43.9	-	-	71.3	77.2	Houam <i>et al.</i> (2014)
3	Fractal dimension, wavelet analysis, Gabor, LBP, DFT, DCT, Laws masks, edge histogram and GLCM		Calcaneal (Manual)	RF	74.1	74.1	-	-	74.1	-	Zheng and Makrogiannis (2016)
4	1D projection modeled as fractional Brownian motion		Calcaneal (Manual)	SVM	96.9	97.6	-	-	94.5	94.3	Tafraouti <i>et al.</i> (2017)

Sl no.	Texture features	ROI (Segmentation)	Dataset	Classifier	Sn	Sp	PPV	NPV	Acc	F1-score	Reference
5	Fractional Brownian model and Rao geodesic distance	Calcaneal	348 cases & 348 controls	KNN	97.8	95.4	-	-	96.6	96.5	El Hassouni <i>et al.</i> (2017)
6	Histogram and GLCM and PCA analysis	Calcaneal (Manual)	87 cases & 87 controls	SVM	97.7	95.4	95.5	97.7	96.6	96.6	Singh <i>et al.</i> (2017)
7	Anisotropic discrete dual-tree wavelet transform	Calcaneal (Manual)	87 cases & 87 controls	SVM	-	93.1	92.9	91.0	91.9	91.9	Oulhaj <i>et al.</i> (2017a)
8	Wavelet decomposition and parametric circular models	Calcaneal (Manual)	87 cases & 87 controls	SVM	100	92.5	91.9	100	95.9	95.8	Oulhaj <i>et al.</i> (2017b)
9	Oriental fractal analysis	Calcaneal (Manual)	87 cases & 87 controls	-	72.0	71.0	72.0	71.0	71.8	72.2	Harrar <i>et al.</i> (2018)
10	BMD, fractal, histomorphometric and skeletal measures	Distal radius	47 cases & 47 controls	SVM	79.0	66.0	-	-	-	-	Lee <i>et al.</i> (2008)

Sl no.	Texture features	ROI (Segmentation)	Dataset	Classifier	Sn	Sp	PPV	NPV	Acc	F1-score	Reference
11	Proposed method	Distal radius (Automated)	60 cases & 60 controls								
(a)	FS-1			KNN	78.3	85.0	83.9	79.7	81.7	81.0	
(b)	CFS			SVM	86.7	65.0	71.2	83.0	75.8	78.2	
(c)	FS-6(b)			SVM	88.3	66.7	72.6	85.1	77.5	79.7	
(d)	FS-6(c)			LR	81.7	76.7	77.8	80.7	79.2	79.7	
(e)	FS-6(d)			SVM	88.3	60.0	68.8	83.7	74.2	77.4	

LR- Logistic regression, RF- Random Forest

mostly used in this thesis capture features in the spatial domain. As the dataset consists of images acquired from different radiography machines at different image acquisition conditions, it is helpful to use texture analysis methods that are less dependent on the illumination variations in images. Use of better texture analysis methods that capture the texture features in transformed domain can help to further improve the classification. Deep learning using CNN is a promising method for extraction of rich texture features. However, this is constrained by the limited availability of data.

5.5 CONCLUSION

In this work, we investigate the ability of cortical radiogrammetric and trabecular texture features to detect subjects with low bone mass due to osteoporosis. Statistical, structural and transform-based texture features are used. Features are selected based on the significance results of statistical t -test, feature ranking by Pearson correlation analysis and feature transformation using PCA. Classifiers are trained for Indian and Swiss sample population. Classifiers trained with features selected using independent sample t -test achieves best results as compared to feature selection by correlation ranking and PCA. ANN classifier trained using significant cortical and texture features (GLRLM and Laws' masks), FS-1, of Indian sample data achieves the best test accuracy of 90.0%. A 10-fold cross validation using KNN achieves the best performance with accuracy of 81.7%. A linear regression model developed with the same set of features achieves a highly significant correlation of 0.671 with DXA-BMD of lumbar spine.

We then investigated texture features (histogram features, GLCM, MGM and Gabor) that are significant to both Indian and Swiss data. Three sets of combined cortical and texture features are selected using independent sample t -test: features significant to both Indian and Swiss data (CFS), features optimal to Indian and Swiss data separately (OFS-I and OFS-S). ANN classifiers are trained for Indian and Swiss population separately using the common and optimal features. Classifiers trained for an ethnic group with the optimal set of features (overall accuracy of 91% with Indian data and 94% with Swiss data) shows better performance than with the common set of features

(overall accuracy of 90% with Indian data and 89% with Swiss data).

In a practical scenario, it is difficult to train different classifiers for different ethnic groups and hence it is essential to develop a common classifier that can be used for many population samples. The performance of the CFS features trained on other classifiers are explored. Weighted KNN shows a better test accuracy of 96% as compared to logistic regression and SVM classifiers. Cross-validation using 10 folds are also analyzed to show the performance of the classifiers using CFS features. SVM achieves the best cross-validation accuracy of 75.8%. The performance of classifiers trained on CFS features is compared with that of classifiers trained on LBP, LLBP and its variants for Indian and Swiss sample data. Classifiers trained on CFS features show the best performance in terms of test accuracy.

CNN features extracted from AlexNet was combined with cortical features and trained on LR, SVM and KNN classifiers. SVM achieves the best test accuracy of 68.7% and 10-fold cross-validation accuracy of 77.5%, as compared to LR and KNN.

In summary, for classifiers trained with Indian sample data, the best performance using holdout validation was obtained for ANN classifiers trained with FS-1 (test accuracy of 90.0%) and CFS (test accuracy of 92.9%). Weighted KNN achieves the best 10-fold cross-validation accuracy of 81.7% with feature set FS-1. For classifiers trained and tested with Indian and Swiss sample data, the best performance using holdout validation was obtained for weighted KNN classifier trained with CFS (test accuracy of 96.2%).

The clinical use of the proposed prescreening tool involves acquisition of a hand and wrist X-ray image of the subject using digital or computed radiography, which is available in almost every hospital in India. The ROIs at the third metacarpal bone and distal radius are automatically segmented from the radiographic images and significant features are extracted. These features are fed into the trained classifier to diagnose the subject as either healthy or having low bone mass. Those subjects diagnosed with low bone mass can be referred to experts for detailed examination and treatment.

CHAPTER 6

CORTICAL VOLUMETRY USING 3D RECONSTRUCTION FROM MULTI-VIEW IMAGES

6.1 INTRODUCTION

In the previous chapters, we discussed the significance of cortical radiogrammetry of the third metacarpal bone of hand in identifying people having low bone mass. These cortical radiogrammetric measurements are measured from radiographic images of the hand. A better cortical bone measurement would be the cortical volume of the metacarpal bone. Calculating the 3D volume of the cortical bone would give better accuracy than with 2D radiogrammetric measurements. However, using 3D imaging modality such as QCT to find the cortical bone volume is expensive. A feasible solution to find the cortical bone volume at a low cost would be to capture a few radiographic images of the bone at different angles and reconstruct a 3D model of the bone from these images. In this chapter, we propose a low cost method to estimate the cortical bone volume of the third metacarpal bone shaft using radiographic images acquired from three views, namely Postero-Anterior (PA) view and two oblique views at 45^0 and 135^0 . Three dimensional reconstruction of metacarpal bone from multi-view radiographic images of the hand for early diagnosis of osteoporosis is a novel approach.

6.2 RELATED WORK

There are mainly two methods for 3D reconstruction of objects from multi-view images- active and passive. In the active method, a dedicated camera with special light effects is used to capture the depth information. Whereas in passive method, depth information is not available directly. Calculation of the depth of objects will require

at least two images of the scene. Two or more cameras, whose position or motion is known, are used to simultaneously capture the scene. The images could be stereo-images, mimicking the human eye, or biplanar images having orthogonal views of the object.

The passive method is most commonly used in orthopedic applications for 3D modeling of a bone, where a few radiographic images of the object is acquired, either simultaneously using two or more X-ray sources or by acquiring the images at various known positions of the X-ray source and 3D reconstruction of the bone is done with the help of a template model of the bone. The various stages involved in the 3D reconstruction of an object from multi-view images are (1) camera calibration, (2) segmentation of the object, (3) registration using feature point detection and mapping, and rigid and non-rigid registration, (4) reconstruction, and (5) surface generation and smoothing.

Camera calibration helps to preserve the metric information of the reconstructed image. The multi-view radiographic images of the bone are acquired by keeping the X-ray source at a fixed distance from the object and at orthogonal orientations. The radiographic images acquired are stored as DICOM images. The X-ray source to object distance and pixel dimension information is obtained from the DICOM header file. The bone of interest which is to be reconstructed is segmented from the radiographic images. Most of the related work use manual segmentation for the extraction of the ROI.

The next stage of the 3D reconstruction is registration of the objects in the multi-view images. Registration comprises of feature detection, feature matching and alignment. The features are detected in the images and a similarity measure is used to match the features. The corresponding features are mapped and aligned to form the model. Feature correspondence matching is usually done using deformable registration. Deformable registration methods may be based on physical model, interpolation and knowledge. Physical model based registration methods comply with a physical model such as elastic body model, viscous fluid flow, diffusion model, diffeomorphic model etc. But the deformation of objects may not always behave according to a physical model or a natural law. Interpolation based registration methods construct the deformation field by using interpolation and approximation theory. Such methods include

radial basis function, elastic body spline, free form deformation, etc. Knowledge based registration methods like finite element method use prior information for deformation of objects.

The feature points can be aligned using different kinds of transformation, such as rigid, affine and perspective transformation. Rigid transformation includes translation, rotation and scaling of objects. It preserves angles and curvature, and gives a good approximation with few parameters. It can be determined with two control points. Affine transformation includes translation, rotation, scaling as well as shear of objects. It preserves straight and parallel lines, but do not preserve angles or lengths. It can be determined by three control points. Perspective projection transformation preserves concurrency, collinearity and straight lines but not parallel lines. It can be determined using four control points. If the distance of the object from the camera is very large, perspective projection approximates to affine transformation.

Surface generation is the process of conversion of 3D point cloud to surface. This includes preprocessing to smoothen out noise and ensure that the points are evenly distributed throughout the cloud. Then, the global topology of the surface of the object is determined by deriving the relationship of the neighboring pixels between adjacent parts of the surface. This is followed by generation of polygonal surface by triangulation. Triangular or tetrahedral networks are created with constraints imposed to preserve the topology. The input cloud data is partitioned into its simplest elements and vertices, edges and faces that meet only shared edges are generated. Surface triangulation methods may be 2D, $2\frac{1}{2}$ D and 3D. 2D triangulation methods generate triangles that intersect only at shared edges and vertices. One such method is the Delaunay triangulation. Delaunay triangulation optimizes several measures such as length of edges, area, etc. simultaneously. $2\frac{1}{2}$ D triangulation method use a set of points in a plane with a unique elevation at each point. It takes the weighted average of elevation of vertices of the triangle containing the point. 3D triangulation, also called tetrahedralization, takes point clouds or polyhedron and partitions them into a collection of tetrahedra that meet only at shared faces. Finally, a post-processing is done for edge corrections, hole filling, triangle insertion, etc.

Three dimensional reconstruction of bones from multi-view radiographic images, for the femur bone, spine, etc. are reported. Statistical shape models (SSM) have been used for the 3D shape reconstruction of the distal femur from stereo X-ray images (Baka *et al.* 2011). Projections of 3D shape and pose estimate are taken and compared with the X-ray contours, automatically detected using Canny edge detector, to find the closest edge correspondence. A weight is assigned to every landmark using 3D distance calculated using the correspondence and angle between normal to the projection points and corresponding image gradients. This provides robustness to incorrect and noise edges. This orientation weighting is used for the reconstruction of the distal femur using SSM. They have tested the method with data from 30 patients and 13 cadaver bones. Non-rigid reconstruction from the biplane fluoroscopy using the SSM (3D-2D) showed root-mean-square point-to-surface (RMS P2S) error of 1.68 mm and average edge-to-surface distance of 0.96mm and took about 5 minutes computation time. SSM to ground truth data (3D-3D) correspondence showed RMS P2S of 0.78 mm and average edge-to-surface distance of 0.84 mm.

Boussaid *et al.* (2011) proposed 3D reconstruction of the proximal femur using ASM. ASM model of the proximal femur was constructed using segmented CT data. The silhouette of the ASM model was extracted by projecting silhouette edges in 2D planes. The contours in 2D planes were automatically detected using geodesic active regions and a rigid and deformable registration is done sequentially. The consistence between these silhouette images and the corresponding X-ray images is computed and the set of parameters used to build the ASM until convergence is achieved. The training is done using 17 surface models and tested on 12 image pairs, Antero-Posterior (AP) and Medio-Lateral (ML) views of dry femur and 4 in-vivo images. The error of the reconstructed model as compared to CT data is 1.5 mm.

Three dimensional reconstruction of spine has been done from PA and lateral view radiographs using contour matching by deformation tolerant generalized hough transform for the estimation of vertebral orientation and location (Zhang *et al.* 2013). This method uses vertebral contours directly and is not based on landmark or statistical inferences. It is robust to missing points, as the information from the whole contour is used,

rather than just the contour points. Spinal midline is first manually identified, followed by finding the best match of the 3D projections with the 2D vertebral contours using deformation tolerant generalized hough transform. This method was evaluated using spinal radiographs from 15 scoliotic patients and a spine model in 24 poses. Accuracy was within 2.8 degree for orientation and 2.4 mm for location. However, this method failed for severely deformed scoliotic vertebrae.

Quijano *et al.* (2013) used digitally reconstructed radiographs from CT scans for the 3D reconstruction of lower limb bones. Anatomical landmarks were obtained from the radiographs, from which main descriptors of the bones were defined. A set of descriptive parameters, obtained using multilinear partial least squares regression, were combined with the main descriptors to form a statistical model called Simplified Personalized Parametric Model. A generic 3D mesh was deformed towards the Simplified Personalized Parametric Model using a rigid global moving least square deformation and a local deformation using the kriging interpolation. This method was implemented on a CT database with 56 cadaveric femurs and 24 cadaveric tibias. A mean shape accuracy of 1.3 mm was obtained for both femur and tibia. The reproducibility of femoral and tibial torsion were 5 degree and 4.2 degree, respectively.

Zheng (2013) proposed 3D reconstruction of proximal femur using PA and ML view radiographic images, for the application of total hip arthroplasty, using a two-stage method. The first stage is partial least squares regression training, where independent statistical shape, displacement and appearance models are used to train partial least squares regression to produce a patient-specific displacement field and patient-specific appearance model. This is followed by 2D/3D shape and intensity reconstruction stage, in which a patient-specific surface model is created from the AP and ML images using feature based 2D/3D surface reconstruction. Finally, patient-specific volumetric intensity distribution is obtained by non-rigidly deforming the patient-specific appearance model to the patient-specific volume using the estimated patient-specific displacement field. This method was tested on CT data of 20 cadaveric proximal femurs. Leave-one-out cross-validation showed average reconstruction error of 0.77 mm, average correlation coefficient of 0.91 ± 0.03 , and an average computation time of 15 seconds.

Karade and Ravi (2015) proposed to reconstruct a patient-specific 3D model of the proximal femur bone using biplanar radiographs of the knee. Prior shape information of the femur is used by creating a template model from CT scans of the knee. The projections of the template model in AP and ML planes were aligned with the corresponding radiographic views of the patient using Iterative Closest Point (ICP) and Self-Organizing Maps (SOM). The 2D-2D correspondence between the projection and X-ray contour points were translated to 2D-3D correspondence using Laplacian Surface Deformation (LSD). The deformation of the template model was done iteratively in both views until the projection and X-ray contours aligned. This method was tested on 22 sets of simulated images of CT and 5 sets of real X-ray images and showed a mean P2S error of 1.2 mm and computation time of less than a minute.

6.3 THREE DIMENSIONAL RECONSTRUCTION OF THIRD METACARPAL

The proposed methodology for 3D reconstruction of third metacarpal bone and cortical volume estimation is shown in Figure 6.1. The cortical volume of the metacarpal bone shaft is extracted by 3D reconstruction of the outer and inner walls of the bone. The basic principle of the 3D reconstruction is that the subject-specific model of the metacarpal bone of a subject can be produced from a common template model, by deforming the template such that it gives the same projections in the three views as that of the X-ray images. A template model of the third metacarpal bone is created from segmentation of a CT scan of the hand. This template model is deformed to create subject-specific models of the third metacarpal bone of other subjects. The projection of the template model in multiple views are registered with the X-ray image contours of the corresponding views. The template model is deformed iteratively according to the changes in the projection contours in each views, in order to create the subject-specific model of the third metacarpal bone. The cortical bone shaft of the reconstructed metacarpal bone is extracted by discarding the head and base regions of the bone and cortical volumetric measurements are determined from the 3D metacarpal bone shaft.

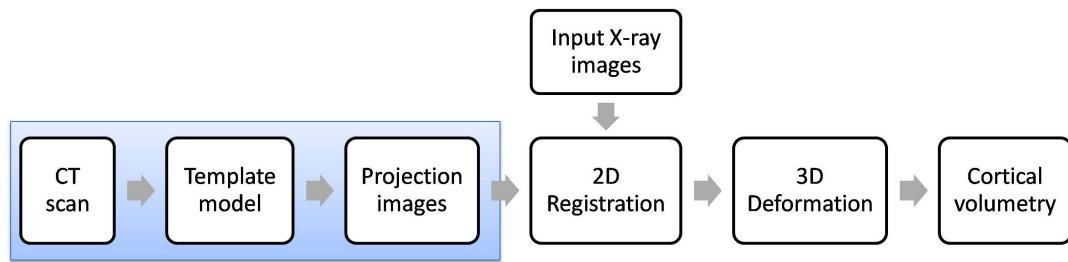


Figure 6.1: Flowchart of the proposed methodology for cortical volumetry

The methodology is similar to the work done on the 3D reconstruction of femur bone by Karade and Ravi (2015). The femur bone was modeled using two image views, namely AP and ML, as described in section 6.2. Three dimensional reconstruction of third metacarpal bone using ML view is difficult because of the large overlap with other metacarpals in the lateral view. Hence, two oblique views of the hand (45° and 135°) along with the PA view of the hand is considered in this work for the 3D reconstruction of the third metacarpal bone, as shown in Figure 6.2. The oblique view hand radiographs are acquired at precise angles with the help of a sponge phantom that do not obstruct the acquisition of bone images using radiography. The tubular bone shaft region of the third metacarpal bone is reconstructed for the volume estimation of the cortical bone. Hence, the outer and inner bone walls of the third metacarpal bone are individually reconstructed using the proposed methodology.

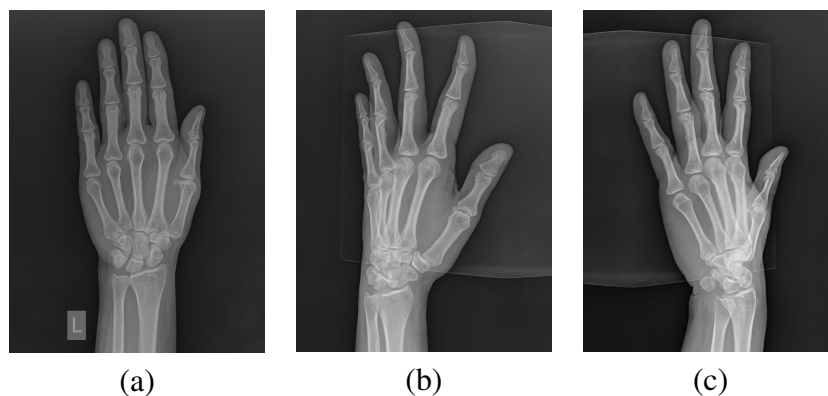


Figure 6.2: Multi-view radiographic images of the hand used for 3D reconstruction: (a) PA view, (b) 45° oblique view and (c) 135° oblique view

6.3.1 Creation of 3D template model

A 3D template model of the third metacarpal bone is created using a CT scan of the hand. The hand CT scan is contrast enhanced and segmented by intensity thresholding using the open-source software, 3D Slicer[®] (Fedorov *et al.* 2012). A lower and upper threshold values are manually set for the thresholding such that only the bone regions of the hand are segmented. The third metacarpal bone is then extracted by eliminating all the other bones. The segmented third metacarpal bone is smoothed and exported as a 3D point cloud.

Since the metacarpal is a hollow bone and the cortical volume is measured from the cortical bone alone, the outer and inner walls of the metacarpal are individually modeled and the difference in their volumes is measured as the cortical volume. In order to create separate template models for the outer and inner bone walls, the 3D point cloud of the third metacarpal bone is separated as an outer mesh and inner mesh using the open-source software, Blender[®] (Blender 2017). The density of the meshes are reduced by Poisson surface reconstruction, using the open-source software MeshLab[®], in order to reduce the computation time of the deformation of the model (Cignoni *et al.* 2008). These meshes are exported as outer bone template and inner bone template models.

6.3.2 3D reconstruction by iterative deformation

The template models of the outer and inner bone walls are deformed iteratively to create the subject-specific bone model, such that it produces the same projection images as that of the X-ray images in the PA and oblique views. For this, the template model of the outer bone is projected onto the PA, 45⁰ and 135⁰ oblique planes to produce a 2D point cloud, using Blender[®] software. The camera distance for the projections are determined from the X-ray source-to-detector distance information in the DICOM header file of the X-ray images. The points in the 2D point cloud are triangulated using Delaunay triangulation. In order to prevent the connection of points outside the bone contour, the edges are constrained by a specifying a minimum distance for the formation of edges. The bone contour is then extracted by removing all triangles that have shared edges

along all three sides, and further removing vertices that have only two adjacent edges. A correspondence dictionary between the 2D contour points and 3D points is created for the three views. Blender[®] software helps in interactive 3D modeling of the bone and has a Python[®] interface, using which the contours of the projection views of the 3D model can be easily extracted.

The bone contours of the X-ray images in the three views are extracted by a manual segmentation of the third metacarpal bone using the open-source software, GIMP[®] (GIMP 2012). It helps to delineate the curved edges of the bone smoothly. Canny edge detection method is used to extract the contour points along the boundary of the segmented bone. Manual segmentation is done as the proposed automated method does not work well in the oblique X-ray views due to the large overlap in the third metacarpal bone with the adjacent metacarpal bones. Thus, a set of three projected outer contours and X-ray outer contours are obtained. Similarly, the projection of the inner bone template in the three views and the corresponding images are used to produce the projected and X-ray inner bone contours.

The projection contour points of the outer bone wall in the PA view is first aligned to the X-ray image contour points in the PA view. For this, a two-step registration may be performed, namely a coarse rigid registration by translation and rotation using ICP algorithm, and a fine non-rigid registration using SOM. ICP helps to align the projection and X-ray contours such that the difference between the closest points of the two contours are minimized. In ICP algorithm, the centroid of the projection and X-ray contours are first aligned. PCA is done to get the principal axes of the projection and X-ray contours and the X-ray contour is rotated such that its principal axes are aligned to those of the projection contour. To equalize the number of points in the projection and X-ray contours, the point along the projection contour which has the least distance with respect to the X-ray contour point is selected to form point pair correspondence. The points along the projection contour not belonging to a point pair correspondence are discarded. A singular value decomposition is then applied to reduce the sum of pairwise distance between the points in the two contours. Figure 6.3 shows the projection and X-ray contours before and after rigid registration using ICP.

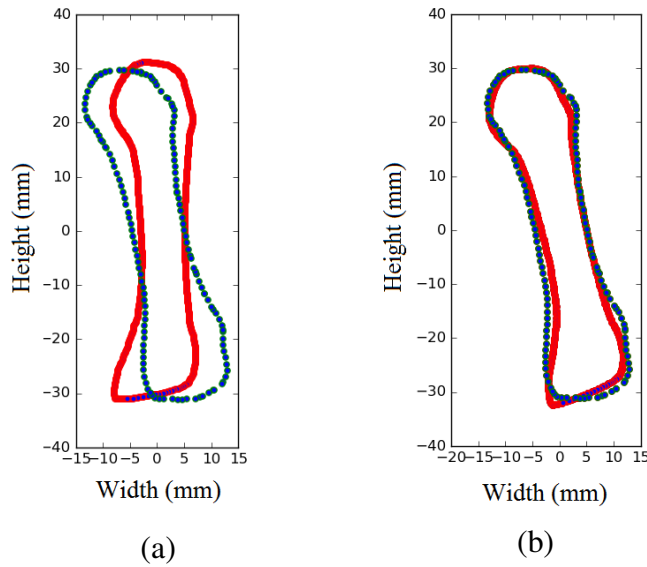


Figure 6.3: Projection contour (in blue) and X-ray contour (in red) (a) before alignment and (b) after rigid registration using ICP.

The rigid registration using ICP is followed by a non-rigid registration using SOM. SOM is a type of unsupervised ANN that helps in dimensionality reduction by using a discretized representation of training data samples. SOM helps to preserve the structural properties of the training samples. Using SOM, the nearest projection contour point to each X-ray contour point is determined and pulled towards the X-ray point along with its neighboring points. The magnitude of the pull depends on the distance of the neighboring points with respect to the projection contour. The closest neighboring points are pulled more towards the X-ray point and the neighboring points further away are pulled less. This helps to preserve the basic shape features. This is iteratively done for all the X-ray contour points until the projection contour is aligned with the X-ray contour. Figure 6.4 shows the projection and X-ray contours before and after non-rigid registration using SOM.

The 2D-2D correspondences of the X-ray and projection contour points after the rigid and non rigid registration is determined. This is converted to 2D-3D correspondence by finding the points in the 3D point cloud that correspond to the projection contour points using ray projections. This 2D-3D correspondences is used for the deformation of the template model. The changes in the projection contour points after registration is reflected onto the 3D template model using LSD. LSD can be employed

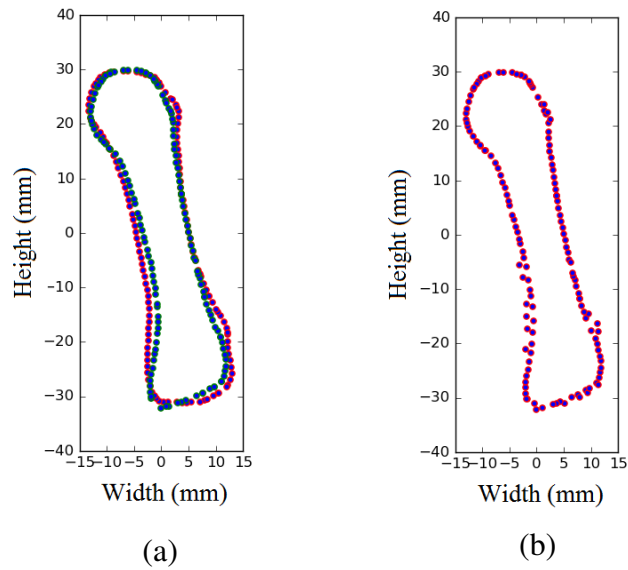


Figure 6.4: Projection contour (in red) and X-ray contour (in blue) (a) before non-rigid registration and (b) projection contour after registration using SOM.

as it helps to preserve the overall topology and shape features, while deforming the template model. In LSD method, each point in the template model is defined, based on differential coordinates, as the difference between the point and its neighboring points. While each point is moved towards its target point, the deformation of the neighboring points is constrained by the Laplacian coordinates. The deformation of the template model using the 2D-3D point correspondences are done using Blender software.

Similarly, the process of contour registration of the projected and X-ray contours and corresponding 3D deformation of the template model is done on the two oblique views. This completes one iteration of the 3D reconstruction in all three views. This 3D reconstruction is repeated for 5 iterations in order to create the subject-specific outer bone model of the third metacarpal bone. The same methodology is applied to the inner bone wall of the template model to create the subject-specific inner bone model of the third metacarpal bone.

6.3.3 Cortical volumetry

The third metacarpal bone is modeled by the 3D reconstruction of the outer and inner bone walls of the metacarpal bone using an outer bone template and inner bone tem-

plate, respectively. The shaft region of the outer bone is extracted by discarding 35% of the bone length from the head and base regions of the metacarpal. The same shaft region is extracted from the inner bone wall. The outer and inner reconstructed bone shafts are re-meshed and converted to solid objects to calculate the volume and surface area in Blender[®] software. The volume of the outer bone shaft and inner bone shaft are determined and denoted as V_{outer} and V_{inner} . Similarly, the surface area of the outer and inner bone shafts, SA_{outer} and SA_{inner} , are measured.

The cortical volumetric measurements extracted from the 3D reconstructed metacarpal bone shaft are cortical volume (CV), ratio of cortical volume to outer bone volume (CV_{OV}), cortical volume normalized by surface area (CV_{SA}) and cortical volume normalized by surface area and length (CV_n). These are computed as

$$CV = V_{outer} - V_{inner} \quad (6.1)$$

$$CV_{OV} = \frac{V_{outer} - V_{inner}}{V_{outer}} \quad (6.2)$$

$$CV_{SA} = \frac{V_{outer}}{SA_{outer}} - \frac{V_{inner}}{SA_{inner}} \quad (6.3)$$

$$CV_n = \frac{CV_{SA}}{L} \quad (6.4)$$

where, L is the length of the metacarpal bone shaft.

6.4 RESULTS AND DISCUSSION

This section discusses about the dataset used for the 3D modeling of third metacarpal bone and the evaluation of the cortical volumetric measurements of the reconstructed bones. The proposed method is implemented using the open-source software tools Blender[®], 3D Slicer[®] and MeshLab[®].

Table 6.1: Clinical characteristics of the study group used for 3D reconstruction of metacarpal bone

Measurements	H (7 subjects) ($\mu \pm \sigma$)	LBM (13 subjects) ($\mu \pm \sigma$)
Age (years)	50.86 \pm 9.92	50.85 \pm 12.03
Height (cm)	157.29 \pm 7.54	159.31 \pm 9.53
Weight (kg)	60.14 \pm 8.09	61.00 \pm 11.36
<i>T</i> -score	-0.2 \pm 0.4	-2.4 \pm 0.8

6.4.1 Dataset

For the work on 3D reconstruction of the third metacarpal bone of hand, hand radiographs of 20 subjects were taken from Tejaswini Hospital, District Wenlock Hospital and A.J.Hospital in Mangalore, Karnataka, India. Men and women above the age of 30 years were included in the study and informed consent was obtained from them. The study protocol was approved by the Institutional Ethics Committee, Kasturba Medical College, Mangalore, Manipal Academy of Higher Education, Karnataka, India. Hand X-ray images are taken from three views, namely PA view and oblique views at 45⁰ and 135⁰, using Digital Radiography Agfa DX-D 300 (X-ray tube voltage=52 kV, X-ray tube current=160 mA, exposure time=32 ms and source-to-object distance in the range of 990 to 1150 mm). DXA scan of the lumbar spine of the 20 subjects were taken using GE Lunar[®] densitometer and CT scans of hand of two subjects were also obtained for the validation of the 3D reconstructed models.

As discussed in Chapter 3, subjects with *T*-score ≥ -1 are healthy (H group) and *T*-score < -1 have low bone mass (LBM group). This dataset comprises of 7 healthy subjects and 13 subjects with low bone mass. The clinical characteristics of this study group is given in Table 6.1.

6.4.2 Validation of 3D bone reconstruction

Figure 6.5 shows the input X-ray images and 3D reconstructed outer and inner model of the third metacarpal bone using the proposed method for a healthy and a LBM subject.

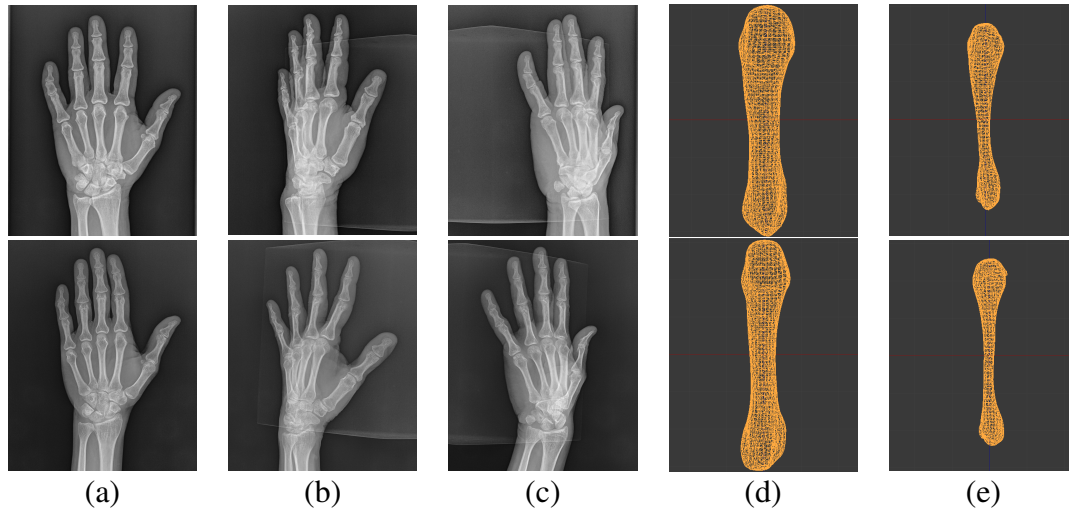


Figure 6.5: Examples of the 3D reconstructed models of the outer and inner bones of the third metacarpal bone for a healthy subject (top row) and a subject with LBM (bottom row) : (a) Hand X-ray image in PA view, (b) hand X-ray image in oblique 45° view, (c) hand X-ray image in oblique 135° view, (d) reconstructed outer bone model and (e) reconstructed inner bone model of the third metacarpal bone using the proposed method. Cortical volumetric measurements of the 3D reconstructed bone shaft are as follows: Healthy subject (top row: $CV = 878.71 \text{ mm}^3$, $CV_{OV} = 0.7672$, $CV_{SA} = 0.6148 \text{ mm}$, $CV_n = 0.0330$), and subject with LBM (bottom row: $CV = 624.64 \text{ mm}^3$, $CV_{OV} = 0.8287$, $CV_{SA} = 0.5853 \text{ mm}$, $CV_n = 0.0314$).

The accuracy of the 3D reconstruction of the metacarpal bone shafts can be evaluated by comparing the bone models with the segmented CT scan of the hand of the same subject. In this dataset, CT scan of hand of only two subjects were available, due to constraints in financial resources, both of which belong to the LBM group. One of the CT scans is used to create the template model, from which the subject-specific models of the remaining subjects are generated. The other CT scan is used to create the ground truth data which is compared with the corresponding reconstructed bone model for the validation of the 3D reconstruction method.

The 3D reconstruction of the outer and inner bone models of the metacarpal bone is done using 5 iterations of the whole process in all three views. The number of iterations for SOM method is fixed to 20.

The metrics used for the evaluation of the 3D reconstructed model with respect to the ground truth are relative volume error, volume overlap error and P2S error. Rel-

ative volume error is the ratio of the difference of the volumes of ground truth and reconstructed bone models to the volume of the ground truth. To calculate the volume error overlap, the ground truth and reconstructed bone models are converted into voxels using dynamic paint tool in Blender[®] software. P2S error between the reconstructed bone model and the ground truth is determined using the open-source software, CloudCompare[®] (CloudCompare 2018). The relative volume error and overlap error are calculated as

$$\text{Relative volume error} = \frac{|V_{GT} - V_r|}{V_{GT}} \times 100 \quad (6.5)$$

$$\text{Volume overlap error} = \left(1 - \frac{A \cap B}{A \cup B}\right) \times 100 \quad (6.6)$$

where, V_{GT} is the volume of the shaft region of the ground truth model, V_r is the volume of the reconstructed bone shaft, A is the set of voxels in ground truth model, and B is the set of voxels in the reconstructed bone shaft.

The bone shaft region used for validation using ground truth is obtained by discarding 30% of the metacarpal bone length from the upper and lower ends of the bone. The reconstructed outer bone shaft shows a volume of 1181.2036 mm^3 and the inner bone shaft shows a volume of 144.9132 mm^3 . The outer and inner volumes of the shaft region of the ground truth model are 1184.4100 mm^3 and 146.500 mm^3 , respectively. Table 6.2 shows the evaluation metrics of the reconstructed outer and inner metacarpal bone shafts with respect to the shaft of the ground truth. The relative volume error and volumetric overlap error of the reconstructed bone are 0.60 and 10.06 for the outer bone and 1.08 and 15.25 for the inner bone, respectively. Mean P2S error of the reconstructed outer and inner bone are 0.21 and 0.15, respectively.

A heat map of the P2S error in the reconstructed outer and inner bone models are created using CloudCompare[®] software. The points in the reconstructed bone which are nearest to the ground truth model are indicated in blue color and the points which are farthest in red color. This helps in easy visualization of the error distribution along the surface of the reconstructed bone models. The heat map of the P2S error of the

Table 6.2: Evaluation metrics of the reconstructed outer and inner bone shafts

Evaluation metrics	Reconstructed outer bone	Reconstructed inner bone
Relative volume error	0.60	1.08
Volumetric overlap error (%)	10.06	15.25
Mean P2S error (mm)	0.21	0.15
SD of P2S error (mm)	0.15	0.12
Min P2S error (mm)	0.00	0.00
Max P2S error (mm)	0.70	0.63

SD- Standard deviation

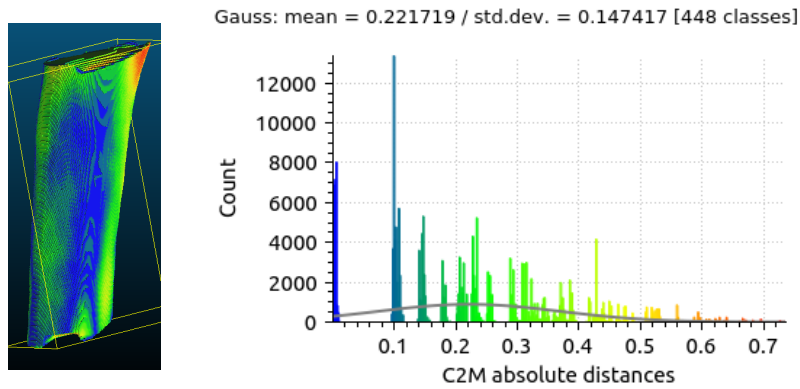


Figure 6.6: Heatmap and histogram of the P2S error of the reconstructed outer bone shaft and ground truth

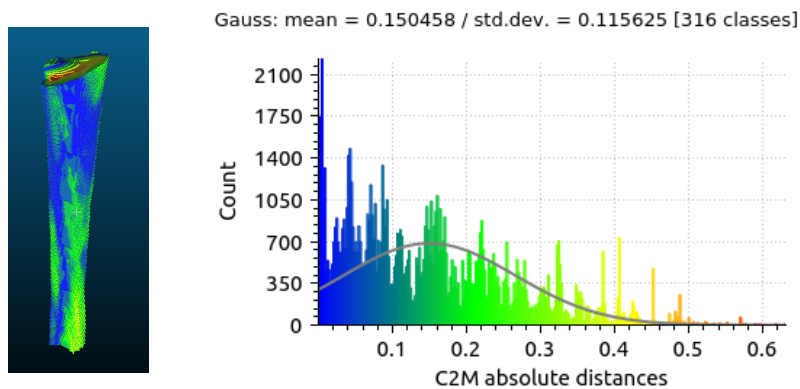


Figure 6.7: Heatmap and histogram of the P2S error of the reconstructed inner bone shaft and ground truth

reconstructed outer and inner bone models and the corresponding error histogram are shown in Figures 6.6 and 6.7.

Table 6.3: Comparison of CCT measurement of PA projections of 3D reconstructed models with those of manually segmented X-ray images

Images	CCT_{manual} (<i>mm</i>)	CCT_{PA} (<i>mm</i>)	Absolute error (<i>mm</i>)	Error percentage (%)
1	4.23	3.52	0.71	16.71
2	3.94	3.49	0.45	11.48
3	3.56	3.22	0.34	9.64
4	4.50	3.90	0.60	13.28
5	3.93	3.45	0.48	12.13
6	5.06	4.52	0.53	10.57
7	4.57	3.94	0.63	13.82
8	5.10	4.46	0.64	12.53
9	3.88	3.52	0.36	9.24
10	4.86	4.39	0.46	9.55
11	4.37	3.79	0.58	13.32
12	3.09	2.46	0.63	20.43
13	4.28	4.02	0.26	6.02
14	4.84	4.24	0.60	12.41
15	3.82	3.71	0.11	2.79
16	4.61	3.85	0.76	16.53
17	4.19	3.92	0.27	6.47
18	3.84	3.59	0.25	6.63
19	4.85	4.24	0.61	12.66
20	4.17	3.87	0.30	7.29
Mean			0.48	11.18

6.4.3 Validation with manually segmented images

The validation of one 3D reconstructed bone is done using 3D ground truth data obtained from CT scan of the same subject. Due to limited funding available, the CT scans of 18 subjects were not taken. As there is no 3D ground truth data to validate the 3D reconstructed models of 18 subjects, the PA projections of the 3D reconstructed bones are compared with the CCT measurements of the PA X-ray images. The CCT measurement of the PA projected view of the 3D reconstructed bone shaft is compared with the corresponding CCT measurement of the X-ray image. Table 6.3 shows the error of the CCT measurements of the projected views and those of the manually segmented X-ray images. The mean absolute error in CCT of the projected views is 0.48 mm and the mean error percentage is 11.18%.

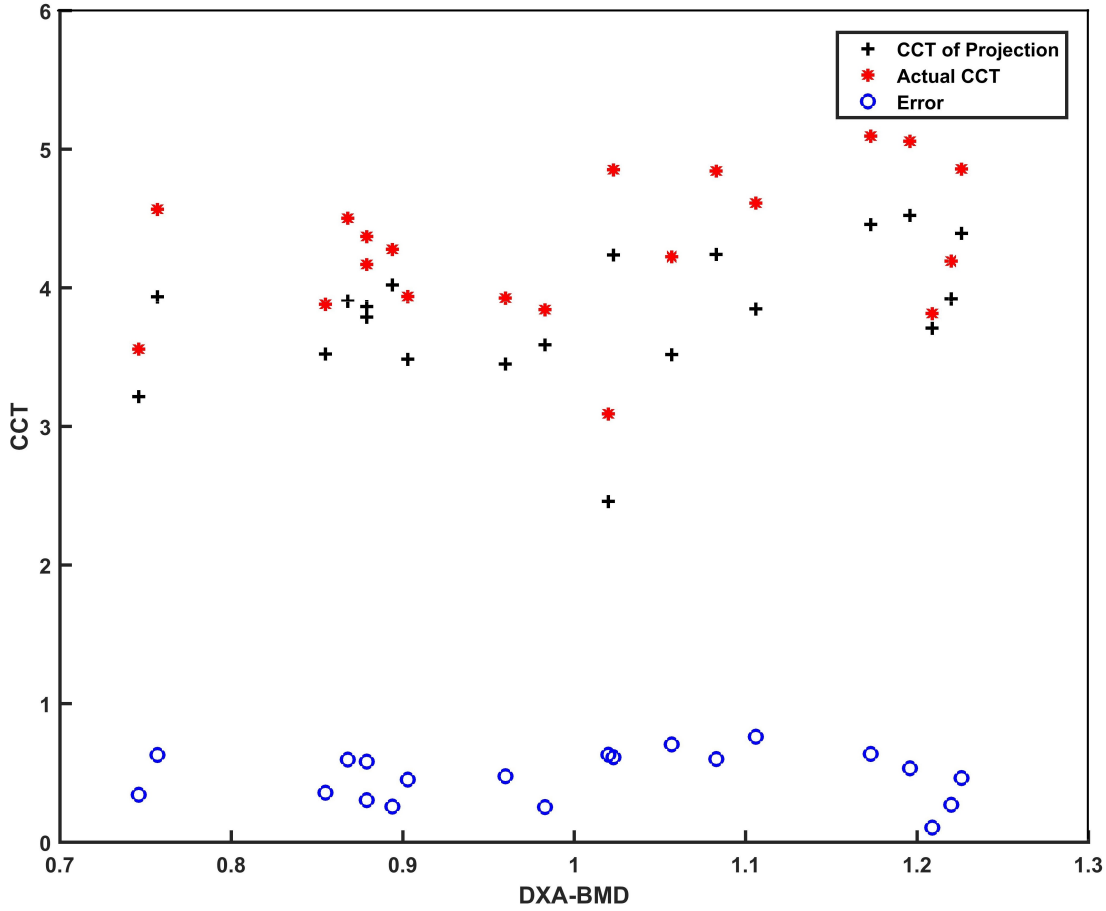


Figure 6.8: Error distribution in CCT of projected images and X-ray images

Figure 6.8 shows the plot of the CCT of projections of deformed 3D models, actual CCT from manually segmented images and the error in CCT. We observe that the error is positive for all the images and thus the projections of deformed models are thinner than the original X-ray images. Since the error margin is similar for all the reconstructed models ($0.48 \pm 0.18 \text{ mm}$), we could expect better results by fine tuning the parameters used for the 3D reconstruction using a larger dataset with ground truth.

6.4.4 Statistical analysis

The cortical volumetric measurements extracted from the 3D reconstructed metacarpal bone shafts of the healthy and LBM groups are shown in Table 6.4. Correlation analysis of the cortical volumetric measurements with CCT of X-ray images, CCT_{manual} and DXA-BMD of lumbar spine is shown in Table 6.5. The correlation analysis is

Table 6.4: Cortical volumetric measurements extracted from the 3D reconstructed models

Measurements	H (7 subjects) ($\mu \pm \sigma$)	LBM (13 subjects) ($\mu \pm \sigma$)
$CV(mm^3)$	837.17 ± 192.12	803.77 ± 195.07
CV_{OV}	0.81 ± 0.05	0.77 ± 0.08
$CV_{SA}(mm)$	0.64 ± 0.07	0.59 ± 0.07
CV_n	0.03 ± 0.00	0.03 ± 0.00
$CCT_{PA}(mm)$	4.16 ± 0.33	3.62 ± 0.45

Table 6.5: Correlation analysis of cortical volumetric measurements of the 3D reconstructed models

Measurements	CCT_{manual}	DXA-BMD
CV	0.3169	0.0913
CV_{OV}	0.7373 ‡	0.2485
CV_{SA}	0.8662 §	0.2879
CV_n	0.7752 §	0.3773
CCT_{PA}	0.9419 §	0.4646*

* $p < 0.05$, † $p < 0.01$, ‡ $p < 0.001$, § $p < 0.0001$

done using Pearson correlation test for 19 data samples after removing outliers (T -score = -3.9). Among the cortical volumetric measurements, normalized cortical volume, CV_n , shows the highest correlation of $r = 0.3773$ with DXA-BMD, but it is not significant. This could be due to the small sample size used for the correlation analysis. All the normalized cortical measurements show a highly significant correlation with CCT of X-ray images with $p < 0.001$. The highest correlated cortical volumetric measurement with CCT_{manual} is CV_{SA} with $r = 0.8662$ and $p < 0.0001$. The CCT of manually segmented images in turn shows a significant correlation with DXA-BMD ($r = 0.4596$, $p < 0.05$). Although the cortical volumetric measurements obtained using the proposed reconstruction method does not show a significant correlation with DXA-BMD, it can be concluded that improving the 3D reconstruction method to reduce the error in CCT measurement using a larger dataset will help to produce a significant correlation with DXA-BMD, which then can be further used for an improved model of the prescreening tool for osteoporosis.

6.4.5 Using the new data to validate the trained classifiers

The 20 subjects belonging to this study group used for 3D bone reconstruction are not part of the dataset used in the previous chapters. Hence the hand X-ray images (PA view) of these 20 subjects are used as test data to validate the trained classifiers of Chapter 5. The X-ray images are segmented using the proposed segmentation method to segment the metacarpal bone for cortical radiogrammetry and the distal radius for texture analysis. Out of the 20 images, the proposed segmentation method segmented the third metacarpal bone shaft in 16 images and the distal radius in 16 images. The total number of poorly segmented images are 6. The reasons for failure of the proposed segmentation in this dataset can be attributed to incorrect localization of the third metacarpal centroid and the wrong detection of the anatomical landmark DRUJ.

The remaining 14 images are used for the extraction of cortical radiogrammetric features and trabecular texture features, and tested on the trained classifiers proposed in Chapter 5. Table 6.6 shows the classification results of the 14 images using the trained Indian classifiers. KNN and LR classifiers trained using CFS features show the best classification with 2 images and 3 images being misclassified, respectively. The ANN classifiers trained with FS-1 and CFS also show a low misclassification of 4 images.

Table 6.6: Classification results of the automatically segmented 14 images using the trained Indian classifiers

Feature set	Classifier	TP	FP	TN	FN	Total misclassified
FS-1	ANN	3	3	7	1	4
	LR	3	5	5	1	6
	SVM	3	3	7	1	4
	KNN	3	4	6	1	5
CFS	ANN	3	3	7	1	4
	LR	2	1	9	2	3
	SVM	4	10	0	0	10
	KNN	2	0	10	2	2
FS-6(b)	LR	2	3	7	2	5
	SVM	4	7	3	0	7
	KNN	0	2	8	4	6

6.5 CONCLUSION

Three dimensional reconstruction of the third metacarpal bone using hand X-ray images from three views is proposed. The CT scan of one subject is used to create a template model. The 3D reconstruction of the bone is done iteratively by registration of projection and X-ray contours using ICP and SOM, and deformation of the template model using Laplacian deformation. The outer and inner bone walls of the metacarpal are modeled separately and the cortical bone shaft is extracted. Cortical volumetric measurements of the third metacarpal bone shaft are determined. The proposed method for the 3D reconstruction of metacarpal bone for cortical volumetry is a novel approach and therefore there are no reported reconstruction error results of prior work to compare with. The comparison of 3D reconstructed models of one subject data is compared to its ground truth and obtained good results. The projections of the reconstructed models are compared with X-ray images for validation. The mean error percentage in CCT error shows 11.18%. A limitation of this work is the need for integration of the various software tools being used. For use in clinical practice, there is a need for a user-friendly GUI that hides the multiple modules. The 3D reconstruction method was developed using limited data due to funding constraints. We feel a larger dataset would help to improve the accuracy of the 3D reconstruction method.

CHAPTER 7

CONCLUSION AND FUTURE WORK

7.1 SUMMARY OF THE WORK

This thesis discusses the development of a low cost prescreening tool for early diagnosis of osteoporosis using hand and wrist radiographs. The tool was evaluated using data of 138 persons from Indian sample population and 65 persons from Swiss sample population.

An automated segmentation method for the detection and segmentation of third metacarpal bone shaft using marker-controlled watershed segmentation was implemented. The proposed segmentation method shows a success rate of 89% and 78% in detecting and segmenting the third metacarpal bone shaft in the Indian and Swiss sample data, respectively. The segmentation accuracy of the proposed method and AAM was evaluated by comparing with manual segmentation of five images. Our method achieved better results in segmenting the metacarpal bone shaft, with mean Jaccard measure of 0.90, percent area difference of 0.03, recall of 0.96, precision of 0.94 and F1-score of 0.95. Cortical radiogrammetric measurements were taken from third metacarpal bone shaft. The radiogrammetric measurements of 14 images obtained using the proposed method and AAM were compared with that of the ground truth measurements. In comparison to AAM, the proposed method achieved lesser mean absolute error of 0.08 mm for cortical width and 0.24 mm for medullary width.

An automated segmentation approach to locate and segment the distal radius ROI was also implemented using automatically detected anatomical landmarks and intensity profiles. The proposed segmentation method shows a success rate of 93.5% and 83% in accurately detecting and extracting the distal radius ROI in the Indian and Swiss sample data, respectively. The trabecular bone region used for texture analysis is the

largest square inscribed within the circular distal radius ROI. Statistical, structural and transform-based texture analysis methods such as first order histogram features, GLCM, GLRLM, MGM, Laws's masks, LBP and its variants, and Gabor filter, were applied to extract features from the distal radius ROI.

The significance of the extracted cortical and texture features were analyzed using independent sample *t*-test. Pearson correlation test was used to find the correlation of the features with DXA-BMD of the lumbar spine. The extracted cortical radiogrammetric features showed a high significance in *t*-test in both Indian and Swiss sample data, as compared to the texture features. The cortical features were also more significantly correlated with DXA-LS than the trabecular texture features. Combined cortical and texture feature sets were selected using results of independent sample *t*-test, Pearson correlation ranking and PCA.

The cortical radiogrammetric features and statistical and structural texture features, namely GLRLM and Laws's masks, were first used to train classifiers using Indian sample data. ANN classifier trained with combined cortical and trabecular texture features showed better performance than ANN trained using only cortical features. Thus, the integration of trabecular texture features with cortical radiogrammetric measurements helps to improve the accuracy of classifiers. Feature set FS-1 selected using statistical *t*-test showed better classification accuracy as compared to features selected using correlation ranking and PCA. Among classifiers trained with FS-1, ANN showed the best test accuracy of 90.0% using holdout validation and weighted KNN showed the best cross-validation accuracy of 81.7% using 10 folds. A linear regression model of the feature set FS-1 achieved significant correlation of 0.671 with DXA-LS.

Next, cortical features and statistical, structural and transform-based texture features, namely histogram, GLCM, MGM and Gabor filter, were used to train classifiers using both Indian and Swiss sample data. The significant features, obtained using *t*-test, were divided into a common feature set, CFS, and optimal feature sets, OFS-I and OFS-S. ANN classifiers trained for an ethnic group with the optimal set of features (overall accuracy of 91% with Indian data and 94% with Swiss data) shows better performance than with the common set of features (overall accuracy of 90% with Indian

data and 89% with Swiss data). CFS was further used to train LR, SVM and KNN classifiers. Weighted KNN showed the best test accuracy of 96% using holdout validation and SVM achieved the best 10-fold cross-validation accuracy of 75.8%.

Finally, classifiers were trained using cortical and LBP and LLBP texture features. Though classifiers trained on LLBP features, that capture directional information, showed good cross-validation accuracy, it did not show good test accuracy using holdout validation. Hence, classifiers trained on statistical and structural texture features showed better performance than those trained on LBP and LLBP features.

Summarizing, ANN classifiers trained with FS-1 (Acc of 90.0%) and CFS (Acc of 92.9%) using holdout validation showed the best performance for Indian sample data. Weighted KNN classifier trained with CFS showed the best test accuracy of 96.2% with Indian and Swiss sample data. The best 10-fold cross validation accuracy of 81.7% was obtained using weighted KNN classifier trained with FS-1.

A low cost technique to measure the cortical bone volume of the third metacarpal bone using 3D reconstruction from hand X-ray images in three views (PA, 45⁰ and 135⁰ oblique views) was implemented. This is a novel method. The segmented third metacarpal bone of one CT scan is taken as the template model for 3D reconstruction of the metacarpal bones of the remaining subjects. The outer and inner bone walls of the metacarpal were modeled separately. The 3D reconstruction of the outer and inner bones were implemented by an iterative registration of the bone contours of the template projection and X-ray views using ICP and SOM, and corresponding deformation of the template model using Laplacian deformation. Cortical volumetric measurements were taken from the reconstructed metacarpal bone shafts. The 3D reconstruction of metacarpal bone shafts were evaluated by comparing the *CCT* of the PA projection of the reconstructed models with the manually segmented PA X-ray images of 20 subjects and a mean absolute error of 0.48 mm (11.18%) was obtained.

7.1.1 Computation time

The techniques used to develop the prescreening tool is implemented using Matlab[®] R2016b and Image Processing, SDC Morphology, Statistics and Machine Learning

toolboxes for Matlab[®] (Dougherty *et al.* 2003). The processing time of the diagnostic technique after X-ray image acquisition is approximately 1.5 minutes on a PC with 8GB RAM, 64-bit OS and Intel[®] Core[™] i7-4790 CPU @3.60 GHz.

7.1.2 Clinical use

The prescreening tool can be used in clinical practice by acquiring a hand and wrist X-ray image of the subject and loading it into the software. The software will automatically segment the third metacarpal bone and distal radius ROIs from which cortical and trabecular texture features are extracted. The tool will use these features to diagnose if the subject has low bone mass. Those subjects diagnosed with low bone mass can then be referred to experts for detailed examination and treatment. As the prescreening can be done for the cost of a single hand and wrist radiograph with no additional equipment cost, it can be a promising low-cost technique for mass screening of people in primary health care centres in non-urban areas where DXA is not available.

7.1.3 Limitations

The proposed segmentation method failed for some images due to wrong detection of DRUJ, close proximity of other metacarpal bones, presence of obstacles like bangles, etc. The segmentation method depends on the intensity variations in the image. It works well for images with a good contrast in the hand and background. However, its performance could be lower for images taken under poor exposure conditions, as it results in a poor gradient and binary image. A prior check on the quality of the hand images during acquisition can help to overcome this problem. The accuracy of the segmentation method can be further improved by contrast enhancement techniques.

For the trabecular texture analysis of distal radius, traditional statistical and structural texture features are used. Features that are robust to image intensity variations can help with a better texture analysis. Recent texture analysis methods such as deep learning, bag of features, etc. can be explored to capture the complex features in images. A preliminary analysis of texture features was done using transfer learning of CNN.

However, a very large dataset is required to improve the accuracy of the prescreening tool using deep features.

The prescreening tool classifies subjects into healthy and low bone mass groups. A diagnostic tool that can classify subjects as healthy, osteopenic and osteoporotic groups would be a good cost-effective alternative to DXA in clinical practice. This work has not addressed a three-group classification due to lack of sufficient data with T -score < -2.5 to train a 3-group classifier.

Cortical volumetric measurements would be a more accurate and sensitive measurement than CCT in detecting people with low bone mass. The volumetric measurements obtained from the reconstruction method do not show a significant correlation with DXA-LS, due to the small sample size. The accuracy of the 3D reconstruction can be further improved with a larger dataset. Cortical volumetric measurements of the reconstructed bones can be then be used to train classifiers in order to further improve the accuracy of the prescreening tool for diagnosis of osteoporosis.

The limited dataset used for training of classifiers and 3D reconstruction method is a limitation of the research work. To our knowledge, there are no publicly available dataset on distal radius radiographs for diagnosis of osteoporosis. DXA and CT scans, which are necessary for the validation of the work, are expensive. In India, the cost of a DXA scan of the lumbar spine range from Rs.1800 to Rs.4500 and the cost of a hand CT scan is about Rs.3000 (International Osteoporosis Foundation, 2013). For this research work, the acquisition of data from a larger sample population was not possible due to lack of funds.

7.2 EXPERTS' FEEDBACK

This section includes the feedback on the work done, obtained from two experienced orthopaedic surgeons. Different stages of the research work and its clinical relevance are graded from levels 5 to 1. A general feedback of the experts on the work done is also obtained.

Expert's Feedback Form

I have gone through the research work done by Ms. Anu Shaju Areckal (Reg.No:138044EC13F06), PhD student of National Institute of Technology Karnataka (NITK), Karnataka, India, on the topic "Early Diagnosis of Osteoporosis Using Metacarpal Radiogrammetry and Texture Analysis". I have evaluated the results of the developed diagnostic technique and have arrived at the following conclusions.

Sl. No.	Technique	Performance reported (in Indian sample data)	Grading given by Experts				
			5	4	3	2	1
1	Automatic segmentation of third metacarpal bone shaft	89%	✓				
2	Automatic segmentation of distal radius region-of-interest	93%		✓			
3	Automatic extraction of cortical radiogrammetric measurements	Mean error of 0.08 mm for CW and 0.24 mm for MW		✓			
4	Classification accuracy of the prescreening tool	Maximum test accuracy of 81.7% using 10-fold cross validation and 96% using holdout validation		✓			
5	Computation time taken by prescreening tool	About 1.5 minutes on a PC with 8GB RAM, 64-bit OS and Intel® Core™ i7-4790 CPU @3.60 GHz.	✓				
6	Relevance of the prescreening tool for clinical practice	Can be used at the cost of a single hand and wrist radiograph, which is affordable and easily accessible in low economies	✓				

The grading levels are indicated as

5-Excellent, 4-Good, 3-Fair, 2-Bad, 1-Very bad

General feedback on the research work done:

Excellent work to be continued for the benefit of larger group of patients to diagnose & screen population suffering from osteopenia and osteoporosis.

(Name and Signature of the Expert with date and seal)



Dr. B.N. JAGANNATH KAMATH
Professor & 'C' Unit Head
Department of Orthopaedics
K.M.C. MANGALORE

Expert's Feedback Form

I have gone through the research work done by Ms. Anu Shaju Areeckal (Reg.No.138044EC13F06), PhD student of National Institute of Technology Karnataka (NITK), Karnataka, India, on the topic "Early Diagnosis of Osteoporosis Using Metacarpal Radiogrammetry and Texture Analysis". I have evaluated the results of the developed diagnostic technique and have arrived at the following conclusions.

Sl. No.	Technique	Performance reported (in Indian sample data)	Grading given by Experts				
			5	4	3	2	1
1	Automatic segmentation of third metacarpal bone shaft	89%		✓			
2	Automatic segmentation of distal radius region-of-interest	93%	✓				
3	Automatic extraction of cortical radiogrammetric measurements	Mean error of 0.08 mm for CW and 0.24 mm for MW	✓				
4	Classification accuracy of the prescreening tool	Maximum test accuracy of 81.7% using 10-fold cross validation and 96% using holdout validation	✓				
5	Computation time taken by prescreening tool	About 1.5 minutes on a PC with 8GB RAM, 64-bit OS and Intel® Core™ i7-4790 CPU @3.60 GHz.	✓				
6	Relevance of the prescreening tool for clinical practice	Can be used at the cost of a single hand and wrist radiograph, which is affordable and easily accessible in low economies	✓				

The grading levels are indicated as
 5-Excellent, 4-Good, 3-Fair, 2-Bad, 1-Very bad

General feedback on the research work done:

Very well done & excellent research. Will be very useful tool in identifying people with potential osteoporosis.

(Name and Signature of the Expert with date and seal)


 ANU SHAJU AREECKAL
 Jayashree Number:

7.3 FUTURE DIRECTIONS

This work is a pilot study and the results obtained are promising. The prescreening tool needs to be validated over a larger dataset before it can be adopted in clinical practice.

The algorithms developed in Matlab can be implemented as executable C codes, to create a standalone software. It can be integrated into the imaging software used in hospitals for clinical practice.

The 3D reconstruction method developed for measuring the cortical volume of metacarpal bone at a low cost can be further improved using a larger dataset. The cortical volumetric measurements would be a more sensitive measurement of cortical bone density than *CCT*, which is an areal measurement. Hence, incorporating the cortical volumetric measurements along with texture features into the prescreening tool can help to increase the accuracy and sensitivity of the tool.

This research work has developed a classification technique to classify people into healthy and those with low bone mass. A multivariate regression analysis could be done with the help of larger dataset to integrate the cortical radiogrammetric and trabecular texture features into a new bone index, that can assess the rate of bone loss in people. This new bone index, developed from radiographic image analysis, could be used as a low-cost and easily accessible alternative to DXA in developing countries.

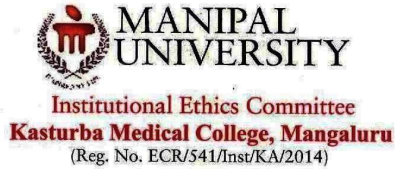
The research work could be further extended for the assessment of fracture risk in people. The bone properties characterized by the cortical radiogrammetric measurements and trabecular texture features obtained from radiographs can be integrated with clinical risk factors of the people to develop a prediction tool for fracture risk. For this, a longitudinal study with baseline data of a large number of people along with subsequent follow-up examinations every year must be initiated. This low cost prescreening and fracture risk prediction tool would benefit the people by an early diagnosis of osteoporosis and fracture risk and a timely intervention for prevention of osteoporosis-related fractures.

Appendix I

APPROVAL LETTERS AND DOCUMENTS USED FOR THE DATA COLLECTION

This chapter includes the approval letters from the Institutional Ethics Committee of Kasturba Medical College (KMC) Hospital, Mangalore, Manipal Academy of Higher Education, Karnataka, India, for the study and the documents used for the data collection.

APPROVAL OF THE INSTITUTIONAL ETHICS COMMITTEE FOR DATA COLLECTION



Communication of the Decision of the Institutional Ethics Committee

Wednesday 16th November, 2016

IEC KMC MLR 11-16/282

Protocol title	:	PROGNOSIS AND DIAGNOSIS OF OSTEOPOROSIS AND FRACTURE RISK ASSESSMENT USING IMAGE PROCESSING TECHNIQUES
Principal Investigator	:	Dr. Jagannath Kamath
Guide/Co-Guide/Co-Investigators	:	Ms. Anu Shaju Areeckal Dr. Sumam David Prof. Michel Kocher Dr. Nikil Jayasheelan Dr. Rajashekar Danda
Name & Address of Institution	:	Department of Orthopedics Kasturba Medical College Mangalore
New / review	:	New
Date of review (DD/M/YYYY)	:	16/11/2016
Decision of the IEC ➤ Approved ➤ Pending ➤ Revision ➤ Rejected	:	Approved from 16/11/2016
Remarks	:	Approved for the study period as mentioned in protocol

Please Note*

- Inform IEC immediately in case any Adverse events and Serious adverse event
- Inform IEC in case of any amendments to the protocol, change of study procedure, site and Investigator and premature termination of study with reasons along with summary.
- Final & Yearly Reports to be submitted to IEC.
- Members of IEC have right to monitor the study with prior intimation.
- A copy of the consent document to be given to the study participant giving the consent.

Shalini Shenoy
Dr. Shalini Shenoy
Member Secretary, IEC



Address : Office of Medical Education Unit, Light House Hill Road, Mangalore-575001, Karnataka, India Phone: 91 824 2422271-Extn No : 5574
Email:meu.kmcmr@manipal.edu. Contact Details: Dr. Shalini Shenoy, Member Secretary of IEC, Mob No. 919845497077

SUBJECT'S INFORMATION SHEET

Study Title: Prognosis and Diagnosis of Osteoporosis and Fracture Risk Assessment Using Image Processing Techniques.

Osteoporosis is a painless disease caused by loss of bone mass. It causes high susceptibility to fragility fracture. Osteoporosis is often undiagnosed until a fragility fracture occurs. The most common forms of fragility fracture are hip and spinal fracture. Once a fragility fracture has occurred, there is a high probability of re-occurrence of fragility fracture.

Fragility fracture can be prevented if osteoporosis is diagnosed early and treatment is taken. The current standard method for diagnosis, DXA scan, is expensive and available in very few hospitals. This study aims to design a low cost method to measure bone mineral density and diagnose osteoporosis using a hand X-ray image. As this technique will only use hand X-ray image, it could be used in any hospitals having an X-ray machine.

This study requires 1 hand X-ray and 1 DXA scan of the participant and a questionnaire to assess the clinical risk factors of fragility fracture of the participant. The data obtained from the hand X-ray and the questionnaire will be used to develop our low cost technique for diagnosis of osteoporosis and prediction of fracture risk. The results of the technique will be validated with DXA scan.

Please note that the radiation exposure due to 1 hand X-ray scan and 1 DXA scan is very less. Also, the cost of the scans will be borne by the investigators. The participants are assured of the confidentiality of the information given by them throughout the course of study.

Investigators: Ms. Anu Shaju Areeckal
Department of E&C,
NITK, Surathkal,
Mangalore.

Contact no: 9916135385

Dr. Jagannath Kamath,
Department of Orthopaedics,
KMC Hospital, Manipal University,
Mangalore.

9845235747

Chairperson,
Institutional Ethics Committee,
KMC, Manipal University, Mangalore.

ರೋಗಿಯ ಗಮನಕ್ಕೆ

ಆಸ್ಪಿಯೋಪೋರೋಸಿಸ್ ಎಂದರೆ ಮೂಳೆಯ ದ್ರವ್ಯರಾಶಿಯ ನಷ್ಟ ಉಂಟು ಮಾಡುವ ಒಂದು ನೋವುರಹಿತ ಖಾಯಿಲೆ. ಇದು ಮೂಳೆಯಲ್ಲಿ ಸೂಕ್ಷ್ಮ ಮಟ್ಟದ ಬಿರುಕುಗಳನ್ನು ಉಂಟು ಮಾಡಿ ನಂತರ ಹೆಚ್ಚಿನ ಪ್ರಭಾವಕ್ಕೆ ಕಾರಣವಾಗುತ್ತದೆ. ಆಸ್ಪಿಯೋಪೋರೋಸಿಸ್ ಖಾಯಿಲೆಯಿಂದಾಗಿ ಮೂಳೆಯಲ್ಲಿ ಸೂಕ್ಷ್ಮ ಮಟ್ಟದ ಬಿರುಕುಗಳು ಆಗುವವರೆಗೂ ಸಾಮಾನ್ಯವಾಗಿ ಕಂಡುಹಿಡಿಯಲಾಗದು ಹಾಗೂ ರೋಗಿಯ ಅರಿವಿಗೆ ಬಾರದು. ಸೂಕ್ಷ್ಮ ಮಟ್ಟದ ಬಿರುಕುಗಳಿಂದ ಸೊಂಟದ ಕೆಳಭಾಗ (ಹಿಪ್) ಮತ್ತು ಬೆನ್ನು ಮೂಳೆ ಮುರಿತ ಉಂಟಾಗುವ ಅಪಾಯ ಇವೆ. ಒಮ್ಮೆ ಸೂಕ್ಷ್ಮ ಮಟ್ಟದ ಬಿರುಕುಗಳು ಸಂಭವಿಸಿದರೆ, ಮತ್ತೊಮ್ಮೆ ಸಂಭವಿಸುವ ಸಾಧ್ಯತೆ ಅಧಿಕ.

ಆಸ್ಪಿಯೋಪೋರೋಸಿಸ್ ಆರಂಭಿಕ ಹಂತದಲ್ಲಿ ಅರಿತುಕೊಳ್ಳಬಹುದು ಮತ್ತು ಚಿಕಿತ್ಸೆ ತೆಗೆದುಕೊಂಡರೆ ತಡೆಗಟ್ಟಬಹುದು. ಪ್ರಸ್ತುತ ರೋಗನಿರ್ಣಯಕ್ಕೆ DXA ಸ್ಕ್ಯಾನ್ ಬಳಕೆ ಮಾತ್ರ ಇದ್ದು ಇದು ಅಧಿಕ ವೆಚ್ಚದಾಯಕ ಹಾಗೂ ಕೆಲವೇ ಆಸ್ಪತ್ರೆಗಳಲ್ಲಿ ಲಭ್ಯ. ಈ ಅಧ್ಯಯನವು ಕಡಿಮೆ ವೆಚ್ಚದಲ್ಲಿ ಮೂಳೆಯ ಖನಿಜಾಂಶಗಳ ಸಾಂದ್ರತೆ ಅಳೆಯಲು ಮತ್ತು ಕೈ ಎಕ್ಸ್‌ರೇ ಚಿತ್ರವನ್ನು ಬಳಸಿಕೊಂಡು ಆಸ್ಪಿಯೋಪೋರೋಸಿಸ್ ಕಂಡುಹಿಡಿಯಲಾಗುತ್ತಿದೆ. ಈ ವಿಧಾನವನ್ನು ಕೈ ಎಕ್ಸ್‌ರೇ ಇಮೇಜ್ ಮೂಲಕ ಬಳಸಬಹುದು. ಇದು ಎಕ್ಸ್‌ರೇ ಯಂತ್ರ ಹೊಂದಿರುವ ಯಾವುದೇ ಆಸ್ಪತ್ರೆಗಳಲ್ಲಿ ಬಳಸಬಹುದು.

ಈ ಅಧ್ಯಯನವು ವೈದ್ಯಕೀಯ ಅಪಾಯಕಾರಿ ಅಂಶಗಳನ್ನು ನಿರ್ಣಯಿಸಲು 1 ಕೈ ಎಕ್ಸ್‌ರೇ ಮತ್ತು DXA ಸ್ಕ್ಯಾನ್ ಯಂತ್ರದ ಅವಶ್ಯಕತೆ ಹೊಂದಿದ್ದು , ಸಿದ್ಧ ಪ್ರಶ್ನಾವಳಿಗಳಿಗೆ ಉತ್ತರಿಸಬೇಕಾದ ಅಗತ್ಯವನ್ನು ಹೊಂದಿದೆ. ಎಕ್ಸ್‌ರೇ ಹಾಗೂ ಪ್ರಶ್ನಾವಳಿಗಳ ಮೂಲಕ ಸಂಗ್ರಹಿಸಿದ ಡಾಟಾವನ್ನು ಆಸ್ಪಿಯೋಪೋರೋಸಿಸ್ ಕಂಡುಹಿಡಿಯಲು ನಾವು ಕಂಡುಹಿಡಿಯುವ ಕಡಿಮೆ ವೆಚ್ಚದ ಯಂತ್ರದ ಅಭಿವೃದ್ಧಿಗೆ ಬಳಸಿಕೊಳ್ಳಲಾಗುವುದು. ಹಾಗೂ ಫಲಿತಾಂಶವನ್ನು DXA ಸ್ಕ್ಯಾನ್ ಯಂತ್ರದ ಫಲಿತಾಂಶದ ಜತೆ ಸಮೀಕರಣ ನಡೆಸಲಾಗುವುದು.

ಕೈ ಎಕ್ಸ್‌ರೇ ಹಾಗೂ DXA ಸ್ಕ್ಯಾನ್‌ನಲ್ಲಿ ವಿಕಿರಣ ಪ್ರಮಾಣ ತೀರಾ ಕಡಿಮೆ ಇರುತ್ತದೆ ಎನ್ನುವುದನ್ನು ದಯವಿಟ್ಟು ಗಮನಿಸಿ. ಅಲ್ಲದೆ, ಸ್ಕ್ಯಾನ್ ವೆಚ್ಚವನ್ನು ಸಂಶೋಧಕರೇ ಭರಿಸುತ್ತಾರೆ. ಸಂಶೋಧನೆಯಲ್ಲಿ ಭಾಗವಹಿಸುವವರು ಹಾಗೂ ನೀಡಿದ ಮಾಹಿತಿಯ ಗೌಪ್ಯತೆ ಕಾಪಾಡಲಾಗುವುದು.

ಕುಮಾರಿ ಅನು ಶಾಜು ಅರೀಕಲ್

ರಾಷ್ಟ್ರೀಯ ತಾಂತ್ರಿಕ ಮಹಾವಿದ್ಯಾಲಯ ಕರ್ನಾಟಕ, ಸುರತ್ಕಲ್
ವಿದ್ಯುನ್ಮಾನ ಸಂವಹನ ಎಂಜಿನಿಯರಿಂಗ್ ವಿಭಾಗ
ಮೊ. ಸಂ. 9916135385

ಡಾ. ಜಗನ್ನಾಥ್ ಕಾಮತ್,

ಆರ್ಥೋಪೀಡಿಸ್ಟ್ ಇಲಾಖೆ
ಕೆಎಂಸಿ ಆಸ್ಪತ್ರೆ,
ಮಣಿಪಾಲ್ ವಿಶ್ವವಿದ್ಯಾಲಯ, ಮಂಗಳೂರು.
ಮೊ. ಸಂ. 9845235747

ಅಧ್ಯಕ್ಷರು,

ನೈತಿಕ ಸಮಿತಿ,
ಕೆಎಂಸಿ ಆಸ್ಪತ್ರೆ,
ಮಣಿಪಾಲ್ ವಿಶ್ವವಿದ್ಯಾಲಯ, ಮಂಗಳೂರು.

വ്യക്തി വിവര പത്രം

പഠന വിഷയം : ഇമേജ് പ്രോസസ്സിങ്ങ് സങ്കേതങ്ങൾ ഉപയോഗിച്ച് അസ്ഥിക്ഷയത്തിന്റെ (Osteoporosis) രോഗപുർവ്വ നിരൂപണവും രോഗനിർണ്ണയവും, അസ്ഥിഭംഗത്തിന്റെ (Fracture) ചികിത്സയിലെ അപകടഘടകങ്ങളുടെ നിർണ്ണയവും.

അസ്ഥി ക്ഷയിക്കുന്നതുമൂലം ഉണ്ടാകുന്ന, വേദനാരഹിതമായ ഒരു രോഗമാണ് ഓസ്റ്റിയോപൊറോസിസ് അഥവാ അസ്ഥിക്ഷയം. ഇതുമൂലം അസ്ഥിഭംഗത്തിനുള്ള സാധ്യത ഏറുന്നു. എല്ലുകളുടെ ദുർബ്ബല്യം മൂലമുള്ള അസ്ഥിഭംഗം (fragility fracture) സംഭവിക്കുന്നതുവരെ ഈ രോഗം കണ്ടുപിടിക്കപ്പെടാതെ പോകുകയാണ് പതിവ്. ഇടുപ്പെല്ലിനും നട്ടെല്ലിനും ആണ് സാധാരണയായി ഇത്തരം അസ്ഥിദുർബ്ബല്യം മൂലമുള്ള ഒടിവുകൾ സംഭവിക്കാറുള്ളത്. ഒരിക്കൽ സംഭവിച്ചാൽ ഇത് വീണ്ടും വീണ്ടും വരാനുള്ള സാധ്യത വളരെ കൂടുതലാണ്.

ഓസ്റ്റിയോപൊറോസിസ് നേരത്തേ കണ്ടെത്തി ചികിത്സിച്ചാൽ അസ്ഥിദുർബ്ബല്യം മൂലം എല്ലുകൾ ഒടിയുന്നത് തടയാം. എല്ലുകളിലെ ധാതുക്കളുടെ സാന്ദ്രത അളക്കാൻ ഉപയോഗിക്കുന്ന ഡി എക്സ് എ (DXA) സ്ക്ാനിങ്ങ് ആണ് നിലവിൽ ഈ രോഗം നിർണ്ണയിക്കാൻ ഉപയോഗിക്കുന്നത്. എന്നാൽ, ഇത് ചെലവേറിയ രീതിയാണ്. മാത്രമല്ല, ഇത് വളരെ കുറച്ച് ആശുപത്രികളിൽ മാത്രമേ ലഭ്യമായിട്ടുള്ളൂ. രോഗിയുടെ ഒരു എക്സ് റേ ചിത്രം മാത്രം ഉപയോഗിച്ച് എല്ലുകളിലെ ധാതുസാന്ദ്രത അളക്കാനും അത് വഴി ഓസ്റ്റിയോപൊറോസിസ് കണ്ടുപിടിക്കാനും വേണ്ടിയുള്ള, ചെലവുകുറഞ്ഞ ഒരു പദ്ധതിയ്ക്ക് രൂപം കൊടുക്കുക എന്നതാണ് ഈ പഠനം കൊണ്ട് ഉദ്ദേശിക്കുന്നത്. രോഗനിർണ്ണയത്തിന് ഒരു എക്സ് റേ ചിത്രം മാത്രം മതിയായും എന്നതിനാൽ എക്സ് റേ സംവിധാനം ഉള്ള ഏത് ആശുപത്രിയിലും ഈ രോഗനിർണ്ണയം സാധ്യമാകും.

രോഗിയുടെ കൈയുടെ ഒരു എക്സ് റേ ചിത്രവും ഒരു ഡി എക്സ് എ സ്ക്ാനും അസ്ഥിഭംഗ ചികിത്സയിലെ അപകടഘടകങ്ങളെ വിലയിരുത്താൻ വേണ്ടിയുള്ള ഒരു ചോദ്യാവലിയും ആണ് ഈ പഠനത്തിന് ആവശ്യമായിട്ടുള്ളത്. ചോദ്യാവലിയിൽ ഉള്ള ചോദ്യങ്ങൾക്ക് രോഗി നൽകുന്ന മറുപടിയിൽ നിന്നും എക്സ് റേ ചിത്രങ്ങളിൽ നിന്നും

INFORMED CONSENT FORM
FOR SUBJECT

I have read the Subject's Information Sheet provided to me. I am voluntarily willing to provide the necessary data and to participate in the study conducted by Ms. Anu Shaju Areeckal, PhD Student, Department of Electronics and Communication Engineering, National Institute of Technology Karnataka, Surathkal, Mangalore on "**Prognosis and Diagnosis of Osteoporosis and Fracture Risk Assessment Using Image Processing Techniques**".

I have been informed that the information provided by me will be kept confidential and used for the above mentioned study only.

Signature of the Participant

Signature of the Investigator

Name of the participant:

Date:

Mobile Number:

ಅಧಿಕೃತ ಒಪ್ಪಿಗೆ ಪತ್ರ

ಭಾಗಿಯಾಗಿರುವ / ಸಂಬಂಧಪಟ್ಟ ವ್ಯಕ್ತಿ :

ರಾಷ್ಟ್ರೀಯ ತಾಂತ್ರಿಕ ಮಹಾವಿದ್ಯಾಲಯ ಕರ್ನಾಟಕ, ಸುರತ್ಕಲ್‌ನ ವಿದ್ಯುನ್ಮಾನ ಸಂವಹನ ಎಂಜಿನಿಯರಿಂಗ್ ವಿಭಾಗದಲ್ಲಿ ಸಂಶೋಧಕಳಾಗಿರುವ ಕುಮಾರಿ ಅನು ಶಾಜು ಅರೀಕಲ್ ಅವರ ಚಿತ್ರ ಪ್ರಕ್ರಿಯೆಯ ತಂತ್ರಗಳನ್ನು ಬಳಸಿ ಪೂರ್ವಸೂಚನೆ ಮತ್ತು ಆಸ್ತಿಯೋಪೋರೋಸಿಸ್ ರೋಗ ಮತ್ತು ಫ್ರಾಕ್ಚರ್ ರಿಸ್ಕ್ ಅಸೆಸ್ಮೆಂಟ್ (Prognosis and Diagnosis of Osteoporosis and Fracture Risk Assessment Using Image Processing Techniques). ಸಂಶೋಧನೆಗೆ ಅವಶ್ಯವಿರುವ ಪ್ರಶ್ನೆಗಳಿಗೆ ತಕ್ಕ ಮಾಹಿತಿಯನ್ನು ಕೊಡುವುದರೊಂದಿಗೆ ಹಾಗೂ ಅದಕ್ಕೆ ಸಂಬಂಧಪಟ್ಟ ಇನ್ನಿತರ ವಿಷಯಗಳಲ್ಲಿ ಭಾಗಿಯಾಗುವುದಕ್ಕೆ ನಾನು ನನ್ನ ಸ್ವ ಇಚ್ಛೆಯಿಂದ ಸಮ್ಮತಿಸಿರುವೆನು.

ನಾನು ತಿಳಿಸಿರುವ ಮಾಹಿತಿಯು ಗೌಪ್ಯವಾಗಿದ್ದು ಈ ಸಂಶೋಧನೆಗೆ ಮಾತ್ರ ಉಪಯೋಗಿಸಲ್ಪಡುತ್ತದೆಂದು ನನಗೆ ಸೂಚಿಸಿದ್ದಾರೆ.

ಭಾಗಿಯಾದ ವ್ಯಕ್ತಿಯ ಸಹಿ

ಸಂಶೋಧಕಳ ಸಹಿ

ಹೆಸರು:

ದಿನಾಂಕ:

ಮೊಬೈಲ್ ನಂ. :

രോഗിയുടെ സമ്മതപത്രം

ഞാൻ, എനിക്കു കിട്ടിയ വ്യക്തിവിവര പത്രം (subject's information sheet) പൂർണ്ണമായി വായിച്ചു മനസ്സിലാക്കിയതാണ്. കുമ്മാരി അനു ഷാജു അരീക്കൽ (പി എച്ച് ഡി സ്റ്റുഡന്റ്, ഡിപ്പാർട്ട്മെന്റ് ഓഫ് ഇ & സി, എൻ ഐ ടി കെ സുറത്കൽ, മാംഗ്ലൂർ) നടത്തുന്ന, "ഇമേജ് പ്രോസസ്സിങ്ങ് സങ്കേതങ്ങൾ ഉപയോഗിച്ച് അസ്ഥിക്ഷയത്തിന്റെ (Osteoporosis) രോഗപൂർവ്വ നിരൂപണവും രോഗനിർണ്ണയവും, അസ്ഥിഭംഗത്തിന്റെ (Fracture) ചികിത്സയിലെ അപകടഘടകങ്ങളുടെ നിർണ്ണയവും" എന്ന പഠനത്തിൽ പങ്കെടുക്കാനും, ആവശ്യമുള്ള വിവരങ്ങൾ നൽകുവാനും ഞാൻ സ്വമനസ്സാലെ തയ്യാറാണ്. ഈ പഠനത്തിനായി ഞാൻ നൽകുന്ന വിവരങ്ങളെല്ലാം രഹസ്യമായി സൂക്ഷിക്കുമെന്നും ഗവേഷണസംബന്ധമായ ആവശ്യങ്ങൾക്കുമാത്രമേ ഈ വിവരങ്ങൾ ഉപയോഗിക്കൂ എന്നും ഗവേഷകർ എനിക്ക് ഉറപ്പുതന്നിട്ടുള്ളതാണ്.

രോഗിയുടെ ഒപ്പ്

ഗവേഷകയുടെ ഒപ്പ്

രോഗിയുടെ പേര്:

തിയ്യതി:

മൊബൈൽ നമ്പർ:

PATIENT PROFORMA

Instructions:

This questionnaire is used to get information on clinical risk factors of osteoporosis and fragility fracture. This information provided by you will be exclusively utilized for research study and will be kept confidential.

Please fill in the following information.

1.	OP number	
2.	Date of examination	
3.	Full Name	
4.	Occupation	
5.	Telephone/Mobile no.	
6.	Age	
7.	Date of birth	
8.	Gender	<input type="checkbox"/> Female <input type="checkbox"/> Male
9.	Height	
10.	Weight	
11.	Age of menopause, if applicable	
12.(a)	Do you currently smoke?	<input type="checkbox"/> Yes <input type="checkbox"/> No
12.(b)	If yes, how many cigarettes per day?	
13.(a)	Do you consume alcohol frequently?	<input type="checkbox"/> Yes <input type="checkbox"/> No
13.(b)	If yes, do you drink 3 or more units* each day?	<input type="checkbox"/> Yes <input type="checkbox"/> No
14.(a)	Is there any previous history of fragility fracture?	<input type="checkbox"/> Yes <input type="checkbox"/> No
14.(b)	Has there been a sudden decrease in	<input type="checkbox"/> Yes <input type="checkbox"/> No

	height in the past few years?	
14.(c)	Have you had a hip replacement surgery?	<input type="checkbox"/> Yes <input type="checkbox"/> No
14.(d)	Have you had back surgery?	<input type="checkbox"/> Yes <input type="checkbox"/> No
14.(e)	Has any of your parents had a fragility fracture?	
15.(a)	How often do you exercise?	<input type="checkbox"/> Daily once a month <input type="checkbox"/> Weekly <input type="checkbox"/> Few times a month
15.(b)	How often did you exercise in your childhood?	<input type="checkbox"/> Daily once a month <input type="checkbox"/> Weekly <input type="checkbox"/> Few times a month
16.	Do you consume milk/ dairy products daily?	<input type="checkbox"/> Yes <input type="checkbox"/> No
17.	Do you take Calcium supplement?	<input type="checkbox"/> Yes <input type="checkbox"/> No
18.	Do you take Vitamin D supplement?	<input type="checkbox"/> Yes <input type="checkbox"/> No
19.	Have you taken glucocorticoid/steroid tablets for over 3 months?	<input type="checkbox"/> Yes <input type="checkbox"/> No

Note:

*A unit of alcohol varies slightly in different countries from 8-10g of alcohol. This is equivalent to a standard glass of beer (285ml), a single measure of spirits (30ml), a medium-sized glass of wine (120ml), or 1 measure of an aperitif (60ml)

The information given above is correct to the best of my knowledge.

Signature of patient _____ Date _____

ರೋಗಿಯ ಪ್ರಶ್ನಾವಳಿ

ಸೂಚನೆ:

ಈ ಪ್ರಶ್ನಾವಳಿಯು ಜನಸಂಖ್ಯೆ ಮತ್ತು ಮಾನವ ಮಾಪನ ವಿಷಯಾಧಾರಿತವಾಗಿರುತ್ತದೆ ಮತ್ತು ನೀವು ತಿಳಿಸಿದ ಮಾಹಿತಿಯು ಗೌಪ್ಯವಾಗಿದ್ದು ಸಂಶೋಧನೆಗೆ ಮಾತ್ರ ಉಪಯೋಗಿಸಲ್ಪಡುತ್ತದೆ.

ದಯಮಾಡಿ ಈ ಕೆಳಗೆ ನಮೂದಿಸಿದ ಮಾಹಿತಿಯನ್ನು ಒದಗಿಸಿ.

1. ಹೊರರೋಗಿಯ ಸಂಖ್ಯೆ:
2. ಪರೀಕ್ಷಿಸಿದ ದಿನಾಂಕ:
3. ಹೆಸರು:
4. ವೃತ್ತಿ:
5. ಮೊಬೈಲ್ ನಂ.:
6. ವಯಸ್ಸು:
7. ಹುಟ್ಟಿದ ದಿನಾಂಕ:
8. ಲಿಂಗ : ಹೆಂಗಸು ಗಂಡಸು
9. ಎತ್ತರ:
10. ತೂಕ:
11. ಮುಟ್ಟುನಿಂತ ವಯಸ್ಸು ಆಗಿದ್ದರೆ:
12. ಧೂಮಪಾನದ ಅಭ್ಯಾಸವಿದೆಯೇ? ಹೌದು ಇಲ್ಲ
13. ಹೌದು ಎಂದಾದಲ್ಲಿ ದಿನದಲ್ಲಿ ಮೂರು ಅಥವಾ ಅದಕ್ಕಿಂತ ಹೆಚ್ಚು
 ಹೌದು ಇಲ್ಲ
14. ಆಗಾಗ ಮದ್ಯಪಾನ ಮಾಡುವಿರಾ? ಹೌದು ಇಲ್ಲ
15. ಹೌದು ಎಂದಾದಲ್ಲಿ ದಿನದಲ್ಲಿ ಎಷ್ಟು ಬಾರಿ?
16. ನೀವು ಗ್ಲೂಕೋಸಿಕ್ರೂಡ್/ ಸ್ಪಿರಾಯ್ಡ್ ಮಾತ್ರೆಗಳನ್ನು ತೆಗೆದುಕೊಂಡಿದ್ದೀರಾ?
 ಹೌದು ಇಲ್ಲ

17. ಕಳೆದ ಕೆಲವು ವರ್ಷಗಳಲ್ಲಿ ನಿಮ್ಮ ಎತ್ತರ ಹಠಾತ್ ಆಗಿ ಇಳಿಕೆ ಕಂಡುಬಂದಿದೆಯೇ?
 ಹೌದು ಇಲ್ಲ
18. ಈ ಹಿಂದೆ ಯಾವಾಗಲಾದರೂ ಮೂಳೆ ಮುರಿತವಾಗಿದೆಯಾ?
 ಹೌದು ಇಲ್ಲ
19. ಈ ಹಿಂದೆ ಯಾವಾಗಲಾದರೂ ಸೊಂಟದ ಎಲುಬಿಗೆ ಶಸ್ತ್ರಚಿಕಿತ್ಸೆ ಆಗಿದೆಯೇ?
 ಹೌದು ಇಲ್ಲ
20. ಬೆನ್ನುಹುರಿ ಶಸ್ತ್ರಚಿಕಿತ್ಸೆ ಆಗಿದೆಯೇ? ಹೌದು ಇಲ್ಲ
21. ನಿಮ್ಮ ತಂದೆ /ತಾಯಿಯರಿಗೆ ಮೂಳೆ ಮುರಿಯುವಿಕೆ ಸಂಭವಿಸಿದೆಯೇ?
 ಹೌದು ಇಲ್ಲ
22. ನೀವು ಎಷ್ಟು ಬಾರಿ ವ್ಯಾಯಾಮ ಮಾಡುತ್ತೀರಿ?
 ಪ್ರತಿದಿನ ವಾರಕ್ಕೊಮ್ಮೆ ತಿಂಗಳಿಗೆ ಕೆಲವು ಬಾರಿ
23. ನಿಮ್ಮ ಬಾಲ್ಯದಲ್ಲಿ ನೀವು ಎಷ್ಟು ಬಾರಿ ವ್ಯಾಯಾಮ ಮಾಡುತ್ತಿದ್ದೀರಿ?
24. ನೀವು ಹಾಲಿನ ಅಂಶವನ್ನು ಪ್ರತಿದಿನ ಸೇವಿಸುವಿರಾ? ಹೌದು ಇಲ್ಲ
25. ನೀವು ಕ್ಯಾಲ್ಸಿಯಂ ಪೂರಕವನ್ನು ಸೇವಿಸುವಿರಾ? ಹೌದು ಇಲ್ಲ
26. ನೀವು ವಿಟಮಿನ್ 'ಡಿ' ಯನ್ನು ಸೇವಿಸುವಿರಾ? ಹೌದು ಇಲ್ಲ
27. ಮೂಳೆಯ ಸಾಂದ್ರತೆ : (DXA - BMD value)

ಈ ಮೇಲೆ ತಿಳಿಸಿದ ಮಾಹಿತಿಯು ನನಗೆ ತಿಳಿದ ಮಟ್ಟಿಗೆ ಸತ್ಯವಾಗಿರುತ್ತದೆ.

ಸಹಿ/-

ದಿನಾಂಕ:

രോഗിയുടെ വിവരങ്ങൾ

നിർദ്ദേശങ്ങൾ :

ഈ ചോദ്യാവലി, അസ്ഥിഭംഗത്തിന്റെയും (fragility fracture) അസ്ഥിക്ഷയത്തിന്റെയും (osteoporosis) ചികിത്സയിലെ അപകടഘടകങ്ങളെക്കുറിച്ചുള്ള വിവരങ്ങൾ ലഭിക്കാൻ വേണ്ടിയുള്ളതാണ്. നിങ്ങൾ നൽകുന്ന വിവരങ്ങൾ പരസ്യപ്പെടുത്തുകയില്ല എന്നും ഗവേഷണ,പഠനാവശ്യങ്ങൾക്കുവേണ്ടിയല്ലാതെ മറ്റൊന്നിനും ഉപയോഗിക്കില്ലെന്നും ഞങ്ങൾ ഉറപ്പ് നൽകുന്നു.

താഴെ കാണുന്ന ഫോറം പൂരിപ്പിക്കുക.

1.	ഒ പി നമ്പർ		
2.	പരിശോധനയ്ക്ക് വന്ന ദിവസം		
3.	മുഴുവൻ പേര്		
4.	തൊഴിൽ		
5.	ഫോൺ/മൊബൈൽ നമ്പർ		
6.	വയസ്സ്		
7.	ജനനത്തീയതി		
8.	ലിംഗം	[]പെൺ	[]ആൺ
9.	ഉയരം		
10.	തൂക്കം		
11.	എത്ര വയസ്സിലാണ് ആർത്തവ വിരാമം ഉണ്ടായത് (ബാധകമെങ്കിൽ)		
12.(a)	ഇപ്പോൾ പുകവലിക്കാറുണ്ടോ ?	[]ഉണ്ട്	[]ഇല്ല
12.(b)	ഉണ്ടെങ്കിൽ ദിവസം എത്ര സിഗററ്റ് വീതം വലിയ്ക്കും?		
13.(a)	പതിവായി മദ്യപിക്കാറുണ്ടോ?	[]ഉണ്ട്	[]ഇല്ല
13.(b)	ഉണ്ടെങ്കിൽ ദിവസവും 3 യൂണിറ്റോ* അതിൽ കൂടുതലോ കഴിയ്ക്കാറുണ്ടോ?	[]ഉണ്ട്	[]ഇല്ല
14.(a)	ഇതിനുമുമ്പ് അസ്ഥിഭംഗം സംഭവിച്ചിട്ടുണ്ടോ	[]ഉണ്ട്	[]ഇല്ല
14.(b)	കഴിഞ്ഞ കുറച്ച് വർഷങ്ങളിൽ ഉയരം പെട്ടെന്ന് കുറഞ്ഞിട്ടുണ്ടോ?	[]ഉണ്ട്	[]ഇല്ല
14.(c)	ഇടുപ്പെല്ല് മാറ്റിവയ്ക്കൽ ശസ്ത്രക്രിയയ്ക്ക് വിധേയനായിട്ടുണ്ടോ ?	[] ഉണ്ട്	[] ഇല്ല
14.(d)	നട്ടെല്ലിലെ ശസ്ത്രക്രിയയ്ക്ക് വിധേയനായിട്ടുണ്ടോ?	[] ഉണ്ട്	[] ഇല്ല

14.(e)	അച്ഛനോ അമ്മയോ അന്ധിദംഗം ഉണ്ടായിട്ടുണ്ടോ?	
15.(a)	എപ്പോഴൊക്കെ വ്യായാമം ചെയ്യാറുണ്ട്?	[] ദിവസേന [] ആഴ്ചയിൽ ഒരിക്കൽ [] മാസത്തിൽ വല്ലപ്പോഴും
15.(b)	കുട്ടിക്കാലത്ത് എപ്പോഴൊക്കെ വ്യായാമം ചെയ്തിരുന്നു ?	[] ദിവസേന [] ആഴ്ചയിൽ ഒരിക്കൽ [] മാസത്തിൽ വല്ലപ്പോഴും
16.	ദിവസവും പാലോ പാലുൽപ്പന്നങ്ങളോ കഴിക്കാറുണ്ടോ?	[] ഉണ്ട് [] ഇല്ല
17.	കാൽസ്യം സപ്ലിമെന്റുകൾ കഴിക്കാറുണ്ടോ?	[] ഉണ്ട് [] ഇല്ല
18.	വിറ്റാമിൻ-ഡി സപ്ലിമെന്റുകൾ കഴിക്കാറുണ്ടോ?	[] ഉണ്ട് [] ഇല്ല
19.	ഗ്ലൂക്കോകോർട്ടിക്കോയിഡ്/ സ്റ്റിറോയ്ഡ് ഗുളികകൾ 3 മാസത്തിൽ കൂടുതൽ കാലം കഴിച്ചിട്ടുണ്ടോ?	[] ഉണ്ട് [] ഇല്ല

കുറിപ്പ്:

മദ്യത്തിന്റെ ഒരു യൂണിറ്റ് എന്നതുകൊണ്ട് ഉദ്ദേശിക്കുന്നത് 8 മുതൽ 10 ഗ്രാം വരെ ആൽക്കഹോൾ എന്നാണ്.

(ഉദാഹരണത്തിന്, ഒരു ഗ്ലാസ്സ് ബിയർ (285 മില്ലി), അല്ലെങ്കിൽ 30 മില്ലി സ്റ്റിരിറ്റ്, അതുവെള്ളകിൽ ഒരു ഇടത്തരം ഗ്ലാസ്സ് വൈൻ (120 മില്ലി)).

മേൽപ്പറഞ്ഞ വിവരങ്ങളെല്ലാം എന്റെ അറിവിൽ പെട്ടിടത്തോളം സത്യമാണ്.

രോഗിയുടെ ഒപ്പ് :

തിയ്യതി :

APPROVAL OF THE INSTITUTIONAL ETHICS COMMITTEE FOR DATA COLLECTION FOR THE WORK ON 3D RECONSTRUCTION

From,

Anu Shaju Areeckal,
Research Scholar,
Department of E&C,
National Institute of Technology Karnataka (NITK), Mangalore, Karnataka

Date: 14/07/17

To,

The Chairperson,
Institutional Ethics Committee,
KMC Mangalore, Manipal University, Karnataka.

Through: Guide

Respected Sir,

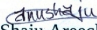
SUB: Request for permission for data collection

I'm a PhD student from NITK, Surathkal working on the project titled 'Prognosis and diagnosis of osteoporosis and fracture risk assessment using image processing techniques', under the guidance of Dr. Sumam David S. and Dr. Michel Kocher and in collaboration with Dr. Jagannath Kamath, Department of Orthopedics, KMC hospital, Mangalore, Manipal University, Karnataka. With approval of the IEC, KMC (Ref No. IEC KMC MLR 11-16/282), we had collected Xray images of hand and wrist and DXA reports of 134 patients and analyzed the data. My objectives 1 and 2 have been achieved wherein, we developed an algorithm to automatically segment hand and wrist radiographs for radiogrammetry and texture analysis and we trained a classifier to identify osteoporotic and healthy subjects. The trained classifier model developed shows a classification accuracy of 91%.

My 3rd objective deals with reconstructing a 3D image of the metacarpal bone from two oblique view hand X-rays. As part of this objective, we would like to take 1 CT scan of hand of patients, who are willing to volunteer, along with DXA of lumbar spine and 2 oblique view hand Xrays. The CT scan and DXA results would be used for validating our results. **These scans would be harmless to the subjects.** I request you to grant me permission to collect the required data.

Thanking you.

Yours sincerely,


Anu Shaju Areeckal

Recommended and forwarded

Sumam David
14.7.2017

Recommended & Forwarded


Dr. B.N. JAGANNATH KAMATH
Professor & 'C' Unit Head
Department of Orthopaedics
K.M.C. MANGALORE



Dr. SUMAM DAVID S
PROFESSOR
DEPT. OF ELECTRONICS & COMMUNICATION ENGG.
NATIONAL INSTITUTE OF TECHNOLOGY, KARNATAKA, SURATHKAL
BENGLURU VASNAGAR-575 025, KARNATAKA, INDIA

REFERENCES

- Adami, S., N. Zamberlan, D. Gatti, C. Zanfisi, V. Braga, M. Broggin, and M. Rossini** (1996). Computed radiographic absorptiometry and morphometry in the assessment of postmenopausal bone loss. *Osteoporosis International*, **6**(1), 8–13.
- Adams, J. E.** (2009). Quantitative computed tomography. *European Journal of Radiology*, **71**(3), 415–424.
- Adler, R. A., M. T. Tran, and V. I. Petkov,** Performance of the osteoporosis self-assessment screening tool for osteoporosis in American men. *In Mayo Clinic Proceedings*, volume 78. Elsevier, 2003.
- Alabort-i Medina, J., E. Antonakos, J. Booth, P. Snape, and S. Zafeiriou,** Menpo: A comprehensive platform for parametric image alignment and visual deformable models. *In Proceedings of the 22nd ACM international conference on Multimedia*. ACM, 2014.
- Alberich-Bayarri, A., L. Marti-Bonmati, R. Sanz-Requena, E. Belloch, and D. Moratal** (2008). In vivo trabecular bone morphologic and mechanical relationship using high-resolution 3-T MRI. *American Journal of Roentgenology*, **191**(3), 721–726.
- Albrand, G., F. Munoz, E. Sornay-Rendu, F. DuBoeuf, and P. Delmas** (2003). Independent predictors of all osteoporosis-related fractures in healthy postmenopausal women: The OFELY study. *Bone*, **32**(1), 78–85.
- Baka, N., B. L. Kaptein, M. de Bruijne, T. van Walsum, J. Giphart, W. J. Niessen, and B. P. Lelieveldt** (2011). 2D–3D shape reconstruction of the distal femur from stereo X-ray imaging using statistical shape models. *Medical Image Analysis*, **15**(6), 840–850.
- Barnett, E. and B. Nordin** (1960). The radiological diagnosis of osteoporosis: A new approach. *Clinical Radiology*, **11**(3), 166–174.

Bauer, D., S. Ewing, J. Cauley, K. Ensrud, S. R. Cummings, E. Orwoll, O. F. in Men (MrOS) Research Group, et al. (2007). Quantitative ultrasound predicts hip and non-spine fracture in men: The MrOS study. *Osteoporosis International*, **18**(6), 771–777.

Benhamou, C.-L., S. Poupon, E. Lespessailles, S. Loiseau, R. Jennane, V. Siroux, W. Ohley, and L. Pothuaud (2001). Fractal analysis of radiographic trabecular bone texture and bone mineral density: Two complementary parameters related to osteoporotic fractures. *Journal of Bone and Mineral Research*, **16**(4), 697–704.

Beucher, S. (1990). *Segmentation d'images et morphologie mathématique*. Ph.D. thesis, Ecole Nationale Supérieure des Mines de Paris.

Biver, E., C. Durosier-Izart, T. Chevalley, B. van Rietbergen, R. Rizzoli, and S. Ferrari (2018). Evaluation of radius microstructure and areal bone mineral density improves fracture prediction in postmenopausal women. *Journal of Bone and Mineral Research*, **33**(2), 328–337.

Black, D., M. Steinbuch, L. Palermo, P. Dargent-Molina, R. Lindsay, M. Hoseyni, and O. Johnell (2001). An assessment tool for predicting fracture risk in postmenopausal women. *Osteoporosis International*, **12**(7), 519–528.

Blain, H., P. Chavassieux, N. Portero-Muzy, F. Bonnel, F. Canovas, M. Chammass, P. Maury, and P. Delmas (2008). Cortical and trabecular bone distribution in the femoral neck in osteoporosis and osteoarthritis. *Bone*, **43**(5), 862–868.

Blender (2017). Blender version 2.79b. <https://www.blender.org/>. (Accessed on August, 2018).

Bo, C., X. Liang, P. Chu, J. Xu, D. Wang, J. Yang, V. Megalooikonomou, and H. Ling, Osteoporosis prescreening using dental panoramic radiographs feature analysis. In *Proceedings of 14th International Symposium on Biomedical Imaging (ISBI)*. IEEE, 2017.

Bonnick, S. L., *Bone Densitometry in Clinical Practice: Application and Interpretation*. Humana Press Inc., 1998.

- Boussaid, H., S. Kadoury, I. Kokkinos, J.-Y. Lazenec, G. Zheng, and N. Paragios**, 3D model-based reconstruction of the proximal femur from low-dose biplanar X-ray images. *In The 22nd British Machine Vision Conference (BMVC)*. 2011.
- Boutroy, S., M. L. Boussein, F. Munoz, and P. D. Delmas** (2005). In vivo assessment of trabecular bone microarchitecture by high-resolution peripheral quantitative computed tomography. *Journal of Clinical Endocrinology and Metabolism*, **90**(12), 6508–6515.
- Brett, A. D. and J. K. Brown** (2015). Quantitative computed tomography and opportunistic bone density screening by dual use of computed tomography scans. *Journal of Orthopaedic Translation*, **3**(4), 178–184.
- Brunet-Imbault, B., G. Lemineur, C. Chappard, R. Harba, and C.-L. Benhamou** (2005). A new anisotropy index on trabecular bone radiographic images using the fast Fourier transform. *BMC Medical Imaging*, **5**(1), 4.
- Buades, A., B. Coll, and J.-M. Morel**, A non-local algorithm for image denoising. *In IEEE Computer Society Conference on Computer Vision and Pattern Recognition (CVPR)*, volume 2. IEEE, 2005.
- Burr, D.** (2016). The use of finite element analysis to estimate the changing strength of bone following treatment for osteoporosis.
- Cabral, H. W. S., B. F. G. Andolphi, B. V. C. Ferreira, D. C. F. Alves, R. L. Morelato, A. Chambo Filho, and L. S. Borges** (2016). The use of biomarkers in clinical osteoporosis. *Revista da Associação Médica Brasileira*, **62**(4), 368–376.
- Cai, J., T.-X. Wu, K. Zhou, and W. Li** (2015). Recognition of osteoporosis based on texture analysis and a support vector machine. *International Journal of Bioautomation*, **19**(1), 107–118.
- Cawthon, P. M., M. Shahnazari, E. S. Orwoll, and N. E. Lane** (2016). Osteoporosis in men: Findings from the Osteoporotic Fractures in Men Study (MrOS). *Therapeutic Advances in Musculoskeletal Disease*, **8**(1), 15–27.

Center, J. R., D. Bliuc, T. V. Nguyen, and J. A. Eisman (2007). Risk of subsequent fracture after low-trauma fracture in men and women. *Jama*, **297**(4), 387–394.

Chang, K. P., J. R. Center, T. V. Nguyen, and J. A. Eisman (2004). Incidence of hip and other osteoporotic fractures in elderly men and women: Dubbo Osteoporosis Epidemiology Study. *Journal of Bone and Mineral Research*, **19**(4), 532–536.

Chappard, C., B. Brunet-Imbault, G. Lemineur, B. Giraudeau, A. Basillais, R. Harba, and C.-L. Benhamou (2005). Anisotropy changes in post-menopausal osteoporosis: Characterization by a new index applied to trabecular bone radiographic images. *Osteoporosis International*, **16**(10), 1193–1202.

Chen, C., X. Zhang, J. Guo, D. Jin, E. M. Letuchy, T. L. Burns, S. M. Levy, E. A. Hoffman, and P. K. Saha (2018). Quantitative imaging of peripheral trabecular bone microarchitecture using MDCT. *Medical Physics*, **45**(1), 236–249.

Cignoni, P., M. Callieri, M. Corsini, M. Dellepiane, F. Ganovelli, and G. Ranzuglia, MeshLab: an Open-Source Mesh Processing Tool. In **V. Scarano, R. D. Chiara, and U. Erra** (eds.), *Eurographics Italian Chapter Conference*. The Eurographics Association, 2008.

ClinRisk (2016). QFracture-2016 risk calculator. www.qfracture.org. (Accessed on April, 2018).

CloudCompare (2018). CloudCompare- 3D point cloud and mesh processing software open source project. <https://www.danielgm.net/cc/>. (Accessed on August, 2018).

Cootes, T. F., G. J. Edwards, and C. J. Taylor (2001). Active appearance models. *IEEE Transactions on Pattern Analysis Machine Intelligence*, (6), 681–685.

Cootes, T. F., C. J. Taylor, D. H. Cooper, and J. Graham (1995). Active shape models- their training and application. *Computer Vision and Image Understanding*, **61**(1), 38–59.

Crawford, R. P., C. E. Cann, and T. M. Keaveny (2003). Finite element models predict in vitro vertebral body compressive strength better than quantitative computed tomography. *Bone*, **33**(4), 744–750.

Dabov, K., A. Foi, V. Katkovnik, and K. Egiazarian (2007). Image denoising by sparse 3-D transform-domain collaborative filtering. *IEEE Transactions on Image Processing*, **16**(8), 2080–2095.

Dagan, N., C. Cohen-Stavi, M. Leventer-Roberts, and R. D. Balicer (2017). External validation and comparison of three prediction tools for risk of osteoporotic fractures using data from population based electronic health records: Retrospective cohort study. *BMJ*, **356**, i6755.

de Jong, J. J., F. L. Heyer, J. J. Arts, M. Poeze, A. P. Keszei, P. C. Willems, B. van Rietbergen, P. P. Geusens, and J. P. van den Bergh (2016). Fracture repair in the distal radius in postmenopausal women: A follow-up 2 years postfracture using HRpQCT. *Journal of Bone and Mineral Research*, **31**(5), 1114–1122.

Dendere, R., G. Kabelitz, and T. S. Douglas, Model-based segmentation of the middle phalanx in digital radiographic images of the hand. *In Proceedings of 35th Annual IEEE International Conference of IEEE Engineering in Medicine and Biology Society (EMBC)*. IEEE, 2013.

Deniz, C. M., S. Hallyburton, A. Welbeck, S. Honig, K. Cho, and G. Chang (2017). Segmentation of the proximal femur from MR images using deep convolutional neural networks.

Diez-Perez, A., J. Gonzalez-Macias, F. Marin, M. Abizanda, R. Alvarez, A. Gimeno, E. Pegenaute, J. Vila, E. study investigators, et al. (2007). Prediction of absolute risk of non-spinal fractures using clinical risk factors and heel quantitative ultrasound. *Osteoporosis International*, **18**(5), 629–639.

Dougherty, E. R., R. A. Lotufo, and T. I. S. for Optical Engineering SPIE, *Hands-on Morphological Image Processing*, volume 71. SPIE Optical Engineering Press, Washington, 2003.

El Hassani, A. S., M. El Hassouni, L. Houam, M. Rziza, E. Lespessailles, and R. Jennane, Texture analysis using dual tree M-band and Rényi entropy: Application to osteoporosis diagnosis on bone radiographs. *In Proceedings of 9th IEEE International Symposium on Biomedical Imaging (ISBI)*. IEEE, 2012.

El Hassouni, M., A. Tafraouti, H. Toumi, E. Lespessailles, and R. Jennane (2017). Fractional Brownian motion and Rao geodesic distance for bone X-Ray image characterization. *IEEE Journal of Biomedical and Health Informatics*, **21**(5), 1347–1359.

Fedorov, A., R. Beichel, J. Kalpathy-Cramer, J. Finet, J.-C. Fillion-Robin, S. Pujol, C. Bauer, D. Jennings, F. Fennessy, M. Sonka, et al. (2012). 3D Slicer as an image computing platform for the quantitative imaging network. *Magnetic Resonance Imaging*, **30**(9), 1323–1341.

Fischer, L. (2009). Using shape particle filters for robust medical image segmentation. Technical report, Vienna University of Technology, Vienna, Austria.

Fisher, A. (2014). Cloud and cloud-shadow detection in SPOT5 HRG imagery with automated morphological feature extraction. *Remote Sensing*, **6**(1), 776–800.

FORE (2012). FORE FRC- 10-year fracture risk calculator version 2.0. <https://riskcalculator.fore.org/>. (Accessed on April, 2018).

Fourati, W. A. and M. S. Bouhleb (2011). Trabecular bone image segmentation using iterative watershed and multi resolution analysis. *International Journal of Bio-Science and Bio-Technology*, **3**(2), 71–82.

Fujiwara, S., T. Sone, K. Yamazaki, N. Yoshimura, K. Nakatsuka, N. Masunari, S. Fujita, K. Kushida, and M. Fukunaga (2005). Heel bone ultrasound predicts non-spine fracture in Japanese men and women. *Osteoporosis International*, **16**(12), 2107–2112.

Gaidel, A. and A. Khramov (2015). Application of texture analysis for automated osteoporosis diagnostics by plain hip radiography. *Pattern Recognition and Image Analysis*, **25**(2), 301–305.

Galloway, M. M. (1975). Texture analysis using gray level run lengths. *Computer Graphics and Image Processing*, **4**(2), 172–179.

Garnero, P., E. Hausherr, M.-C. Chapuy, C. Marcelli, H. Grandjean, C. Muller, C. Cormier, G. Breart, P. Meunier, and P. D. Delmas (1996). Markers of bone resorption predict hip fracture in elderly women: The EPIDOS prospective study. *Journal of Bone and Mineral Research*, **11**(10), 1531–1538.

Garvan (2008). Garvan fracture risk calculator. www.garvan.org.au/promotions/bone-fracture-risk/calculator. (Accessed on April, 2018).

Geddam, J. J. B. (2009). *Osteoporosis in Andhra Pradesh, India, determinants and their correlation with bone parameters of men and women with osteoporosis hip fractures case control study*. Master's thesis, Amsterdam, The Netherlands.

Geusens, P., M. C. Hochberg, D. J. van der Voort, H. Pols, M. van der Klift, E. Siris, M. E. Melton, J. Turpin, C. Byrnes, and P. D. Ross, Performance of risk indices for identifying low bone density in postmenopausal women. *In Mayo Clinic Proceedings*, volume 77. Elsevier, 2002.

Ghosh, S., R. S. Alomari, V. Chaudhary, and G. Dhillon, Automatic lumbar vertebra segmentation from clinical CT for wedge compression fracture diagnosis. *In Proceedings of SPIE*, volume 3. 2011.

GIMP (2012). GIMP- the free and open source image editor. <https://www.gimp.org/>. (Accessed on August, 2018).

Gl, M. G., H. W. Minne, C.-C. Gl, A. D. Lazarescu, M. Pfeifer, F. H. Perschel, R. Fitzner, W. Pollähne, T. Schlotthauer, M. Pospeschill, et al. (2005). Prospective identification of postmenopausal osteoporotic women at high vertebral fracture risk by radiography, bone densitometry, quantitative ultrasound, and laboratory findings: Results from the PIOS study. *Journal of Clinical Densitometry*, **8**(4), 386–395.

Gomberg, B. R., P. K. Saha, and F. W. Wehrli (2003). Topology-based orientation analysis of trabecular bone networks. *Medical Physics*, **30**(2), 158–168.

- Gregory, J. S., A. Stewart, P. E. Undrill, D. M. Reid, and R. M. Aspden** (2004). Identification of hip fracture patients from radiographs using Fourier analysis of the trabecular structure: A cross-sectional study. *BMC Medical Imaging*, **4**(1), 4.
- Gullberg, B., O. Johnell, and J. Kanis** (1997). World-wide projections for hip fracture. *Osteoporosis international*, **7**(5), 407–413.
- Hallyburton, S., G. Chang, S. Honig, K. Cho, and C. M. Deniz** (2017). Automatic segmentation of MR images of the proximal femur using deep learning, 3986.
- Hannan, M. T., D. T. Felson, and J. J. Anderson** (1992). Bone mineral density in elderly men and women: Results from the Framingham osteoporosis study. *Journal of Bone and Mineral Research*, **7**(5), 547–553.
- Hans, D., F. Hartl, and M. Krieg** (2003). Device-specific weighted T-score for two quantitative ultrasounds: Operational propositions for the management of osteoporosis for 65 years and older women in Switzerland. *Osteoporosis International*, **14**(3), 251–258.
- Haralick, R. M.** (1979). Statistical and structural approaches to texture. *Proceedings of the IEEE*, **67**(5), 786–804.
- Harrar, K. and L. Hamami** (2013). An interconnectivity index for osteoporosis assessment using X-ray images. *Journal of Medical and Biological Engineering*, **33**(6), 569–575.
- Harrar, K. and R. Jennane** (2015). Trabecular texture analysis using fractal metrics for bone fragility assessment. *International Journal of Biomedical and Biological Engineering*, **9**(9), 683–688.
- Harrar, K., R. Jennane, K. Zaouchi, T. Janvier, H. Toumi, and E. Lespessailles** (2018). Oriented fractal analysis for improved bone microarchitecture characterization. *Biomedical Signal Processing and Control*, **39**, 474–485.
- Harvey, N. C., E. V. McCloskey, P. J. Mitchell, B. Dawson-Hughes, D. D. Pierroz, J.-Y. Reginster, R. Rizzoli, C. Cooper, and J. A. Kanis** (2017). Mind the (treatment)

gap: a global perspective on current and future strategies for prevention of fragility fractures. *Osteoporosis International*, **28**(5), 1507–1529.

Hernlund, E., A. Svedbom, M. Ivergård, J. Compston, C. Cooper, J. Stenmark, E. V. McCloskey, B. Jönsson, and J. A. Kanis (2013). Osteoporosis in the European Union: medical management, epidemiology and economic burden. *Archives of Osteoporosis*, **8**(1-2), 136.

Hippisley-Cox, J. and C. Coupland (2012). Derivation and validation of updated QFracture algorithm to predict risk of osteoporotic fracture in primary care in the United Kingdom: Prospective open cohort study. *BMJ*, **344**, e3427.

Hollaender, R., F. Hartl, M. Krieg, A. Tyndall, C. Geuckel, C. Buitrago-Tellez, M. Manghani, M. Kraenzlin, R. Theiler, and D. Hans (2009). Prospective evaluation of risk of vertebral fractures using quantitative ultrasound measurements and bone mineral density in a population-based sample of postmenopausal women: Results of the Basel Osteoporosis Study. *Annals of Rheumatic Diseases*, **68**(3), 391–396.

Houam, L., A. Hafiane, A. Boukrouche, E. Lespessailles, and R. Jennane, Texture characterization using local binary pattern and wavelets: Application to bone radiographs. In *Proceedings of 3rd International Conference on Image Processing Theory, Tools and Applications (IPTA)*. IEEE, 2012.

Houam, L., A. Hafiane, A. Boukrouche, E. Lespessailles, and R. Jennane (2014). One dimensional local binary pattern for bone texture characterization. *Pattern Analysis and Applications*, **17**(1), 179–193.

Huddleston, A. L., *Quantitative Methods in Bone Densitometry*. Kluwer Academic Publishers, 1988.

Hui, S. L., S. Gao, X.-H. Zhou, C. C. Johnston, Y. Lu, C. C. Glüer, S. Grampp, and H. Genant (1997). Universal standardization of bone density measurements: A method with optimal properties for calibration among several instruments. *Journal of Bone and Mineral Research*, **12**(9), 1463–1470.

Hwang, J. J., J.-H. Lee, S.-S. Han, Y. H. Kim, H.-G. Jeong, Y. J. Choi, and W. Park (2017). Strut analysis for osteoporosis detection model using dental panoramic radiography. *Dentomaxillofacial Radiology*, **46**(7), 20170006.

Ikuta, A., S. Kumasaka, and I. Kashima (2000). Quantitative analysis using the star volume method applied to skeleton patterns extracted with a morphological filter. *Journal of Bone and Mineral Metabolism*, **18**(5), 271–277.

Insider (2013). Choosing a clinical centre for a bone/joint health human study. www.naturalproductsinsider.com/articles/2013/08/choosing-a-clinical-center-for-a-bone-joint-health.aspx. (Accessed on January, 2016).

International Osteoporosis Foundation (2013). Asia-Pacific regional audit on epidemiology, costs and burden of osteoporosis in 2013. Technical report, IOF Regionals 4th Asia-Pacific Osteoporosis Meeting, Hong Kong.

International Society for Clinical Densitometry (2012). A basic primer on vertebral fracture assessment (VFA). <https://www.iscd.org/publications/osteoflash/a-basic-primer-on-vertebral-fracture-assessment-vfa/>. (Accessed on April, 2018).

International Society for Clinical Densitometry (2015). ISCD official positions. <https://www.iscd.org/official-positions/2015-iscd-official-positions-adult/>. (Accessed on April, 2018).

Jennane, R., R. Harba, G. Lemineur, S. Bretteil, A. Estrade, and C. L. Benhamou (2007). Estimation of the 3D self-similarity parameter of trabecular bone from its 2D projection. *Medical Image Analysis*, **11**(1), 91–98.

Jennane, R., W. J. Ohley, S. Majumdar, and G. Lemineur (2001). Fractal analysis of bone X-ray tomographic microscopy projections. *IEEE Transactions on Medical Imaging*, **20**(5), 443–449.

Jennane, R., J. Touvier, M. Bergounioux, and E. Lespessailles, A variational model for trabecular bone radiograph characterization. *In Proceedings of 11th IEEE International Symposium on Biomedical Imaging (ISBI)*. IEEE, 2014.

- Jeong, H., J. Kim, T. Ishida, M. Akiyama, and Y. Kim** (2013). Computerised analysis of osteoporotic bone patterns using texture parameters characterising bone architecture. *British Journal of Radiology*, **86**(1021), 1–10.
- Jhamaria, N., K. Lal, M. Udawat, P. Banerji, and S. Kabra** (1983). The trabecular pattern of the calcaneum as an index of osteoporosis. *Bone and Joint Journal*, **65**(2), 195–198.
- Jiang, H., C. J. Yates, A. Gorelik, A. Kale, Q. Song, and J. D. Wark** (2018). Peripheral quantitative computed tomography (pQCT) measures contribute to the understanding of bone fragility in older patients with low-trauma fracture. *Journal of Clinical Densitometry*, **21**(1), 140–147.
- Johnell, O. and J. Kanis** (2005). Epidemiology of osteoporotic fractures. *Osteoporosis International*, **16**(2), S3–S7.
- Kanis, J. A.** (2002). Diagnosis of osteoporosis and assessment of fracture risk. *The Lancet*, **359**(9321), 1929–1936.
- Kanis, J. A., E. V. McCloskey, H. Johansson, A. Oden, L. J. Melton, and N. Khaltsev** (2008). A reference standard for the description of osteoporosis. *Bone*, **42**(3), 467–475.
- Karade, V. and B. Ravi** (2015). 3D femur model reconstruction from biplane X-ray images: a novel method based on Laplacian surface deformation. *International Journal of Computer Assisted Radiology and Surgery*, **10**(4), 473–485.
- Karunanithi, R., S. Ganesan, T. Panicker, M. P. Korath, and K. Jagadeesan** (2007). Assessment of bone mineral density by DXA and the trabecular microarchitecture of the calcaneum by texture analysis in pre-and postmenopausal women in the evaluation of osteoporosis. *Journal of Medical Physics*, **32**(4), 161–168.
- Kass, M., A. Witkin, and D. Terzopoulos** (1988). Snakes: Active contour models. *International Journal of Computer Vision*, **1**(4), 321–331.

Kathirvelu, D. and **M. Anburajan** (2014). Prediction of low bone mass using a combinational approach of cortical and trabecular bone measures from dental panoramic radiographs. *Proceedings of the Institution of Mechanical Engineers, Part H: Journal of Engineering in Medicine*, **228**(9), 890–898.

Kavitha, M. S., P. Ganesh Kumar, S.-Y. Park, K.-H. Huh, M.-S. Heo, T. Kurita, A. Asano, S.-Y. An, and S.-I. Chien (2016). Automatic detection of osteoporosis based on hybrid genetic swarm fuzzy classifier approaches. *Dentomaxillofacial Radiology*, **45**(7), 20160076.

Kini, U. and **B. Nandeesh**, Physiology of bone formation, remodeling, and metabolism. *In Radionuclide and Hybrid Bone Imaging*. Springer, 2012, 29–57.

Koh, L., W. B. Sedrine, T. Torralba, A. Kung, S. Fujiwara, S. Chan, Q. Huang, R. Rajatanavin, K. Tsai, H. Park, et al. (2001). A simple tool to identify Asian women at increased risk of osteoporosis. *Osteoporosis International*, **12**(8), 699–705.

Korchiyne, R., S. M. Farssi, A. Sbihi, R. Touahni, and M. T. Alaoui (2014). A combined method of fractal and GLCM features for MRI and CT scan images classification.

Korfatis, V., S. Tassani, and G. K. Matsopoulos (). An independent active contours segmentation framework for bone micro-CT images.

Kovalovs, M. and **A. Glazs** (2013). Trabecular bone segmentation by using an adaptive contour. *Rigas Tehniskas Universitates Zinatniskie Raksti*, **14**, 6.

Krieg, M.-A., J. Cornuz, C. Ruffieux, G. Van Melle, D. Büche, M. A. Dambacher, D. Hans, F. Hartl, H. J. Häuselmann, M. Kraenzlin, et al. (2006). Prediction of hip fracture risk by quantitative ultrasound in more than 7000 Swiss women 70 years of age: Comparison of three technologically different bone ultrasound devices in the SEMOF study. *Journal of Bone and Mineral Research*, **21**(9), 1457–1463.

Krizhevsky, A., I. Sutskever, and G. E. Hinton, Imagenet classification with deep convolutional neural networks. *In Advances in Neural Information Processing Systems*. 2012.

- Kuse, M., Y.-F. Wang, V. Kalasannavar, M. Khan, and N. Rajpoot** (2011). Local isotropic phase symmetry measure for detection of beta cells and lymphocytes. *Journal of Pathology Informatics*, **2**.
- Lahari, M. S., M. Anburajan, et al.**, Finite element analysis of femur in the evaluation of osteoporosis. In *Proceedings of 3rd International Conference on Electronics and Computer Technology (ICECT)*, volume 3. IEEE, 2011.
- Laws, K. I.** (1980). Textured image segmentation. Technical report, University of Southern California, Los Angeles, California.
- Lee, S., S. Cho, and Y. M. Ro** (2011). Enhanced distal radius segmentation in DXA using modified ASM. *IEICE Transactions on Information and Systems*, **94**(2), 363–370.
- Lee, S., J. W. Lee, J.-W. Jeong, D.-S. Yoo, and S. Kim**, A preliminary study on discrimination of osteoporotic fractured group from nonfractured group using support vector machine. In *Proceedings of 30th Annual International Conference of the IEEE Engineering in Medicine and Biology Society (EMBS)*. IEEE, 2008.
- Legrand, E., D. Chappard, C. Pascaretti, M. Duquenne, S. Krebs, V. Rohmer, M.-F. Basle, and M. Audran** (2000). Trabecular bone microarchitecture, bone mineral density, and vertebral fractures in male osteoporosis. *Journal of Bone and Mineral Research*, **15**(1), 13–19.
- Lemineur, G., R. Harba, R. Jennane, A. Estrade, and L. Benhamou**, Fractal anisotropy measurement of bone texture radiographs. In *Proceedings of 1st International Symposium on Control, Communications and Signal Processing*. IEEE, 2004.
- Leslie, W. D., S. R. Majumdar, S. N. Morin, and L. M. Lix** (2015). Why does rate of bone density loss not predict fracture risk? *The Journal of Clinical Endocrinology and Metabolism*, **100**(2), 679–683.
- Lespessailles, E., C. Gadois, I. Kousignian, J. Neveu, P. Fardellone, S. Kolta, C. Roux, J. Do-Huu, and C. Benhamou** (2008). Clinical interest of bone texture

analysis in osteoporosis: A case control multicenter study. *Osteoporosis International*, **19**(7), 1019–1028.

Ligesh, C. A. S., N. Shanker, A. Vijay, M. Anburajan, and C. Glueer, Estimation of bone mineral density from the digital image of the calcanium bone. In *3rd International Conference on Electronics Computer Technology (ICECT)*, volume 3. IEEE, 2011.

Lin, J., M. Amling, D. Newitt, K. Selby, S. Srivastav, G. Delling, H. Genant, and S. Majumdar (1998). Heterogeneity of trabecular bone structure in the calcaneus using magnetic resonance imaging. *Osteoporosis International*, **8**(1), 16–24.

Link, T. M. (2012). Osteoporosis imaging: state of the art and advanced imaging. *Radiology*, **263**(1), 3–17.

Link, T. M., V. Vieth, J. Matheis, D. Newitt, Y. Lu, E. J. Rummeny, and S. Majumdar (2002). Bone structure of the distal radius and the calcaneus vs BMD of the spine and proximal femur in the prediction of osteoporotic spine fractures. *European Radiology*, **12**(2), 401–408.

Liu, X. S., A. Cohen, E. Shane, P. T. Yin, E. M. Stein, H. Rogers, S. L. Kokolus, D. J. McMahon, J. M. Lappe, R. R. Recker, et al. (2010). Bone density, geometry, microstructure, and stiffness: Relationships between peripheral and central skeletal sites assessed by DXA, HR-pQCT, and cQCT in premenopausal women. *Journal of Bone and Mineral Research*, **25**(10), 2229–2238.

Liu, X. S., E. M. Stein, B. Zhou, C. A. Zhang, T. L. Nickolas, A. Cohen, V. Thomas, D. J. McMahon, F. Cosman, J. Nieves, et al. (2012). Individual trabecula segmentation (its)-based morphological analyses and microfinite element analysis of HR-pQCT images discriminate postmenopausal fragility fractures independent of DXA measurements. *Journal of Bone and Mineral Research*, **27**(2), 263–272.

Looker, A., D. Bauer, C. Chesnut Iii, C. Gundberg, M. Hochberg, G. Klee, M. Kleerekoper, N. Watts, and N. Bell (2000). Clinical use of biochemical markers of bone remodeling: current status and future directions. *Osteoporosis International*, **11**(6), 467–480.

Loussot, T., R. Harba, G. Jacquet, C. L. Benhamou, E. Lespessailles, and A. Julien, An oriented fractal analysis for the characterization of texture. Application to bone radiographs. *In Proceedings of 8th European Signal Processing Conference (EUSIPCO)*. IEEE, 1996.

Lu, Y., T. Fuerst, S. Hui, and H. Genant (2001). Standardization of bone mineral density at femoral neck, trochanter and Wards triangle. *Osteoporosis International*, **12**(6), 438–444.

Luis-Garcia, D., M. Martin-Fernández, J. I. Arribas, C. Alberola-López, et al., A fully automatic algorithm for contour detection of bones in hand radiographs using active contours. *In Proceedings of International Conference on Image Processing (ICIP)*, volume 3. IEEE, 2003.

Majumdar, S., T. M. Link, J. Millard, J. C. Lin, P. Augat, D. Newitt, N. Lane, and H. K. Genant (2000). In vivo assessment of trabecular bone structure using fractal analysis of distal radius radiographs. *Medical Physics*, **27**(11), 2594–2599.

Mallard, F., B. Bouvard, P. Mercier, P. Bizot, P. Cronier, and D. Chappard (2013). Trabecular microarchitecture in established osteoporosis: Relationship between vertebrae, distal radius and calcaneus by x-ray imaging texture analysis. *Orthopaedics & Traumatology: Surgery & Research*, **99**(1), 52–59.

Marcu, F., F. Bogdan, G. Mutiu, and L. Lazar (2011). The histopathological study of osteoporosis. *Rom Journal of Morphol Embryol*, **52**(1), 321–325.

Materka, A., P. Cichy, and J. Tuliszkiwicz (2000). Texture analysis of X-ray images for detection of changes in bone mass and structure. *Series in Machine Perception and Artificial Intelligence*, **40**, 189–196.

Mccreadie, B. R. and S. A. Goldstein (2000). Biomechanics of fracture: Is bone mineral density sufficient to assess risk? *Journal of Bone and Mineral Research*, **15**(12), 2305–2308.

Medscape (2001). Fracture index with known bone mineral density. <https://reference.medscape.com/calculator/fracture-index-bone-mineral-density>. (Accessed on April, 2018).

Medscape (2002). OSTA- osteoporosis self assessment tool for women. <https://reference.medscape.com/calculator/osteoporosis-self-assessment-women>. (Accessed on April, 2018).

Mei, K., F. K. Kopp, R. Bippus, T. Köhler, B. J. Schwaiger, A. S. Gersing, A. Fehringer, A. Sauter, D. Münzel, F. Pfeiffer, et al. (2017). Is multidetector CT-based bone mineral density and quantitative bone microstructure assessment at the spine still feasible using ultra-low tube current and sparse sampling? *European Radiology*, **27**(12), 5261–5271.

Melton, L. J. (2000). Who has osteoporosis? A conflict between clinical and public health perspectives. *Journal of Bone and Mineral Research*, **15**(12), 2309–2314.

Mengko, T. R. and J. T. Pramudito, Implementation of Gabor filter to texture analysis of radiographs in the assessment of osteoporosis. *In Proceedings of Asia-Pacific Conference on Circuits and Systems (APCCAS)*, volume 2. IEEE, 2002.

Mengko, T. R. and J. T. Pramudito (2004). Texture analysis of proximal femur radiographs for osteoporosis assessment. *WSEAS Transactions on Computers*, **3**(1), 92–97.

Meyer, F. (1994). Topographic distance and watershed lines. *Signal Processing*, **38**(1), 113–125.

Mishra, A. K., D. Kim, and I. Andayana, Development of three dimensional binary patterns for local bone structure analysis. *In Proceedings of IEEE International Conference on Bioinformatics and Biomedicine Workshops (BIBMW)*. IEEE, 2011.

Muramatsu, C., K. Horiba, T. Hayashi, T. Fukui, T. Hara, A. Katsumata, and H. Fujita (2016). Quantitative assessment of mandibular cortical erosion on dental panoramic radiographs for screening osteoporosis. *International Journal of Computer Assisted Radiology and Surgery*, **11**(11), 2021–2032.

- Myers, W.** (2013). Who gets early-onset osteoporosis? <https://www.everydayhealth.com/osteoporosis/who-gets-early-onset-osteoporosis.aspx>. (Accessed on October, 2018).
- Naik, A. M., S. V. Tikhe, S. D. Bhide, K. Kaliyamurthie, and T. Saravanan** (2016). Designing a feature vector for statistical texture analysis of mandibular bone. *Indian Journal of Science and Technology*, **9**(33), 1–4.
- Nasser, Y., M. El Hassouni, A. Brahim, H. Toumi, E. Lespessailles, and R. Jennane,** Diagnosis of osteoporosis disease from bone X-ray images with stacked sparse autoencoder and SVM classifier. *In International Conference on Advanced Technologies for Signal and Image Processing (ATSIP)*. IEEE, 2017.
- Naylor, K. E., E. V. McCloskey, R. Eastell, and L. Yang** (2013). Use of DXA-based finite element analysis of the proximal femur in a longitudinal study of hip fracture. *Journal of Bone and Mineral Research*, **28**(5), 1014–1021.
- Nguyen, N. D., H. G. Ahlborg, J. R. Center, J. A. Eisman, and T. V. Nguyen** (2007). Residual lifetime risk of fractures in women and men. *Journal of Bone and Mineral Research*, **22**(6), 781–788.
- Njeh, C., D. Hans, J. Li, B. Fan, T. Fuerst, Y. He, E. Tsuda-Futami, Y. Lu, C. Wu, and H. Genant** (2000). Comparison of six calcaneal quantitative ultrasound devices: Precision and hip fracture discrimination. *Osteoporosis International*, **11**(12), 1051–1062.
- Numayama, S., S. Kumasaka, and I. Kashima** (2002). Application of node-strut analysis to skeletal patterns on digital radiographic images. *Oral Radiology*, **18**(2), 31–39.
- Ohlsson, C., D. Sundh, A. Wallerek, M. Nilsson, M. Karlsson, H. Johansson, D. Mellström, and M. Lorentzon** (2016). Cortical bone area predicts incident fractures independently of areal bone mineral density in older men. *Journal of Clinical Endocrinology and Metabolism*, **102**(2), 516–524.

Orwoll, E., J. B. Blank, E. Barrett-Connor, J. Cauley, S. Cummings, K. Ensrud, C. Lewis, P. M. Cawthon, R. Marcus, L. M. Marshall, et al. (2005). Design and baseline characteristics of the osteoporotic fractures in men (MrOS) study: a large observational study of the determinants of fracture in older men. *Contemporary Clinical Trials*, **26**(5), 569–585.

Otsu, N. (1975). A threshold selection method from gray-level histograms. *Automatica*, **11**(285-296), 23–27.

Oulhaj, H., M. Rziza, A. Amine, H. Toumi, E. Lespessailles, M. El Hassouni, and R. Jennane (2017a). Anisotropic discrete dual-tree wavelet transform for improved classification of trabecular bone. *IEEE Transactions on Medical Imaging*, **36**(10), 2077–2086.

Oulhaj, H., M. Rziza, A. Amine, H. Toumi, E. Lespessailles, R. Jennane, and M. El Hassouni (2017b). Trabecular bone characterization using circular parametric models. *Biomedical Signal Processing and Control*, **33**, 411–421.

Pal, A. B. and M. Anburajan, Digital image processing of calcaneum X-ray in the evaluation of osteoporosis in women: A comparison with DXA bone densitometer as a standard. In *Proceedings of IEEE Sponsored 3rd International Conference on Electronics and Communications Systems (ICECS)*. 2016.

Pande, K., S. Pande, D. de Takats, and E. McCloskey (2005). Modified calcaneal index: A new screening tool for osteoporosis based on plain radiographs of the calcaneum. *Journal of Orthopaedic Surgery*, **13**(1), 27–33.

Paul, R., S. Alahamri, S. Malla, and G. J. Quadri (2017). Make your bone great again: A study on osteoporosis classification.

Petpon, A. and S. Srisuk, Face recognition with local line binary pattern. In *Proceedings of 5th International Conference on Image and Graphics (ICIG)*. IEEE, 2009.

Petrantonaki, M., T. Maris, and J. Dailakis (2005). MRI techniques for the examination of trabecular bone structure. *Current Medical Imaging Reviews*, **1**(1), 35–41.

- Popp, A. W., S. Meer, M.-A. Krieg, R. Perrelet, D. Hans, and K. Lippuner** (2016). Bone mineral density (BMD) and vertebral trabecular bone score (TBS) for the identification of elderly women at high risk for fracture: the SEMOF cohort study. *European Spine Journal*, **25**(11), 3432–3438.
- Pothuaud, L., C. Benhamou, P. Porion, E. Lespessailles, R. Harba, and P. Levitz** (2000). Fractal dimension of trabecular bone projection texture is related to three-dimensional microarchitecture. *Journal of Bone and Mineral Research*, **15**(4), 691–699.
- Pothuaud, L., P. Carceller, and D. Hans** (2008). Correlations between grey-level variations in 2D projection images (TBS) and 3D microarchitecture: Applications in the study of human trabecular bone microarchitecture. *Bone*, **42**(4), 775–787.
- Pramudito, J., S. Soegijoko, T. Mengko, F. Muchtadi, and R. Wachjudi** (2007). Trabecular pattern analysis of proximal femur radiographs for osteoporosis detection. *Journal of Biomedical and Pharmaceutical Engineering*, **1**(1), 45–51.
- Quijano, S., A. Serrurier, B. Aubert, S. Laporte, P. Thoreux, and W. Skalli** (2013). Three-dimensional reconstruction of the lower limb from biplanar calibrated radiographs. *Medical Engineering & Physics*, **35**(12), 1703–1712.
- Rachidi, M., C. Chappard, A. Marchadier, C. Gadois, E. Lespessailles, and C. L. Benhamou**, Application of Laws' masks to bone texture analysis: An innovative image analysis tool in osteoporosis. In *Proceedings of 5th IEEE International Symposium on Biomedical Imaging: From Nano to Macro (ISBI)*. IEEE, 2008.
- Raheja, A. J.** (2008). *Automated analysis of metacarpal cortical thickness in serial hand radiographs*. Master's thesis, Department of Biomedical, Industrial and Human Factors Engineering, Wright State University, Dayton, Ohio.
- Rajapakse, C., E. Phillips, W. Sun, M. Wald, J. Magland, P. Snyder, and F. Wehrli** (2014). Vertebral deformities and fractures are associated with MRI and pQCT measures obtained at the distal tibia and radius of postmenopausal women. *Osteoporosis International*, **25**(3), 973–982.

Razmkhah, O. and H. Ghasemnejad (2016). Explicit finite element analysis to predict impact damage response of osteoporosis hip bone. *Computer Methods in Biomechanics and Biomedical Engineering: Imaging and Visualization*, **4**(1), 17–29.

Reddy, M. V. K., B. Ganesh, K. Bharathi, and P. ChittiBabu (2016). Use of finite element analysis to predict type of bone fractures and fracture risks in femur due to osteoporosis. *Journal of Osteoporosis and Physical Activity*, 1–8.

Ripamonti, C., L. Lisi, A. Buffa, S. Gnudi, and R. Caudarella (2018). The trabecular bone score predicts spine fragility fractures in postmenopausal Caucasian women without osteoporosis independently of bone mineral density. *Medical Archives*, **72**(1), 46–50.

Roberts, M., T. F. Cootes, and J. E. Adams (2006). Vertebral morphometry: Semiautomatic determination of detailed shape from dual-energy X-ray absorptiometry images using active appearance models. *Investigative Radiology*, **41**(12), 849–859.

Roberts, M. G., J. Graham, and H. Devlin (2013). Image texture in dental panoramic radiographs as a potential biomarker of osteoporosis. *IEEE Transactions on Biomedical Engineering*, **60**(9), 2384–2392.

Rock Creek Wellness (2018). Body composition analysis. <https://www.rockcreekwellness.com/dxa-analysis/>. (Accessed on April, 2018).

Rosdi, B. A., C. W. Shing, and S. A. Suandi (2011). Finger vein recognition using local line binary pattern. *Sensors*, **11**(12), 11357–11371.

Rosholm, A., L. Hyldstrup, L. Baeksgaard, M. Grunkin, and H. Thodberg (2001). Estimation of bone mineral density by digital X-ray radiogrammetry: Theoretical background and clinical testing. *Osteoporosis International*, **12**(11), 961–969.

Roux, S., F. Cabana, N. Carrier, M. Beaulieu, P.-M. April, M.-C. Beaulieu, and G. Boire (2014). The World Health Organization Fracture Risk Assessment Tool (FRAX) underestimates incident and recurrent fractures in consecutive patients with fragility fractures. *Journal of Clinical Endocrinology and Metabolism*, **99**(7), 2400–2408.

- Santhoshini, P., R. Tamilselvi, and R. Sivakumar** (2013). Automatic segmentation of femur bone features and analysis of osteoporosis. *Lecture Notes on Software Engineering*, **1**(2), 194–198.
- Sapthagirivasan, V. and M. Anburajan** (2013). Diagnosis of osteoporosis by extraction of trabecular features from hip radiographs using support vector machine: An investigation panorama with DXA. *Computers in Biology and Medicine*, **43**(11), 1910–1919.
- Sapthagirivasan, V., M. Anburajan, and V. Mahadevan** (2013). Bone trabecular analysis of femur radiographs for the assessment of osteoporosis using DWT and DXA. *International Journal of Computer Theory and Engineering*, **5**(4), 616–620.
- Saville, P. D.** (1973). The syndrome of spinal osteoporosis. *Clinics in Endocrinology and Metabolism*, **2**(2), 177–185.
- Schmah, T., N. Marwan, J. S. Thomsen, and P. Sapparín** (2011). Long range node-strut analysis of trabecular bone microarchitecture. *Medical Physics*, **38**(9), 5003–5011.
- Schott, A., D. Hans, F. Duboeuf, P. Dargent-Molina, T. Hajri, G. Breart, and P. Meunier** (2005). Quantitative ultrasound parameters as well as bone mineral density are better predictors of trochanteric than cervical hip fractures in elderly women. Results from the EPIDOS study. *Bone*, **37**(6), 858–863.
- Sela, E. I., S. Hartati, A. Harjoko, R. Wardoyo, and M. Munakhir** (2013). Segmentation on the dental periapical X-ray images for osteoporosis screening. *International Journal of Advanced Computer Science Applications*, **4**(7), 147–51.
- Shirvaikar, M., N. Huang, and X. N. Dong** (2016). The measurement of bone quality using gray level co-occurrence matrix textural features. *Journal of Medical Imaging and Health Informatics*, **6**(6), 1357–1362.
- Silva, B. C. and W. D. Leslie** (2017). Trabecular bone score. *Endocrinology and Metabolism Clinics*, **46**(1), 153–180.

Singh, A., M. K. Dutta, R. Jennane, and E. Lespessailles (2017). Classification of the trabecular bone structure of osteoporotic patients using machine vision. *Computers in Biology and Medicine*, **91**, 148–158.

Singh, M., A. Nagrath, and P. Maini (1970). Changes in trabecular pattern of the upper end of the femur as an index of osteoporosis. *Journal of Bone and Joint Surgery*, **52**(3), 457–467.

Siris, E., H. Genant, A. Laster, P. Chen, D. Misurski, and J. Krege (2007). Enhanced prediction of fracture risk combining vertebral fracture status and BMD. *Osteoporosis International*, **18**(6), 761–770.

Siris, E. S., P. D. Miller, E. Barrett-Connor, K. G. Faulkner, L. E. Wehren, T. A. Abbott, M. L. Berger, A. C. Santora, and L. M. Sherwood (2002). Identification and fracture outcomes of undiagnosed low bone mineral density in postmenopausal women: Results from the national osteoporosis risk assessment. *Obstetrical and Gynecological Survey*, **57**(4), 220–221.

Sornay-Rendu, E., F. Munoz, P. Garnero, F. Duboeuf, and P. D. Delmas (2005). Identification of osteopenic women at high risk of fracture: the OFELY study. *Journal of Bone and Mineral Research*, **20**(10), 1813–1819.

Statista (2018a). Number of computer tomography (CT) scanners in selected countries as of 2016 (per million population). <https://www.statista.com/statistics/266539/distribution-of-equipment-for-computer-tomography/>. (Accessed on April, 2018).

Statista (2018b). Number of magnetic resonance imaging (MRI) units in selected countries as of 2016 (per million population). <https://www.statista.com/statistics/282401/density-of-magnetic-resonance-imaging-units-by-country/>. (Accessed on April, 2018).

Suprijanto, E. Juliastuti, Y. Diputra, M. Mayantasari, and Azhari, Dental panoramic image analysis on mandibular bone for osteoporosis early detection. In *Proceedings of 3rd International Conference on Instrumentation Control and Automation (ICA)*. IEEE, 2013.

Tafraouti, A., M. El Hassouni, H. Toumi, E. Lespessailles, and R. Jennane, Osteoporosis diagnosis using frequency separation and fractional Brownian motion. *In Proceedings of International Conference on Wireless Networks and Mobile Communications (WINCOM)*. IEEE, 2017.

Tanaka, T., T. Sakurai, and I. Kashima (2001). Structuring of parameters for assessing vertebral bone strength by star volume analysis using a morphological filter. *Journal of Bone and Mineral Metabolism*, **19**(3), 150–158.

The Study of Osteoporotic Fractures (SOF) (1986). The study of osteoporotic fractures. <https://sofonline.epi-ucsf.org>. (Accessed on April, 2018).

Thevenot, J., J. Koivumäki, V. Kuhn, F. Eckstein, and T. Jämsä (2014). A novel methodology for generating 3D finite element models of the hip from 2D radiographs. *Journal of Biomechanics*, **47**(2), 438–444.

Thodberg, H., R. Van Rijn, T. Tanaka, D. Martin, and S. Kreiborg (2010). A paediatric bone index derived by automated radiogrammetry. *Osteoporosis International*, **21**(8), 1391–1400.

Thodberg, H. H. and A. Rosholm (2003). Application of the active shape model in a commercial medical device for bone densitometry. *Image and Vision Computing*, **21**(13), 1155–1161.

Tomasi, C. and R. Manduchi, Bilateral filtering for gray and color images. *In 6th International Conference on Computer Vision*. IEEE, 1998.

Touvier, J., R. Winzenrieth, H. Johansson, J. Roux, J. Chaintreuil, H. Toumi, R. Jennane, D. Hans, and E. Lespessailles (2015). Fracture discrimination by combined bone mineral density (BMD) and microarchitectural texture analysis. *Calcified Tissue International*, **96**(4), 274–283.

University of Orleans (2014). Challenge IEEE-ISBI: bone texture characterization. www.univ-orleans.fr/i3mto/challenge-ieee-isbi-bone-texture-characterization. (Accessed on April, 2018).

University of Sheffield (2008). FRAX fracture risk assessment tool. <https://www.sheffield.ac.uk/FRAX/tool.jsp>. (Accessed on April, 2018).

Unnanuntana, A., B. P. Gladnick, E. Donnelly, and J. M. Lane (2010). The assessment of fracture risk. *The Journal of Bone and Joint Surgery*, **92**(3), 743.

Valentinitsch, A., J. Patsch, D. Mueller, F. Kainberger, and G. Langs, Texture analysis in quantitative osteoporosis assessment: Characterizing microarchitecture. *In Proceedings of IEEE International Symposium on Biomedical Imaging: From Nano to Macro (ISBI)*. IEEE, 2010.

Varkevisser, C. M., I. Pathmanathan, and A. T. Brownlee, *Designing and Conducting Health Systems Research Projects*, volume 1. IDRC, 2003.

Veenland, J. F. (1999). *Texture analysis of the radiographic trabecular bone pattern in osteoporosis*. Ph.D. thesis, Erasmus University Rotterdam, Rotterdam, Netherlands.

Vokes, T., D. Lauderdale, S.-L. Ma, M. Chinander, K. Childs, and M. Giger (2010). Radiographic texture analysis of densitometric calcaneal images: Relationship to clinical characteristics and to bone fragility. *Journal of Bone and Mineral Research*, **25**(1), 56–63.

Wayne, N., *An Introduction to Digital Image Processing*. Prentice Hall, Eaglewood Cliffs, New Jersey, 1986.

Wehrli, F. W. (2007). Structural and functional assessment of trabecular and cortical bone by micro magnetic resonance imaging. *Journal of Magnetic Resonance Imaging*, **25**(2), 390–409.

Werman, M. and S. Peleg, Multiresolution texture signatures using min-max operators. *In Proceedings of 7th International Conference on Pattern Recognition*. 1984.

WHO (2007). Assessment of osteoporosis at the primary health care level. Summary report of a WHO scientific group. Technical report, WHO Scientific Group. WHO, Geneva.

- Wigderowitz, C., C. Paterson, H. Dashti, D. McGurty, and D. Rowley** (2000). Prediction of bone strength from cancellous structure of the distal radius: can we improve on DXA? *Osteoporosis International*, **11**(10), 840–846.
- Xu, W., J. Xu, J. Zhao, and J. Sun** (2016). Finite element analysis of osteoporosis models based on synchrotron radiation. *Journal of Instrumentation*, **11**(04), C04002.
- Yger, F.** (2014). Challenge IEEE-ISBI/TCB: Application of covariance matrices and wavelet marginals.
- Zhang, J., L. Lv, X. Shi, Y. Wang, F. Guo, Y. Zhang, and H. Li** (2013). 3-D reconstruction of the spine from biplanar radiographs based on contour matching using the hough transform. *IEEE Transactions on Biomedical Engineering*, **60**(7), 1954–1964.
- Zhang, Z., J. Liu, R. Wang, and T. Li**, Study on medical image segmentation methods of humerus. *In Proceedings of 29th Chinese Control and Decision Conference (CCDC)*. IEEE, 2017.
- Zheng, G.**, 3D volumetric intensity reconstruction from 2D X-ray images using partial least squares regression. *In 10th International Symposium on Biomedical Imaging (ISBI)*. IEEE, 2013.
- Zheng, K. and S. Makrogiannis**, Bone texture characterization for osteoporosis diagnosis using digital radiography. *In Proceedings of IEEE 38th Annual International Conference of Engineering Medicine and Biology Society (EMBC)*. IEEE, 2016.
- Zhou, K., J. Cai, Y.-H. Xu, and T.-X. Wu** (2016). Osteoporosis recognition based on similarity metric with SVM. *International Journal of Bioautomation*, **20**(2), 253–264.

LIST OF PUBLICATIONS FROM THE THESIS

Refereed International Journals

1. Anu Shaju Areeckal, Nikil Jayasheelan, Jagannath Kamath, Sophie Zawadynski, Michel Kocher, and Sumam David S. (2018), “Early Diagnosis of Osteoporosis using Radiogrammetry and Texture Analysis from Hand and Wrist Radiographs in Indian Population”, *Osteoporosis International*, Springer Nature, Vol. 29, No. 3, pp.665-673, DOI: 10.1007/s00198-017-4328-1, SCI/WoS/Scopus indexed.
2. Anu Shaju Areeckal, Jagannath Kamath, Sophie Zawadynski, Michel Kocher and Sumam David S. (2018), “Combined Radiogrammetry and Texture Analysis for Early Diagnosis of Osteoporosis Using Indian and Swiss data”, *Computerized Medical Imaging and Graphics*, Elsevier, Vol. 68, No. 9, pp.25-39, DOI: 10.1016/j.compmedimag.2018.05.003, SCIE/WoS/Scopus indexed.
3. Anu Shaju Areeckal, Michel Kocher and Sumam David S. (2019), “Current and Emerging Diagnostic Imaging-Based Techniques for Assessment of Osteoporosis and Fracture Risk”, *IEEE Reviews in Biomedical Engineering*, Vol. 12, No. 1, pp.254-268, DOI: 10.1109/RBME.2018.2852620, Scopus indexed.

Refereed International Conferences

1. Anu Shaju Areeckal, Sumam David S., Michel Kocher, Nikil Jayasheelan, and Jagannath Kamath (2016), “Fully Automated Radiogrammetric Measurement of Third Metacarpal Bone from Hand Radiograph”, *11th IEEE International Conference on Signal Processing and Communication (SPCOM)*, Bangalore, India, pp.1-5, June 12-15, 2016, DOI: 10.1109/SPCOM.2016.7746608, WoS/Scopus indexed.
2. Mathew Sam, Anu Shaju Areeckal, and Sumam David S. (2017), “Early Diagnosis of Osteoporosis Using Active Appearance Model and Metacarpal Radiogrammetry”, *13th IEEE International Conference on Signal Image Technology and Internet Based Systems (SITIS)*, Jaipur, India, pp.173-178, December 4-7, 2017, DOI: 10.1109/SITIS.2017.38, Scopus indexed.
3. Anu Shaju Areeckal, Mathew Sam, and Sumam David S. (2018), “Computerized Radiogrammetry of Third Metacarpal Using Watershed and Active Appearance Model”, *19th IEEE International Conference on Industrial Technology (ICIT)*, Lyon, France, pp.1490-1495, February 20-22, 2018, DOI: 10.1109/ICIT.2018.8352401, Scopus indexed.

4. Avinash D. Jayakar, Gautham Sambath, Anu Shaju Areeckal and Sumam David S. (2018), “Cortical Volumetry using 3D Reconstruction of Metacarpal Bone from Multi-view Images”, *4th IEEE International Conference on Recent Advances in Computational Systems (RAICS)*, Thiruvananthapuram, India, pp.79-83, December 6-8, 2018, DOI: 10.1109/RAICS.2018.8635067, Scopus indexed.

National Conference/Graduate Student Workshop

1. Anu Shaju Areeckal, Sumam David S., and Michel Kocher (2019), “Early diagnosis of osteoporosis using metacarpal radiogrammetry and texture analysis”, *Graduate Student Day Workshop, 25th National Conference on Communications (NCC)*, Indian Institute of Science (IISc), Bangalore, India, February 21, 2019 (Second position).

CURRICULUM VITAE

Anu Shaju Areeckal

Research Scholar,

Department of Electronics and Communication Engineering,

National Institute of Technology Karnataka, Surathkal,

Mangalore, India-575025

email: anu017@gmail.com

Qualification:

1. M.Tech. in VLSI Design from Department of Electronics and Communication Engineering, Karunya University, Tamil Nadu, India, in 2012.
2. B.Tech. in Electronics and Communication Engineering from Mahatma Gandhi University, Kerala, India, in 2010.

Teaching Experience:

1. Assistant Professor, Holy Grace Academy of Engineering, Mala, Kerala, India, from June 11, 2012 to January 1, 2014 (1 year 6 months).

Research Interests:

Image Processing, Machine learning.

Publications:

No.of International Journal Publications: 3

No.of International Conference Proceedings / Publications: 6